UNIVERSITÉ DU QUÉBEC À MONTRÉAL

SYNTHÈSE SOLVOTHERMIQUE ET FONCTIONNALISATION DE CADRES ORGANIQUES COVALENTS (COFS): SUPERCONDENSATEURS ET APPLICATIONS À L'ÉLECTROCATALYSE

THÈSE
PRÉSENTÉ(E)
COMME EXIGENCE PARTIELLE
DU DOCTORAT EN CHIMIE

PAR
AMIR KHOJASTEHNEZHAD GOLMAKANI

Mai 2024

REMERCIEMENTS

Je tiens à exprimer ma plus profonde gratitude envers mon estimé directeur de thèse de doctorat, le professeur Mohammed Siaj, dont les conseils inébranlables et l'expertise ont été essentiels à la réussite de mon parcours doctoral. La direction du professeur Siaj, ses commentaires perspicaces et son encouragement constant ont considérablement influencé la trajectoire de mes recherches et de mes activités académiques. Son engagement à favoriser un environnement collaboratif et intellectuellement stimulant a été inestimable, me permettant de développer des compétences de pensée critique et une compréhension approfondie de mon domaine de recherche. Je me considère vraiment chanceux d'avoir eu le privilège de travailler sous la direction du professeur Siaj, et je reconnais son rôle déterminant dans le façonnement de ma croissance académique et personnelle tout au long de mes études doctorales.

J'exprime ma sincère appréciation envers mon estimé directeur de thèse de doctorat, le professeur Hani El-Kaderi, pour ses conseils inestimables et ses commentaires précieux tout au long du processus de recherche. Les commentaires perspicaces du professeur Hani ont considérablement enrichi la profondeur et la qualité de mon travail, soulignant son engagement envers l'excellence académique. Sa direction a été une pierre angulaire de mon parcours académique, et je suis reconnaissant du privilège de bénéficier de son expertise et de son soutien.

J'apprécie tous les collaborateurs qui ont consacré leur temps et leur expertise pour promouvoir les progrès de cette thèse. Je remercie le professeur Farid Moeinpour de l'Université Azad (Iran), le Dr. Mohammad Shehab du groupe du professeur Hani El-Kaderi, ainsi que le Dr. Khaled Rhili et le Dr. Maziar Jafari de notre groupe.

Il est important de reconnaître la contribution significative de mes membres de comité aux progrès de cette thèse. Leurs questions et commentaires pendant la période d'évaluation m'ont permis de voir plus clairement où j'en étais et ce que j'avais omis. Un merci spécial aux professeurs Sylvain Canesi, professeur David Dewez et professeur Ali Nazemi de l'UQAM pour avoir accepté le rôle de membre du comité, ainsi qu'à la professeure Allison Wustrow de l'Université de Sherbrooke à titre d'arbitre externe.

À ceux avec qui j'ai passé la majeure partie de mon temps au cours de ces années, tous les membres du groupe Siaj, Zhiyuan, Elena, Hichem, Su, Ghizelane, Imane, Issa et Abeer, un grand merci pour votre soutien quotidien et votre humour qui ont rendu mes jours au Canada plus délicats.

La recherche ne pourrait avancer sans le soutien technique des professeurs Alexandre et Gwénaël, les excellents services de l'atelier de chimie de Luc et Chantal, l'aide aimable et bienveillante de Pascale et Mylène et de tous les techniciens du Département de chimie de l'UQAM notamment Jacqueline.

En fin de compte, merci à tous mes nouveaux amis, vieux amis et ma famille qui ont été avec moi pendant ces jours ordinaires précieux.

DÉDICACE

Je tiens à exprimer ma plus sincère gratitude envers ma famille, en particulier envers mon amour, Negin, pour avoir été des piliers de soutien indéfectibles tout au long des années exigeantes de mon parcours doctoral. L'encouragement infini, la compréhension et les sacrifices de Negin ont joué un rôle crucial en m'aidant à naviguer dans les complexités de la vie académique. Sa présence constante et sa foi en mes capacités ont été une source de force, me motivant à persévérer en période de défis. Je suis également extrêmement reconnaissant envers ma fille, Bahar, pour sa patience et sa compréhension alors qu'elle témoignait des longues heures consacrées à la recherche et à l'étude. L'amour et le soutien de ma famille ont été ma force motrice, et je suis vraiment reconnaissant pour leur engagement durable envers ma réussite.

TABLE DES MATIÈRES

LISTE DES FIGURES

LISTE DES ABRÉVIATIONS, DES SIGLES ET DES ACRONYMES

COF	Cadres Organiques Covalents
MOF	Cadres Métalliques Organiques
NP	Nanoparticule
DCM	Dichlorométhane
DMF	Diméthylformamide
DMSO	Diméthyl sulfoxyde
Et_2O	Diéthyléther
MeCN	Acétonitrile
THF	Tétrahydrofurane
PVP	Polyvinylpyrrolidone
VSM	Magnétomètre à échantillon vibrant
EDX	Spectrométrie de dispersion d'énergie des rayons X
ICP-OES	Spectrométrie d'émission optique à plasma couplé par induction
RMN	Résonance Magnétique Nucléaire
TEM	Microscopie électronique en transmission
SEM	Microscopie électronique à balayage
TGA	Analyse thermogravimétrique
UV-vis	Ultraviolet-visible
XPS	Spectroscopie photoélectronique à rayons X
PXRD	Diffraction des rayons X sur poudre
BET	Brunauer–Emmett–Teller
FT-IR	Spectroscopie infrarouge à transformée de Fourier

LISTE DES SYMBOLES ET DES UNITÉS

λ	Longueur d'onde
Đ	Dispersité
Mn	Poids moléculaire moyen en nombre
V	Volt
eV	Électronvolt
M	Mole/Litre
mM	Millimole/Litre
g	Gramme
mg	Milligramme
µg	Microgramme
L	Litre
mL	Millilitre
µL	Microlitre
nm	Nanomètre
mol	Mole
ppm	Parties par million (mg/L)
m^2/g	Mètre carré par gramme
kcal/mol	Kilocalorie par mole
Ɵ	Theta
mg L^{-1}	Mili gramm pro liter
$emug^{-1}$	Electromagnetic unit

RÉSUMÉ

Ma recherche peut être divisée en deux sections distinctes. La première section se concentre sur la synthèse et la fonctionnalisation de divers cadres organiques covalents (COFs) à base d'imine en 2D et 3D. J'ai préparé un COF magnétique à liaison imine avec une structure cœur-coquille, suivi d'une modification post-synthétique par des ligands thiol, permettant une élimination sélective et efficace des métaux lourds, notamment des ions mercure, des eaux usées. Cette approche offre une solution prometteuse pour atténuer la pollution environnementale et assurer des ressources en eau plus propres. Dans la deuxième partie de cette section, différentes méthodes et conditions ont été développées pour présenter de nouvelles méthodologies et de nouveaux catalyseurs pour la synthèse de divers COFs à base d'imine en 2D et 3D. Notamment, l'utilisation de catalyseurs à base d'acides hétéropolyacides s'est révélée être la condition la plus efficace. Ces catalyseurs ont considérablement accéléré la synthèse des COFs à base d'imine, réduisant le temps de réaction de plusieurs jours à quelques heures, tout en améliorant la cristallinité et le rendement des produits finaux. De manière impressionnante, certains de ces COFs ont montré des résultats prometteurs pour des applications de supercondensateurs, soulignant leur potentiel pour des solutions de stockage d'énergie avancées. La deuxième section impliquait la conception et la synthèse de réseaux organiques mésoporeux magnétiques à structure cœur-coquille (MONs). Après leur fonctionnalisation, des nanoparticules de Pd et de Cu ont été ancrées sur leur surface. Des tests futurs sont prévus pour évaluer leur efficacité en tant que catalyseurs magnétiques de métaux de transition dans la fixation du CO2 et les réactions de couplage croisé. Il est intéressant de noter que les nanoparticules de Pd chargées sur les MONs magnétiques à structure cœur-coquille sont capables de catalyser les réactions de couplage croisé de Suzuki et de Sonogashira dans des conditions douces et avec des temps de réaction courts, et les nanoparticules de Cu immobilisées sur les structures cœur-coquille pourraient catalyser la synthèse de dérivés carbonatés avec de bons à hauts rendements.

Mots clés: Cadres organiques covalents, réseaux organiques mésoporeux, catalyseur, eaux usées, supercondensateur, réactions de couplage croisé.

ABSTRACT

My research could be divided into two distinct sections. The first section focuses on the synthesis and functionalization of various 2D and 3D imine-based covalent organic frameworks (COFs). In which, I prepared a core-shell magnetic imine-linked COF and then post-synthetic modification by thiol ligands, enabling selective and efficient removal of heavy metals, particularly mercury ions, from wastewater. This approach offers a promising solution for mitigating environmental pollution and ensuring cleaner water resources. In the second part of this section, different methods and conditions to present new methodologies and catalysts for the synthesis of various 2D and 3D imine-based COFs were developed. Notably, the use of heteropoly acid catalysts emerged as the most effective condition. These catalysts notably expedited the synthesis of imine-based COFs, reducing the reaction time from days to mere hours, while also enhancing the crystallinity and yield of the final products. Impressively, some of these COFs demonstrated promising results for supercapacitor applications, highlighting their potential for advanced energy storage solutions. The second section involved the design and synthesis of a core-shell magnetic mesoporous organic networks (MONs). After its functionalization, Pd and Cu nanoparticles were anchored onto its surface. Future tests are planned to evaluate its efficacy as a magnetic transition metal catalyst in CO_2 fixation and cross-coupling reactions. Interestingly, the Pd NPs loaded on core-shell magnetic MONs are able to catalyze the Suzuki and Sonogashira cross coupling reactions in mild condition and short reaction times and Cu NPs immobilized on the core-shell structures could catalyze synthesis of carbonate derivatives in good to high yileds.

Keywords: Covalent organic frameworks, mesoporous organic networks, catalyst, waste water, supercapacitor, cross-coupling reaction.

INTRODUCTION

1.1 Cadres organiques covalents

1.1.1 Histoire et développements

Les matériaux organiques poreux et cristallins reliés par des liaisons covalentes entre des éléments légers sont connus sous le nom de COFs. Ces structures cristallines poreuses, caractérisées par un réseau bidimensionnel et tridimensionnel (2D et 3D), présentent des propriétés exceptionnelles qui les rendent très recherchées dans diverses applications scientifiques et industrielles.[1] Une grande surface spécifique, une haute porosité, une capacité de structures préconçues, un transfert efficace d'électrons et une stabilité thermique et chimique élevée ne sont que quelques-unes des qualités notables des matériaux COFs.[2] La synthèse des COFs implique la formation de liaisons covalentes fortes entre des unités de construction organiques, souvent par le biais de réactions réversibles, permettant un contrôle précis de l'architecture du cadre.[3] Cette nature modulaire et personnalisable a conduit à l'exploration de diverses applications pour les COFs, allant du stockage et de la séparation de gaz à la catalyse et à la détection.[4] Ils présentent également des structures diverses, en particulier des conformation éclipsée et décalée. Dans la structure éclipsée, les blocs de construction organiques adjacents s'alignent directement les uns sur les autres, donnant une disposition plus compacte, tandis que la conformation décalée implique un alignement plus espacé, contribuant à une porosité accrue et à une surface améliorée dans le cadre COF (Figure 1).

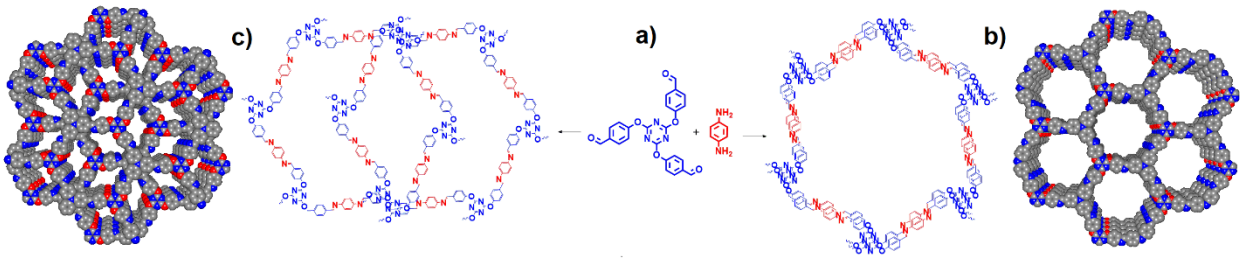

Figure 1 Synthèse schématique du COF lié par imine (a), différentes structures de COF; conformation éclipsée (b) et conformation décalée (c).

Le voyage dans le domaine des COFs a commencé avec le travail révolutionnaire d'Omar M. Yaghi et de ses collaborateurs, qui ont rapporté les premiers exemples de ces matériaux en 2005.[5] Les premières recherches se sont concentrées sur la compréhension des principes fondamentaux régissant la synthèse des COFs, mettant l'accent sur la formation de liaisons covalentes réversibles

entre les unités de construction organiques. À mesure que le domaine progressait, les chercheurs se sont aventurés dans une exploration étendue de diverses liaisons et unités de construction, aboutissant à la création d'un spectre diversifié de structures COF dotées de propriétés uniques (Figure 2).[3b] Des liaisons distinctes telles que l'imine, l'hydrazone, le cétokénamine, l'imide, le spiroborate, et ainsi de suite, ont été étudiées, permettant l'ajustement des attributs des COFs pour des applications spécifiques.[6] L'évolution de la synthèse des COFs a connu une innovation continue, offrant aux scientifiques la capacité d'ingénierie méticuleuse des structures, des porosités et des fonctionnalités. Au cœur des COFs réside leur architecture unique, qui les distingue d'autres matériaux poreux tels que les cadres organométalliques (MOFs) et les zéolithes.[7] Les liaisons covalentes connectant les unités organiques dans les COFs leur confèrent une stabilité et une robustesse remarquables, les rendant adaptés à une large gamme d'applications. La nature modulaire des COFs permet un contrôle précis de leurs structures, permettant la conception de matériaux aux propriétés spécifiques adaptées à des fins diverses.

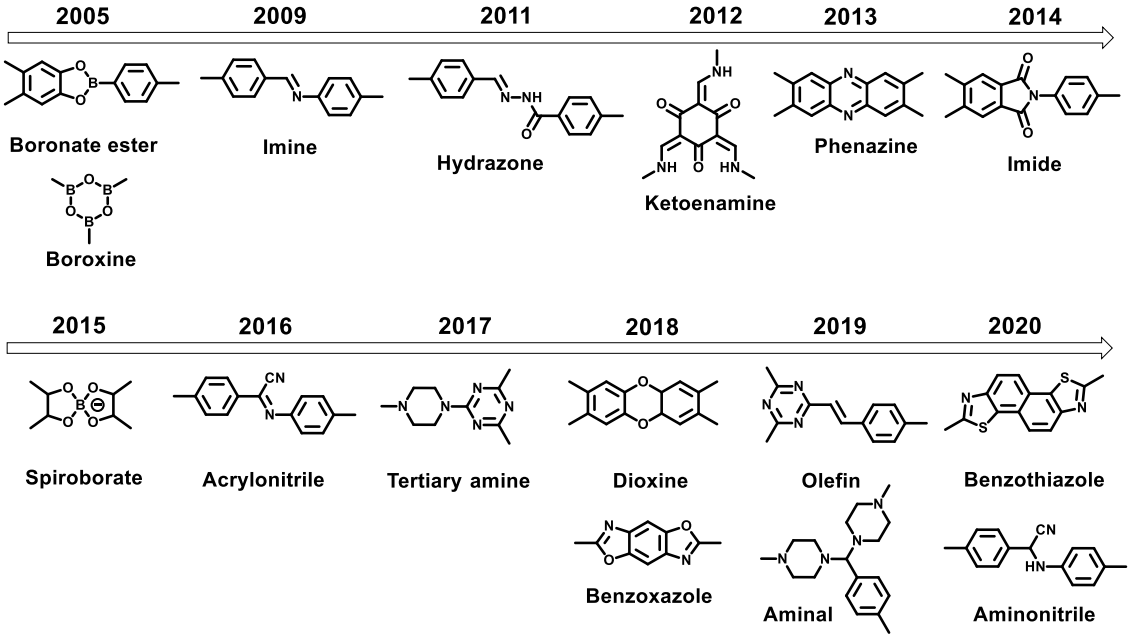

Figure 2 Synthèse historique de différents COFs avec diverses liaisons.

1.1.2 Unités de construction

Il est possible de concevoir topologiquement des COFs en utilisant des parties aromatiques comme précurseurs ayant diverses géométries (Figure 3). Il est crucial de comprendre les composants de

symétrie qui en résultent, en particulier la symétrie de rotation liée aux monomères correspondants. Trouver les axes de rotation des matériaux de départ est une façon d'accomplir cela. L'axe de rotation est généralement désigné par Cn, et les rotations de (360°/n) ramènent les molécules à leur orientation initiale. Afin de garantir une croissance de chaîne bien définie en deux ou trois dimensions, les unités de construction sont généralement des cycles aromatiques à ossature rigide permettant un guidage spatial de la formation des liaisons et de la propagation de la chaîne. Il a été possible de développer des unités de construction telles que les arènes, les macrocycles, les unités riches en azote, les unités riches en soufre et d'autres squelettes π.

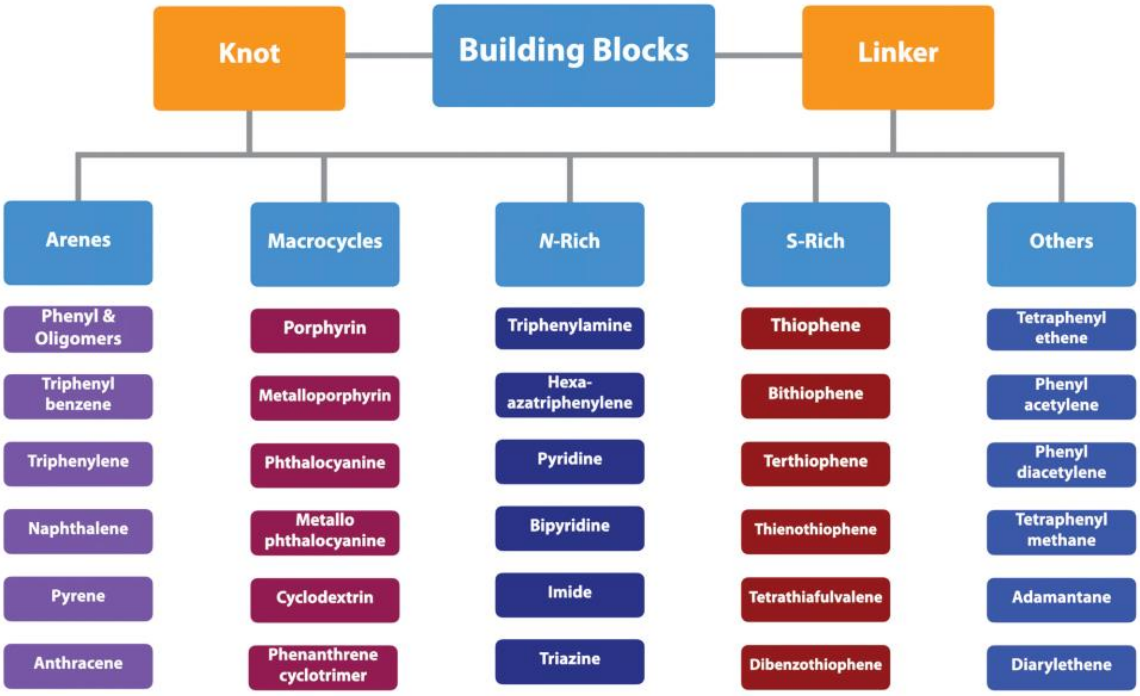

Figure 3 Divers squelettes π pour la conception des COFs.

Les principaux monomères sont représentés dans la Figure 4 en fonction de leurs unités réactives et de leurs géométries. Pour garantir une expansion topologique dans tout le réseau, les sites réactifs sont généralement répartis dans les systèmes aromatiques pour générer une géométrie particulière. À l'exception de l'auto-condensation, la création de COFs nécessite un minimum de deux monomères, l'un agissant comme un nœud et l'autre comme un connecteur. Les unités de nœud sont positionnées aux sites de branchement et se lient aux connecteurs par des liaisons covalentes pour créer des squelettes polygonaux. Dans le but d'ingénierie de l'interface paroi-pore, les monomères peuvent être combinés avec des groupes fonctionnels en plus des sites réactifs. Ainsi,

les unités de construction fournissent une base à la fois pour la conception des COFs et pour comprendre leurs attributs et leurs objectifs. Les groupes fonctionnels les plus importants des matériaux de départ pour la synthèse des COFs sont $B(OH)_2$, OH, C=O, NH_2, $CONHNH_2$ et CN (Figure 4).[8] La création de COFs dépend du choix minutieux des matériaux précurseurs, en particulier de ceux contenant des groupes fonctionnels essentiels qui contrôlent le processus de formation de liaisons covalentes à l'intérieur du réseau. Les groupes fonctionnels carbonyle, tels que les aldéhydes et les cétones, jouent un rôle fondamental dans la synthèse des COFs en raison de leur capacité à participer à des réactions de condensation avec des amines ou d'autres composés nucléophiles. Les groupes amine sont essentiels pour leur réactivité nucléophile, participant à des réactions avec les groupes carbonyle pour former des liaisons imine ou Schiff.[9] La présence de ces groupes fonctionnels clés dans les précurseurs n'affecte pas seulement l'architecture des COFs, mais dicte également leurs propriétés, y compris la porosité et la stabilité chimique. Comprendre et incorporer stratégiquement ces groupes fonctionnels dans le processus de synthèse sont primordiaux pour ajuster les COFs avec les caractéristiques désirées pour des applications diverses.[10]

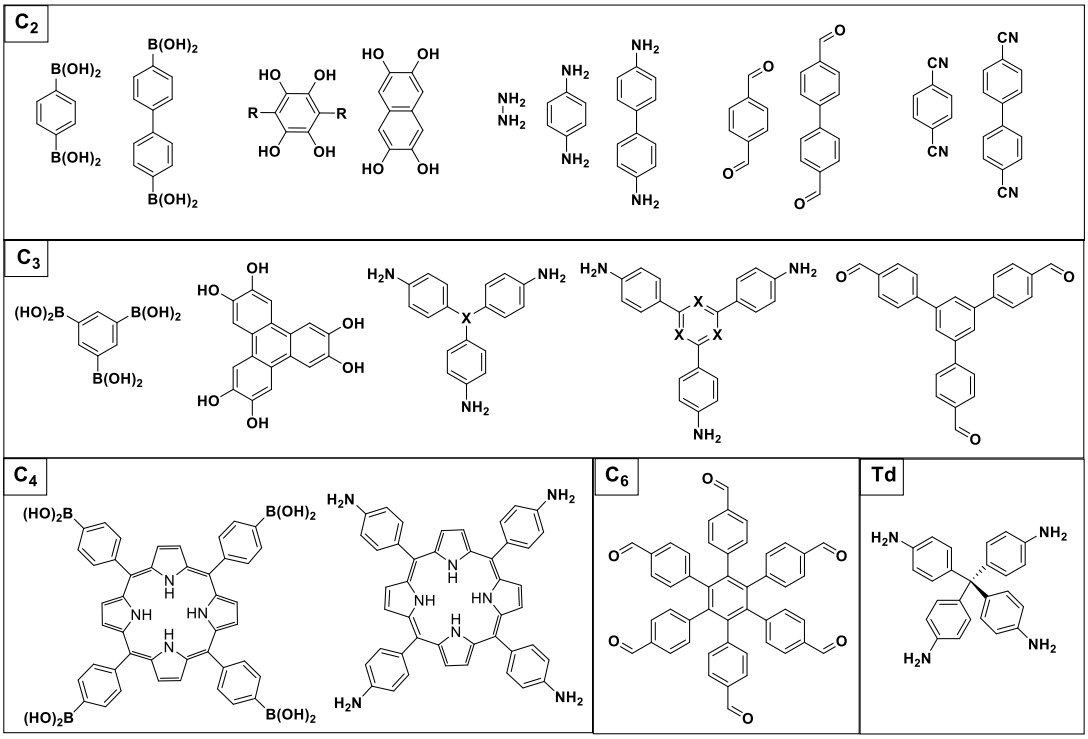

Figure 4 Blocs de construction typiques avec différentes géométries pour la construction de COFs.

1.1.3 Conception de diagrammes topologiques

Des diagrammes topologiques, dans lesquels des nœuds et des connecteurs de différentes géométries sont condensés pour former des structures polygonales étendues, peuvent être utilisés pour concevoir des COFs. Pour les COFs en 2D et 3D, des diagrammes topologiques distincts sont nécessaires. Jusqu'à aujourd'hui, différents diagrammes topologiques ont été créés jusqu'à présent pour les conceptions de COFs en 2D et 3D. Les monomères peuvent être classés en géométries C_1, C_2, C_3, C_4, C_6 et T_d en fonction de leur géométrie; la conception de COFs en 3D nécessite la géométrie Td (Figure 4). La self-condensation d'un monomère ou la co-condensation de deux monomères donne lieu à une topologie symétrique. La conception de COFs hexagonaux en 2D est rendue possible dans le cas de self-condensation par la combinaison de monomères C_2 [C_2 + C_2 + C_2] (Figure 5a). La co-condensation crée un réseau polygonal à liaison alternée en joignant deux monomères en tant que nœud et connecteur. Par exemple, la combinaison des monomères symétriques C_3- et C_2 ou C_3- et C_3 donne lieu à une topologie hexagonale dans les diagrammes [C_3 + C_2] et [C_3 + C_3], respectivement (Figures 5b et 5c). Un grand nombre de polymères 2D et de COFs sont développés dans ce diagramme de géométrie en raison de la grande variété de monomères symétriques C_3- et C_2-symétriques. Une autre topologie majeure avec une structure tétragonale peut être conçue avec le diagramme [C_4 + C_2] ou [C_4 + C_4] contenant des monomères symétriques en C_4 et C_2 (Figures 5d et 5e). Dans le cas de [C_4 + C_4], les deux monomères occupent les nœuds des réseaux. En utilisant un diagramme [C_2 + C_2] et en réduisant la symétrie C_4 à la symétrie C_2, on obtient une topologie rhombique plutôt qu'une topologie tétragonale (Figure 5f). La topologie trigonale peut être construite avec un diagramme [C_2 + C_6] avec un monomère C_6 en nœud et C_2 comme connecteur (Figure 5g). Les topologies hexagonale, tétragonale, trigonale et rhombique sont les structures les plus importantes des COFs en 2D. Pour faire croître les squelettes polymères en trois dimensions, une unité de nœud avec une symétrie T_d ou orthogonale est nécessaire pour concevoir des COFs en trois dimensions avec différentes topologies, y compris des structures dia, pts, ctn, bor, srs et hélicoïdales. Par exemple, en raison de la grande variété de connecteurs symétriques en C_2, le réseau 3D dia est créé en utilisant les diagrammes [T_d + C_2] ou [T_d + T_d], qui donnent lieu à la plus grande famille de COFs en 3D (Figure 5h et 5i). Le réseau 3D srs, ctn ou bor peut être formé décrit par une condensation [T_d + C_3] (Figure 5j).

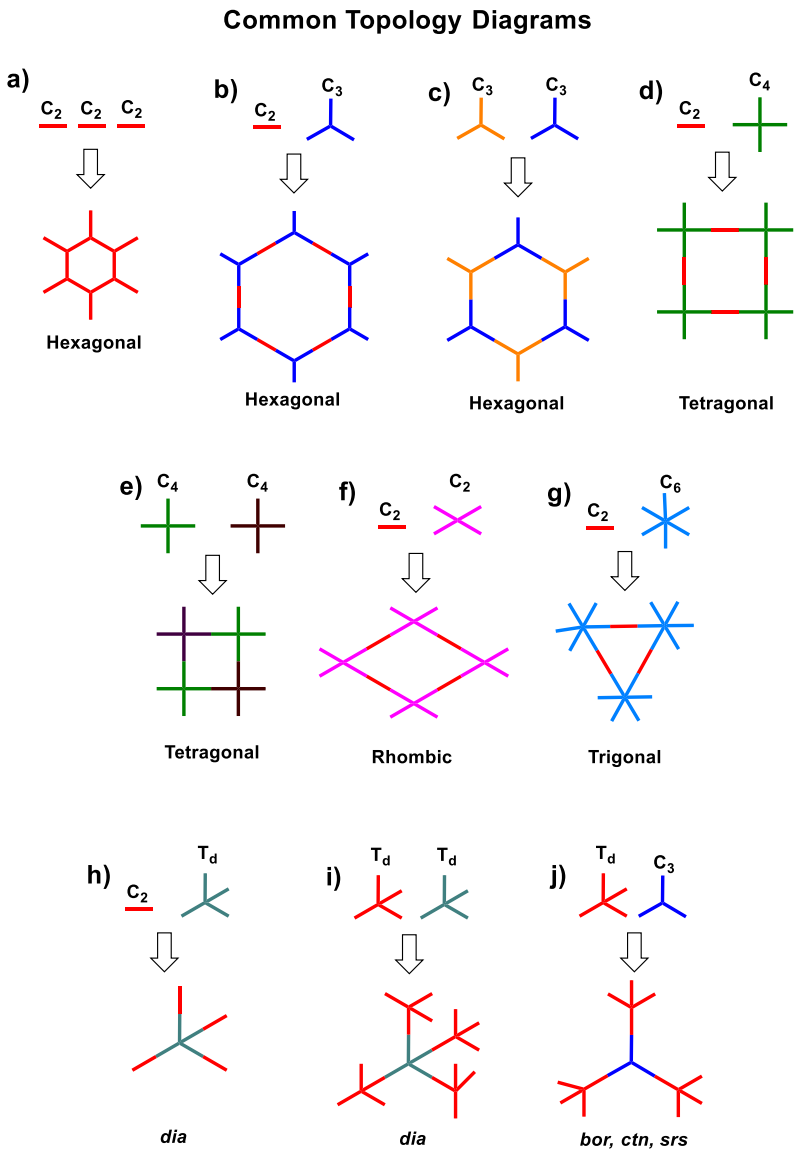

Figure 5 Diagrammes topologiques courants pour la conception de COFs en 2D et 3D afin de créer différentes structures et pores.

1.1.4 Synthèse des COFs

1.1.4.1 Méthodes synthétiques traditionnelles

La synthèse des COFs a connu une vaste gamme de méthodes, chacune adaptée pour atteindre des structures et des propriétés spécifiques. La synthèse des COFs implique la formation de liaisons covalentes par le biais de réactions réversibles entre des unités de construction organiques soigneusement choisies. Cette polyvalence synthétique a conduit à l'exploration de nombreuses variations dans les unités de construction, les liaisons et les fonctionnalités, donnant lieu à une

vaste bibliothèque de COFs aux propriétés distinctes. La capacité d'intégrer différentes unités organiques permet aux chercheurs d'ajuster finement les COFs pour des applications spécifiques, allant du stockage et de la séparation des gaz à la catalyse, la détection et la délivrance de médicaments.[4a, 11] Bien que les applications potentielles des COFs soient vastes et prometteuses, des défis subsistent, et les efforts de recherche en cours sont axés sur leur résolution. La scalabilité et la reproductibilité des méthodes de synthèse des COFs sont des domaines d'investigation actifs, les chercheurs travaillant à développer des approches efficaces et rentables pour une production à grande échelle. De plus, la compréhension des principes fondamentaux régissant les propriétés des COFs est essentielle pour faire progresser leur conception et leur application.[12]

1.1.4.1.1 Méthode solvothermale

En général, la majorité des COFs rapportés ont été produits dans un tube haute pression scellé dans des conditions solvothermiques où les matériaux de départ organiques subissent une réaction de polycondensation en présence de solvants à des températures élevées.[13] En fait, dans cette méthode, les matériaux de départ, les solvants et l'acide acétique sont ajoutés au tube haute pression, puis après plusieurs cycles de congélation-pompage-dégel, il est scellé pour protéger les molécules d'eau générées et maintenir la réversibilité de la réaction. Ensuite, le tube est placé dans un four ou dans un bain d'huile à une température spécifique pendant plusieurs jours pour préparer un COF hautement cristallin (Figure 6).[6] Cependant, plusieurs facteurs influent significativement sur la cristallinité des COFs pendant le processus de synthèse, notamment les quantités de catalyseur, les ratios de volume de solvant, le temps de réaction, la pression et la température de la réaction. Obtenir des COFs de haute qualité demande un travail approfondi et un engagement pour identifier les conditions de réaction optimales, en particulier par le biais du criblage des solvants, ce qui représente un obstacle substantiel au développement des COFs. De plus, même lorsque des conditions optimisées sont établies, des variations significatives entre lots persistent en raison de la sensibilité de la qualité des COFs aux conditions de synthèse. Par conséquent, l'exploration de nouvelles stratégies de synthèse pour générer des COFs de haute qualité avec reproductibilité est à la fois très recherchée et difficile.

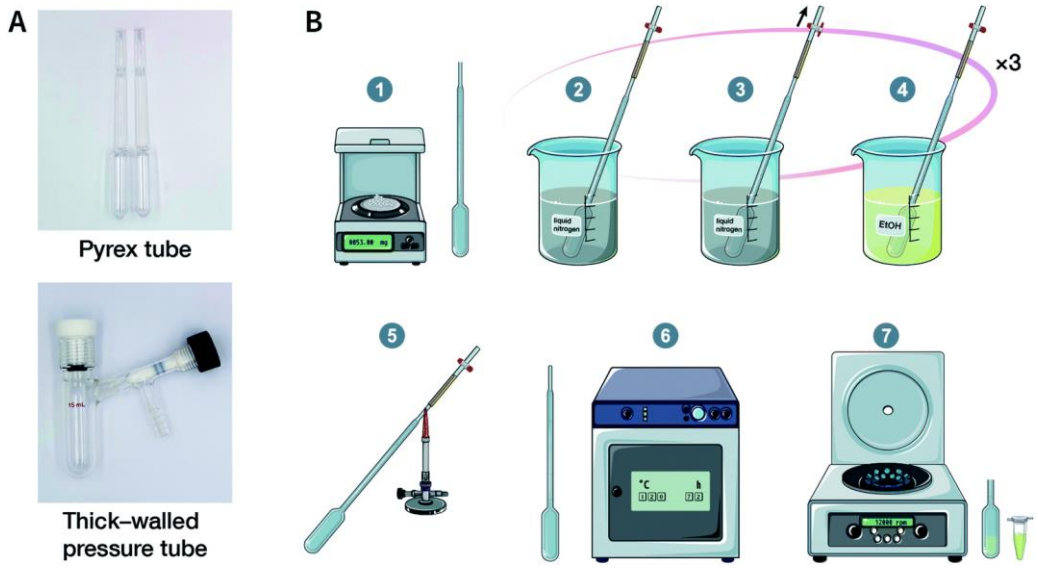

Figure 6 Synthèse solvothermale de COFs; Photographies numériques d'un tube en Pyrex et d'un tube sous pression à paroi épaisse pour la synthèse solvothermale de COF (A). Étapes conventionnelles dans la synthèse solvothermale de COF (B). Mélange des matières premières (1); congélation avec de l'azote liquide (2); pompage vers le bas (3); décongélation (4); scellement par flamme (5); chauffage au four (6); séparation des solides (7). Reproduit avec l'autorisation de la référence [[6]]. Copyright @ 2020 Royal Society of Chemistry.

1.1.4.2 Nouvelles méthodes synthétiques

1.1.4.2.1 Méthode par micro-ondes

La méthode de synthèse qui fait usage du chauffage par micro-ondes est associée à la synthèse par micro-ondes. Il est couramment admis que la synthèse de polymères organiques et de structures métalliques organiques peut être réalisée efficacement grâce à l'irradiation par micro-ondes.[14] Dans la méthode par micro-ondes, contrairement à l'approche conventionnelle du chauffage externe, le chauffage par micro-ondes est intrinsèque, ce qui signifie que le sujet chauffé sert de source de génération de chaleur, éliminant ainsi le besoin de conduction de chaleur et permettant un chauffage rapide et uniforme. Par exemple, Cooper et ses collaborateurs ont utilisé, pour la première fois en 2009, la méthode synthétique par micro-ondes pour la préparation d'un COF cristallin à base de bore avec un rendement élevé (68%).[15] Ils ont préparé un COF fortement cristallin en un temps de réaction court (environ 20 minutes), comparé à la méthode solvothermale (72 heures). De plus, le COF préparé a montré une aire spécifique BET plus élevée (2019 m^2/g) par rapport au COF précédemment rapporté dans des conditions solvothermales (1590 m^2/g) (Figure 7). Cette instance montre de manière indiscutable que réagir sous micro-ondes peut

grandement accélérer et augmenter les taux de réaction. Dans le même temps, la surveillance en ligne est rendue possible par la synthèse par micro-ondes, ce qui est significativement plus difficile à accomplir avec une synthèse basée sur un solvant.

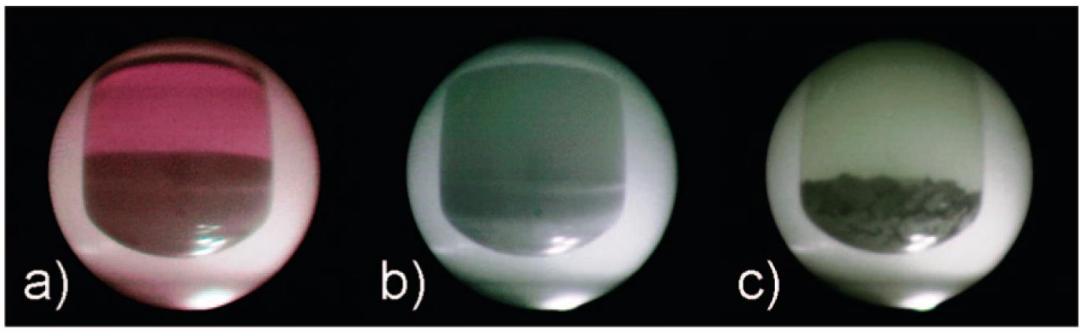

Figure 7 Photographie enregistrée depuis le réacteur à micro-ondes montrant la synthèse et la purification de COF: poudre de COF gris-violet produite après la synthèse primaire (a); élimination des matières restantes par un processus d'extraction aux micro-ondes (b); l'extraction aux micro-ondes secondaire donne une poudre de COF gris purifiée (c). Reproduit avec l'autorisation de la référence [[15]]. Copyright @ 2009 American Chemical Society.

1.1.4.2.2 Méthode mécano-chimique

L'approche synthétique mécano-chimique est une méthode de préparation de COFs qui implique l'utilisation de forces mécaniques, telles que le broyage ou le fraisage, pour induire des réactions chimiques entre les molécules précurseurs.[16] Au lieu de la chaleur ou des solvants pour faciliter les réactions, la mécano-chimie s'appuie sur l'énergie mécanique générée pendant le processus de broyage pour faire avancer la réaction. Cette technique offre plusieurs avantages, dont la simplicité, un impact environnemental réduit (car elle élimine souvent le besoin de solvants) et la capacité d'accéder à de nouvelles voies de réaction. La synthèse mécano-chimique a suscité l'attention dans le domaine des COFs car elle offre une voie alternative, plus durable, pour créer ces matériaux poreux cristallins. Dans le but de préparer des COFs fortement cristallins, au moins quatre types différents de méthodes synthétiques mécaniques ont été développés, notamment: extrudeuse, broyeur à billes, mortier et imprimante 3D.[16-17] De plus, étant donné que la synthèse mécano-chimique utilise peu ou pas de solvants, elle est également considérée comme une méthode de synthèse verte. Par exemple, trois COFs chimiquement et thermiquement stables ont été préparés avec succès en peu de temps et à température ambiante sous broyage mécanique sans solvant. La progression de la réaction peut être simplement détectée par le changement de couleur du matériau lors du broyage (Figure 8).[18] Cependant, les COFs préparés présentaient une faible porosité et

cristallinité, et les principaux avantages de cette méthode étaient sa faisabilité pour la synthèse à grande échelle, sa facilité d'opération et ses conditions respectueuses de l'environnement. Probablement en raison de l'exfoliation des couches 2D pendant le processus de broyage, les COFs préparés avaient tendance à montrer des structures en feuille.

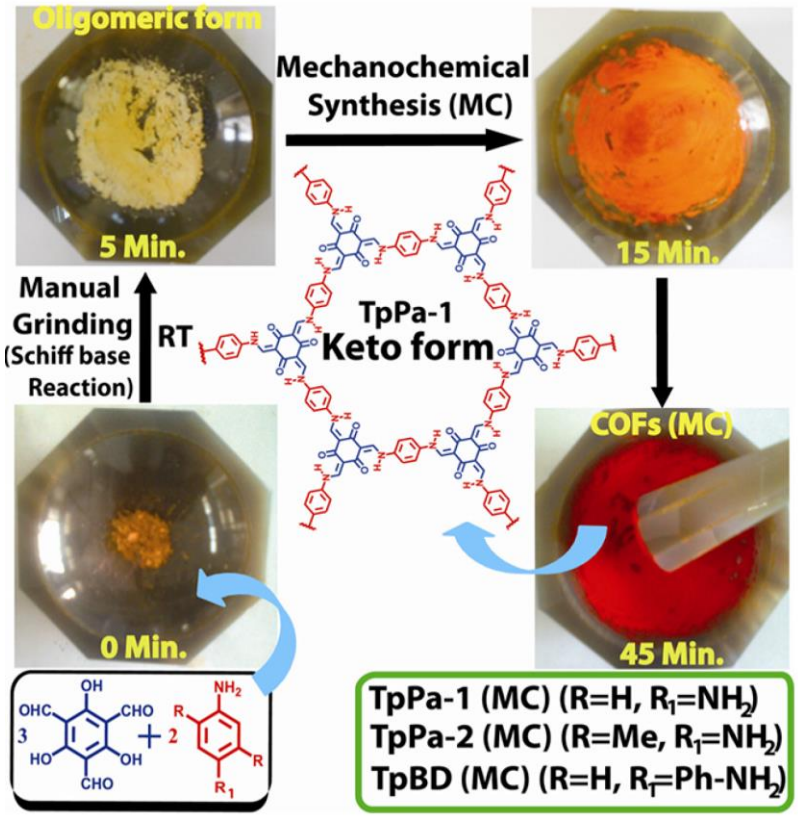

Figure 8 Synthèse mécano-chimique de différents COFs par une simple réaction de base de Schiff effectuée par broyage à l'aide d'un mortier et d'un pilon. Reproduit avec l'autorisation de la référence [[18]]. Copyright @ 2013 American Chemical Society.

1.1.4.2.3 Méthode ionothermale

La synthèse ionothermale est une méthode unique pour la synthèse des COFs. Dans la synthèse ionothermale, un liquide ionique (ILs) sert à la fois de solvant et de modèle pour la formation du COF.[19] Les ILs sont des sels qui sont à l'état liquide à la température ambiante ou environ.[20] Les ILs sont largement utilisés comme solvants respectueux de l'environnement car ce sont des substituts recyclables aux solvants organiques volatils conventionnels, et ils ont montré beaucoup de promesses pour les applications industrielles car les risques de sécurité liés à la pression sont évités.[21] De plus, la méthode ionothermale offre des avantages en termes de réglabilité, de contrôle des conditions de réaction et de capacité à influencer la structure du COF résultant. Par exemple,

en 2018, trois COFs 3D différents ont été préparés à partir de la réaction de polycondensation de la base de Schiff entre le monomère tétraédrique du tétrakis(4-formylphényl)méthane, trois monomères d'amines linéaires, et en présence de bis(trifluorométhylsulfonyl)imide de 1-butyl-3-méthylimidazolium ([BMIm]NTf_2) en tant que IL. Dans cette recherche, ils ont réussi à synthétiser trois COFs 3D avec des structures dia interpenétrées (Figure 9).[22] Les principaux avantages de cette étude étaient la synthèse des COFs à température ambiante et la réduction du temps de réaction de 3 jours à 12 heures en présence d'ILs. Cependant, l'élimination des ILs des pores et des cavités des COFs 3D n'était pas facile, limitant ainsi leur utilisation générale (Figure 9).

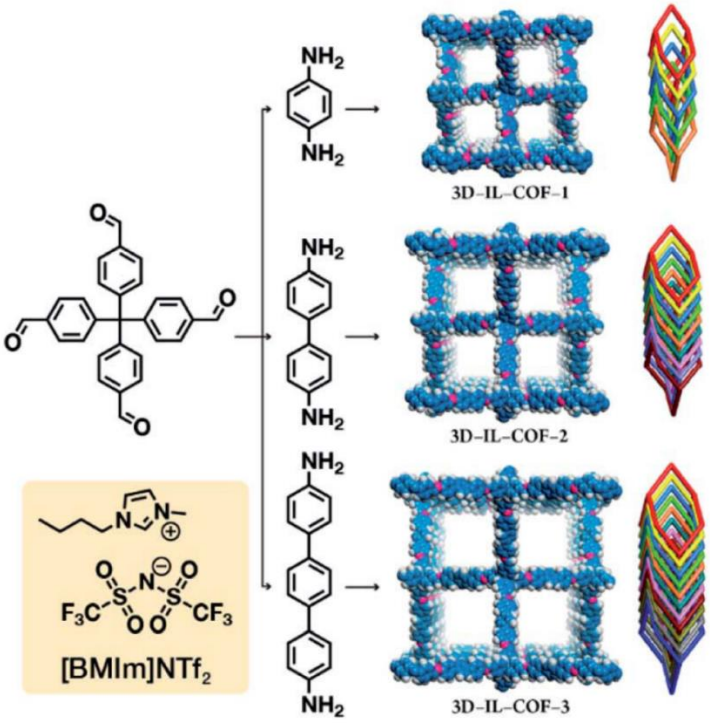

Figure 9 Synthèse ionothermale de COFs 3D en présence de liquide ionique ([BMIm]NTf_2). Reproduit avec la permission de la reference [[22]]. Copyright @ 2018 American Chemical Society.

1.1.4.2.4 Méthode de synthèse atmosphérique en solution

La synthèse des COFs sous pression atmosphérique et à température ambiante présente plusieurs avantages, notamment la simplicité, la rentabilité et l'accessibilité. Cette approche est particulièrement attrayante car elle élimine le besoin de réactions à haute pression et de températures élevées, la rendant plus respectueuse de l'environnement et pratique. D'autre part, la majorité des monomères de construction utilisés pour la synthèse des COFs sont instables à des températures élevées, ce qui rend l'utilisation d'une méthode à température ambiante pour la

préparation des COFs encore plus cruciale. De plus, une étape de protection gazeuse n'est pas nécessaire pour le COF préparé à température ambiante. De plus, l'utilisation de la température, en particulier des méthodes de synthèse à haute température, peut être risquée et dangereuse car certains des matériaux utilisés peuvent changer avec la température et produire des sous-produits qui peuvent altérer la morphologie du COF préparé et, par conséquent, réduire sa stabilité. La plupart des méthodes synthétiques des COFs sont chronophages. La synthèse des COFs peut être plus précisément contrôlée lorsqu'elle est effectuée à température ambiante. Malgré sa facilité d'utilisation, le COF produit en utilisant une méthode à température ambiante présente une excellente stabilité dans des milieux abrasifs, ainsi qu'une grande surface et une capacité d'adsorption. L'approche de synthèse à température ambiante a également l'avantage d'être une méthode synthétique simple et efficace qui peut être appliquée à grande échelle. Un autre avantage important de l'utilisation de la méthode de synthèse à température ambiante est l'utilisation de matériaux naturellement présents, tels que les biomolécules, en tant que monomères, qui deviennent instables à des températures plus élevées.

Ainsi, pour la première fois en 2015, des COFs liés par imine ont été synthétisés par la réaction de condensation de la base de Schiff à température ambiante et sous pression atmosphérique par Zamora et al.[23] Le 1,3,5-tris(4-aminophényl)benzène et le benzène-1,3,5-tricarbaldehyde ont été utilisés comme matériaux de départ et agités dans le DMSO pendant deux jours pour obtenir un COF en poudre blanche. Cette étude a ouvert de nouvelles perspectives pour la synthèse à grande échelle de différents COFs. Dans une autre recherche, Peng et al. ont rapporté la synthèse en lot à température ambiante de trois types de COFs 2D via la réaction de condensation de la base de Schiff de divers monomères d'amines et d'aldéhydes avec différents types de liaisons et en présence d'acide acétique.[24] Les COFs préparés présentaient une cristallinité et une porosité élevées (410–1537 $m^2\ g^{-1}$). Cette approche a créé de nouvelles opportunités pour la synthèse pratique et l'utilisation des COFs, en plus d'être rapide et efficace pour la production commerciale à grande échelle de COFs. Des interactions π fortes et des blocs de construction stables avec une haute solubilité sont nécessaires pour cette méthode (Figure 10). Cependant, la synthèse à température ambiante des COFs présente quelques inconvénients majeurs, tels que des études non approfondies et superficielles, des procédures laborieuses, une portée de monomère étroite et des temps de réaction longs.[23, 25] Ainsi, il est urgent de développer de nouvelles méthodes basées sur des conditions douces.

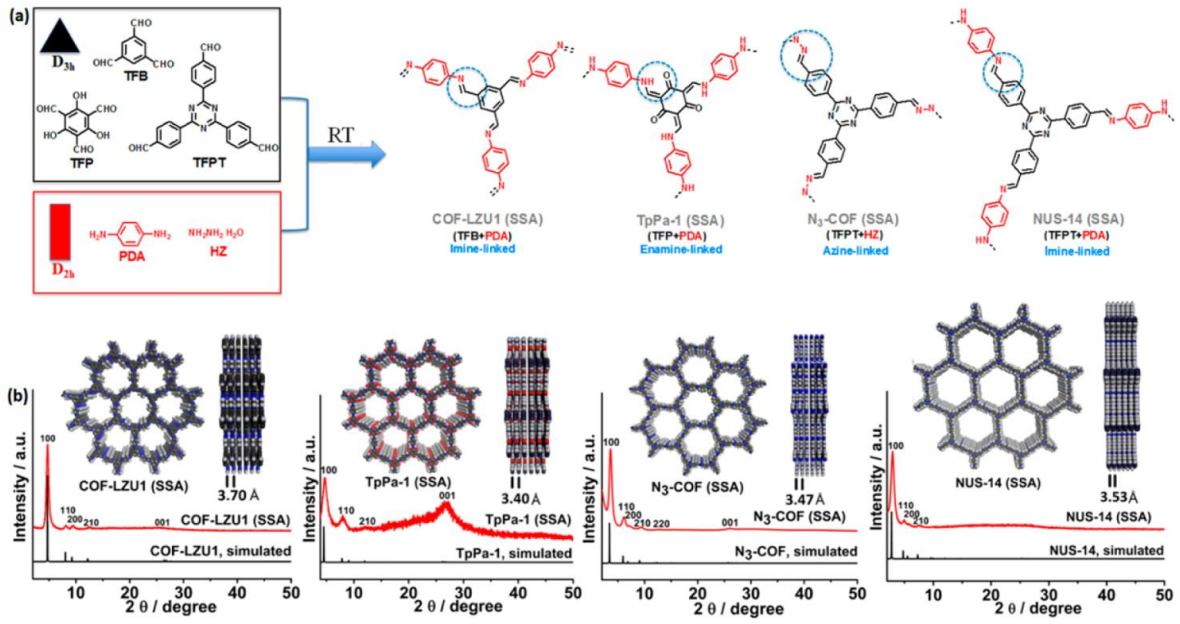

Figure 10 Représentation schématique de la synthèse de différents COFs avec des squelettes hexagonaux 2D à température ambiante (a). Diagrammes de diffraction des rayons X simulés et expérimentaux de différents COFs préparés (b). Reproduit avec la permission de la référence [[24]]. Copyright @ 2016 American Chemical Society.

1.1.4.2.5 Méthodes catalytiques

La synthèse catalytique des COFs implique l'utilisation de catalyseurs pour faciliter et contrôler la formation de liaisons covalentes entre les monomères organiques de liaison et les nœuds. Les catalyseurs jouent un rôle central dans l'amélioration de la cinétique de réaction, la promotion de la sélectivité et l'influence sur la structure globale du COF résultant. Diverses stratégies catalytiques, comprenant des sels métalliques, des acides organiques, ainsi que des catalyseurs acides ou basiques de Lewis,[26] ont été employées pour orienter la synthèse des COFs vers des architectures et des fonctionnalités spécifiques. Ces catalyseurs permettent souvent aux réactions de se dérouler dans des conditions plus douces, telles que des températures plus basses ou des temps de réaction plus courts, contribuant à des méthodes de synthèse plus durables et efficaces. L'approche catalytique offre aux chercheurs un plus grand contrôle sur la morphologie, la cristallinité et la distribution de la taille des pores des COFs, élargissant la gamme d'applications potentielles. L'exploration continue de nouveaux systèmes catalytiques et de nouvelles stratégies continue d'avancer le domaine, ouvrant de nouvelles possibilités pour adapter les propriétés des COFs à des applications diverses.

La synthèse de matériaux COF à base d'imine a été le sujet de nombreuses publications récentes en raison de leur importance, et la majorité de ces publications ont utilisé de l'acide acétique conventionnel comme catalyseur pour la synthèse des COFs.[27] Les techniques conventionnelles présentent des inconvénients en raison de leur faible cristallinité et porosité, en plus des problèmes liés à leurs temps de réaction prolongés et à leurs conditions de réaction sévères.[28] Certaines recherches ont abordé ce problème en synthétisant des COFs à base d'imine en utilisant des techniques alternatives, telles que l'utilisation de la lumière,[29] la sonication,[30] le micro-ondes,[31] ou l'irradiation par faisceau d'électrons.[32] Les chercheurs ont également rapporté d'autres catalyseurs que l'acide acétique, tels que les nitrates de métaux de transition,[33] les halogénures métalliques,[34] les triflates métalliques,[35] ou l'acide *p*-toluènesulfonique.[36] Cependant, ils présentent un certain nombre d'inconvénients importants, tels que la nécessité d'utiliser beaucoup de catalyseur dans des conditions scellées, le coût élevé des catalyseurs, la plage limitée de monomères étudiés, le manque de recherche approfondie et superficielle, et les procédures laborieuses qui les rendent inadaptés à la production à grande échelle.[33-34, 36] Par exemple, ces procédures ont toutes été limitées à la synthèse de COFs à base d'imine en 2D présentant des structures planes et plus simples. Par conséquent, il est fortement conseillé de concevoir et développer un nouveau catalyseur alternatif pour la synthèse douce et rapide de matériaux COF avec des structures cristallines et poreuses élevées.[37]

La synthèse catalytique la plus importante des COFs a été rapportée par Dichtel et ses collaborateurs.[35] Ils ont préparé différents COFs liés par imine en utilisant des triflates métalliques acides de Lewis à basse température (Figure 11a). Même à des charges de catalyseur très faibles, les triflates métalliques ont pu augmenter considérablement la vitesse de formation d'imine et la synthèse des COFs. Parce que Sc(III) a un rayon ionique plus petit que les autres triflates métalliques, le triflate de scandium a montré la plus grande activité catalytique de tous ces catalyseurs de triflate métallique (Figure 11b). Comparé à la méthode traditionnelle, le COF synthétisé avec une méthode catalytique a montré une aire de surface élevée de 2175 m^2/g et une cristallinité, en présence seulement de 0,02 équivalents de triflate de scandium, et seulement 10 minutes et à température ambiante. Cependant, avec l'augmentation de la quantité de catalyseur à 0,1 équivalent, la cristallinité des COFs préparés a diminué, ce qui montre que davantage de catalyseur entrave le processus d'échange d'imine. De plus, cette méthode a été utilisée pour

construire deux COFs liés par imine hexagonaux 2D supplémentaires, démontrant la polyvalence et la tolérance de cette polymérisation catalysée par triflate métallique.

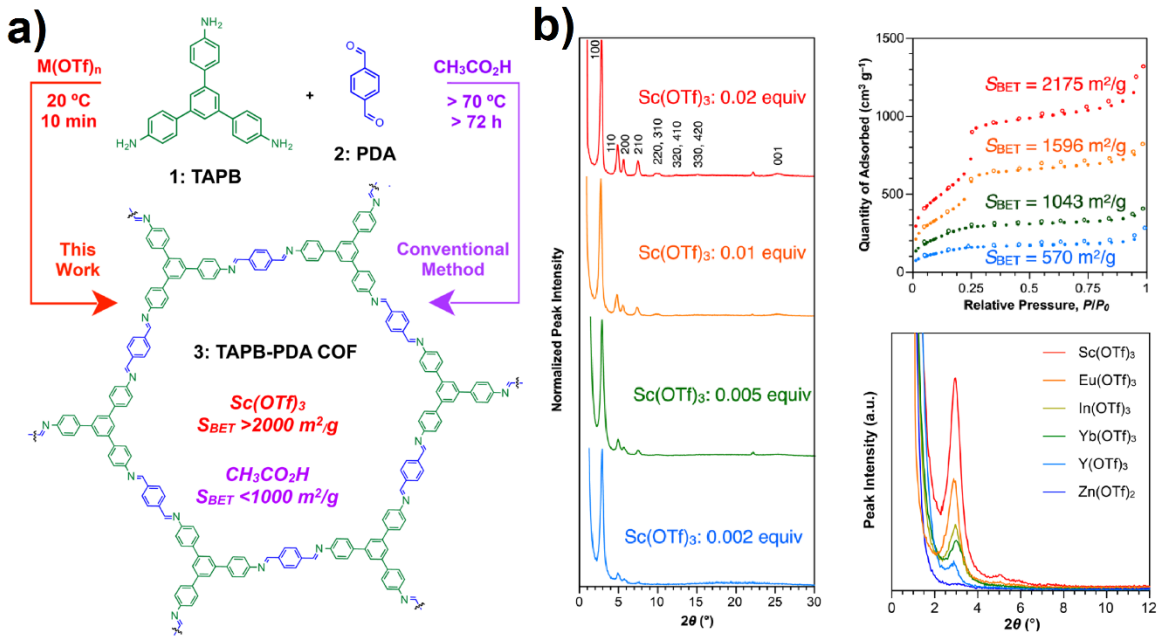

Figure 11 Synthèse traditionnelle du COF TAPB-PDA avec de l'acide acétique et de l'acide de Lewis (a). Diagrammes de diffraction des rayons X (PXRD) et isothermes de désorption d'azote des COFs préparés en présence de différents catalyseurs et optimisation de la quantité de catalyseur (b). Reproduit avec la permission de la référence [[35]]. Copyright @ 2017 American Chemical Society.

Dans une autre étude, une nouvelle méthode catalytique basée sur une approche de cristallisation médiatisée par le sel a été rapportée par Banerjee et ses collègues pour la synthèse rapide de différents COFs.[36] Afin de réparer les défauts et d'induire la réversibilité dans les réseaux de COFs, l'acide *p*-toluènesulfonique a été utilisé comme organisateur moléculaire (Figure 12). Cette méthode offre une approche facile et a permis de produire des COFs de haute cristallinité avec des aires de surface ultrahautes allant jusqu'à 3000 m^2/g. Ainsi, dans un premier temps, le matériau de départ diamine (Pa-1) et l'acide p-toluènesulfonique ont été mélangés, puis le 1,3,5-triformylphloroglucinol (Tp) et de l'eau ont été ajoutés au mélange. Ensuite, le mélange a été chauffé à 170 °C pendant une minute (Figure 12). Dans ce projet, l'acide *p*-toluènesulfonique remplit deux fonctions : d'abord, il agit en tant que catalyseur, et ensuite, il réagit de manière acide pour former des sels acide p-toluènesulfonique-amine, qui peuvent ensuite être utilisés comme

modèles pour contrôler la cristallisation en 2D des COFs par interaction par liaison hydrogène. Une extrudeuse à vis jumelée pourrait être utilisée pour synthétiser les COFs à grande échelle.

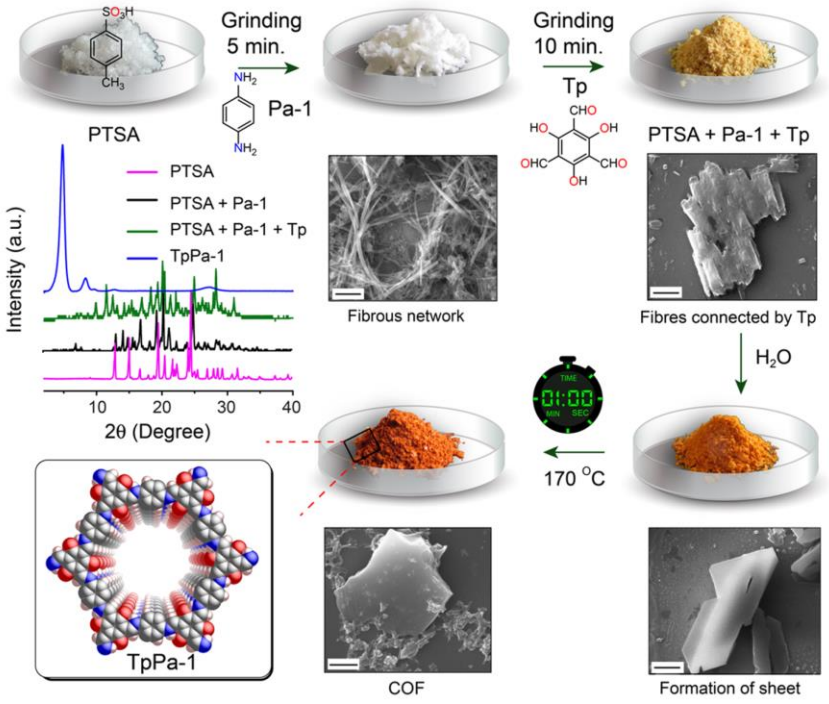

Figure 12 Une approche d'organisation moléculaire pour la synthèse de COF avec des diffractions des rayons X séquentielles et des images de microscopie électronique à balayage (SEM) de chaque étape individuelle de cristallisation. Reproduit avec la permission de la reference [[36]]. Copyright @ 2017 American Chemical Society.

1.1.4.3 Modification post-synthétique des COFs

Des méthodes de modification post-synthétique (PSM) ont également émergé, permettant la modification de COFs préformés pour introduire des fonctionnalités souhaitées. L'interaction de ces diverses stratégies synthétiques a permis aux chercheurs d'explorer l'immensité de l'espace chimique et de libérer le potentiel des COFs pour différentes applications. L'évolution continue des méthodologies synthétiques souligne la nature dynamique de la recherche sur les COFs, avec des efforts permanents visant à améliorer la scalabilité, la reproductibilité et à élargir l'arsenal pour la conception de ces matériaux polyvalents. Deux des caractéristiques les plus intrigantes de ces matériaux sont la nature ordonnée et poreuse des structures COF. Les espèces chimiques réactives peuvent diffuser à l'intérieur des pores du matériau et atteindre presque toutes les moitiés organiques de la structure grâce à la grande surface exposée. Plusieurs PSM pour la liaison ont été

développées en utilisant cette caractéristique. En utilisant diverses réactions en état solide en une ou plusieurs étapes, le PSM est une approche flexible permettant de lier un COF d'imine pré-synthétisé à des moitiés plus fonctionnelles, telles que des amides, des quinoléines et des benzoazoles.

1.1.4.3.1 PSM en une seule étape

Il existe différents groupes fonctionnels à la surface et dans les pores des COF qui ont la capacité d'être fonctionnalisés. L'un des plus importants est le groupe fonctionnel imine.[38] Lorsqu'il est exposé aux agents redox appropriés, la liaison imine C=N peut être réduite en amine secondaire ou directement oxydée en amide. Pour la première fois en 2018, la réduction des liaisons imine en amine secondaire a été étudiée par Deng et al. pour les COFs 3D et 2D. Dans cette étude, les groupes fonctionnels imine ont été réduits par le borohydrure de sodium et l'acide téréphtalique (Figure 13a).[39] Les observations de la diffraction des rayons X (PXRD) ont montré une diminution de la cristallinité des COFs après le PSM et la réaction de réduction, attribuée à la conversion de l'hybridation du carbone de sp^2 à sp^3. Dans l'ensemble, il a été découvert que la topologie sous-jacente restait inchangée. Les échantillons modifiés et non modifiés ont été placés dans des solutions aqueuses avec des valeurs de pH basses et élevées pendant une durée de 12 heures, démontrant la stabilité chimique améliorée du COF modifié par rapport au matériau d'origine. Après les traitements, les matériaux non modifiés se dissolvaient complètement dans des milieux acides et perdaient partiellement leur structure en conditions basiques, tandis que les COFs modifiés à l'amine conservaient leur cristallinité. Yaghi et al. ont converti les groupes fonctionnels imine en groupe fonctionnel amide via une réaction d'oxydation directe dans des conditions douces (Figure 13b).[40] Cette réaction a été réalisée à température ambiante et en présence de NaClO2 comme agent oxydant. L'analyse PXRD des échantillons n'a montré aucune réorganisation structurale significative du matériau pendant la transformation. De plus, après avoir placé les COFs modifiés et non modifiés dans différentes conditions acides et basiques pour vérifier la stabilité, les COFs à amide ont montré une rétention significativement plus élevée de la cristallinité, confirmant la plus grande stabilité cinétique de la liaison. Cette transformation a également été observée dans une autre étude rapportée par Han et ses collaborateurs.[41] Ils ont converti les groupes fonctionnels imine des COFs 3D en groupes fonctionnels amide tout en maintenant les structures cristallines des échantillons. Dans une autre étude intéressante, Lotsch et ses collègues

ont rapporté la réaction de condensation du soufre élémentaire avec deux COFs différents pour synthétiser des COFs liés par benzothiazole avec une rétention totale de la cristallinité et de la porosité (Figure 13c).[42] Cette modification post-synthétique entraîne une amélioration considérable de la stabilité chimique et électronique, permettant une étude à haute résolution de la structure réelle du cadre. Dans la procédure suivante, les réactions de Strecker et d'aza-Diels Alder ont été effectuées sur le COF via une stratégie de PSM en une seule étape à l'état solide et une réaction en une seule étape par Dong et al. (Figures 13d et 13e).[43] Ces réactions ont été réalisées en présence de TMSCN et de styrène en tant que sources de cyanure et d'alkyne et dans des conditions solvothermiques. Comparées à la réaction en une seule étape, les COFs modifiés synthétisés avec l'approche de PSM ont montré la même structure avec une cristallinité plus faible.

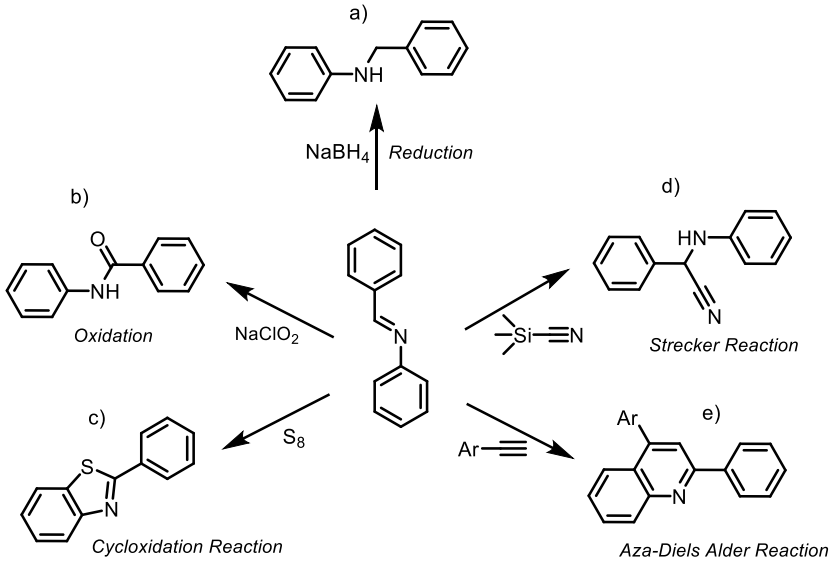

Figure 13 Modification en une seule étape des liaisons imine du COF. Réaction de réduction (a), réaction d'oxydation (b), réaction de cycloxydation (c), réaction de Strecker (d) et réaction d'aza-Diels Alder (e).

1.1.4.3.2 PSM multi-étapes

La modification multi-étapes des COFs implique une altération séquentielle et contrôlée de la structure du cadre après sa synthèse initiale. Cette approche permet l'incorporation de divers groupes fonctionnels, conduisant à des propriétés et des fonctionnalités améliorées.[44] La nature multi-étapes du processus permet un réglage précis des caractéristiques chimiques et physiques du COF, telles que la taille des pores, la chimie de surface et les propriétés électroniques. Cette stratégie offre aux chercheurs un outil polyvalent pour adapter les COFs à des applications spécifiques.[45] De plus, la nature modulaire de la modification multi-étapes permet la création de

matériaux avancés aux propriétés sur mesure, contribuant au développement continu des COFs en tant que candidats prometteurs pour diverses applications technologiques.[45c]

La première étude a été rapportée par Yaghi et ses collaborateurs sur une modification multi-étapes des COFs à base d'imines (Figure 14).[46] Dans ce rapport, ils ont converti avec succès les groupes fonctionnels imine des COFs en COFs de carbamate et de thiocarbamate par une stratégie de PSM en trois étapes. Sur cette base, le COF à base d'imine a été préparé solvothermiquement par la réaction de condensation entre le 2,5-diméthoxybenzène-1,4-dicarboxaldéhyde et le (E)-3,3',5,5'-tétrakis(4-aminophényl)stilbène, puis il a été utilisé comme matériau de départ pour la PSM en trois étapes. La première étape de la PSM concernait la déméthylation des groupes méthoxy sur le COF, suivie de la réaction de réduction des groupes fonctionnels imine en ligands aminés en présence de $NaCNBH_3$ et d'acide acétique dans le THF. Enfin, les COFs liés par carbamate et thiocarbamate cycliques ont été construits par la réaction de condensation des COFs modifiés avec le 1,1'-carbonyldiimidazole ou le 1,1'-thiocarbonyldiimidazole dans le DCM (Figure 14a). Il est à noter que la cristallinité et la porosité du COF préparé ont diminué après la deuxième étape de la PSM, mais elles ont été restaurées après la dernière étape de la PSM pour préparer les COFs liés par carbamate et thiocarbamate cycliques (Figures 14a-c).

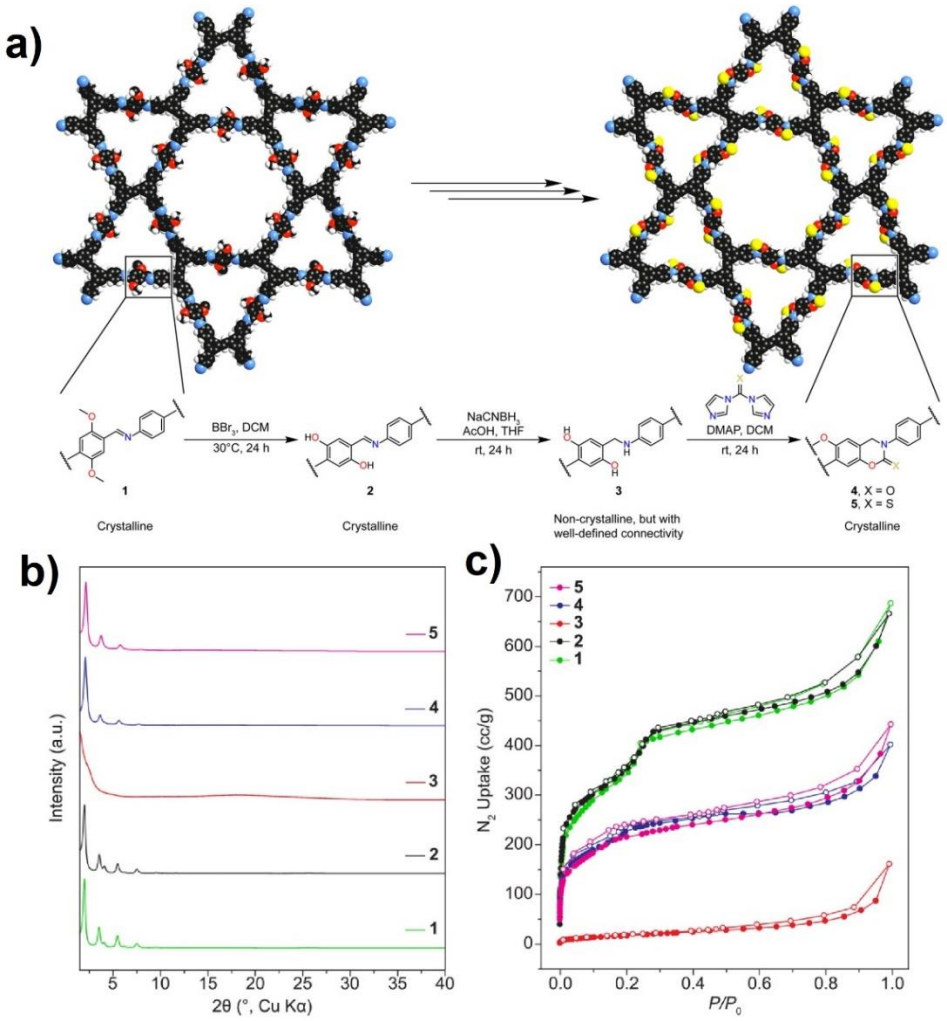

Figure 14 Modification en trois étapes des liaisons imine du COF pour les convertir en COFs liés par carbamate et thiocarbamate cycliques (a). Motifs PXRD (b) et isothermes d'adsorption-désorption de N2 pour les trois étapes de la PSM (c). Reproduit avec la permission de la reference [[46]]. Copyright @ 2019 American Chemical Society.

Récemment, Yaghi et al. ont rapporté une autre étude sur la modification en deux étapes des COFs liés par imine avec une application de stockage de gaz (Figure 15).[47] Cela a été réalisé en synthétisant un COF lié par imine avec une cristallisation élevée, connu sous le nom de COF-609-Im, puis en utilisant une cycloaddition aza-Diels-Alder pour changer sa liaison imine en une liaison tétrahydroquinoléine stable à la base, et enfin en incorporant de manière covalente la tris(3-aminopropyl)amine dans le cadre pour la synthèse d'un COF modifié avec une chaîne d'amine aliphatique (Figure 15a). En comparaison avec le cadre d'origine, le COF-609 final obtenu montre une augmentation de 1360 fois de la capacité d'absorption du CO_2, et en présence d'humidité, une amélioration supplémentaire de 29%. Les résultats ont montré que la cristallinité et la porosité des

cadres après la première et la deuxième étape de la PSM ont diminué et seule une structure amorphe a été obtenue pour le COF modifié final (Figure 15b et c). La diminution de la cristallinité du cadre après la première étape de la PSM peut être attribuée à la non-planéité du ligand tétrahydroquinoléine et à la présence possible de stéréoisomères. De plus, la forte diminution de la cristallinité du cadre après la deuxième étape de la PSM peut être attribuée au désordre actuel du cadre ainsi qu'à la grande population d'amines aliphatiques qui ont été introduites dans les canaux poreux et à la surface du COF. Cependant, même après l'installation de l'amine, la connectivité du cadre reste inchangée, ce qui rend le produit final approprié pour la capture du CO_2.

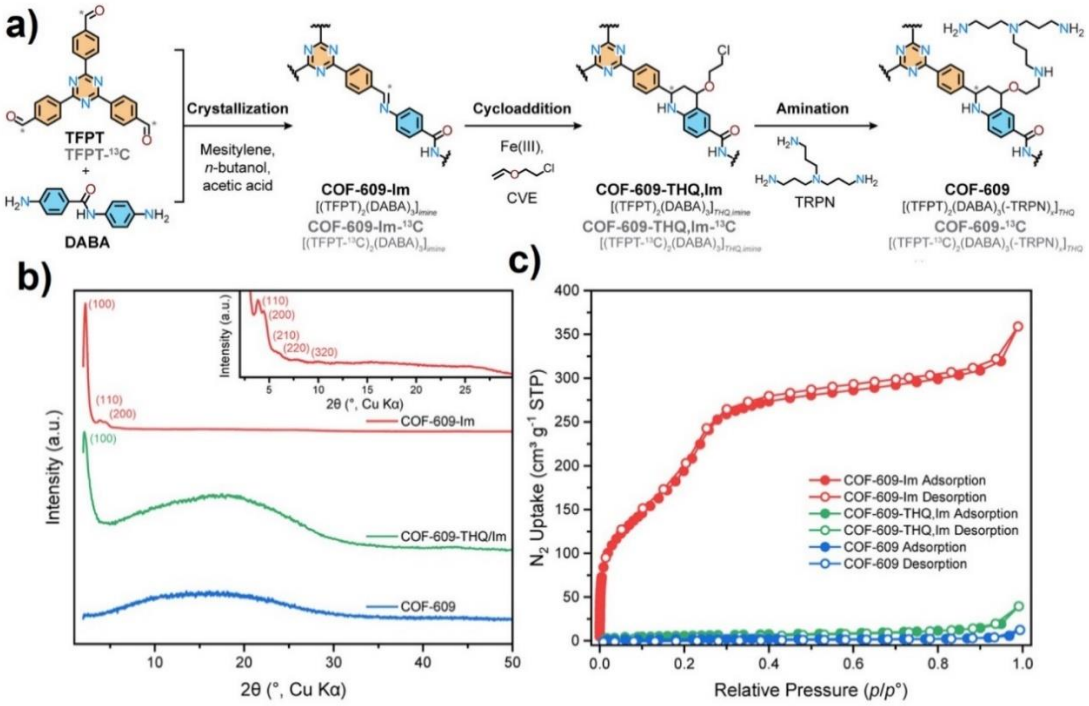

Figure 15 Modification en trois étapes des liaisons imine du COF pour les convertir en COFs fonctionnalisés par des amines (a). Motifs PXRD (b) et isothermes d'adsorption-désorption de N2 pour les trois étapes de la PSM (c). Reproduit avec la permission de la reference [[47]]. Copyright @ 2022 American Chemical Society.

1.1.5 Application des COFs

Les COFs présentent une gamme diversifiée d'applications en raison de leurs propriétés structurales et chimiques uniques. Dans le domaine du stockage et de la séparation des gaz, les COFs ont montré leur potentiel pour stocker des gaz tels que l'hydrogène et le méthane, essentiels pour les applications d'énergie propre. Leurs tailles de pores ajustables et leurs grandes surfaces en font

d'excellents candidats pour une adsorption efficace des gaz. De plus, les COFs ont été explorés dans le domaine de la catalyse, où leurs structures bien définies offrent des plates-formes pour la conception de catalyseurs avec une haute sélectivité et activité. Dans le domaine des technologies de détection, les COFs ont démontré une sensibilité à divers analytes, les rendant précieux dans le développement de capteurs pour la surveillance environnementale ou les diagnostics médicaux. De plus, leur capacité à conduire l'électricité dans certains cas a conduit à des applications dans les dispositifs électroniques. Ces matériaux polyvalents continuent d'attirer l'attention dans la recherche interdisciplinaire, mettant en valeur leur potentiel dans des domaines variés, allant du stockage d'énergie à la détection environnementale et au-delà.

1.1.5.1 Application des COF dans le stockage et la séparation des gaz

L'une des applications les plus prometteuses des COFs est dans le domaine du stockage et de la séparation des gaz. Les pores bien définis et ajustables des COFs en font d'excellents candidats pour l'adsorption de gaz tels que l'hydrogène, le méthane et le dioxyde de carbone, à des capacités élevées.[48] Cette propriété revêt une importance primordiale pour relever les défis énergétiques mondiaux, notamment dans le contexte du stockage et du transport d'énergie propre. La grande surface des COFs, associée à leurs structures ordonnées, facilite les processus efficaces d'adsorption et de désorption des gaz, les rendant cruciaux dans le développement de matériaux avancés pour les applications énergétiques durables. Par rapport aux structures en couches 2D, les COFs 3D avec des surfaces et des volumes de pores plus importants ont montré des capacités de stockage plus importantes.[49] Un bon exemple du développement de COFs avec une application de stockage du dioxyde de carbone a été introduit par Ping Loh et al. en 2018.[50] Le matériau de départ à base de tétraphényléthane (TPE) a été utilisé pour former une variante structurelle inhabituelle [2 + 4] de la normale [4 + 4] tétraphényléthane-COF en utilisant différents solvants. TPE-COF-I avec un réseau entièrement lié est préparé par la voie traditionnelle [4 + 4] (Figure 16a), tandis que TPE-COF-II avec un réseau de liaison contrariée est préparé par la voie inhabituelle [2 + 4] (Figure 16b). Plus intéressant encore, TPE-COF-II avec des groupes fonctionnels non réagis disposés autour des cavités des COFs et une surface BET plus grande a présenté une meilleure performance d'adsorption du dioxyde de carbone (118,8 cm^3/g, 23,2 % en poids), comparée au COF normal (TPE-COF-I) avec une performance d'adsorption du dioxyde de

carbone de 68,6 cm^3/g, qui est l'une des capacités d'adsorption de CO_2 les plus élevées pour les matériaux COF à ce jour.

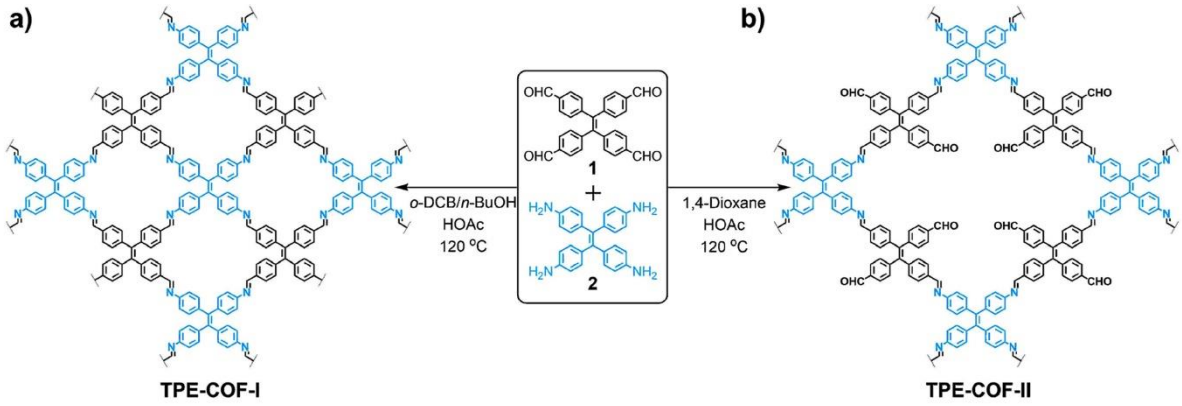

Figure 16 Synthèse des TPE-COFs avec différents solvants: TPE-COF-I avec la voie traditionnelle et normale [4 + 4] (a). TPE-COF-II avec la voie inhabituelle [2 + 4] (b). Reproduit avec permission de la reference [[50]]. Copyright @ 2018 American Chemical Society.

1.1.5.2 Application des COF dans le stockage d'énergie

Dans le domaine du stockage d'énergie, les COF ont montré un potentiel en tant qu'approche novatrice pour faire progresser la technologie des batteries. Parce que les COF peuvent accueillir et stabiliser les ions porteurs de charge, ils peuvent être utilisés dans le développement de dispositifs de stockage d'énergie tels que des batteries et des supercondensateurs.[51] Le contrôle précis de l'arrangement des groupes fonctionnels rendu possible par les structures bien définies des COF affecte les performances électrochimiques de ces matériaux.[52] De plus, parce que les COF sont modulaires, ils peuvent être personnalisés pour améliorer des caractéristiques spécifiques de stockage d'énergie telles que la stabilité cyclique, la capacité et les taux de charge-décharge.[53] L'utilisation des COF a un énorme potentiel pour faire progresser la création de technologies de stockage d'énergie de pointe et respectueuses de l'environnement, à mesure que le marché des solutions de stockage d'énergie efficaces et durables continue de s'étendre. Dans ce domaine, Patra et ses collaborateurs ont conçu certains COF modifiés avec un polymère conducteur pour une application de supercondensateur (Figure 17).[54] Ainsi, ils ont préparé deux COF liés par imine différents, puis ils ont été modifiés avec de la polyaniline par polymérisation in situ de l'aniline dans les structures (Figure 17a et b). En modifiant les COF de manière post-synthétique avec des polymères conducteurs, leur conductivité peut être améliorée. Les matériaux composites ont

présenté une conductivité de 1,4 à 1,9 × 10^{-2} S cm^{-1} et une capacité spécifique qui était 20 fois supérieure à celle des structures d'origine (Figure 17c-d).

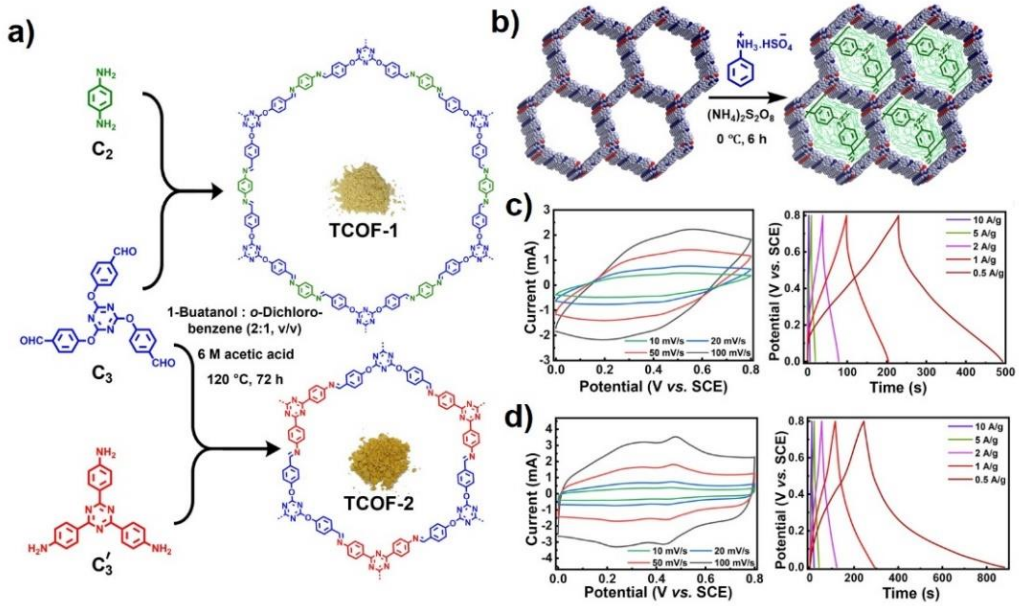

Figure 17 Synthèse de deux COF liés par imine (a), modification du COF avec de la polyaniline (b), performances électrochimiques des matériaux composites, PANI@TCOF-1 (c) et PANI@TCOF-2 (d). Adopté avec permission de la référence [[54]]. Copyright @ 2021 Wiley.

1.1.5.3 Application des COF en catalyse et photocatalyse

L'application des Cadres Organiques Covalents (COF) en catalyse et photocatalyse représente un domaine de recherche en plein essor avec des perspectives prometteuses pour faire progresser les transformations chimiques durables et efficaces.[11b, 55] COF, caractérisés par leurs structures bien définies et leurs grandes surfaces, présentent des propriétés exceptionnelles qui en font des candidats idéaux pour des applications catalytiques. En catalyse, les COF peuvent servir de catalyseurs hétérogènes, fournissant une plateforme stable et réglable pour diverses réactions. La porosité inhérente des COF permet un transport efficace des masses, améliorant les taux de réaction et la sélectivité. De plus, la nature modulaire des COF facilite l'incorporation de groupes fonctionnels spécifiques, permettant la création de sites catalytiques sur mesure pour des réactions ciblées. Dans le domaine de la photocatalyse, les COF présentent une excellente absorption de la lumière et des capacités de séparation de charges, les rendant précieux pour exploiter l'énergie solaire afin de stimuler des transformations chimiques.[9b, 55b, 56] Leur capacité à générer des intermédiaires réactifs sous irradiation lumineuse ouvre des voies pour des itinéraires de synthèse

propres et durables. L'application des COF en catalyse et photocatalyse a non seulement le potentiel de révolutionner les processus chimiques traditionnels, mais s'aligne également sur l'impératif croissant de technologies plus vertes et plus respectueuses de l'environnement.[11b, 55a] Les chercheurs explorent activement les COF en tant que catalyseurs pour un large éventail de réactions, y compris les transformations organiques et les processus industriels, démontrant ainsi leur polyvalence et leur adaptabilité dans le domaine de la catalyse.

Sur cette base, Lu et ses collaborateurs ont fourni un COF magnétique à coquille-core immobilisé avec des nanoparticules d'or pour une application catalytique hétérogène.[57] Dans cette étude, les NPs magnétiques ont d'abord été préparées, puis entourées de matériau COF pour préparer le matériau coquille-core abrégé Fe_3O_4@COF. Enfin, les nanoparticules d'or ont été uniformément synthétisées via une méthode de post-réduction et immobilisées à la surface du matériau COF en tant que plateforme poreuse pour former Fe_3O_4@COF-Au (Figure 18). L'analyse microscopique a montré des structures magnétiques coquille-core très uniformes avec une immobilisation dispersée et homogène des nanoparticules d'or à la surface du COF (Figure 18a-g). De plus, le catalyseur hétérogène préparé a présenté d'excellentes performances catalytiques, une stabilité chimique et thermique élevée, et une séparabilité magnétique pratique dans la réduction du 4-nitrophénol et du bleu de méthylène. De plus, cette méthode de synthèse peut être utilisée pour créer des nanomatériaux hybrides multifonctionnels pour des applications de catalyse avec d'autres nanoparticules métalliques nobles.

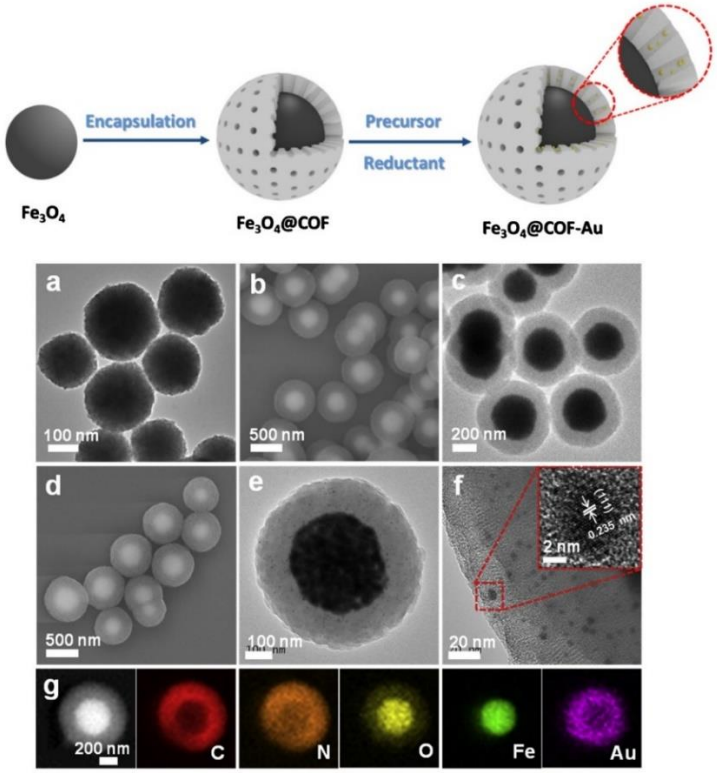

Figure 18 Synthèse de COF magnétique à coquille-core immobilisé avec des NPs d'or : image TEM de Fe3O4 (a), images SEM et TEM du COF magnétique à coquille-core (b-e) et images TEM et cartographie TEM du COF magnétique à coquille-core immobilisé avec des NPs d'or (e-g). Adopté avec permission de la référence [[57]]. Copyright @ 2020 Elsevier.

Certains COF à base de soufre ont été rapportés par Copper et ses collègues avec une application photocatalytique en 2018.[58] Dans ce projet, ils ont préparé le COF sans groupe fonctionnel sulfone (TP-COF) et le COF avec un (S-COF) et deux groupes fonctionnels sulfone (FS-COF) (Figure 19). Les résultats ont montré que le nombre de groupes fonctionnels sulfone peut avoir un effet direct sur l'évolution de l'hydrogène. Selon les observations, le FS-COF avec deux groupes fonctionnels sulfone, une plus grande surface spécifique BET et une structure cristalline plus élevée, a montré un taux d'évolution de l'hydrogène plus élevé de 10,1 mmol g^{-1} h^{-1} par rapport au COF avec un (S-COF, 4,44 mmol g^{-1} h^{-1}) et sans groupe fonctionnel sulfone (TP-COF, 1,6 mmol g^{-1} h^{-1}). Il est possible de réduire les angles de contact avec l'eau en ajoutant des groupes sulfone. Avec les plus bas angles de contact avec l'eau, le FS−COF interagit bien avec l'eau par rapport aux autres COF. Le FS−COF a montré une photoactivité supérieure en raison de sa bande interdite plus étroite, de sa plus grande surface spécifique et de sa plus grande cristallinité.

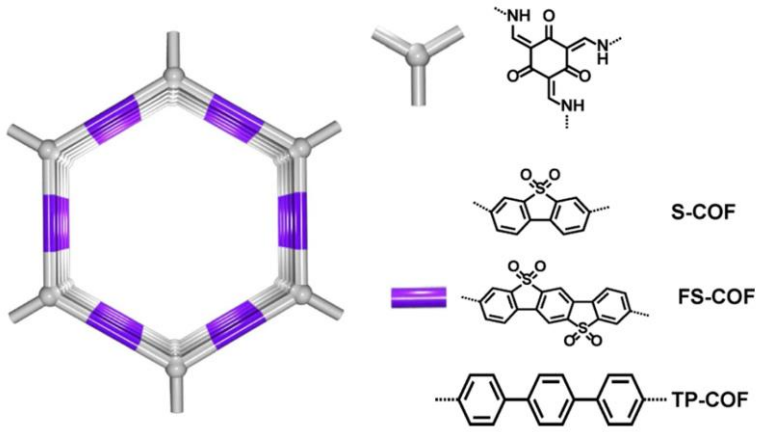

Figure 19 Structures chimiques de différents COF et COF à base de soufre, S−COF, FS−COF et TP−COF. Adopté avec permission de la référence [[58]]. Copyright @ 2018 Springer Nature.

1.1.5.4 Application des COF dans la détection

Au-delà du stockage de gaz, de la séparation et de la catalyse, les COF ont fait d'importants progrès dans les applications de détection.[59] La structure ordonnée des COF permet l'incorporation de molécules invitées dans leurs structures, entraînant des changements dans leurs propriétés en présence d'analytes spécifiques. Cette capacité de détection unique positionne les COF comme des matériaux prometteurs pour le développement de capteurs avec une sensibilité et une sélectivité élevées.[60] L'adaptabilité des COF en termes de fonctionnalisation et de modification renforce encore leur aptitude aux applications de détection, ouvrant des possibilités pour la détection d'une gamme diversifiée d'analytes dans la surveillance environnementale, les soins de santé et la sécurité. Sur ce sujet, un COF lié par hydrazone contenant des sites de chélation O,N,O′ pour la détection sélective du fer a été rapporté par Zhang et al.[61] Ainsi, ils ont préparé le COF lié par hydrazone par réaction de condensation de la base de Schiff entre la benzène-1,3,5-tricarbohydra-zide (Bth) et le 2,5- 2,5-diméthoxytéréphtalaldéhyde (Dma) (Figure 20). Le COF préparé a montré une forte activité de fluorescence aussi bien en dispersion en solution que dans l'état solide. Il est intéressant de noter que le COF préparé présente une sélectivité et une sensibilité exceptionnelles lorsqu'il est utilisé comme capteur de fluorescence éteinte pour la détection des ions Fe(III) en solution aqueuse. L'extinction de la fluorescence peut être attribuée à l'interaction de coordination entre les sites de chélation O,N,O′ du COF et les ions de fer, comme confirmé par les analyses NMR et XPS (Figure 20).

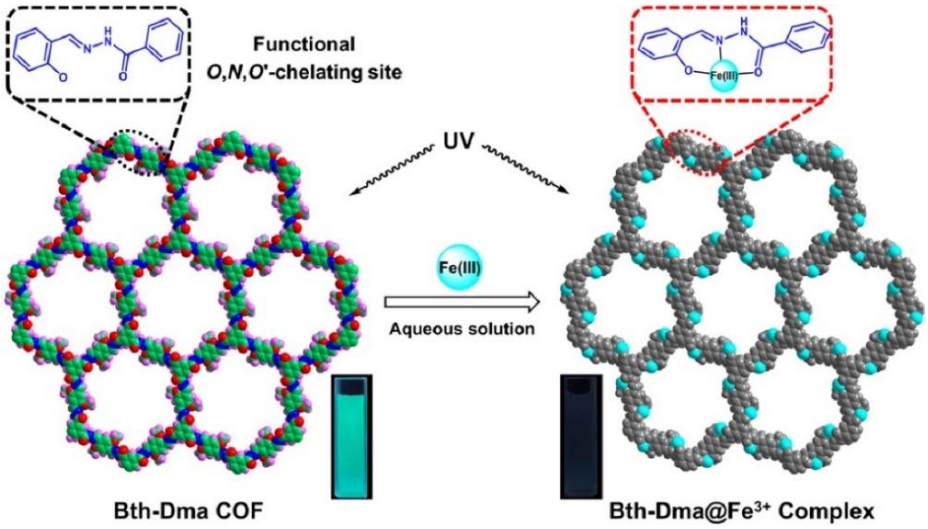

Figure 20 Illustration schématique de la synthèse conçue de COF lié par hydrazone contenant des sites de chélation O,N,O′ pour la détection sélective du Fe(III) par extinction. Reproduit avec la permission de la référence [[61]]. Copyright @ 2018 American Chemical Society.

1.1.5.5 Application des COF dans la délivrance de médicaments

Dans le domaine de la délivrance de médicaments, la porosité inhérente des COF permet l'encapsulation de molécules invitées, permettant une libération contrôlée dans le temps.[11c, 62] Cette propriété est particulièrement avantageuse dans les applications pharmaceutiques, où un contrôle précis de la cinétique de libération du médicament est crucial pour optimiser les résultats thérapeutiques. Les COF peuvent être adaptés pour accueillir des médicaments spécifiques, et leur biocompatibilité et leur dégradabilité les rendent attractifs pour les systèmes de délivrance de médicaments.[63] Les chercheurs explorent le potentiel des COF dans la délivrance ciblée de médicaments, visant à améliorer l'efficacité des traitements tout en minimisant les effets secondaires. Les matériaux COF comportant des liaisons covalentes dégradables par l'acide présentent un grand potentiel pour la délivrance de médicaments et la libération intracellulaire sensible aux stimuli.[64] Par exemple, le COF lié par imine TAPB-DMTP a été rapporté par Liu et ses collègues, utilisant une réaction de polycondensation de la base de Schiff entre le 2,5-diméthoxytéréphtaldéhyde (DMTP) et le 1,3,5-tris(4-aminophényl) benzène (TAPB) pour la délivrance et la libération pH-réactive de la doxorubicine (DOX) (Figure 21).[65] De manière intéressante, lorsque la DOX a été chargée in situ dans le COF, la taille moyenne des particules hautement cristallisées est passée de 200 nm à une plage de 200 à 400 nm (Figure 21a-d). De plus, la morphologie des particules est passée de matériaux sphériques uniformes monodispersés à des particules non uniformes. De plus, la réduction marginale apparente de la cristallinité du COF

chargé en DOX est probablement due à la réaction de base de Schiff entre le DMTP susmentionné et le groupe fonctionnel amino de la DOX. Environ 50% du médicament chargé a été libéré dans un milieu PBS avec un pH de 7,4 au cours des deux premières heures, tandis que la décomposition du support COF à des valeurs de pH plus basses a considérablement augmenté la libération du médicament, indiquant la caractéristique pH-réactive de DOX@COF.[66] Cela peut être attribué aux doubles liaisons C=N dans le COF TAPB-DMTP avec la capacité de cliver dans des environnements acides, ce qui conduit à la déconstruction des matériaux COF.

Figure 21 Illustration de la synthèse et de l'application de DOX@COF. Images SEM du COF (a et b) et de DOX@COF (c et d). Adopté avec permission de la référence [[65]]. Copyright @ 2019 Wiley.

1.1.5.6 Application des COF dans le traitement des eaux usées

Les COF sont des matériaux qui montrent un grand potentiel dans le traitement des eaux usées car ils apportent des solutions créatives aux problèmes environnementaux. En raison des propriétés spéciales des COF, telles que leur grande surface, leur stabilité chimique et leur porosité ajustable, ils excellent dans l'absorption et l'élimination des impuretés des eaux usées.[67] Les COF offrent une méthode flexible de purification de l'eau, pouvant être conçus avec des fonctionnalités personnalisées pour capturer sélectivement des polluants spécifiques, tels que des composés organiques et des métaux lourds.[68] De plus, la structure poreuse des COF permet un transfert rapide de masse, améliorant l'efficacité des procédures de traitement des eaux usées. La demande croissante de technologies respectueuses de l'environnement dans la remédiation de l'eau est en phase avec les caractéristiques durables des COF.[69] En utilisant les COF dans le traitement des eaux usées, nous pouvons contribuer à réduire la pollution dans l'environnement et fournir de l'eau propre.

Sur cette base, un COF modifié par éther couronné a été préparé par Das et al. pour l'élimination sélective du mercure.[70] Pour la préparation du COF modifié par éther couronné, ils ont d'abord synthétisé un matériau de départ diamine aromatique lié à un récepteur macrocyclique d'éther couronné pour l'adsorption sélective de Hg^{2+} (Figure 22). Avec une activité de suppression à haute capacité de 605 mg/g, le COF modifié par éther couronné préparé a pu éliminer sélectivement les ions de mercure à des niveaux de ppb dans une solution aqueuse contaminée sur une large plage de pH (3−9) avec une recyclabilité excellente, faisant du COF modifié un candidat viable pour des applications pratiques en plein air. Les matériaux poreux à surface élevée et cristalline, tels que les COF, sont principalement décorés de groupes fonctionnels thiol ou thioéther sur leurs surfaces poreuses pour cibler le Hg^{2+} dans une solution aqueuse en tirant parti du principe de liaison métal−ligand "soft−soft".[70-71]

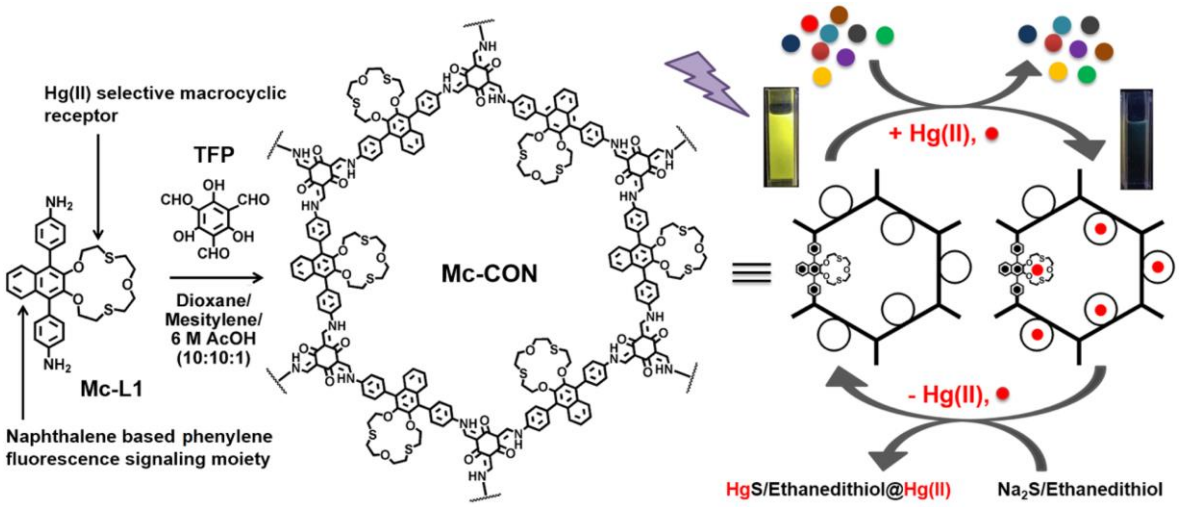

Figure 22 Illustration de la synthèse de COF modifié par éther couronné pour l'élimination sélective du mercure. Reproduit avec la permission de la référence [[70]]. Copyright @ 2021 American Chemical Society.

1.1.6 Objectifs

La synthèse de COFs hautement cristallins et poreux présente plusieurs défis qui nécessitent une considération attentive et des solutions innovantes. Un obstacle significatif est la réalisation d'un contrôle précis de la cristallinité de la structure COF, ce qui implique la formation de liaisons covalentes robustes et bien définies entre les blocs de construction organiques. La nature dynamique de certaines liaisons COF, telles que les liaisons imine ou ester boronate, peut entraîner des défauts potentiels et un désordre dans le réseau cristallin lors de la synthèse. De plus, l'optimisation des conditions de réaction pour favoriser la croissance de grands domaines cristallins

ordonnés tout en minimisant la formation de régions amorphes reste un défi. En outre, l'incorporation de groupes fonctionnels ou de molécules invitées pour des applications spécifiques sans compromettre la cristallinité pose des défis supplémentaires. Les innovations dans les méthodologies synthétiques, les techniques de purification et une compréhension plus approfondie des relations structure-propriété sont essentielles pour surmonter ces défis et faire progresser la synthèse de COFs de haute qualité aux propriétés adaptées à diverses applications, notamment la catalyse, le stockage de gaz et l'adsorption. Ainsi, dans ce projet, nous avons tenté de surmonter certains des défis mentionnés ci-dessus.

Les objectifs de la première recherche englobent le développement, la caractérisation et l'application d'un nouvel adsorbant COF magnétique avec une fonctionnalisation à la thiosemicarbazide pour l'élimination sélective du mercure. Utiliser une approche de PSM pour fonctionnaliser la coque COF avec différents ligands organiques, en particulier la thiosemicarbazide. Cette approche améliore la polyvalence des COFs pour des applications ciblées. L'étude vise à faire progresser le domaine des matériaux d'adsorption, contribuant à des solutions efficaces pour l'élimination des métaux lourds et favorisant la durabilité dans les processus de traitement de l'eau.

Les objectifs de la deuxième recherche visent à inaugurer une approche transformative de la synthèse de COF, en exploitant les HPAs (acides hétéropolyacides) de Keggin comme catalyseurs pour réaliser une production rapide, douce et évolutive de COFs 2D et 3D hautement cristallins et poreux. Départir des conditions difficiles traditionnelles impliquant la polycondensation par base de Schiff et l'acide acétique comme catalyseurs. Mettre l'accent sur les aspects de la chimie verte de la synthèse catalytique développée, minimisant l'impact environnemental et favorisant la durabilité. Fournir des idées sur le potentiel de production à grande échelle de matériaux COF pour la récupération d'énergie. Synthétiser avec succès un nouveau COF 2D lié par imine appelé TAPA-TPT dans des conditions de réaction douces, mettant l'accent sur une cristallinité élevée et une bonne porosité. Le travail contribue à faire progresser le domaine des matériaux COF et explore leurs applications potentielles dans les supercondensateurs, alignées sur les principes de la chimie verte. Évaluer les applications de supercondensateurs des COFs synthétisés, en mettant particulièrement l'accent sur les performances de TAPA-TPT. Mesurer la capacitance spécifique, démontrant le potentiel des COFs en tant que matériaux de stockage d'énergie.

Les objectifs de la troisième recherche sont centrés sur le développement et la caractérisation d'un nouveau catalyseur nanohétérogène pour la catalyse de la formation de liaisons C-C par le biais des réactions de couplage croisé, avec un accent particulier sur la réaction de Suzuki. Initiée par la préparation de matériaux de réseau organique microporeux (MON) à coque magnétique par la combinaison de Fe_3O_4 et d'un réseau organique microporeux, fournissant une matrice stable et poreuse pour l'immobilisation ultérieure du catalyseur. Réaliser l'absorption physique uniforme de nanoparticules de Pd à la surface externe du matériau MON, mettant en avant l'importance des nanoparticules de Pd de taille contrôlée pour une performance catalytique améliorée. Mettre l'accent sur l'importance du développement de catalyseurs hétérogènes recyclables et verts pour réduire l'impact environnemental et réduire les coûts associés aux méthodes catalytiques traditionnelles, conformément aux principes de la synthèse chimique durable et respectueuse de l'environnement.

L'objectif principal de la dernière recherche est de concevoir, synthétiser et caractériser un nouveau nanocatalyseur hétérogène pour la réaction de fixation du CO_2 afin de produire des carbonates précieux. L'accent est mis sur le développement d'un MON magnétique à coque magnétique décoré avec des nanoparticules de cuivre Cu immobilisées uniformément de tailles variées, y compris le cuivre métallique et l'oxyde de cuivre. Les objectifs clés comprennent l'analyse des propriétés structurales et compositionnelles du catalyseur à l'aide de différentes techniques, la confirmation de la chélation des nanoparticules de Cu par des groupes aminés et l'évaluation de l'efficacité du catalyseur en termes de temps de réaction, de rendements et de réutilisabilité. L'objectif global est de contribuer à un catalyseur durable et efficace pour le domaine de la fixation du CO_2, abordant les préoccupations environnementales et promouvant les principes de la chimie verte.

CHAPITRE 2

MODIFICATION POST-SYNTHÉTIQUE DE CADRES ORGANIQUES COVALENTS MAGNÉTIQUES À COQUE POUR L'ÉLIMINATION SÉLECTIVE DU MERCURE

2.1 2.1 Introduction

Dans cette partie de la thèse, nous nous sommes concentrés sur la synthèse et la fonctionnalisation d'un COF à base d'imine en deux dimensions. Pour ce faire, j'ai préparé un COF lié par imine à coquille-core magnétique, et ensuite, après modification post-synthétique par certains ligands organiques, en particulier le ligand thiol, il a été capable d'éliminer sélectivement les métaux lourds, en particulier les ions mercure, des eaux usées.

2.2 Article publié pour cette étude

Post-Synthetic Modification of Core-Shell Magnetic Covalent Organic Frameworks for the Selective Removal of Mercury, ACS Applied Materials Interfaces, 2023, 15, 23, 28476–28490. https://pubs.acs.org/doi/abs/10.1021/acsami.3c02914.

Post-Synthetic Modification of Core-Shell Magnetic Covalent Organic Frameworks for the Selective Removal of Mercury

Amir Khojastehnezhad[a], Farid Moeinpour[b], Maziar Jafari[a], Mohammad K. Shehab[c], Ahmad Samih ElDouhaibi[d], Hani M. El-Kaderi[c], and Mohamed Siaj[a*]

[a]Department of Chemistry, University of Quebec at Montreal, Montreal, QC H3C3P8, Canada

[*]Corresponding Email: siaj.mohamed@uqam.ca

[b]Department of Chemistry, Bandar Abbas Branch, Islamic Azad University, Bandar Abbas, Iran

[c]Department of Chemistry, Virginia Commonwealth University, Richmond, Virginia 23284, United States

[d]Department of Chemistry, Lebanese University, College of Science III, Mont Michel, Tripoli, Lebanon

Abstract

Core-shell magnetic COF materials were prepared, followed by shell material functionalization with different organic ligands, including thiosemicarbazide, through a post-synthetic modification approach. The structures of the prepared samples were characterized with various techniques, including PXRD, BET, TGA, PiFM, TEM, SEM, XPS and solid ^{13}C-NMR. PXRD and BET studies revealed that the crystalline and porous nature of the functionalized COFs is well maintained after three steps of post-synthetic modification. On the other hand, solid ^{13}C-NMR, TGA and PiFM

analyses confirmed the successful functionalization of COF materials with good covalent linkage connectivity. The use of the resulting functionalized magnetic COF for selective and ultrafast adsorption of Hg(II) has been investigated. The observations displayed rapid kinetics with adsorption dynamics conform to the quasi-second-order kinetic model and the Langmuir adsorption model. Furthermore, this prepared crystalline magnetic material demonstrated a high Langmuir Hg(II) uptake capacity, reaching equilibrium in only 5 minutes. Thermodynamic calculations proved that the adsorption process is endothermic and spontaneous.

Keywords: Covalent organic frameworks (COFs), wastewater purification, water filtration, Hg(II) removal, heavy metal capture

1. Introduction

Heavy metal water pollution is a significant environmental issue that has widely attracted interest in the research community. Mercury is one of many harmful metals that has drawn a lot of attention. Due to its ability to bind to the sulfhydryl group in proteins and enzymes, mercury is one of the most hazardous elements and can lead to chronic illnesses or even death.[72] In the chemical, petrochemical, pharmaceutical, and dyeing industries, mercury, and its compounds are employed. Therefore, it is crucial to remove mercury from water and industrial wastewater. If not, methylmercury, the most toxic form of mercury, will be absorbed by aquatic organisms after being released into the environment, accumulating biologically through the food chain until it eventually threatens the life and health of the final consumers.[73] Chemical precipitation, ion exchange, reverse osmosis, and adsorption are some of the methods for removing mercury.[74] The removal of low concentrations of mercury from treated wastewater has a high potential for success. Due to its low cost, flexible operation, lack of byproducts, and ability to be reused, adsorption has long been acknowledged as one of the most effective methods for the removal of traces of heavy metals.[75] Resins, activated carbon, nanoscale metal oxides, and zeolites are just a few of the many adsorbents used in wastewater treatment for Hg(II) removal.[76] Adsorbents are only marginally useful due to their poor selectivity, slow kinetics, and low adsorption capacity, particularly for the rapid remediation of unanticipated Hg(II) pollution incidents.[77] The creation of extremely powerful adsorbents is essential for the selective capture of mercury.[78] Hg(II) has been successfully removed from wastewater using a variety of recently improved adsorbents. To address Hg(II) removal from chlorinated water, several advanced sorbents were developed, including graphene oxide (GO) modified with 4-amino-5-hydrazinyl-2,4-dihydro-3H-1,2,4-triazole-3-

thione,[79] metal-organic frameworks (MOFs),[80] sulfur-functionalized magnetic organic polymers,[81] and chitosan-lignin composite with polyethyleneimine functionalization.[82] The difficult regeneration process, high material cost, and challenging preparation process continue to hinder the widespread application of porous adsorbents. Among porous crystalline polymers,[83] covalent organic frameworks (COFs) are a new type of versatile porous crystalline materials with modifiable and designable structures.[84] COFs are constructed by linking organic building blocks using strong covalent linkages.[5, 85] The large surface area, superior chemical selectivity, superior constructional stability, adjustable pore size, and distinctive delocalization of electron systems are just a few of many advantages of COFs.[86] Recently, COFs have grown in popularity as adsorbents in sample pre-treatment.[87] COFs can interact with substances that have specific structures by using the size effect, hydrogen bonding, π-π forces, and other mechanisms.[88] The ordered structure and sizable surface areas of COFs allow for sufficient interaction between the active sites and the target.[89] Since COFs consist of a variety of building blocks, their functionalization to significantly change their physicochemical characteristics, such as host-guest interaction, stability, and opto-electric ability to accommodate the demands of different usages is a simple process.[8b, 90] Due to these unique characteristics, COFs show promise as effective sorbents for the removal of heavy metals.[91]

Development of functionalized COFs as an adsorbing material remains scarce.[1a, 92] To immobilize the functional groups onto the pores and surfaces of COFs, all functionalized COFs were made from the bottom up or through post-synthetic modification.[91a, 93] Bottom-up approach has some limitations because it needs somewhat lengthy synthetic steps and may have a direct effect on the COF's formation. In contrast, post-synthetic functionalization of COFs affords higher versatility and more convenient to modify COFs' structures to target specific applications.[42, 46-47] For example, Yaghi *et al*. reported the multistep post-synthetic modification of imine-linked COFs, in which the imine-functional groups on the COFs were converted to carbamate and thiocarbamate-linked groups with almost unchanged porosity and crystallinity.[46] In another study, the same group incorporated the reactive aliphatic amine species into the COF materials in two solid-state post-synthetic steps. It was observed that the amine-functionalized COFs showed a 1360-fold enhancement in CO_2 adsorption compared to the pristine COF.[47] Amidation, esterification and thioesterification of carboxyl COFs have also been studied by Yaghi's research group. In this research, a novel 2D COF with carboxyl groups on its structure was prepared and then, various

organic ligands were linked onto the carboxyl groups to prepare a couple of adsorbents for efficient removal of different pollutants.[94] These findings prompted us to think about post-synthetic modification of COFs for Hg(II) separation.

In this study, we first prepared the core-shell magnetic imine-linked COFs to enable sorbents' recovery magnetically. They were then functionalized with thiosemicarbazide via three steps of post-synthetic modification to produce magnetic thiocarbonyl-linked COFs (Scheme 1). After functionalization, the latter demonstrated very good crystallinity, porosity, and covalent connectivity, as well as a high performance in the selective and ultrafast removal of Hg(II) from water, with an uptake capacity of 1400.9 mg g^{-1}.

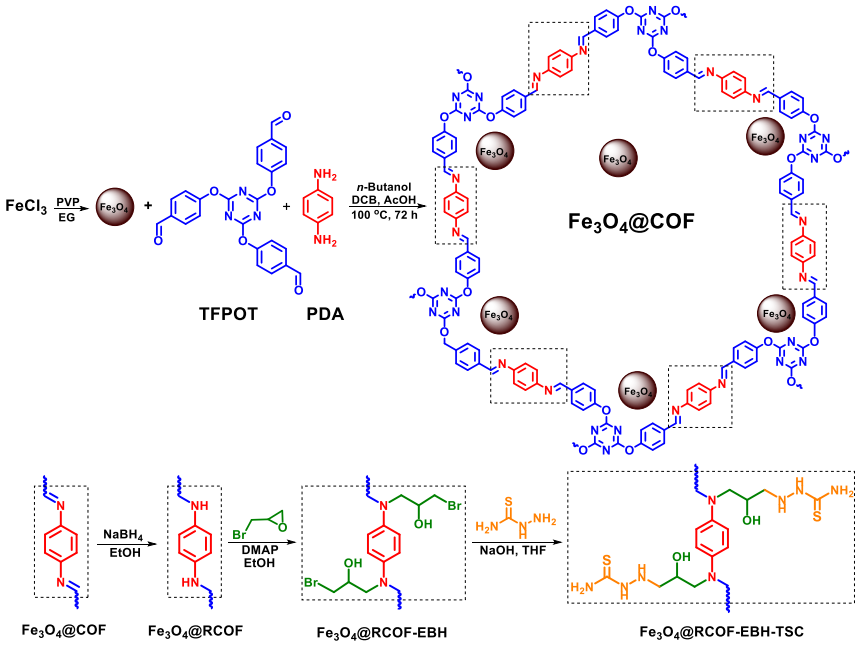

Scheme 1. Synthesis of functionalized magnetic COFs.

2. Experimental Section

2.1. Materials

Acetone, *o*-dichlorobenzene (DCB), tetrahydrofuran (THF), *n*-butanol (n-BuOH), ethanol (EtOH) acetone, and acetic acid (AcOH) were purchased from local chemical distributors. Chemicals were listed as follows: iron(III) chloride hexahydrate ($FeCl_3$ $6H_2O$, 98% purity, Sigma-Aldrich), *p*-phenylenediamine ($C_6H_4(NH_2)_2$, 98% purity, Sigma-Aldrich), epibromohydrin (C_3H_5BrO, 98% purity, Sigma-Aldrich), *p*-hydroxy benzaldehyde ($C_7O_2H_6$, 98% purity, Sigma-Aldrich), thiosemicarbazide ($NH_2CSNHNH_2$, 98% purity, Sigma-Aldrich), *p*-phenylenediamine ($C_6H_4(NH_2)_2$, 98% purity, Sigma-Aldrich), *p*-(dimethylamino)pyridine ($C_7H_{10}N_2$, 98% purity,

Sigma-Aldrich), polyvinylpolypyrrolidone (98% purity, Sigma-Aldrich) and sodium borohydride ($NaBH_4$, 98% purity, Sigma-Aldrich). All chemicals were used without any further purification.

2.1.1. Material Characterization

To characterize the morphologies and sizes of prepared samples, transmission electron microscopy (TEM), high-resolution TEM (HR-TEM) along with the energy-dispersive spectroscopy elemental characterization and mapping (STEM-EDX) (Oxford Instruments, Abingdon, Oxfordshire, UK) and the field-emission scanning electron microscope (FESEM, JSM7600F, JEOL, Akishima, Tokyo, Japan) were used. X-ray photoelectron spectroscopy (XPS) was done on an XPS PHI 5600-ci (Physical Electronics, Eden Prairie, MN, USA) to study the surface compositions and states. X-ray diffraction (XRD) with Cu Kα radiation (Bruker D8 advance, Billerica, MA, USA) was used to analyze the crystalline structures of the prepared samples. Further morphology and spectroscopy characterization were carried out by photo-induced force microscopy (PiFM) (VistaOne, MolecularVista.Inc, San-José, California, USA) by simultaneously measuring topography and assigning chemical identities to observed high-resolution features measuring less than the diffraction limit of light. Inductively coupled plasma optical emission spectrometry (ICP-OES) (Agilent model 5100, Santa-Clara, CA, USA) analysis was performed using radial mode.

2.2. Methods

2.2.1. Synthesis of 2,4,6-tris-(4-formylphenoxy)-1,3,5-triazine (TFPOT)

The *p*-hydroxy benzaldehyde (14.64 mmol, 1800 mg) and NaOH (14.64 mmol, 585 mg) was dissolved in a 100 mL round bottom flask and in the mixture of acetone:water (24:24 mL) and then, it was brought to 0 ^{o}C in an ice bath. Cyanuric chloride (4.88 mmol, 900 mg) was dissolved in 24 mL of acetone and added to the previous solution dropwise in a lapse of 60 minutes. During the addition, a white solid was formed. The reaction continued for 12 h at room temperature. After reaction completion, the white solid was filtered and washed with copious water. Finally, it was recrystallized in ethanol before being dried in a vacuum oven at 80 ^{o}C. A final pure white solid product was obtained with 92 % of yield .[54]

2.2.2. Synthesis of COF

To a 15 mL high-pressure glass tube, the 2,4,6-tris(4-formylphenoxy)-1,3,5-triazine (TFPOT) (0.2 mmol, 88 mg), *p*-pheneylenediamine (PDA) (0.3 mmol, 32.5 mg), *n*-butanol (1 mL), and 1,2-dichlorobenzene (1 mL) were added. The mixture was stirred vigorously for 10 min and sonicated for 10 min to obtain a homogeneous solution. Acetic acid (0.2 mL, 6 M) was added without stirring.

The mixture was purged with N_2, capped, and heated at 100 °C without stirring for 72 h. The reaction mixture was cooled to room temperature, then isolated by filtration using a medium glass frit. The product was washed extensively with acetone and THF then characterized by XRD (yellow solid, yield 92%) (Scheme 2).[54]

2.2.3. Synthesis of Core-Shell Magnetic COF (Fe_3O_4@COF)

Iron oxide NPs have been prepared according to the literature.[95] Synthesis of magnetic COF was performed according to the following method: to a 35 mL high-pressure glass tube, 2,4,6-tris(4-formylphenoxy)-1,3,5-triazine (TFPOT) (0.4 mmol, 176 mg), *p*-pheneylenediamine (PDA) (0.6 mmol, 65 mg), *n*-butanol (2 mL), and 1,2-dichlorobenzene (2 mL) were added. The mixture was stirred vigorously for 10 min and sonicated for 10 min to obtain a homogeneous solution. While stirring, Fe_3O_4 magnetic NPs (40 mg) dispersed in *n*-butanol and dichlorobenzene (0.5:0.5 mL, 1:1 ratio) were added dropwise, then acetic acid (0.4 mL, 6 M) was added without stirring. Finally, the mixture was purged with N_2, capped, and heated at 100 °C without stirring for 72 h. The reaction mixture was cooled to room temperature and the precipitate was recovered by filtration using a medium glass frit. The product was washed extensively with acetone and THF, then directly characterized by XRD (light brown solid, yield 88%) (Scheme 1).

2.2.4. Synthesis of Fe_3O_4@RCOF

The magnetic COF (50 mg) was sonicated in EtOH (30 mL) followed by mechanical stirring for 10 minutes. A solution of $NaBH_4$ (30 mg) in a mixture of EtOH/H_2O (10/10 mL, 1:1 ratio) was added dropwise to the previous solution and the mixture was shook for 12h at room temperature. After completion of the reduction reaction, the reduced COF (Fe_3O_4@RCOF) was separated from the mixture by an external magnet and washed with ethanol and water in a Soxhlet extractor for 12h and dried in a vacuum oven for 12 h at 80 °C to obtain the Fe_3O_4@RCOF.[39, 96]

2.2.5. Synthesis of Fe_3O_4@RCOF-EBH

The Fe_3O_4@RCOF (50 mg) was sonicated in EtOH (30 mL), followed by dropwise addition of a solution of 4-dimethylaminopyridine (25 mg), epibromohydrin (EBH) (50 mg) and EtOH (20 mL). The reaction mixture was mechanically stirred at 60 °C for 12 h. After completion of the reaction, the Fe_3O_4@RCOF-EBH was separated from the solution by an external magnet and washed with ethanol in a Soxhlet extractor for 12 h and dried in a vacuum oven for another 12 h at 80 ^oC to obtain the Fe_3O_4@RCOF-EBH.[97]

2.2.6. Synthesis of Fe_3O_4@RCOF-EBH-TSC

Magnetic Fe_3O_4@RCOF-EBH (50 mg) was sonicated in THF (30 mL), followed by dropwise addition of a solution of NaOH (25 mg), thiosemicarbazide (TSC) (50 mg) and THF (20 mL). The reaction mixture was mechanically stirred at 60 °C for 24 h. After completion of the reaction, the magnetic solid was separated from the solution by an external magnet and washed with ethanol in a Soxhlet extractor for 12 h and dried in a vacuum oven for 12 h at 80 °C to obtain the magnetic Fe_3O_4@RCOF-EBH-TSC.

2.2.7. Adsorption experiment

All adsorption experiments were carried out in a 250 mL Erlenmeyer flask-containing initial concentrations of metal ions and specific amounts of Fe_3O_4@RCOF-EBH-TSC at various times and under discontinuous conditions. Different solutions of Hg(II) with the required concentrations have been prepared by thinning the Hg(II) solution (1000 ppm). To find the optimum condition, the effects of pH (1–7) and time (5 to 360 minutes) have been investigated on the removal procedures. The initial concentration of Hg(II) and adsorbing dosage of adsorbent were considered from 5.0 to 200 mg/L and from 1.0 to 50 mg/100 mL respectively. Finally, to perform the experiments, after adsorption equilibrium, the adsorbent was separated from the mixture by using an external magnet and the remaining solution was analyzed by ICP. All experiments were repeated three times.

2.2.8. General procedure for selective Hg(II) adsorption

Fe_3O_4@RCOF-EBH-TSC (10.0 mg) was added to an Erlenmeyer flask (250 mL) containing a 10 ppm 50-mL aqueous buffer solution of $Hg(NO_3)_2$, $Pb(NO_3)_2$, $Zn(NO_3)_2$, $Fe(NO_3)_3$, $Cd(NO_3)_2$, $Ni(NO_3)_2$, $Mn(NO_3)_2$ and $AgNO_3$ at pH = 6. The mixture, in the form of slurry, was stirred at room temperature for 5 min. After, the adsorbent was separated from the mixture by filtration and the filtrate was analyzed by ICP to determine the remaining metal contents.

2.2.9. General procedure for recycling

Fe_3O_4@RCOF-EBH-TSC (10.0 mg) was added to an Erlenmeyer flask (250 mL) containing $Hg(NO_3)_2$ solution (50 mL) at 10 ppm. The mixture was stirred at room temperature for 5 min, separated by using an external magnet and washed with 50 mL water. The Fe_3O_4@RCOF-EBH-TSC sample was stirred in 50 mL HCl solution (0.1 M) for 30 min, separated and washed with 50 mL water. The air dried Fe_3O_4@RCOF-EBH-TSC was regenerated and used for the next cycle.

3. Results and Discussion

Thiocarbonyl-functionalized core-shell magnetic COF (Fe_3O_4@RCOF-EBH-TSC) was prepared with the following different synthesis steps. First of all, the magnetic Fe_3O_4 materials were prepared according to the literature.[95] Next, it has been used for the synthesis of core shell magnetic COF materials (Fe_3O_4@COF) from the imine condensation reaction between 4-phenylenediamine (PDA) and 2,4,6-tris(4-formylphenoxy)-1,3,5-triazine (TFPOT) in a mixture of *n*-butanol, 1,2-dichlorobenzene and acetic acid at 100 °C for three days. Afterwards, the imine functional groups of the COF were reduced to amine groups by $NaBH_4$ to prepare the Fe_3O_4@RCOF. Then, the amine group was functionalized by reactions with epibromohydrin and thiosemicarbazide to prepare the thiocarbonyl-functionalized magnetic COF material (Fe_3O_4@RCOF-EBH-TSC) (Scheme 1)[98] Finally, the chemical structure of the prepared materials was fully characterized by various techniques, including solid state ^{13}C-NMR, FT-IR, HR-TEM, TEM, SEM, EDX, TGA, XPS, BET, PiFM, ICP and XRD.

3.1. Material Characterization

3.1.1. TEM and SEM Analyses

We studied the size and morphology of the prepared samples with TEM and SEM techniques. TEM and SEM images of Fe_3O_4 magnetic nanoparticles showed a spherical morphology with about 200 nm diameter (**Fig. 1a** and **Fig. S1**). TEM studies also exhibited thin crystal lattices stacked on each other for COF and confirmed the crystalline structure of the prepared COF material (**Fig. 1b** and **Fig. S2**).[99] The core-shell structure of magnetic COF was approved by subsequent TEM images (**Fig. 1c-e**).[100] TEM-EDX mapping was also used to study the core-shell structure and elemental contribution of the magnetic COF after reduction and functionalization. As shown in **Fig. 1f**, the core structures contain iron and oxygen, while shell structures include nitrogen, carbon and also sulfur which confirmed the proper chemical grafting of ligands on the surface of magnetic COF.[101]

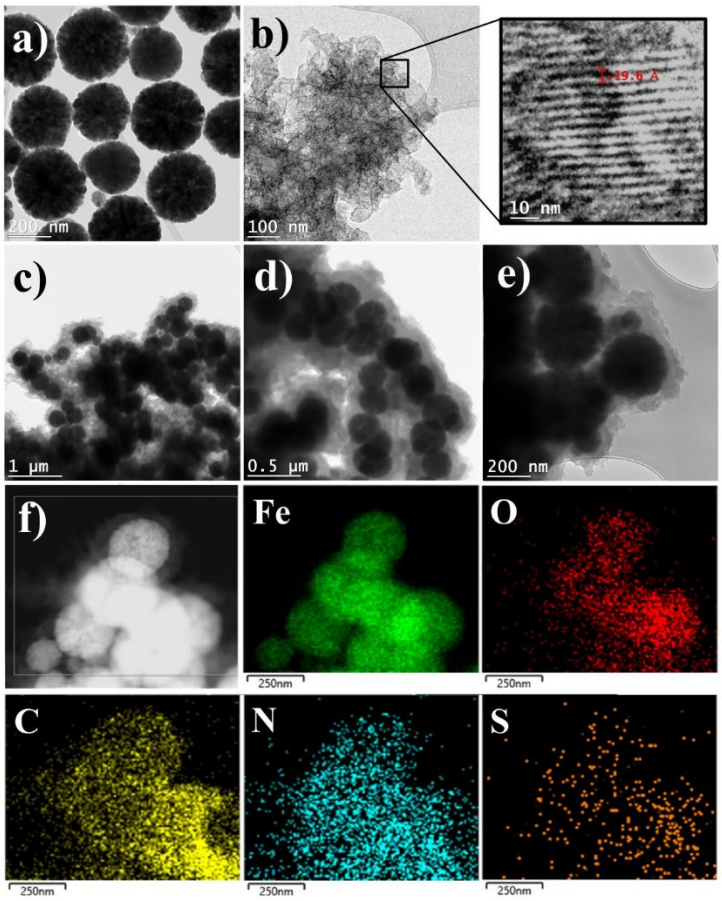

Fig. 1. TEM images of Fe_3O_4 nanoparticles (**a**), COF (**b**), Fe_3O_4@RCOF-EBH-TSC (**c**-**e**) and TEM mapping of Fe_3O_4@RCOF-EBH-TSC (**f**).

3.1.2. XRD, BET, TGA and FT-IR Analyses

For evaluating the crystal structure of the prepared materials, XRD technique was utilized. **Fig. 2a** and **b** showed the XRD patterns of the prepared materials including Fe_3O_4 MNPs, COF, Fe_3O_4@COF and functionalized COF such as RCOF, RCOF-EBH and RCOF-EBH-TSC. XRD analysis for iron oxide MNPs (**Fig. 2a**, black pattern) exhibited six characteristic peaks at 2Θ = 30.09, 35.5, 43.0, 53.2, 57.2 and 62.11 with cubic planes of Fe_3O_4 (2 2 0), (3 1 1), (4 0 0), (4 2 2), (5 1 1) and (4 4 0) (JCPDS card No. 19–0629).[102] The XRD pattern related to COF showed a relatively sharp peak at around at 2.68° and four weak diffraction peaks at 4.7, 5.4, 7.2, and 9.5 assigned to the (1 0 0), (1 1 0), (2 0 0), (2 1 0), and (2 2 0) planes, respectively (**Fig. 2a**, red pattern and **2b**, black pattern).[54] The last XRD pattern in **Fig. 2a** (blue pattern) corresponded to core-shell Fe_3O_4@COF material, all diffraction peaks of Fe_3O_4 and COF materials are present which confirms the crystalline structure of COF material is retained after the preparation of the core-shell materials.

Maintaining the crystalline and porous structure of COF materials after post-synthetic modification is very important. Thus, XRD and BET analyses were performed on all materials after modification. As shown in **Fig. 2b**, the crystalline structure of COF is very well retained after the reduction reaction (**Fig. 2b**, red pattern),[103] although, it decreased somewhat after post-synthetic functionalization with EBH and TSC (**Fig. 2b**, blue and pink patterns). Also, the porosity and BET surface area of all samples were investigated by N_2 adsorption-desorption isotherms (**Fig. 2c** and **Fig. S3** and **S4**). Consistent with the mesoporous nature of the prepared COFs, the nitrogen adsorption-desorption isotherms exhibited type-IV isotherms with H1 hysteresis loop and cylindrical-like pore channels.[54, 104] The BET surface area of COF, Fe_3O_4@COF, Fe_3O_4@RCOF, Fe_3O_4@RCOF-EBH and Fe_3O_4@RCOF-EBH-TSC were found to be 1325, 1157, 1104, 909 and 548 $m^2\ g^{-1}$, respectively (**Fig. S3**). These values indicate that pore functionalization was accomplished without compromising porosity while XRD studies indicated retained crystallinity.[105] Moreover, the pore volume of all samples were seen to decrease and pore size showed some changes.[54] Accordingly, the pore volumes of COF, Fe_3O_4@COF, Fe_3O_4@RCOF, Fe_3O_4@RCOF-EBH and Fe_3O_4@RCOF-EBH-TSC were 1.07, 1.05, 0.83, 0.72 and 0.55 $cm^3\ g^{-1}$, respectively and pore size were 3.16, 3.71, 3.02, 3.17 and 4.01 nm, respectively (**Fig. S4**). TGA analysis was used to confirm the thermal and chemical stability of the materials. As can be seen in **Fig. 2d**, COF material is stable until 400 °C and it indicated 100% weight loss at around 600 °C (**Fig. 2d**, black curve). With a lesser weight loss, this curve is similar to the TGA curve for core-shell Fe_3O_4@COF material and showed about 82% weight loss. This decrease (18%) is assigned to the Fe_3O_4 NPs (**Fig. 2d**, red curve). Interestingly, the results showed that the TGA curve for reduced magnetic COF (**Fig. 2d**, blue curve) is similar to the previous one with also a lesser weight loss. However, a greater weight loss (about 12%) after functionalization with EBH and TSC was observed (**Fig. 2d**, pink curve). This analysis is in accordance with previous studies and approves the successful post-synthetic functionalization of COF materials. FT-IR studies confirmed the successful synthesis of COF (**Fig. S5**). According to this analysis, both adsorption peaks related to amine functional group of PDA and carbonyl functional group of TFPOT at around 3400 and 1700 cm^{-1} disappeared in the FT-IR spectrum of COF material. The appearance of a new peak at 1621 cm^{-1} corresponding to C=N confirmed the successful synthesis of COF. Besides, FT-IR spectra of Fe_3O_4, COF, Fe_3O_4@COF-EBH and Fe_3O_4@RCOF-EBH-TSC were compared and the FT-IR spectrum of Fe_3O_4@COF showed all peaks related to Fe_3O_4 (broad peak at 585 cm^{-1}) and COF

were present, which confirmed the successful synthesis of magnetic COF (**Fig. S6**). Also, after the functionalization of Fe_3O_4@COF with EBH and TSC, the broad peak at around 3400 cm^{-1} and three sharp peaks between 3200 to 3400 cm^{-1} approved the successful post-synthetic modification of COF with EBH and TSC, respectively (**Fig. S6**).

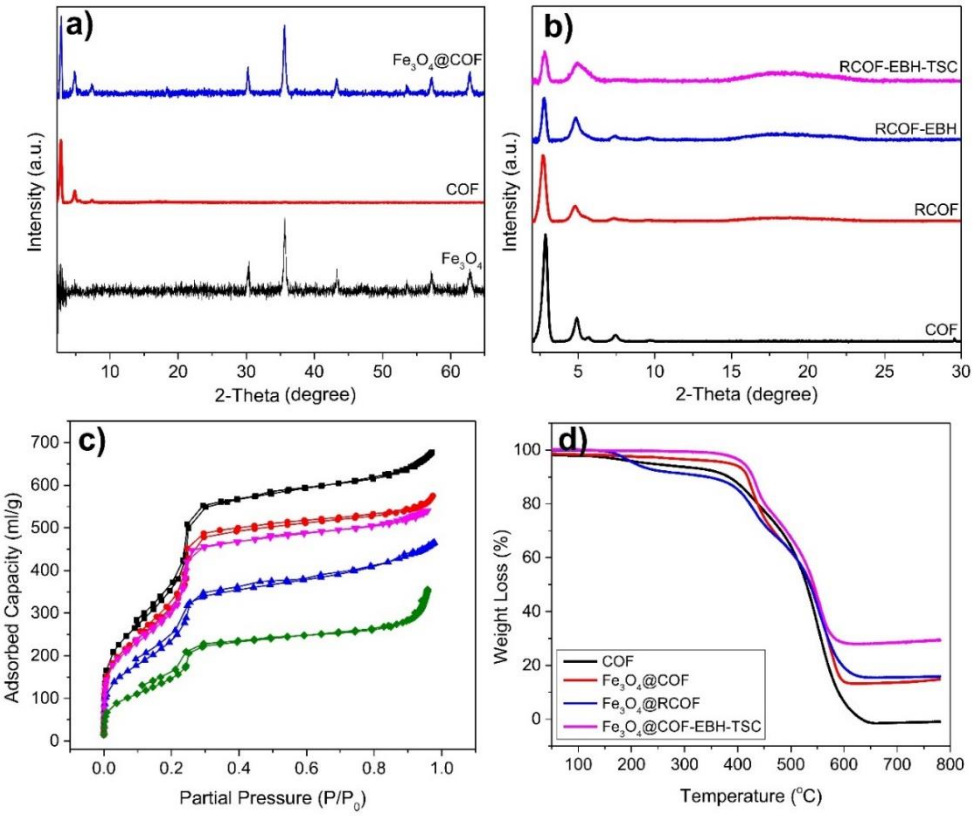

Fig. 2. XRD patterns of Fe_3O_4 MNP, COF and Fe_3O_4@COF (**a**); XRD patterns of COF, RCOF, RCOF-EBH, and RCOF-EBH-TSC (**b**); N_2 adsorption−desorption isotherms of COF (black curve, **c**), Fe_3O_4@COF (red curve, **c**), Fe_3O_4@RCOF (pink curve, **c**), Fe_3O_4@RCOF-EBH (blue curve, **c**), and Fe_3O_4@RCOF-EBH-TSC (green curve, **c**); TGA plots of COF (black curve, **d**), Fe_3O_4@COF (red curve, **d**), Fe_3O_4@RCOF (blue curve, **d**), and Fe_3O_4@RCOF-EBH-TSC (pink curve, **d**).

The crystalline structures of COF and the post-modified COF (RCOF-EBH-TSC) were also confirmed by simulation (**Fig. 3**). The COF and RCOF-EBH-TSC were simulated using the space group of P6/mmm with optimized lattice parameters of a = b = 39.187 Å, c = 3.673 Å and α = 89.5°, β = 69.3°, and γ = 120°. As can be found in the COF and RCOF-EBH-TSC, the experimental PXRD patterns are in a good match with the simulated patterns of the models with a P6/mmm space group. Furthermore, both COF and RCOF-EBH-TSC showed the same diffraction patterns at crystal planes of (100), (110), and (210), which indicates that the hexagonal dimensions toward

the X and Y axes of the framework stayed intact after the post-synthetic modification. However, the diffraction pattern of the RCOF-EBH-TSC at 19º indicates that the post-synthetic modification process caused an increase in the interlayer spacing distance (d-spacing) of the (0 0 1) crystal plane from 3.67 Å to 4.50 Å where the peak shifts to lower 2θ o angle by increasing the d-spacing. Environmental stability of the RCOF-EBH-TSC was evaluated in different acidic and basic conditions (**Fig. S7**). The functionalized COF was stable in both acidic and basic conditions and no substantial changes in PXRD patterns were observed.[24, 106]

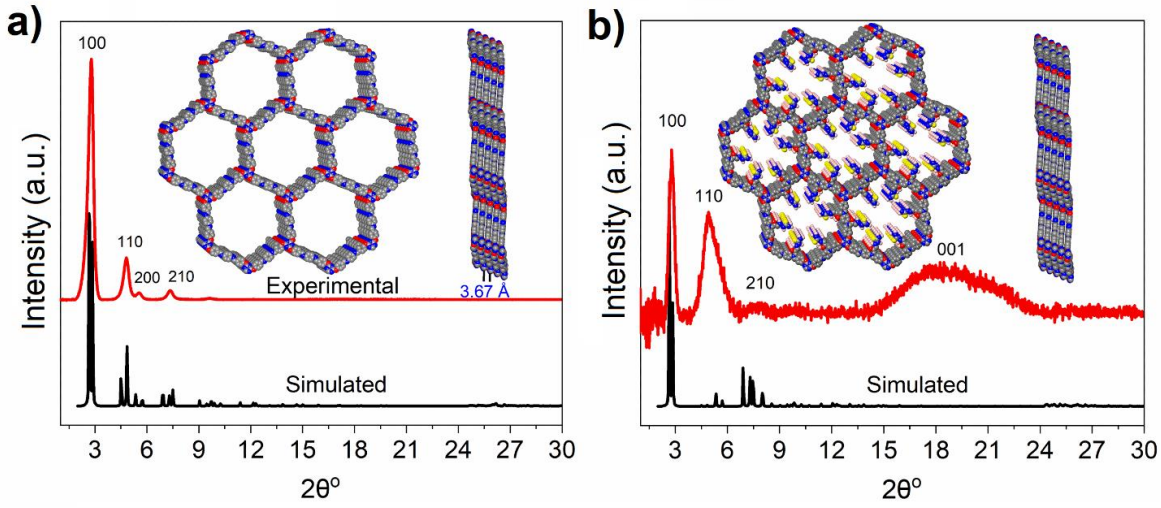

Fig. 3. PXRD for the simulated (black) and experimental (red) patterns for COF before (**a**) and after post-synthetic modification (Fe_3O_4@RCOF-EBH-TSC) (**b**).

3.1.3. Solid State ^{13}C CP-MAS NMR Analysis

To monitor the post-synthetic functionalization of COF materials, ^{13}C CP-MAS NMR analysis was performed. This experiment was done on COF, RCOF, RCOF-EBH and RCOF-EBH-TSC without the Fe_3O_4 shell material (**Fig. 4**). The spectrum of COF indicated seven carbon peaks at 122, 130, 135, 149, 154, 165, and 173 ppm that confirmed the successful synthesis of COF, according to literature (**Fig. 4a**).[107] After chemical reduction of the imine functional group on the surface of COF materials into amine groups, a new carbon peak related to amine formation appeared at 49 ppm (**Fig. 4b**).[39, 103] Also, after the chemical reaction between the amine functional groups of COF with EBH, the final functionalized COF material showed some new peaks between 15 to 70 ppm. The peaks at 41, 54 and 64 are assigned to the EBH connected to the amine groups and the peaks at lower ppm are owed to the physical adsorbing of EBH on the surface of COF (**Fig. 4c**).[47, 71b] In

the last reaction between TSC and functionalized COF, a new peak appeared at 175 ppm, attributed to the carbon of TSC, and the remaining EBH carbon atoms were shifted to the upper ppm after chemical bonding with TSC (**Fig. 4d**).[90b, 108] The peaks related to the EBH and TSC are weaker than those of the COF because some functional imine groups in the pores and between the layers of COF could not be reduced into amines.[47]

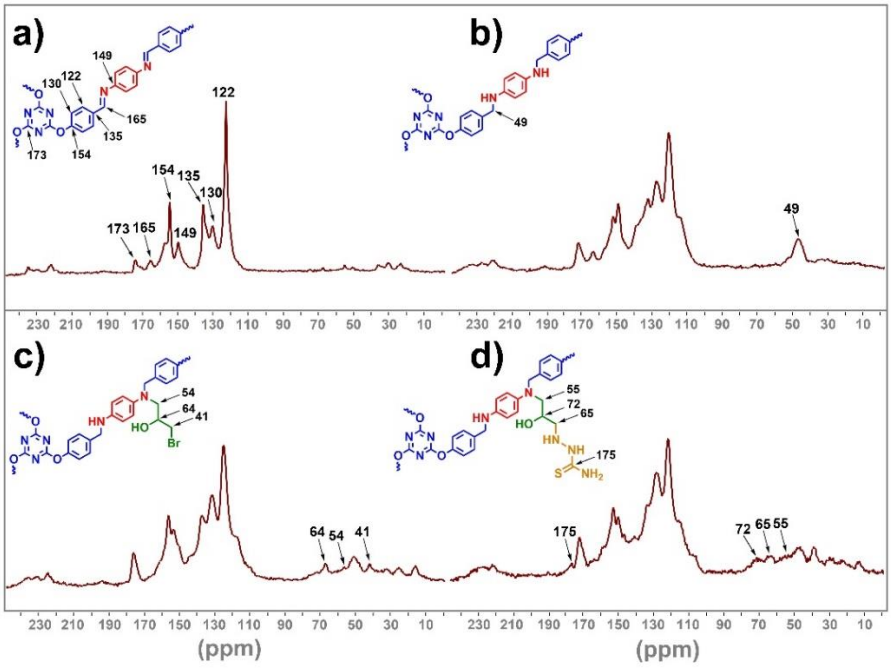

Fig. 4. ^{13}C CP/MAS NMR spectra of COF (**a**), RCOF (**b**), RCOF-EBH (**c**) and RCOF-EBH-TSC (**d**).

3.1.4. PiFM analysis

PiFM characterization was used to better understand the COF materials from a morphological and chemical perspective. Topography measurements revealed loosely packed spherical structures of ~300 nm in diameter and several hundred nanometers in height, in both Fe_3O_4@COF, with and without the functionalization (**Fig. 5a**). Interestingly, it was seen that each larger spherical structure related to Fe_3O_4 magnetic particles had been surrounded with smaller spheres of COF materials. The PiFM spectra returned undisputable evidence of the chemistry between the COF material and the added ligands (**Fig. 5b**). Both Fe_3O_4@COF and Fe_3O_4@RCOF-EBH-TSC showed a strong absorption at ~1500 cm^{-1} ascribed to the aromatic C=C vibrations. The reporter vibration mode on the bare COF material was the strong-sharp C=N peak at 1625 cm^{-1} wavenumber.[109] After reduction and functionalization, this peak disappeared[109] and a new peak at 1250 cm^{-1} related to

C–N vibrations appeared which explained the imine becoming an amine.[39] Since the ligand bore alcohol functionalities, a medium-sharp peak at around 1450 cm^{-1}, was assigned to O-H bending vibrations of alcohol bonds.[110] These observations are in agreement with previous characterization studies and confirm the successful post-synthetic functionalization of COFs.

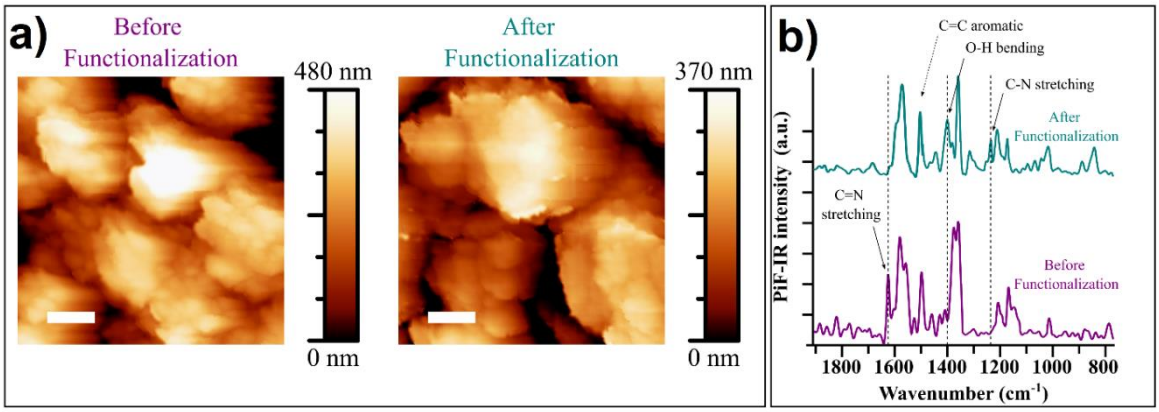

Fig. 5. Surface of magnetic COF material viewed by AFM, before (Fe_3O_4@COF) and after post-synthetic functionalization (Fe_3O_4@RCOF-EBH-TSC) (**a**). The scale bars are 300 nm. PiFM spectra of both COF materials with arrows pointing at key resonance modes (**b**).

3.2. Studies on Adsorption

The Fe_3O_4@RCOF-EBH-TSC product was used to show how contact time affects Hg(II) adsorption (**Fig. 6a**). It was observed that the initial Hg(II) adsorption was rapid, and the equilibrium was reached in only 5 minutes. Adsorption of Hg(II) ions did not increase after 5 minutes. Hg(II) ions were rapidly adsorbed in the early stages due to access to numerous open surface sites on the surface of the Fe_3O_4@RCOF-EBH-TSC.[111] pH is one of the main factors influencing the efficient removal of Hg(II). To prevent mercury hydroxides (Hg(OH), $Hg(OH)_2$, etc.) from forming when Hg(II) precipitates with –OH,[112] the pH was set at 1.0 to 7.0. As can be seen in **Fig. 6b,** during the pH change, the removal rate generally showed an initial increase prior to declining. When pH = 6.0, the removal rate was at its highest. Low removal rates occurred when pH was below 6, because a large amount of H^+ caused Fe_3O_4@RCOF-EBH-TSC to protonate, which repelled Hg(II) in the same charge. The interaction between adsorbent and Hg(II) was enhanced as pH rose, deprotonation took place, and the removal rate rose accordingly. When pH was greater than 6.0, Hg(II) would experience weak hydrolysis, causing a difficult-to-adsorb hydroxide precipitation, which would slow down the rate of removal. As a result, pH = 6.0 was

chosen as the study's optimal pH for Fe_3O_4@RCOF-EBH-TSC. In order to better understand how the adsorbent interacts with Hg(II), the point of zero charge (PZC) was used to measure the surface charge density of Fe_3O_4@RCOF-EBH-TSC. Typically, when pH is below pH_{PZC}, the adsorbent's surface is positively charged, which will cause electrostatic repulsion between the adsorbent and positively charged Hg(II) ions. Conversely, when pH is greater than pH_{PZC}, the reaction is facilitated by pH_{PZC}, which has greater attraction due to opposite charges to the metal cation. According to **Fig. 6c**, the adsorbent's pH_{PZC} is 3.16, which is below the ideal pH. The adsorption of Hg(II) ions is undoubtedly aided by the electrostatic attraction that exists between the adsorbent and mercury ions at this pH. Notably, the removal rate of Hg(II) exceeds 77% at pH 3-7. Since this adsorbent can be used in a variety of pH ranges, it can handle complex environments and is predicted to be of great use in the future. It is worth mentioning that to check more closely, a blank control experiment was conducted using Fe_3O_4@RCOF-EBH as an adsorbent in Hg(II) removal and the result was obtained that in the optimal pH, the percentage of mercury removal was negligible (about 5%).

Various experiments ranging from 1.0 to 50 mg/100 mL of Fe_3O_4@RCOF-EBH-TSC were conducted to optimize the adsorbent's dosage (**Fig. 6d**). It was noticed that as the amount of Fe_3O_4@RCOF-EBH-TSC increased, the amount of Hg(II) that was adsorbed increased as well because the Hg(II) ion would have more adsorption sites to bind. Only 10 mg/100 mL of Fe_3O_4@RCOF-EBH-TSC sufficed to remove 99.46% of the Hg(II) ions; further dosage increases were found to have no appreciable effect on the Hg(II) ion removal fraction. The uptake of Hg(II) by Fe_3O_4@RCOF-EBH-TSC was also carried out at various concentrations of Hg(II) ions (5-200 mg/L), while time, pH, and adsorbent dosage were kept constant at 5 minutes, 6.0, and 10 mg/100 mL, respectively. It was observed that as Hg(II) concentration increased from 5 to 200 mg/L, the Hg(II) uptake rate reduced from 99.8% to 69.9% (**Fig. 6e**). Due to the higher concentration of the Hg(II) ions, there were fewer adsorption sites available on the surface of the Fe_3O_4@RCOF-EBH-TSC, resulting in a decrease of adsorption. A blank control experiment was conducted using COF, Fe_3O_4@COF, Fe_3O_4@RCOF, and Fe_3O_4@RCOF-EBH, as adsorbents in Hg(II) removal in the optimal conditions (time, pH, adsorbent dosage, and Hg(II) at 5 minutes, 6.0, and 10 mg/100 mL and 10 mg/L), the adsorption capacity for Hg(II) was 10.2, 14.6, 21.4, and 32.1 mg/g respectively. While the adsorption capacity for Hg(II) under the same experiment conditions was 99.8 mg/g. Therefore, it was certain that the thiosemicarbazides played a critical role in adsorption

performance. For practical applications, adsorption costs must be reduced through the desorption of adsorbed Hg(II) from Fe_3O_4@RCOF-EBH-TSC and its regeneration. It has been found that the desorption was greatest in 0.1 M HCl. Following four cycles of reusing the adsorbent, the adsorption percentage showed only a loss of 6.7%, demonstrating the material's good ability to regenerate (**Fig. 6f**). To confirm the regeneration of COF after removal activity, the structure of RCOF-EBH-TSC was studied with PXRD analysis (**Fig. S8**). PXRD pattern of this RCOF-EBH-TSC after regeneration is similar as the pristine RCOF-EBH-TSC confirming a successful regeneration and highly stable functionalized COF. As a result, Fe_3O_4@RCOF-EBH-TSC is considered a cost-effective and efficient adsorbent for Hg(II) removal from polluted wastewater.

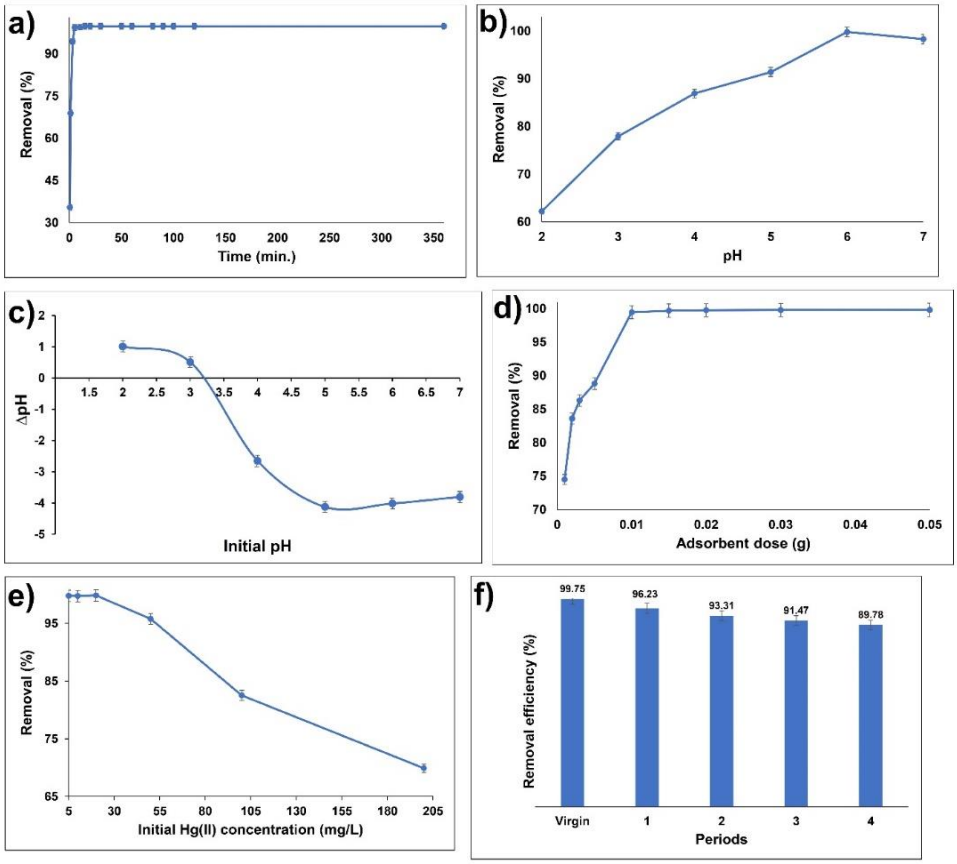

Fig. 6. Hg(II) removal utilizing Fe_3O_4@RCOF-EBH-TSC at various times (0.01 g/100 mL adsorbent, pH = 6.0, Hg(II) concentration = 10 mg/L and T = 298 K) (**a**), Hg(II) removal utilizing Fe_3O_4@RCOF-EBH-TSC at various pH (0.01 g/100 mL adsorbent, time = 5 min. Hg(II) concentration = 10 mg/L and T = 298 K) (**b**), pH_{PZC} determination for Fe_3O_4@RCOF-EBH-TSC (**c**), Hg(II) removal utilizing various doses of adsorbent (time = 5 min, pH = 6.0, Hg(II) concentration = 10 mg/L and T = 298 K) (**d**), Hg(II) removal utilizing Fe_3O_4@RCOF-EBH-TSC at various initial concentrations of Hg(II) (0.01 g/100 mL adsorbent, time = 5 min, pH = 6 and T = 298 K) (**e**), Recycling of Fe_3O_4@RCOF-EBH-TSC by means of 0.1 M HCl solution (**f**).

3.3. Adsorption Kinetics

Here, the adsorption kinetics of the adsorbent were assessed using a 10 mg/L Hg(II) solution. First, 100 mL of a 10 mg L^{-1} $HgCl_2$ solution with a pH of 6.0 were treated with 10 mg of Fe_3O_4@RCOF-EBH-TSC adsorbent. The ability of Fe_3O_4@RCOF-EBH-TSC to capture Hg(II) was subsequently measured and calculated using a ICP analyzer. When the adsorption tended to the equilibrium state, very fast kinetics could be seen, meaning that Fe_3O_4@RCOF-EBH-TSC can adsorb and remove more than 99.3% of mercury in just 5 minutes (**Fig. 6a**). We used a quasi-second-order model (Eq. 1) to fit the data and describe the kinetics of mercury ion adsorption as was used in Ref.[113]:

$$\frac{t}{q_t} = \frac{1}{k_2 q_e^2} + \frac{t}{q_e} \qquad (1)$$

The apparent quasi-second-order rate constant is denoted by the symbol k_2 (g $mg^{-1}min^{-1}$), and q_t and q_e are the adsorption values at time t (min) and equilibrium time, respectively, with units of mg/g. In **Fig. S9,** the linear curve that fit is displayed. The corresponding equation and k_2 value are shown in **Table S1**. The calculated k_2 value is 0.038 g $mg^{-1}min^{-1}$, which indicates that Fe_3O_4@RCOF-EBH-TSC has fast binding kinetics for each Hg(II).

3.4. Adsorption Isotherms

Adsorbate molecule distribution between the solid and liquid phases at equilibrium can be determined using adsorption isotherm studies. The Langmuir and Freundlich isotherm models were used in the current study to analyze the isotherm results (**Fig. 7**). According to the Langmuir model, monolayer adsorption, considering null interactions between adsorbed molecules, is used to adsorb adsorbate molecules onto a homogeneous surface with a finite number of adsorption sites. The Langmuir isotherm model is expressed linearly as follows.[114]:

$$\frac{C_e}{q_e} = \frac{1}{K_L q_m} + \frac{C_e}{q_m} \qquad (2)$$

Where q_m and K_L are the respective values of the Langmuir constants for maximum monolayer adsorption capacity and adsorption energy, respectively. The intercept and slope of linear graphs of C_e/q_e vs. C_e were used to calculate the values of q_m and K_L in accordance with **Table S2**. It was noted that the amounts of q_m increased as the temperature rose, demonstrating the endothermic nature of the Hg(II) uptake onto the Fe_3O_4@RCOF-EBH-TSC.

The R_L, the dimensionless equilibrium variable, is described as[115]:

$$R_L = \frac{1}{1+K_L C_0} \qquad (3)$$

It is used to express the fundamental property of the Langmuir isotherm, where C_0 (mg L^{-1}) is the primary Hg(II) concentration and K_L is the Langmuir constant (L/mg). Consequently, the adsorption process is viewed favorably if $0 < R_L < 1$. The R_L values in the current study were in the range of 0.337-0.006, demonstrating the successful adsorbing of Hg(II) onto the Fe_3O_4@RCOF-EBH-TSC. The Freundlich isotherm is useful for determining the adsorption process in heterogeneous adsorbent media. According to the heat of sorption model, the adsorption sites are presumptively distributed exponentially to derive this Freundlich isotherm. The following equation[116] represents the Freundlich isotherm in its linearized form:

$$\log q_e = \log K_F + \frac{1}{n} \log C_e \quad (4)$$

Where, K_F and n are the Freundlich adsorption constants which were calculated from the intercept and slope of the linear graphs of log q_e vs. log C_e, respectively.

Table S2 includes a list of the Langmuir and Freundlich parameters. The Langmuir model's higher correlation coefficient values (R^2 > 0.916) than the Freundlich model suggested monolayer adsorption rather than multilayer adsorption took place onto the Fe_3O_4@RCOF-EBH-TSC. The Freundlich isotherm model was unable to adequately explain the correlation between the values of adsorbed Hg(II) ions and their equilibration concentrations in the solutions because of the model's lower correlation coefficient value.

3.5. Adsorption selectivity

In practical applications, the interference of other metal ions on the adsorption performance of the adsorbent is a considerable challenge. To account for this, we conducted a competitive experiment on Fe_3O_4@RCOF-EBH-TSC to determine the amount of Hg(II) adsorbed in the presence of other metal ions. We used Fe_3O_4@RCOF-EBH-TSC to perform selective adsorption experiments on a mixed solution composed of the same concentration of ions, [Ag(I), Fe(III), Cd(II), Pb(II), Zn(II), Mn(II), Ni(II), and Hg(II) (10 mg/L)], filtered and analyzed the ion contents in the solution by ICP. As shown in **Fig. S10**, Fe_3O_4@RCOF-EBH-TSC can effectively adsorb Hg(II) within 5 min, and the removal rate of Hg(II) is greater than 99%, whereas the removal rate of other metal ions is less than 18%. This result irrevocably shows that the competition effect of other metal ions is weightless.

The distribution coefficient (K_d) determination is one indicator of how well a sorbent binds to a particular metal ion. The formula for the K_d is $K_d = (C_0\text{-}C_e)\ V/C_e\ m$, where C_0 is the primary concentration of ions, C_e is the equilibration concentration of ions, V is the volume of the solution (mL), and m is the mass of the adsorbent (g). K_d represents an important aspect of an adsorbent's

performance index for adsorbing metal ions, and a K_d value of 1.0×10^5 mL/g is usually considered to be an excellent value [117]. A new alternative metric is the selectivity factor, or $\alpha_{t/c}$, for target (t) and competitor (c) adsorbates (Eq. 5).

$$\alpha_{t/c} = \frac{q_t C_{e,c}}{q_c C_{e,t}} \quad (5)$$

Where $C_{e,c}$ is the equilibrium concentration of the competitive ion in the mixed ion system, and $C_{e,t}$ is the equilibrium concentration of the target ion (Hg(II) in the mixed ion system).[118]

When the value of $\alpha_{t/c}$ is greater than 1, the adsorbent is selective and the target pollutant is preferred.[119] The K_d and $\alpha_{t/c}$ were used in this study to examine the affinity of Fe_3O_4@RCOF-EBH-TSC. The larger K_d value of Hg(II) can be seen in **Table S3**, which shows that Hg(II) can bind to Fe_3O_4@RCOF-EBH-TSC preferentially and is more inclined to oust other metal ions from the active sites on Fe_3O_4@RCOF-EBH-TSC. Additionally, the high affinity and robust interaction between Fe_3O_4@RCOF-EBH-TSC and Hg(II) were suggested by the large $\alpha_{t/c}$ value for this ion.

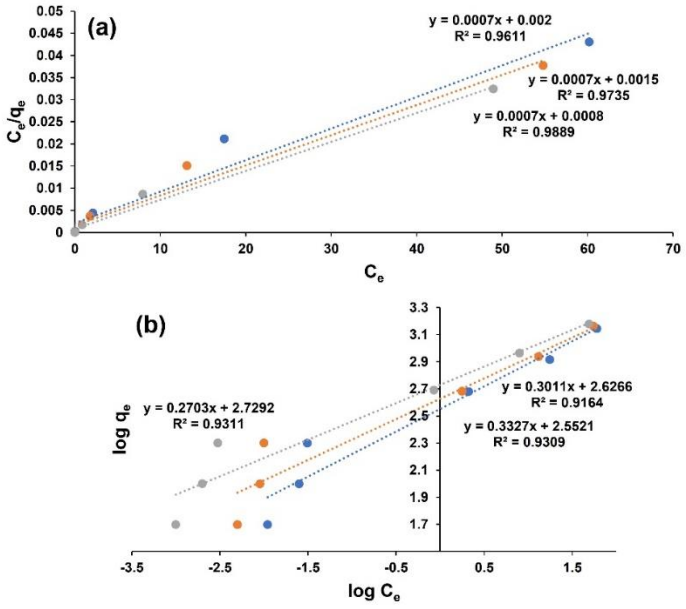

Fig. 7. (**a**) Langmuir isotherm and (**b**) Freundlich isotherm plots for the adsorption of Hg(II) on Fe_3O_4@RCOF-EBH-TSC at different temperatures.

3.6. Thermodynamic Studies

The adsorption capacity of an adsorbent is clearly impacted by temperature. At various temperatures (25-50 °C), the uptake of the Hg(II) ion onto the Fe_3O_4@RCOF-EBH-TSC was

studied. It was observed that as temperature rose, adsorption increased, indicating that the adsorption process is endothermic (in agreement with previous observations) (**Fig. S11**). To determine the viability and make sense of the uptake process, the thermodynamic variables $\Delta G°$ (standard-free energy change), $\Delta H°$ (standard enthalpy change), and $\Delta S°$ (standard entropy change) were assessed. The slopes and intercepts of the plots of ln K_c vs. $1/T$ (**Fig. S12**) were utilized to compute the values of $\Delta H°$ and $\Delta S°$. The values were then computed using the following equations.

$$\ln(K_c) = \ln\left(\frac{q_e}{C_e}\right) = \frac{-\Delta G}{RT} \qquad (6)$$

$$\ln(K_c) = \frac{-\Delta H}{RT} + \frac{\Delta S}{R} \qquad (7)$$

$$\Delta G = \Delta H - T\Delta S \qquad (8)$$

Where K_c (L mg^{-1}), is the constant of standard thermodynamic equilibration determined by q_e/C_e, R (8.314 kJ mol^{-1} K^{-1}) is the gas constant and T (K) is absolute temperature. For Hg(II) uptake onto adsorbent, the amounts of $\Delta G°$ and $\Delta H°$, $\Delta S°$ are provided in **Table S4**. It is clear from this table that the positive value of $\Delta H°$ demonstrated an endothermic character of adsorption. At the solid/solution interface during the uptake process, the randomness increased, as indicated by the positive values of $\Delta S°$. Hg(II) adsorption onto the Fe_3O_4@RCOF-EBH-TSC was more spontaneous at higher temperatures (298 K to 323 K), as indicated by the more negative values of $\Delta G°$.

3.7. Evaluations of Performance

The Fe_3O_4@RCOF-EBH-TSC nanocomposite's maximum adsorption capacity for Hg(II) was evaluated against that of other adsorbents mentioned in literature (**Table 1**). The high porosity of the synthetic magnetic COF, which provides a high surface area for Hg(II) to adsorb, makes it clear that it is an advantage. It thus entails a high adsorption capacity (1400 mg g^{-1}) and quick removal (up to 5 min). Therefore, Fe_3O_4@RCOF-EBH-TSC is a promising candidate for the efficient and selective removal of Hg(II).

Table 1. Comparison of maximum adsorption capacities of Hg(II) utilizing different adsorbents

Adsorbent	Langmuir adsorption capacity q_m (mg/g)	References
JNU-3	960.0	[90b]
UiO-66-$(SH)_2$	236.4	[120]
UiO-66-NH_2	232.5	[121]
Zr-MOF-NAC	594.0	[122]
COF-SH-2	526.3	[123]
TAPB-BMTTPA-COF	734.0	[117]
SMCOP-1	1329.0	[124]
Fe_3O_4@RCOF-EBH-TSC	1400.9	This study

3.8. XPS and SEM Analyses Before and After Removal Processes

To confirm the Hg(II) capture onto the surface of functionalized COF, XPS analysis of Fe_3O_4@RCOF-EBH-TSC before and after Hg adsorption has been provided. As can be seen in **Fig. 8a**, the existence of sulfur in these two spectra confirmed the post-synthetic modification of COF materials and its stability.[71b] In addition, after placing thiocarbonyl-functionalized magnetic COF in the Hg solution (red spectrum), new peaks related to Hg (Hg 4f and Hg 4d) appeared, confirming Hg binding to the surface of COF. According to the "soft−soft" metal−ligand binding principle, mercury connects to sulfur atoms.[70-71] On this basis, in the high-resolution XPS spectrum of Hg 4f, the double peaks with binding energies of 101.3 and 105.5 eV were attributed to the Hg $4f_{7/2}$ and Hg $4f_{5/2}$, respectively, and confirmed Hg inclusion within functionalized COF (**Fig. 8b**).[71b] On the other hand, the high-resolution XPS spectrum of S 2p before and after Hg adsorption was performed (**Fig. 8c** and **d**). As shown in these spectra, the binding energies of S $2p_{3/2}$ in Fe_3O_4@RCOF-EBH-TSC before and after Hg(II) adsorption was seen at 163.2 and 163.6 eV, respectively, in accordance with organosulfur compounds.[125] This 0.4 eV positive shift confirmed the successful interaction between sulfur and Hg ions.[70-71, 90b] Finally, the high-resolution XPS spectrum of N 1s before and after Hg(II) adsorption was studied. Unlike the sulfur element, nitrogen functional groups did not have any interactions with Hg ions and we did not observe any significant shift in binding energies before and after Hg(II) adsorption (**Fig. 8e** and **f**).

Additionally, to visualize the elemental content of the samples after functionalization and also Hg(II) adsorption, EDX and SEM mapping were provided for Fe_3O_4@COF, Fe_3O_4@RCOF-EBH-TSC and Fe_3O_4@RCOF-EBH-TSC + Hg (**Fig. S13**). As seen, before post-synthetic modification

of COF, there are principally C, O, N and Fe in the EDX spectrum and mapping (**Fig. S13a**). However, after post-synthetic modification with thiosemicarbazide and after Hg adsorption, S and Hg were detected on the EDX spectrum and maps. Confirming the successful post-synthetic modification and removal activity of COF (**Fig. S13b** and **c**).

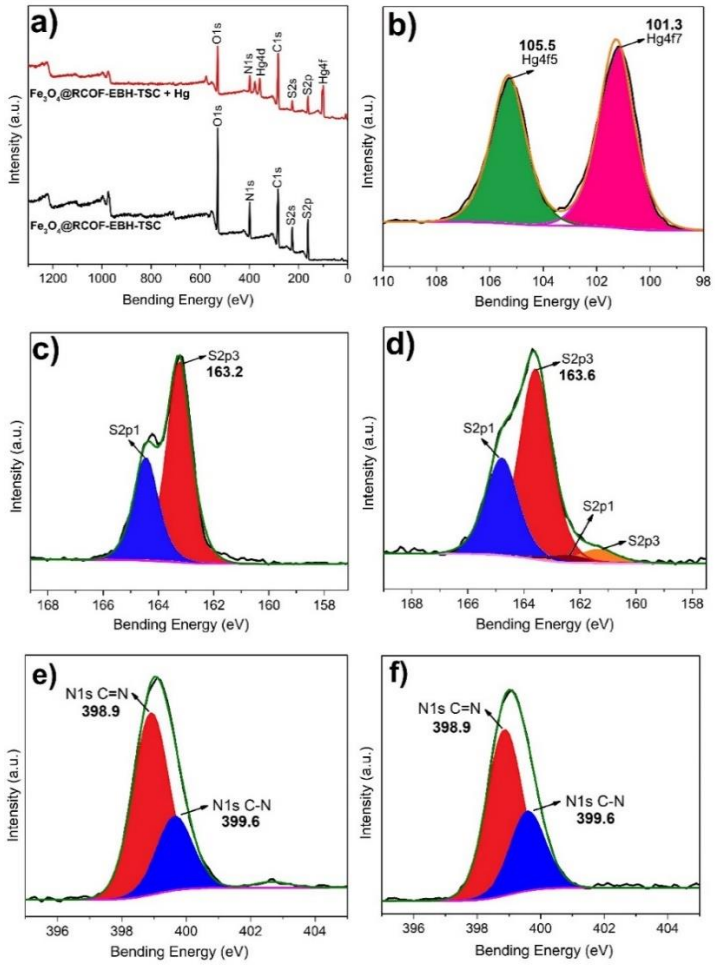

Fig. 8. XPS survey of Fe_3O_4@RCOF-EBH-TSC before and after being placed in Hg solution (**a**), high-resolution XPS spectrum of Hg4f in Fe_3O_4@RCOF-EBH-TSC when bound with Hg (**b**), high-resolution XPS spectrum of S2p in Fe_3O_4@RCOF-EBH-TSC before (**c**) and after Hg(II) adsorption (**d**), high-resolution XPS spectrum of N1s in Fe_3O_4@RCOF-EBH-TSC before (**e**) and after Hg(II) adsorption (**f**).

3.9. Mechanism for adsorption and desorption

Scheme 2 illustrates the suggested mechanism for the adsorption and desorption of Hg(II) ions onto Fe_3O_4@RCOF-EBH-TSC. Functionalized magnetic COFs contained a number of hydroxyl, amine and more importantly thiocarbonyl groups. These groups, in accordance with the hard and soft acid base theory, are electron-rich species with a propensity to donate an electron to an

electropositive metal. Due to electrostatic attractions, these groups were consequently joined to the Hg(II) ion. The sulfur-free imine-linked Fe_3O_4@COF and amine-linked Fe_3O_4@RCOF were employed as control samples to investigate the contribution of the imine and amine donors in the uptake of Hg(II). Under the same conditions, the Fe_3O_4@COF and Fe_3O_4@RCOF adsorbed only 14.6% and 21.4% Hg(II) from the aqueous solutions, respectively. This result also indicated that the imine and amine donors in the COF materials contribute little to the capture of Hg(II).

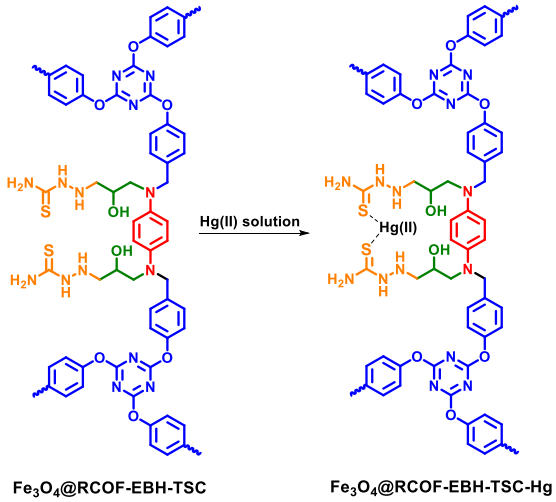

Scheme 2. Proposed mechanism for Hg(II) adsorption.

4. Conclusion

In summary of this research, a core-shell magnetic thiocarbonyl-linked COF material was synthesized *via* three steps of post-synthetic modification strategy. The product had good crystallinity, porosity, and covalent linkage connectivity. This nanomagnetic and porous adsorbent was able to remove Hg(II) ions from water with a high uptake capacity of 1400.9 mg g^{-1} and rapid kinetics conform to the quasi-second-order kinetic model. This thiocarbonyl-functionalized crystalline material also showed excellent selectivity and an ability to be reused more than 5 times with approximately no significant decrease in removal efficiency.

Supporting Information

The Supporting Information is available free of charge athttps://pubs.acs.org.

Additional SEM and TEM images of the prepared materials; specific BET surface area and pore size distributions of all samples; FT-IR spectrum of TFPOT, PDA and prepared functionalized COFs; PXRD patterns of functionalized COF under different conditions; PXRD patterns of fresh and regenerated RCOF-EBH-TSC; Linearized pseudo-second-order plot for Hg(II) adsorption;

Kinetic model variables for Hg(II) adsorption; Langmuir and Freundlich isotherm factors; thermodynamic variables for the adsorption of Hg(II); the removal efficiency of adsorbent for Hg(II) in presence of other competing metal ions; temperature effect on Hg(II) removal; and EDX and SEM mapping of Fe_3O_4@COF and Fe_3O_4@RCOF-EBH-TSC and Fe_3O_4@RCOF-EBH-TSC after placing in Hg(II) solution.

Acknowledgments

This work was supported by Natural Science and Engineering Research Council of Canada (NSERC), the Canada Research Chairs program (CRC) and Canada Foundation for Innovation. We acknowledge all the characterization centers including NanoQAM, QCAM and LCM.

Funding Sources

This research was funded by Natural Science and Engineering Research Council of Canada, Canada Research Chairs program and Canada Foundation for Innovation.

Author Contributions

The manuscript was written through contributions of all authors. All authors have given approval to the final version of the manuscript.

Declaration of Competing Interest

There are no conflicts to declare.

2.3 Informations complémentaires

Les informations complémentaires relatives aux procédures expérimentales et aux caractérisations sont disponibles dans l'annexe A et sur le site web.
https://pubs.acs.org/doi/10.1021/acsami.3c02914.

2.4 Contribution des auteurs pour cette étude

Le premier auteur de cet article, également l'auteur de cette thèse, a réalisé la plupart de la synthèse et des caractérisations.
Le deuxième auteur, le Professeur Farid Moeinpour, a effectué l'analyse cinétique et thermodynamique de l'application des eaux usées.
Le troisième auteur, Maziar Jafari, a réalisé l'analyse PiFM.
Le quatrième auteur, Mohammad K. Shehab, a réalisé l'analyse de simulation PXRD pour les COFs synthétisés.
Le cinquième auteur, le Professeur Ahmad Samih ElDouhaibi, nous a assistés dans la synthèse de certains matériaux de départ et COFs.
Le sixième auteur, le Professeur Hani M. El-Kaderi, était conseiller pour ce projet et nous a aidés dans l'analyse de simulation.
L'auteur correspondant, le Professeur Mohamed Siaj, a contribué au manuscrit et au processus de soumission.

CHAPITRE 3
SYNTHÈSE RAPIDE, DOUCE ET CATALYTIQUE DE COFS 2D ET 3D AVEC DES APPLICATIONS PROMETTEUSES EN SUPERCONDENSATEURS

3.1 Introduction

Dans la deuxième partie, différentes méthodes et conditions ont été développées pour présenter de nouvelles méthodologies et catalyseurs pour la synthèse de divers COF à base d'imine en 2D et 3D. Notamment, l'utilisation de catalyseurs à base d'acides hétéropoly a émergé comme la condition la plus efficace. Ces catalyseurs ont notablement accéléré la synthèse des COF à base d'imine, réduisant le temps de réaction de plusieurs jours à quelques heures seulement, tout en améliorant la cristallinité et le rendement des produits finaux. De manière impressionnante, certains de ces COF ont présenté des résultats prometteurs pour des applications de supercondensateurs.

3.2 Article publié pour cette étude

Rapid, Mild, and Catalytic Synthesis of 2D and 3D COFs with Promising Supercapacitor Applications, ACS Applied Energy Materials. 2023, 6, 24, 12216–12225.
https://pubs.acs.org/doi/abs/10.1021/acsaem.3c01913.

Rapid, Mild and Catalytic Synthesis of 2D and 3D COFs with Promising Supercapacitor Applications

Amir Khojastehnezhad[a], Khaled Rhili[a], Mohammad Shehab[b], Hichem Gamraoui[a], Zhiyuan Peng[a], Ahmad Samih ElDouhaibi[c], Rachid Touzani[d], Belkheir Hammouti[e], Hani El-Kaderi[b], and Mohamed Siaj[a]

[a]Department of Chemistry, University of Quebec at Montreal, Montreal, QC H3C3P8, Canada

[b]Department of Chemistry, Virginia Commonwealth University, Richmond, Virginia, United States

[c]Department of Chemistry, Lebanese University, College of Science, Mont Michel, Lebanon

[d]Laboratory of Applied and Environmental Chemistry, Mohammed first University, Oujda, Morocco

[e]Department of Chemistry, Euromed University of Fes, Fes Morocco

Abstract

An approach based on Keggin heteropoly acids (HPAs) has been presented for the mild and fast synthesis of five different structures of imine and azine-linked two-dimensional (2D) and three-dimensional (3D) covalent organic frameworks (COFs). Traditionally, these crystalline materials have been synthesized via the Schiff base polycondensation reaction between different aldehydes

and amines at harsh condition and in the presence of acetic acid. Herein, two different Keggin-type heteropolyacids (HPAs) have been exploited as catalysts which are both Bronsted and Lewis acid, to speed up the synthesis of 2D and 3D COFs and improve their materials quality. The catalyst led to prepare the imine and azine-linked COFs with high crystallinity and porosity under mild condition and short reaction time. According to the results, the amine building blocks with two amine functional groups, formed the COFs with higher crystallinity, porosity, and yield compared to amine with three functional groups and non-planar structure. On this basis, under mild reaction conditions, a new 2D COF named TAPA-TPT was successfully prepared with high crystallinity and good porosity. The developed TAPA-TPT COF exhibit a very good performance when used in supercapacitor application. This COF showed excellent specific capacitance of 205 F g^{-1} at a current density of 0.5 A g^{-1}, which is a very attractive value for supercapacitors. This study provides a synthetic approach that can lead to large-scale production of COF materials for energy harvesting.

Keywords: Imine linked-COF, Azine-linked COF, Triazine COF, Heteropoly Acids, Keggin, 2D and 3D COFs.

1. Introduction

Nowadays, catalysts are a main player in modern organic synthesis, and they are necessary to develop a successful chemistry society. The greatest strategy to reduce energy consumption in chemical reactions, which are almost always energy-dependent, is to use effective catalysts. Traditional mineral acid catalysts are extensively used by scientists to catalyze various reactions,[126] but in order to produce the desired products, these catalysts need a lengthy reaction period, high temperatures, and pressure to proceed.[127] In addition to these restrictions these catalysts are corrosive and some of them emit various gases, resulting in several health and safety issues that are not in accordance with the green chemistry approach.[128] Instead of using large amounts of these traditional catalysts, low amount of modern catalysts can prepare the final product with high yield and quality.[129] Hence, there is an urgent need now to develop efficient, and robust new generation catalysts.

COFs are the versatile porous crystalline polymers with modifiable and designable structures that are entirely constructed from different light elements and linked by strong covalent bonds and linkages. The interesting features of COFs, like regular porosity, adjustability, structural tenability and especially high surface area, convert them to the efficient platforms for various applications.[2a-

[c, 130] Among these fantastic crystalline polymers, the COFs constructed with imine covalent bonds show high chemical stability compared to other systems owing to the high nitrogen content.[3a] Recently, due to the great importance of imine-based COF materials, many publications have been devoted to the synthesis of these materials and most of them used the traditional acetic acid to catalyze the COF synthesis.[27a] Conventional synthesis methods are not only hampered by long reaction times and harsh conditions, but also by low crystallinity and porosity of the resulting product.[28] To address this difficulty, a number of investigations have resorted to different methods for the synthesis of imine-based COFs, such as electron beam irradiation,[32] sonication,[30] and microwave.[31] On the other hand, instead of acetic acid, some other catalysts like *p*-toluenesulfonic acid,[36] metal triflates,[35] metal halides,[34] and transition-metal nitrates,[33] have been reported. But they have some significant limitations including the use of a large amount of catalyst under sealed condition, catalysts cost, narrow monomer scope, non-deep and superficial studies and hard work-up procedures which are inconvenient for production scaling.[33-34, 36] Almost, all these processes have been limited to the synthesis of simple and planer 2D imine-linked COFs. Thus, it is strongly recommended to design and develop a novel alternative catalyst for rapid and mild synthesis conditions of COF materials with a high crystalline and porous structure[1a, 37] that can be used as supercapacitor.

Supercapacitors are promising energy storage systems in a carbon-neutral economy due to their fast charge-discharge capabilities, high power density, long lifetime, and high coulombic efficiency.[131] Amorphous polymer materials with carbon-based structures have been investigated widely as supercapacitors due to their high packing density and large specific surface area. Although, the lack of porous structure and control over the pore size distribution often results in a slow ion diffusion and undesirable capacity loss during rapid charge-discharge process.[132] COF materials with special pore functionality, controlled pore size distribution and also porous crystalline structures are very appropriate for supercapacitor applications.[133]

HPAs are known as popular acidic catalysts that can be reused in organic reactions.[134] They are mostly utilized as acid catalysts, because they have low charge density and almost no charge localization and so they are 100 times stronger than sulfuric acid.[135] Also, owing to the high solubility in polar and green solvents like water and alcohol, showed high efficiency to catalyze different chemical reactions.[102], Ishikawa, et al. [136]a, [136b-d Among them, Keggin-type HPAs with formula of $[XM_{12}O_{40}]$ (X = As, Ge, P, Si and M = W, Mo), is a strong and efficient HPA which

has been used as a catalyst more than other HPAs due to the low price, commercial availability, high Bronsted acidic activity, high-oxidizing ability and good thermal stability.[137]

Taking these considerations in mind, in this research, an efficient approach has been developed for the mild and rapid synthesis of different 2D and 3D COFs in the presence of Keggin HPAs with high yields, crystallinity and porosity (**Scheme 1**). The present catalyst was able to synthesize imine- and azine-linked COFs from the Schiff base polycondensation reaction between different amines and aldehydes. Because these COFs have been traditionally synthesized in the presence of acetic acid. While, other COFs prepared in the presence or absence of other materials. For example, boroxine-based COFs do not require any base or acid and they can be prepared in just organic solvents with high crystallinity and porosity.[5, 138] The sp^2 carbon-conjugated COFs prepared from different condensation reactions that need base to proceed. Thus, the application of our catalysts were tested only for the synthesis of imine and azine-linked 2D and 3D COFs.[139] All these planar and non-planar COFs can be prepared in short reaction time at mild conditions (**Scheme 1**). Using the developed mild reaction conditions, we successfully prepared a new 2D imine-linked COF (TAPA-TPT) with high yield, high crystallinity and good porosity and finally. This prepared new COF showed very good performance in supercapacitor application.

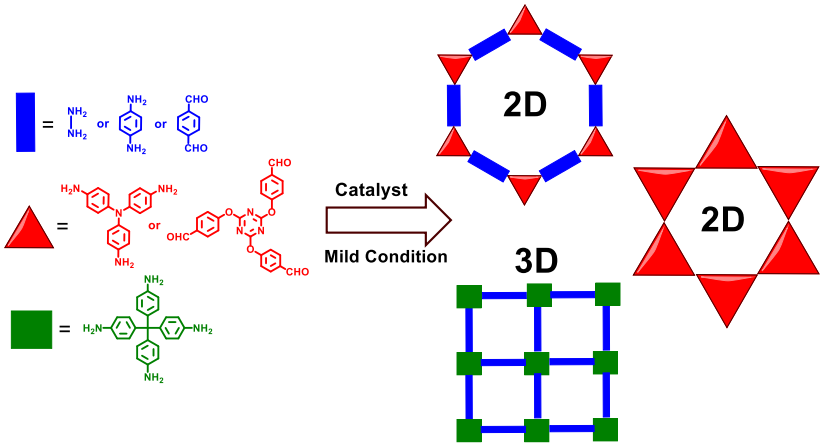

Scheme 1. Catalytic synthesis of different imine- and azine-linked 2D and 3D COFs.

2. Result and Discussion

2.1. Catalytic synthesis of COFs

Room temperature synthesis of imine-linked COFs has been reported before.[23, 25] But they have some major disadvantages, like long reaction times, narrow monomer scope, non-deep and

superficial studies and hard work-up procedures.[23, 25] Thus, in this research, we tried to present a deeper insight on the synthesis of 2D and 3D imine and azine-linked COFs at room temperature and short reaction time, with the use of efficient and powerful catalysts. Therefore, at first, the effects of two different Keggin HPAs including phosphotungstic (PTA, $H_3PW_{12}O_{40}$) and phosphomolybdic acid (PMA, $H_3PMo_{12}O_{40}$) were investigated for the synthesis of TPT-PDA COF from the Schiff base polycondensation reaction between 2,4,6-tris(4-formylphenoxy)-1,3,5-triazine (TPT) and *p*-pheneylenediamine (PDA) with the aid of PXRD analysis (**Scheme S2**).[140] Similar to the acetic acid, HPAs as a Bronsted acid can produce a proton (H^+) to catalyze the Schiff base polycondensation reaction between aldehyde and amine (**Scheme S3**). Hence, at first, the aldehyde can be activated with a proton to be ready for an amine attack and then after loss of one H_2O molecule, the final Schiff base product can be produced. Synthesis of this COF was selected as a model COF because it showed high crystalline and porous structure under different reaction conditions. Thus, the starting materials, including TPT and PDA were placed in a glass tube with solvents and then the mixture was stirred vigorously and sonicated to obtain the homogeneous mixture. Upon adding the catalyst, cloudy and yellowish solid was formed and the reaction continued for 2 h at room temperature without nitrogen purging. Upon completion of the reaction, the prepared COF was filtered and washed with ethanol, acetone and THF and immediately characterized with PXRD analysis. No peaks from the catalyst and starting materials were found in the PXRD pattern, signifying the formation of pure crystalline TPT-PDA COF. Besides, in order to analysis the possible remaining PTA in the prepared COF, the content of tungsten in the sample was studied with ICP analysis. ICP studies showed that only 0.0012 wt% of W was observed that confirmed approximately all catalyst was rinsed with the solvent during the work up the procedure. The PXRD pattern related to TPT-PDA COF showed a sharp peak at around 2.7° and four weak diffraction peaks at 4.7°, 5.4°, 7.2°, and 9.5° assigned to the (1 0 0), (1 1 0), (2 0 0), (2 1 0), and (2 2 0) crystal planes, respectively (**Fig. 1a**, and **2a**).[54] To evaluate the effects of shorter reaction times for the synthesis of TPT-PDA COF, the TPT-PDA COF was prepared in the presence of catalyst and different times (1 to 120 minutes). As shown in **Fig. S2**, no crystallinity was observed after one minute running the reaction, however, with increasing the time of the reaction, the cystallinity of the COF was improved. These observations confirmed that the reversibility of the reaction needs time to perform the correction of the structural defects during crystallization processes. The highest crystallinity was obtained after 2h running the reaction (**Fig. S2**, purple

PXRD pattern) and the crystallinity of the materials were not satisfactory in the shorter reaction times. On the other hand, according to the PXRD analysis, PTA was able to catalyze the synthesis of TPT-PDA COF with higher yield and crystallinity compared to PMA due to the stronger acidic activity of tungsten to molybdenum in only 2 h at room temperature (**Fig. 1a** and **Fig. S3**).[137c] Thereby, the next experiments were performed in the presence of PTA. In order to find the best amount of PTA, different amounts of PTA were tested for the synthesis of TPT-PDA COF **(Fig. 1b** and **Fig. S4**). The highest yield and crystallinity of TPT-PDA COF was obtained in the presence of 1.0 mol% of catalyst (relative to NH_2 functional groups) and with the use of lower and higher of this amount, the crystallinity of COF decreased somewhat (**Fig. 1b,** red and violet PXRD patterns). Also, it is worth mentioning that the crystallinity of TPT-PDA COF was decreased after running the reaction for 3 days (**Fig. 1b,** green PXRD pattern). We speculate that due to the strong acidity of PTA, it can damage the crystallinity of the COF after long time reaction. The next step was to find the best reaction temperature. Hence, the synthesis of TPT-PDA COF was examined at different temperatures and the results were studied with both PXRD and N_2 adsorption-desorption analyses (**Fig. 1c** and **1d**). PXRD analysis displayed that with the decrease of the temperature from 120 ^oC to 50 ^oC, the cystallinity was greatly increased and it was decreased a little from 50 to 25 ^oC (**Fig. S5**). However, synthesis of TPT-PDA COF at ambient temperature exhibited high crystalline structure based on PXRD analysis (**Fig. 1c,** pink PXRD pattern). BET surface area and porous structure of TPT-PDA COF was studied with N_2 adsorption-desorption isotherms at 77 K (**Fig. 1d,** and **Fig. S6**). N_2 adsorption-desorption isotherms of TPT-PDA COF revealed type-IV isotherms with H1 hysteresis loop, cylindrical-like pore channels and a sharp N_2 uptake at low relative pressure (**Fig. 1d** and **3a**).[54, 104] The N_2 adsorption-desorption isotherms of prepared TPT-PDA COF in different temperatures (120, 80, 50, 25^oC) showed different BET surface areas to be 1079, 1220, 1277 and 1180 $m^2\ g^{-1}$, respectively (**Fig. S6**). These values are in accordance with PXRD analysis and the lowest surface area was obtained at 120 ^oC (**Fig. 1d**, green curve) and the highest one was at 50 ^oC (**Fig. 1d**, blue curve). Although, the BET surface area was great (1180 $m^2\ g^{-1}$) at room temperature as well (**Fig. 1d**, pink curve). In addition, the pore volume and pore size of all prepared COFs at different temperatures were similar and pore sizes were 3.6, 3.5, 3.0 and 3.7 nm, respectively (**Fig. S7**). Therefore, the room temperature and 1.0 mol% of the catalyst was chosen as an optimum reaction condition for the synthesis of different imine and azine-linked COFs. FT-IR and ^{13}C CP-MAS NMR studies were other techniques to confirm the successful synthesis

of TPT-PDA COF (**Fig. S8** and **S9**). Based on IR analysis, both adsorption peaks related to amine functional group of PDA and carbonyl functional group of TPT at around 3400 and 1700 cm^{-1} disappeared and a new peak at 1620 cm^{-1} corresponding to C=N appeared, which confirmed the successful synthesis of TPT-PDA COF (**Fig. S8**).[107] The ^{13}C CP-MAS NMR spectrum of TPT-PDA COF also indicated seven carbon peaks at 122, 130, 135, 149, 154, 165, and 173 ppm, thus further confirming the successful synthesis of TPT-PDA COF (**Fig. S9**).[107] The crystalline structure of this COF was also confirmed by simulation studies (**Fig. 2a**). The TPT-PDA COF was simulated using the space group of P6/mmm with optimized lattice parameters of a = b = 39.187 Å, c = 3.673 Å and α = 89.5º, β = 69.3°, and γ = 120°. As can be seen in this figure, the experimental PXRD pattern is in a good match with the simulated patterns of the models with a P6/mmm space group (**Fig. 2a**). Finally, **Fig S10** depicted thin crystal lattices TPT-PDA COF and confirmed the complete crystalline structure of this COF prepared in the presence of PTA at room temperature.

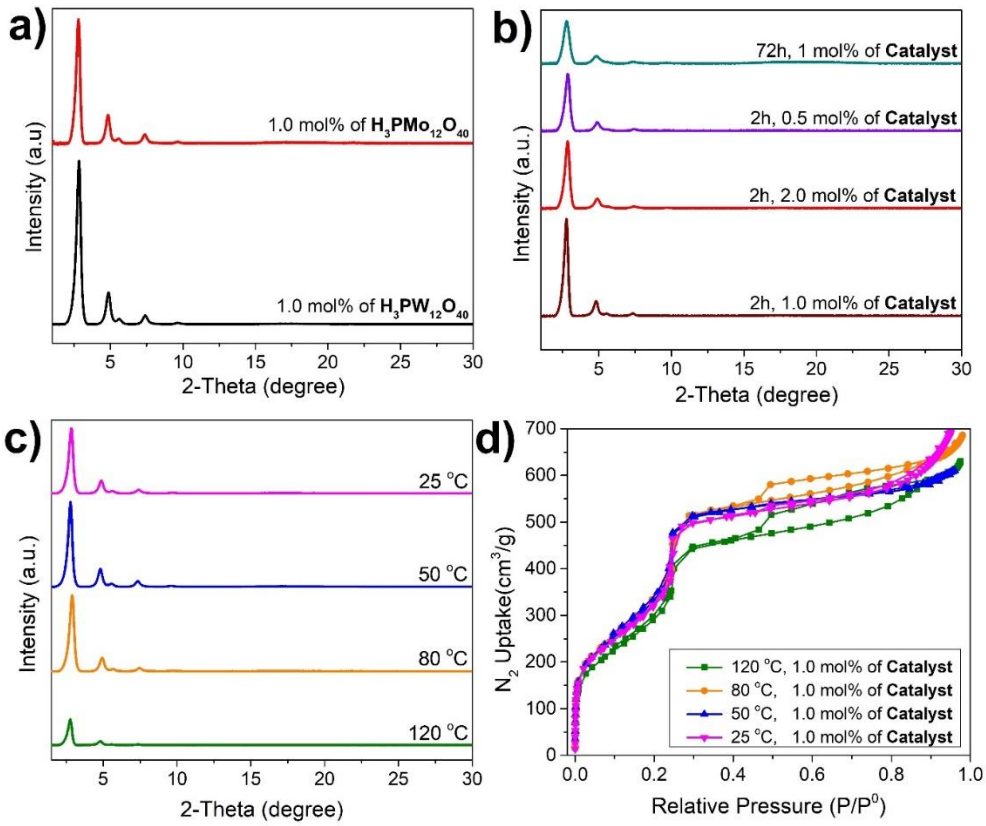

Fig. 1. PXRD patterns of prepared TPT-PDA COF in the presence of different catalysts (PTA and PMA) (**a**), different amounts of catalyst (**b**), different temperatures (**c**) and N_2 adsorption-desorption isotherms of prepared TPT-PDA COF in different temperatures (**d**).

After finding the optimum reaction condition, the scope and feasibility of the approach were investigated for the synthesis of different COFs with 2D and 3D structures. Hence, in the next step, instead of PDA, hydrazine monohydrate (HZ) was selected for the synthesis of TPT-HZ COF (**Scheme S4**). PTA was able to synthesize this COF with high crystallinity and porosity according to PXRD and BET analyses at room temperature (**Fig. 2b** and **3b**). The PXRD pattern corresponds to TPT-HZ COF indicating a pure crystalline COF with two sharp peaks at around 3.3° and 5.9° and two weak diffraction peaks at 6.2°, and 9.1° assigned to the (1 0 0), (1 1 0), (2 0 0), and (2 1 0) planes, respectively (**Fig. 2b**).[107, 141] In addition, experimental PXRD pattern of TPT-HZ COF has a very good match with simulation studies (**Fig. 2b**). N_2 adsorption-desorption isotherms were similar to the TPT-PDA COF with a high BET surface area of 815 m^2 g^{-1} (**Fig. 3b** and **Fig. S11**). The pore size of this COF was smaller than the previous COF and it was 2.5 nm that could be assigned to the smaller structure of HZ to PDA (**Fig. S11**).[141] Similar to the previous COF, FT-IR and ^{13}C CP/MAS NMR studies confirmed the successful synthesis of TPT-HZ COF (**Fig. S12 and S13**). In the next step, the effects of the catalyst were examined for the synthesis of another COF named TAPA-TPA COF from the amine building block with three functional groups and trigonal structure in a nitrogen center (**Scheme S5**). Due to the trigonal and non-planar structure of a nitrogen center, a high crystallinity and porosity have not been reported for this COF and synthesis of this COF is more challenging.[142] As a result, the Schiff base condensation reaction between tris(4-aminophenyl)amine (TAPA) and terephthaldehyde (TPA) was performed in the optimized reaction condition. In addition to room temperature, higher temperatures (50 and 80 ^oC) were examined for the synthesis of this non-planar COF to obtain the high crystallinity (**Fig. S14**). The best crystalline structure was obtained at 50 ^oC and with the use of a higher temperature (80 ^oC), the crystallinity decreased somewhat (**Fig. S14**, blue PXRD pattern). However, the crystallinity of this COF was lower compared to the TPT-PDA and TPT-HZ COFs due to the non-planar structure of the amine building block. We believe that the lower crystallinity in higher temperatures could be ascribed to the strong acidity of the catalyst. Both high temperature and strong acidity of the catalyst may interfere with the crystallization process.[23-24, 28, 143] FT-IR (**Fig. S15**) and ^{13}C CP/MAS NMR (**Fig. S16**) results confirmed that our catalyst could catalyze the synthesis of this COF successfully.[142b] PXRD pattern of this COF exhibited a pure crystalline COF with two relatively sharp peaks at around 3.2° and 6.1° and two minor diffraction peaks at 6.9°, and 9.2° corresponding to the (1 0 0), (1 1 0), (2 0 0), and (2 1 0) planes, respectively (**Fig. 2c**).[144] This

COF also displayed a broad hump peak between 2θ = 15-25° that could be attributed to the defects in the π–π stacking between the successive COF layers.[145] We speculate that the amine building block with trigonal structure in a center nitrogen can effect on the π–π stacking interactions between the successive COF layers and consequently interfere with the crystallization process.[24] These observations are in agreement with low BET surface of this COF to be 226 $m^2 g^{-1}$ according to N_2 adsorption-desorption isotherms (**Fig. 3c**). However, it is higher than some previously reported values (42 and 76 $m^2 g^{-1}$).[142]

Generally, COF materials are formed from the organic starting materials on self-assembly via reversible covalent linkages under dynamic covalent chemistry.[1a, 3a, 146] The reversibility of the reactions leads to the correction of structural defects during crystallization processes. Mild reaction conditions and efficient catalysts may provide the sufficient driving forces for the error-correction process.[23-24, 28, 143] Moreover, in this study, the structure of monomers plays an important role in the crystallization process.[24] We realized that the non-planar structure of TAPA with the trigonal structure of nitrogen center has effects on the π–π stacking interactions between monomers and oligomers during the initial and the subsequent error-correction process and it has a big impact on the crystallinity and porosity of the materials. To prove this claim, the synthesis of a new COF named TAPA-TPT COF from the Schiff base polycondensation reaction between TAPA (amine with the trigonal structure of center nitrogen) and TPT (aldehyde with three functional groups and non-planar structure) was carried out (**Scheme S6**). At first, the solvothermal synthesis of this COF was performed in different conditions and in the presence of acetic acid. We found that synthesis of this COF is very sensitive to the solvent due to the non-planar structure of building blocks, thus obtaining the COF with high crystallinity and porosity is another challenge (**Fig. S17**). After checking the effects of different solvents and their ratio in solvothermal conditions, high crystallinity was formed in the mixture of *n*-butanol and DCB (ratio of 3:1) and acetic acid at 120 ^oC for 3 days (**Fig. S17**). Consequently, the catalytic synthesis of this COF was carried out in this mixture at ambient temperature. Crystallinity was good at room temperature, but similar to the TAPA-TPA COF and to increase the crystallinity, the catalytic synthesis of this new COF was carried out at higher temperatures (50 and 80 ^oC) (**Fig. S18**). According to the PXRD analysis, the highest crystallinity was observed at 50 ^oC and higher temperatures (80 ^oC) could not increase the crystallinity of this COF as well (**Fig. S18**). Compared to the solvothermal method with high temperature and long reaction time, the resultant COF from the catalytic method under mild

conditions, indicated a similar or even better crystalline and porous structure (**Fig. 17,** and **S18**). The PXRD patterns of TAPA-TPT COF indicated that this new COF has the most intense peak with interlayer spacing distance (d spacing) of 20.67 Å corresponding to the (100) crystal plane. On the other hand, the other diffraction peaks with d spacing of 11.93, 10.33, 7.81, and 5.17 Å are attributed to the (110), (200), (210), and (400) crystal planes, respectively (**Fig. 4a**). To investigate the direction of the stacking layers and the d spacing, eclipsed (AA stacking) and staggered (AB stacking) configurations for TAPA-TPT COF were modeled, and the lattice parameters were optimized using Material Studio software (8.0). A space group of P6/mmm was utilized to model the eclipsed configuration, and the lattice parameters were optimized to be a = b = 23.867 Å, c (d-spacing) = 3.478 Å and α = β = 90 °, γ = 120 ° for the hexagonal unit cell. On the other hand, to model the staggered configuration of TAPA-TPT COF, a space group of $P6_3/mmc$ was used and the optimized lattice parameters were a = b = 24.214 Å, c (d-spacing) = 6.588 Å and α = β = 90 °, γ = 120 °. The most probable structure of TAPA-TPT COF has eclipsed layered sheets since the PXRD experimental patterns almost match the simulated patterns of the eclipsed rather than the staggered model. Furthermore, a significant PXRD peak at 14^o in the staggered structure was missed in the experimental PXRD patterns, which seconds the eclipsed structure of the TAPA-TPT COF (**Fig. 4a**). Rietveld refinement of TAPA-TPT COF was conducted to refine the position of the atoms in the model. The profile fitting factors (refinement parameters) R_p and R_{wp} were obtained to be 3.416% and 4.478%, respectively, and showed a minimal difference between the fitted and the observed patterns. The low percentages of the refinement parameters indicate the high crystallinity degree of TAPA-TPT COF. This COF also has a wide hump peak between 2θ = 15-25° due to the defects in the π–π stacking between the successive COF layers (**Fig. 4a**). N_2 adsorption-desorption isotherms of this COF displayed type-II isotherms based on IUPAC classification,[104] demonstrating the porous structure of TAPA-TPT COF (**Fig. 4b**). The BET surface area of this COF was 120 $m^2\ g^{-1}$ according to N_2 adsorption-desorption isotherms and pore size and pore volume were 5.5 nm and 0.17 $cm^3\ g^{-1}$ respectively (**Fig. S19**). FT-IR spectrum of TAPA-TPT COF exhibits a stretching band corresponding to C=N at 1620 cm^{-1}. In addition, no peaks were observed related to the aldehyde and amine starting materials at around 1700 and 3400 cm^{-1}, indicating the successful formation of imine-linked bonds (**Fig. 4c**). The ^{13}C CP-MAS NMR spectrum of TAPA-TPTCOF also indicated seven carbon peaks at 122, 129, 133, 145, 154, 165, and 171 ppm that is the next confirmation to the successful synthesis of TPT-PDA COF (**Fig. S20**).

SEM and TEM images of TAPA-TPT COF showed that this COF has both spherical and cylindrical morphologies and the SAED patterns further exhibited the crystalline structures of the framework (**Fig. S21**). After checking the effect of PTA on the synthesis of three different 2D COFs, the catalyst was used for the synthesis of COF-300 as a 3D COF. 3D COFs are interconnected with completely covalent systems, whereas 2D COFs contain separate planar sheets with non-covalent interlayer stacking (**Scheme S7**). Catalytic synthesis of this 3D COF also showed more challenges and to have the higher crystallinity and porosity, we examined the higher temperatures and similar to TAPA-TPA and TAPA-TPT COFs, the highest crystallinity and porosity were obtained at 50 ^{o}C. However, at higher temperature (80 ^{o}C), the crystallinity and porosity decreased (**Fig. S22 and S23**).[147] The BET surface area of COF-300 was 612 m^2 g^{-1} according to N_2 adsorption-desorption isotherms and pore size and pore volume were 2.5 nm and 0.35 cm^3 g^{-1} respectively (**Fig. 3d** and **S24**). As shown in **Fig. 3d**, the COF-300 with completely covalent systems and with more complicated structures compared to 2D COFs has a type H2a hysteresis. Type H2 hysteresis is associated with more complex pore structures, having internal restrictions or pore blocking with narrow or restrictive pore entrances on the neck. The gradual slope of the adsorption isotherm is due to the larger pore cavities lying beneath the pore neck with greater variability in size, leading to a steep desorption step in the isotherm.[104, 148] FT-IR (**Fig. S25**) and ^{13}C CP/MAS (**Fig. S26**) analyses were also obtained to further confirm the successful synthesis of COF-300.[147a, 147c, 149] Finally, TGA analysis was performed on all five synthesized COFs (**Fig. S27**). As predicted, due to the complete covalent system of 3D COFs, COF-300 is more stable than the 2D COFs and it exhibited high thermal stability up to 500 °C (**Fig. S27**, green curve). Besides, between 2D COFs, a new TAPA-TPT COF is more stable with thermal stability up to 400 ^{o}C (**Fig. S27**, pink curve). The lowest stability was observed for TPT-HZ COF (**Fig. S27**, blue curve).

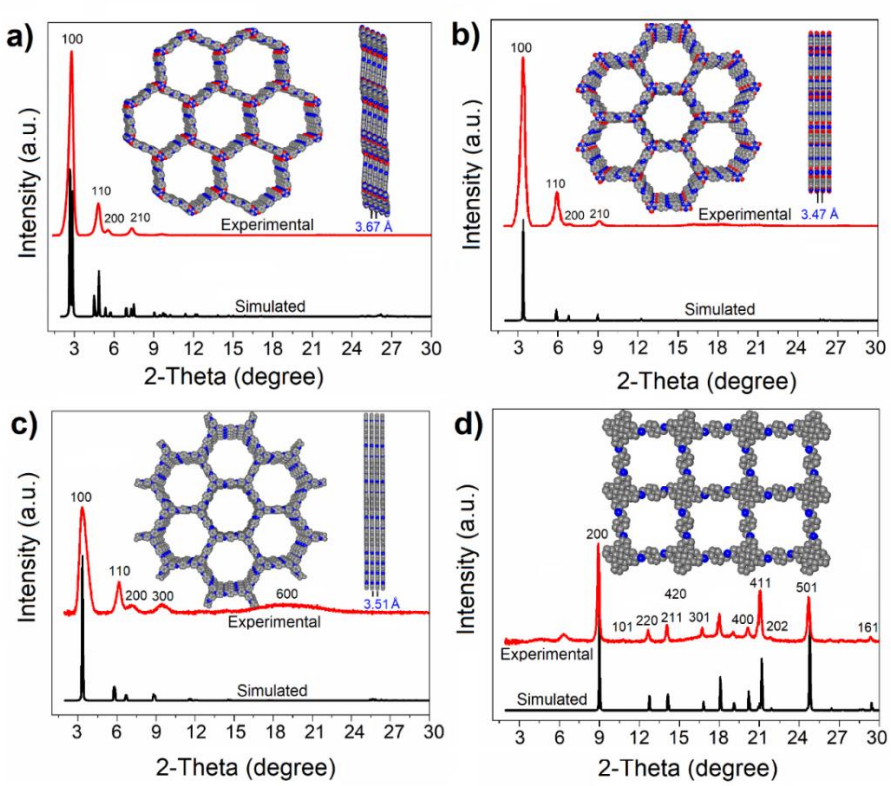

Fig. 2. Experimental and simulated PXRD patterns of prepared TPT-PDA COF (**a**), TPT-HZ COF (**b**), TAPA-TPA COF (**c**) and COF-300 (**d**).

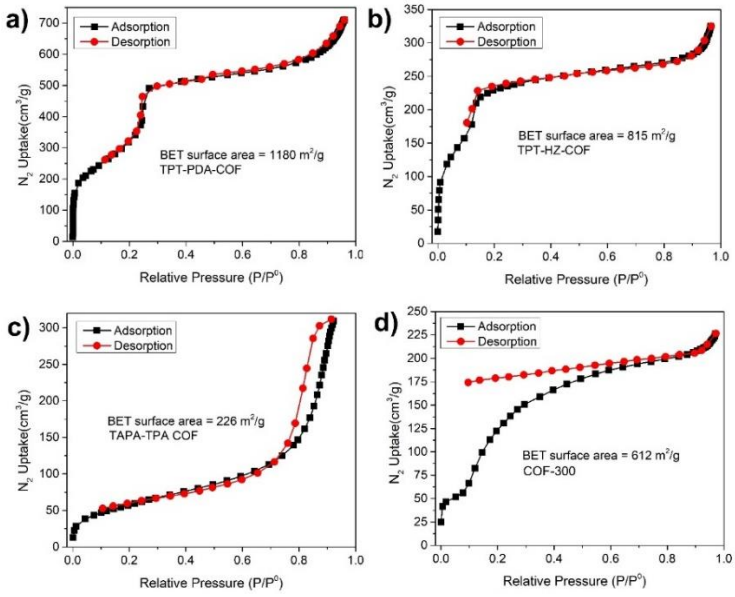

Fig. 3. N_2 adsorption-desorption isotherms of prepared TPT-PDA COF (**a**), TPT-HZ COF (**b**), TAPA-TPA COF (**c**) and COF-300 (**d**).

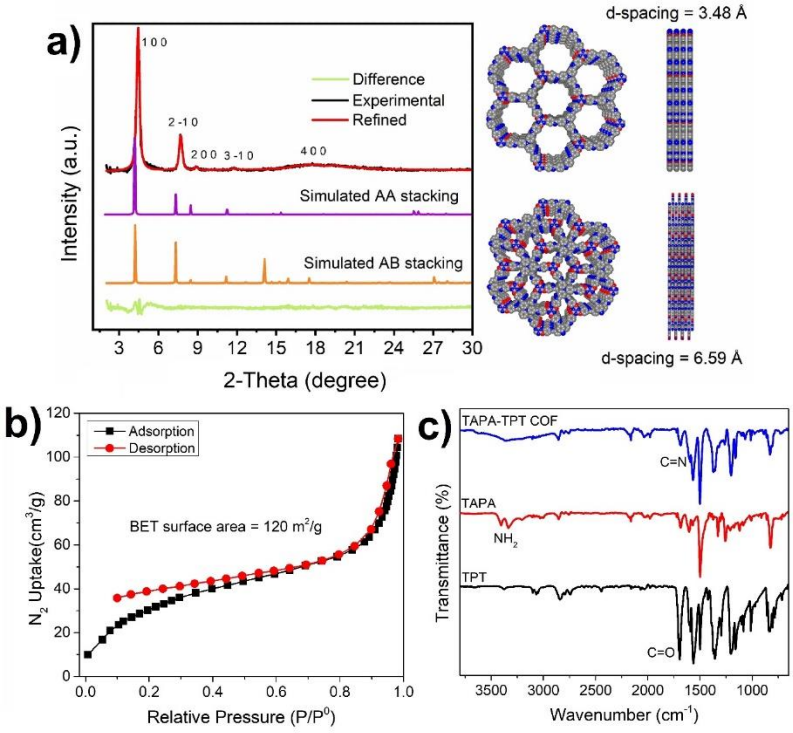

Fig. 4. PXRD patterns of TAPA-TPT COF; where the experimental in black, the Rietveld refinement is in red showing very minimal difference (green line) with Rp and Rwp of 3.416% and 4.478%, respectively. The simulated PXRD patterns for the AA eclipsed and AB staggered structures are in purple and orange, respectively (**a**), N_2 adsorption-desorption isotherms (**b**), and FT-IR spectra of TAPA, TPT and TAPA-TPT COF (**c**).

2.2. Supercapacitor Application

In this work, five different types of 2D and 3D COFs catalytically prepared that the TAPA-TPT COF was a new 2D COF and so, its application was investigated for supercapacitors. At first, the TAPA-TPT COF was carbonized under argon atmosphere at 800 ^{o}C for 2 h with a heating rate of 5 ^{o}C/min. **Fig. 5a** presents the CV curves of the TAPA-TPT COF recorded at different scan rates, from 5 to 200 mVs^{-1} in the potential window from 0 to 0.8 V. All the CV curves are quasi-rectangular, even when recorded at the highest scan rate of 100 mVs^{-1}, indicating ideal capacitive behavior.[54, 150] **Fig. 5b** shows the GCD curves of TAPA-TPT COF at different current density (0.5–20 A g^{-1}). The shapes of the charge/discharge curves are approximately linear and symmetrical, which implies that the material has good charge/discharge reversibility and cycle performance. The specific capacitance was calculated from the GCD curves using the equation (1) as shown in **Fig. 5c**. The TAPA-TPT COF exhibited excellent specific capacitance of 205 F g^{-1} at a current density of 0.5 A g^{-1} which was decreased to 95 F g^{-1} when the current density was

increased to 20 A g^{-1}, which is a very attractive value for supercapacitors. In comparison our COF performance with other reported COFs, the specific capacitance values obtained for TAPA-TPT COF are higher than other COFs including β-ketoenamine-linked COF (122 F g^{-1} at 1.56 A g^{-1}),[151] boroxine-linked COF (99.6 F g^{-1} at 0.5 A g^{-1}),[152] and imine-linked COF (116 F g^{-1} at 0.5 A g^{-1}).[153] Moreover, the electrochemical performance of the TAPA-TPT COF prepared with traditional method was compared with the TAPA-TPT COF prepared with catalytic method (**Fig. S28**). As shown in **Fig. S28**, and due to the same crystalline and porous structure of these two COFs, the CV and galvanostatic charge-discharge curves of the traditional COF are almost the same to the catalytic one. This result could be attributed to the porous structure of COF material and also the presence of heteroatoms (nitrogen), which allow easier accessibility of electrolytes to the surface of the electrode.[154] Moreover, the cycling stability of TAPA-TPT COF was tested through 10000 charge/discharge cycles at a current density of 15 A g^{-1} (**Fig. 5d**). The retention ratio of the capacitance value was 95% after 5000 cycles, suggesting higher stability and excellent cycle performance.

Electrochemical impedance spectroscopy (EIS is further adopted to study the accessibility of electrolyte ions through the materials. The measured real part of the resistance (Z') is the ohmic resistance originating from the electrolyte and the contact between the electrode and the current collector. **Fig. S29** shows the Nyquist plots of the obtained electrode materials. Theoretically, the Nyquist plot consists of two parts: at low frequencies, the straight line is related to the Warburg resistance (Z_w), which indicates the ability of ions to diffuse from the electrolyte to the electrodes, and the nearly vertical line at low-frequency region shows the electrical double-layer capacitive behavior.[155] According to the Nyquist plots (**Fig. S29**), two parts can be clearly observed, including a semicircle in the high frequency region and a vertical-like slope in the low-frequency region. In the high-frequency region, the semicircle corresponds to the charge-transfer resistance (R_{ct}) at the electrode/electrolyte interface, and a smaller semicircle corresponding to lower charge transfer resistance.[156] The horizontal axis intercept of the Nyquist plot represents the equivalent series resistance (R_S) which can be comprised of the intrinsic resistance within the electrolyte, resistance between the interface of the electrode and electrolyte and contact resistance between electrode and current collector.[157] The value of R_S for TAPA-TPT COF is 2.4 Ω, indicating a small resistance to charge transfer, which is consequently related to its high electrical conductivity.

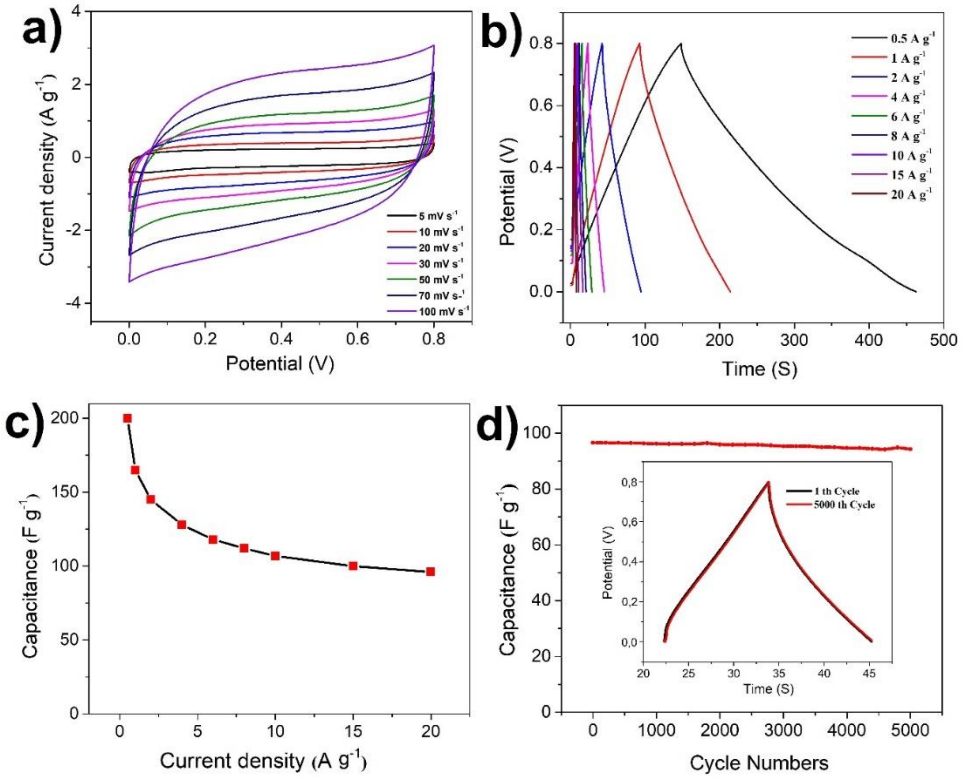

Fig. 5. Electrochemical performance of the TAPA-TPT COF (catalytically prepared) electrode in 1M H_2SO_4, measured using a three-electrode system: (**a**) CV curves recorded at various scan rates, (**b**) galvanostatic charge-discharge curves recorded at various current density, (**c**) corresponding specific capacitances recorded at various current density, and (**d**) cycling performance recorded at a current density of 15 Ag^{-1}, and the inset showing first and last cycles of GCD curves.

3. Conclusion

In this study, five different imine and azine-linked 2D and 3D COFs were catalytically prepared with high yield, crystallinity and porosity under mild conditions and short reaction time. The results revealed that the amine building blocks with two amine functional groups, formed the COFs with higher crystallinity, porosity and yield of the products compared to amine with three functional groups and a non-planar structure. The higher crystallinity and porosity of the COFs with two amine functional groups can be attributed to the planar structures of these COFs and subsequently, stronger π–π stacking interactions between oligomers through the initial and the successive error-correction crystallization process. This research presents a fast, low-cost and efficient approach for the catalytic synthesis of both 2D and 3D COFs and opens a new way to the scaled-up synthesis of these worthwhile crystalline polymers.

Author Contributions

The manuscript was written through contributions of all authors. All authors have given approval to the final version of the manuscript.

Declaration of Competing Interest

There are no conflicts to declare.

Supporting Information

The Supporting Information is available free of charge athttps://pubs.acs.org.

Experimental section; additional PXRD, BET and pore size distributions of all samples to confirm the crystalline and porous structures; FT-IR and ^{13}C CP/MAS NMR analyses to confirm the successful synthesis of COFs; TEM and SEM analysis of TAPA-TPT COF to confirm the morphology and size of material; TGA analysis and the electrochemical performance of the TAPA-TPT COF.

Acknowledgments

This work was supported by Natural Science and Engineering Research Council of Canada (NSERC), the Canada Research Chairs program (CRC) and Canada Foundation for Innovation. We acknowledge all the characterization centers including NanoQAM, QCAM and LCM. H.M.E. acknowledges the support provided by the Institute for Sustainable Energy and Environment (ISEE) at Virginia Commonwealth University.

Funding Sources

This research was funded by NSERC, CRC and CFI Canada.

3.3 Informations complémentaires

Les informations complémentaires relatives aux procédures expérimentales et aux caractérisations sont disponibles dans l'annexe B et sur le site web.
https://pubs.acs.org/doi/10.1021/acsaem.3c01913.

3.4 Contribution des auteurs pour cette étude

Le premier auteur de cet article, qui est également l'auteur de cette thèse, a réalisé la plupart de la synthèse et des caractérisations.
Le deuxième auteur, le Dr Khaled Rhili, a mené l'analyse des supercondensateurs.
Le troisième auteur, Mohammad K. Shehab, a réalisé l'analyse de simulation PXRD pour les COFs synthétisés.
Le quatrième auteur, Hichem Gamraoui, nous a aidés dans la synthèse de certains matériaux de départ et COFs.
Le cinquième auteur, Zhiyuan Peng, nous a assistés dans l'interprétation de certaines analyses.
Le sixième auteur, le Professeur Ahmad Samih ElDouhaibi, nous a assistés dans la synthèse de certains matériaux de départ et COFs.
Les septième et huitième auteurs, le Professeur Rachid Touzani et le Professeur Belkheir Hammouti, nous ont assistés dans l'interprétation de certaines analyses.
Le neuvième auteur, le Professeur Hani El-Kaderi, a été conseiller pour ce projet et nous a assistés dans l'analyse de simulation.
L'auteur correspondant, le Professeur Mohamed Siaj, a contribué au manuscrit et au processus de soumission.

CHAPITRE 4
ACTIVITÉ CATALYTIQUE DÉPENDANTE DE LA TAILLE DES NANOPARTICULES DE PALLADIUM DÉCORÉES SUR DES RÉSEAUX ORGANIQUES MICROPORUEUX MAGNÉTIQUES À COQUE

4.1 Introduction

La troisième section de ce projet a impliqué la conception et la synthèse de réseaux organiques mésoporeux (MONs) magnétiques à coquille-core. Après sa fonctionnalisation, des nanoparticules de Pd ont été ancrées à sa surface. Les catalyseurs nanohétérogènes préparés peuvent catalyser la formation de liaisons C-C dans des conditions douces, avec des solvants écologiques, et des temps de réaction courts, produisant des rendements allant de bons à excellents.

4.2 Article publié pour cette étude

Size-Dependent Catalytic Activity of Palladium Nanoparticles Decorated on Core–Shell Magnetic Microporous Organic Networks, ACS Applied Nano Materials. 2023, 6, 19, 17706–17717.
https://pubs.acs.org/doi/full/10.1021/acsanm.3c02990.

Size-Dependent Catalytic Activity of Palladium Nanoparticles Decorated on Core-Shell Magnetic Microporous Organic Networks

Amir Khojastehnezhad[a], Hichem Gamraoui[a], Maziar Jafari[a], Zhiyuan Peng[a], Farid Moeinpour[b], and Mohamed Siaj[a*]

[a]*Department of Chemistry, University of Quebec at Montreal, Montreal, QC H3C3P8, Canada*

[b]*Department of Chemistry, Bandar Abbas Branch, Islamic Azad University, Bandar Abbas, Iran*

Abstract

It is of supreme importance to develop recyclable and green heterogeneous catalysts due to their potential to reduce environmental impact and cutting costs associated with their use. Hence, in this research, an initial development was made of a core-shell magnetic structure composed of Fe_3O_4 and a microporous organic network (MON), followed by the physical absorption of palladium nanoparticles (NPs) onto the outer surface of this shell substance. The results of TEM and EDX analyses indicated that Pd NPs of varying sizes, which were produced using different reducing agents, were evenly bound to the MON shell materials. The use of PiFM and XPS analyses

provided evidence that there was effective bonding between Pd nanoparticles, and the amine groups present on the surface of MON materials. Besides, the successful immobilization of palladium NPs was also approved by N_2-sdsorption desorption analyses with the decrease of the surface from 328 to 227 m^2/g after palladium inclusion. The prepared nanoheterogeneous catalysts can catalyze the C-C formation in mild conditions, green solvents, short reaction times with good to excellent yields. The results revealed that the catalyst with smaller palladium NPs sized 1-5 nm and in medium abundance has better catalytic performance towards C-C formation, compared to those with bigger Pd NPs sized 5-15 nm and in both low and high Pd contents.

Keywords: Microporous organic network; nanocatalyst; Suzuki reaction, Sonogashira reaction, cross-coupling reaction, palladium nanoparticles

1. Introduction

Magnetic MONs are a novel class of catalysts with potential applications in a variety of fields, ranging from heterogeneous catalysis to nanotechnology.[158] MONs are composed of organic molecules linked together by covalent bonds and embedded within a porous matrix of magnetic particles. These networks provide an ideal platform for the development of catalytic reactions due to their unique structure and properties. The MONs offer high surface area, good porosity, tunable chemical composition, and high selectivity for specific catalytic reactions. Additionally, they possess excellent thermal and mechanical stability, making them suitable for use in harsh conditions. [159] MONs can be tailored to suit specific catalytic requirements by incorporating different organic molecules and magnetic particles into the network. The organic molecules present in the MONs can be functionalized with various functional groups, providing greater control over the reaction conditions,[160] and the magnetic properties of these networks allow for easy separation and recovery from reaction mixtures, making them highly efficient and selective catalysts for a variety of chemical transformations.[161]

In recent years, there has been a growing interest in developing green catalysts for chemical reactions due to their potential to reduce environmental impact and cutting costs associated with their use.[162] Catalysts based on noble metals such as palladium are widely used because of their high selectivity and activity in many organic transformations;[163] however, they are expensive and toxic which makes them unsuitable for green catalysis.[164] To address this issue, researchers have developed various strategies to immobilize metal nanoparticles onto different supports to improve

their stability while maintaining their catalytic activity.[165] One such approach is using core-shell magnetic microporous organic networks (MONs).[166]

The cross-coupling reaction catalyzed by palladium is a group of extremely effective reactions that has recently been crucial in the creation of a diverse range of significant chemical structures, including heterocyclic structures, natural products, organic complexes, and conjugated polymers.[167] Consequently, significant efforts have focused on developing diverse catalysts containing the transition metal palladium.[168] The methodologies that execute carbon-carbon linkage reactions through Pd catalysis exhibit advantages such as mild conditions, strong tolerance towards functional groups, cost-effectiveness, stability of reactants, ease of accessibility, and facile separation of reaction products.[169] These days, the field of organic synthesis has progressed through the use of Pd-catalyzed cross coupling reactions, which include the Suzuki−Miyaura,[170] Heck,[171] Negishi,[172] Sonogashira,[173] and Kumada.[174] Regarding this matter, cross-coupling processes are specifically concentrated on producing diverse symmetrical and asymmetrical heteroaromatic and biaromatic compounds, which are crucial components for the preparation of natural substances, medicines such as those used for treating diabetes, high blood pressure, fungal infections, disinfection, calming agents, antiseptics, and anticancer drugs.[175]

Therefore, for this investigation, the researchers initially created magnetic core-shell MON materials. Following that, they evenly coated the surfaces of these materials with Pd NPs of various sizes. The ultimate achievement was a nano heterogeneous magnetic Pd catalyst known as Fe_3O_4@MON-Pd (Scheme 1). The examination of TEM and EDX revealed that there is a solid metal oxide core enclosed by a transparent organic layer. It was also observed that there are uniformly distributed Pd speckles, measuring less than 5 nm and 15 nm, which are firmly attached to the surface of the organic layer. XPS and PiFM provided valuable information about the chemical composition of the catalyst. Furthermore, they enabled the spectroscopic evaluation of the impact of Pd NPs chelation. The synthesized nano heterogeneous catalysts exhibited the capability to facilitate the formation of C-C bonds under mild reaction conditions, resulting in highly satisfactory yields.

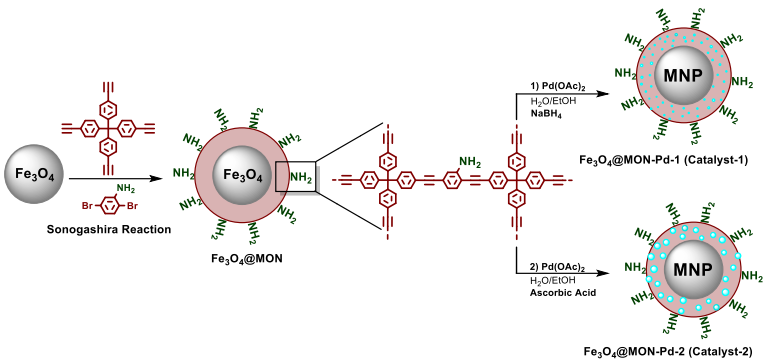

Scheme 1. Preparation of catalysts (catalyst-1 and catalyst 2).

2. Experimental Section

Nanoheterogeneous magnetic palladium catalysts (Fe_3O_4@MON-Pd-1 abbreviated as catalyst-1 and Fe_3O_4@MON-Pd-2 abbreviated as catalyst-2) were developed using these subsequent synthetic procedures. Firstly, the magnetic NPs (Fe_3O_4) and core-shell magnetic MON materials (Fe_3O_4@MON) were synthesized according to the literature.[95, 176] After, Pd NPs were immobilized onto the MON shell materials in different concentrations (low, medium and high, abbreviated as LC, MC and HC) and in various sizes based on the strength of the reducing agents (sodium borohydride and ascorbic acid) (Scheme 1).

2.1. Materials

No additional purification was performed on the chemicals. The chemicals used were specified as follows: "tetrakis(4-ethynylphenyl)methane ($C_{33}H_{20}$, 98% purity, TCI America), bis(triphenylphosphine)palladium(II) dichloride ($Pd(PPh_3)_2Cl_2$, 98% purity, Sigma-Aldrich), polyvinylpyrrolidone (PVP) ($(C_6H_9NO)_n$, 98% purity, Sigma-Aldrich), 2,5-dibromoaniline ($C_6H_5Br_2N$, 98% purity, Sigma-Aldrich), palladium(II) acetate ($Pd(CH_3COO)_2$, 98% purity, Sigma-Aldrich), sodium borohydride ($NaBH_4$, 98% purity, Sigma-Aldrich), potassium hexachloropalladate(IV) (K_2PdCl_6, 98% purity, Sigma-Aldrich), ascorbic acid ($C_6H_8O_6$, 98% purity, Sigma-Aldrich), phenylboronic acid ($C_6H_5B(OH)_2$, 98% purity, Sigma-Aldrich).

2.1.1. Material Characterization

The materials' crystalline structures and phases were examined using XRD (X-ray diffraction) with Cu Kα radiation on a Bruker D8 advance instrument (Billerica, MA, USA). To assess the surface compositions and states, XPS (X-ray photoelectron spectroscopy) was conducted on an XPS PHI 5600-ci instrument (MN, USA). The morphologies and microstructures of the materials were

characterized using TEM (transmission electron microscopy), HRTEM (high-resolution TEM), and STEM-EDX (energy-dispersive spectroscopy) on a JEM-2100F instrument (JEOL, Tokyo, Japan) coupled to a EDX detector (Abingdon, Oxford Instruments, UK). Additionally, the chemical identities and topography of observed high-resolution features, measuring below the diffraction limit of light, were simultaneously determined using photo-induced force microscopy (PiFM) on a VistaOne instrument (MolecularVista.Inc, CA, USA). The TMAX-BSD-PM2 BET instrucment (TMAXCN, China) measurements were utilized to ascertain the surface areas of the samples. The adsorption and desorption analyses of nitrogen were conducted at a temperature of 76.5 K. Finally, ICP-OES (inductive coupled plasma optical emission spectrometry) analysis was conducted in radial mode with an Agilent model 5100 instrument. The magnetic hysteresis measurements of the samples were analyzed using a VSM magnetometer (model 7400, Lake Shore).

2.2. Methods

2.2.1. Preparation of Fe_3O_4@MON nanocomposites with core-shell structure

At first, the iron oxide NPs were prepared from the solvothermal reaction of ferric chloride hexahydrate ($FeCl_3.6H_2O$), and in the presence of sodium acetate, poly(vinylpyrrolidone) (PVP) and ethylene glycol.[95] Next, the core-shell Fe_3O_4@MON NPs was synthesized from the Sonogashira cross-coupling reaction of tetrakis(4-ethynylphenyl)methane (25.0 mg), 2,5-dibromobenzenamine (30 mg) with Fe_3O_4 (100 mg) and in the presence of CuI (0.50 mg), $Pd(PPh_3)_2Cl_2$ (1.7 mg), and triethylamine (7.5 mL) in toluene (7.5 mL).[176]

2.2.2. Preparation of Fe_3O_4@MON-Pd-1 with core-shell structure (Catalyst-1)

To create nanoscale Pd-1 NPs fixed onto Fe_3O_4@MON substances, a solution containing 10 mg of Fe_3O_4@MON material was evenly distributed in a combination of ethanol and water (in a ratio of 10:5 mL) for 30 minutes inside an ultrasonic bath. Subsequently, mechanical stirring was employed at a temperature of 50 ^oC, and varying amounts of palladium acetate (2.5, 5, and 10 mg, corresponding to low, medium, and high Pd concentrations, respectively) were introduced. The reaction proceeded for 6 hours after the addition. The final catalyst-1 (Fe_3O_4@MON-Pd-1) was obtained by adding a solution of $NaBH_4$ (2.5, 5 and 10 mg) in water (5 mL) dropwise (30 min) at room temperature and stirring for 12 hours. The resulting black magnetic materials were then separated using an external magnet, washed with water (three times, 30 mL) and ethanol (once, 30 mL), and dried at 80 ^oC for 24 hours.[177]

2.2.3. Synthesis of Fe_3O_4@MON-Pd-2 with core-shell structure (Catalyst-2)

In order to create Pd-2 NPs supported on Fe_3O_4@MON, 10 mg of Fe_3O_4@MON was evenly distributed in a solution containing ethanol and water (in a ratio of 10:5 mL) for a duration of 30 minutes while exposed to ultrasound waves. Subsequently, 5 mg of palladium acetate was introduced into the solution while it was mechanically stirred at a temperature of 50 °C and the reaction resumed for 6 h. Next, the temperature was decreased to ambient temperature and then a solution of 200 mg ascorbic acid in water (10 mL) was added dropwise (30 min) and it was stirred for 12 h. The mixture was ultimately parted from the black magnetic substances through the utilization of an outer magnet. Subsequently, the black magnetic materials were cleansed using 30 mL of water thrice and 30 mL of ethanol once. To complete the process, the materials were then dried at a temperature of 80 ^oC for a period of 24 hours, resulting in the production of the ultimate catalyst-2, denoted as Fe_3O_4@MON-Pd-2.[178]

2.2.4. Protocol for Synthesis of Biaryl Derivatives via the Suzuki Cross-Coupling Reaction

At first, the catalyst (0.2 mol%) was dispersed in a mixture of H_2O/EtOH (2 mL, 1:1) by ultrasound for 15 minutes and was then added to a mixture of aryl halides (1.0 mmol), phenylboronic acid (1.2 mmol), K_2CO_3 (2.0 mmol) in H_2O/EtOH (3.0 mL). The final mixture was stirred in a capped tube at room temperature for the times mentioned in Table 2. After the reaction was completed, the magnetic catalyst was easily separated from the reaction mixture by an external magnet, washed with EtOH and H_2O and dried at 80 ^oC for 24 h to use for the next run. The precipitated reaction products were centrifuged, washed with water, and extracted with acetonitrile. Finally, the decanter funnel was employed to separate, and sodium sulfate was used to dry the organic layers. To obtain purified biaryl derivatives, a silica-gel solid-phase column chromatography technique with a mixture of ethyl acetate and hexane as mobile-phase was employed.

2.2.5. Protocol for Synthesizing Biaryl Derivatives via Sonogashira Reaction

At first, the catalyst (0.2 mol%) was dispersed in a mixture of H_2O/DMF (2 mL, 1:1) by ultrasound for 15 minutes and was then added to a mixture of aryl halides (1.0 mmol), phenylacetylene (1.2 mmol), NaOAc (2.0 mmol) in H_2O/ DMF (3.0 ml). The final mixture was stirred in a capped tube at 50 ^oC for the times mentioned in Table 3. After the reaction was completed, the magnetic catalyst was easily separated from the reaction mixture by an external magnet, washed with EtOH and H_2O and dried at 80 ^oC for 24 h to use for the next run. The liquid portion was allowed to dry out, and the resulting substances were rinsed with water and separated using ethyl acetate. Finally, the

decanter funnel was used to separate and dry the organic layers with sodium sulfate. In order to purify the ultimate biaryl Sonogashira derivatives, column chromatography was employed with a mixture of ethyl acetate and hexane.

3. Results and Discussion

In this research, differently sized Pd NPs immobilized on core-shell magnetic MON were prepared based on different reducing agents (sodium borohydride and ascorbic acid) (Scheme 1). The results showed that the size of Pd NPs depends on the reducing agents.[179] When the $NaBH_4$ was used as a reducing agent, the size of Pd NPs were smaller compared to those when ascorbic acid was used. The use of a mild (ascorbic acid) and a strong (sodium borohydride) reducing agent resulted in different sizes of NPs due to the affected seeding and growth processes. On catalyst-1, the stronger reducing agent accelerated seed formation enabling a greater number of particle formation, although smaller in size because of a deficiency in particle growth. In contrast, on catalyst-2, the milder reducing agent promoted fewer nucleation sites, but insisted on the particles' growth yielding spheres of larger diameter. Fe_3O_4 NPs has been physically encapsulated with MON polymer material and the larger Pd nanoparticles were attached to the surfaces of the MON materials through a chelation process that involved bonding between the Pd nanoparticles and the amine functional groups, however the smaller NPs could also be immobilized into the cavities of the MON materials. The catalysts were characterized using various techniques, in order to fully understand their core-shell morphologies, crystalline and porous structures.

3.1. Catalyst Characterization

3.1.1. Evaluation of Microscopic Structures: TEM and SEM Assessments

SEM and TEM were utilized to examine the dimensions and structure of the nanomaterials that were prepared. TEM and SEM analyses showed that both Fe_3O_4 (Fig. 1a and 1b) and Fe_3O_4@MON MNPs with core-shell structures (Fig. 1c, 1d and S1) have regular spherical morphologies with an around 50 nm diameter shell structures.[176] On the other hand, as explained above, Pd NPs were prepared with different sizes and concentrations based on different reducing agents. TEM analysis (Fig. 1e and 1f) confirmed both Pd NPs (Pd-1 and Pd-2 with different sizes) were immobilized uniformly on the surface of MON shell materials. Sizes of these NPs are between 1 to 5 and 5 to 15 nm when we used sodium borohydride and ascorbic acid respectively, as reducing agents (Fig. 1e, 1f, S2 and S3). Moreover, TEM analysis confirmed the different distributions and abundances of Pd NPs on the MON materials (Fig. S4). Additionally, the mapping images obtained using

transmission electron microscopy (TEM) provide a visual representation of the elemental composition analysis for catalyst-1 and catalyst-2. These images can be seen in Figures 1g, 1h, and S5. The presence of palladium, in addition to iron, oxygen, carbon, and nitrogen confirms the successful immobilization of Pd NPs (Pd-1 and Pd-2) on the MON's surface. Another confirmation of the elemental analysis was EDX, and the results are in agreement with TEM mapping and ICP analysis and show the presence of Pd in the catalyst structure (Fig. S6a-c). According to EDX analysis, the amount of Pd in the catalyst-1 with low, medium, and high Pd concentration were 6.77, 12.56 and 16.54 wt%, respectively. Besides, the exact amount of Pd in the samples was determined with Inductive Coupled Plasma (ICP). According to the results, the amount of palladium in the prepared catalysts with low, medium, and high Pd concentrations was 7.44, 12.36 and 16.99 wt%, respectively, an excellent agreement with other observations.

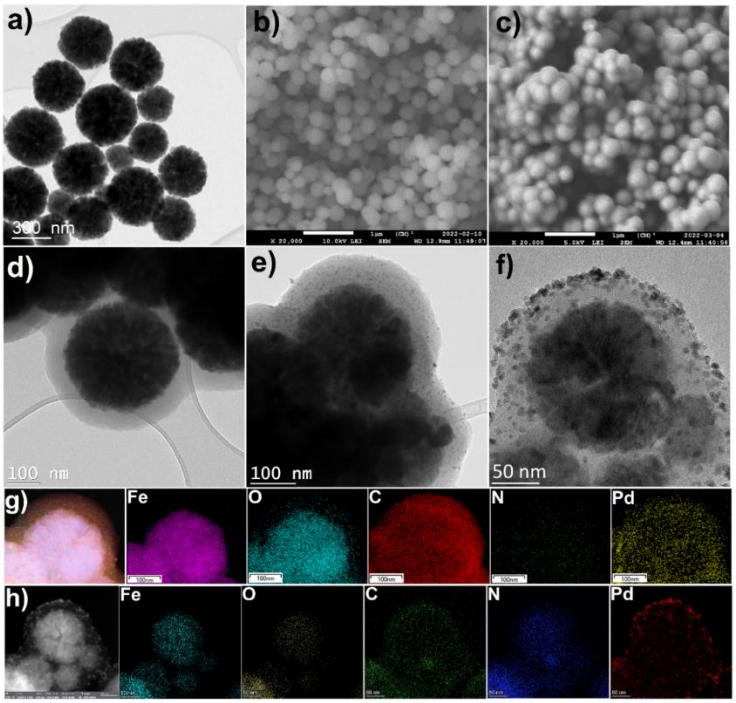

Fig. 1. TEM and SEM images of Fe_3O_4 MNP (a and b), SEM and TEM images of core-shell Fe_3O_4@MON (c and d), TEM image of catalyst-1-MC (e), TEM image of catalyst-2-MC (f), and TEM mapping of catalyst-1-MC (g) and catalyst-2-MC (h).

3.1.2. XRD and BET Analyses

To assess the crystal phase of the samples that were produced, analysis using PXRD was utilized. As can be seen in Fig. 2a, all prepared materials including Fe_3O_4 MNPs, Fe_3O_4@MON and catalyst-1 NPs were studied with this analysis. The violet pattern in Figure 2a shows the PXRD of

Fe_3O_4 MNPs. It displays six distinct peaks at 2Θ = 30.09, 35.5, 43.0, 53.2, 57.2, and 62.11, which match with the characteristic peaks of Fe_3O_4's cubic phase according to JCPDS card No. 19-0629.[102] In the XRD analysis of Fe_3O_4@MON materials, it was observed that a broad peak at approximately 15 to 25 degrees corresponds to the amorphous characteristics of MON materials (as indicated by the red pattern shown in Figure 2a).[180] In the XRD pattern of catalyst-1 (Fig. 2a, green pattern), there are some new peaks assigned to the Pd(0) NPs (2Θ = 40.5 (1 1 1), 46.3 (2 2 0) and 67.8 (2 2 0), JCPDF file no. 46-1043).[181] The presence of these peaks affirms that the Pd(0) NPs have been effectively attached to the core-shell MON materials, which aligns with findings from other studies. On the other hand, the N_2 adsorption-desorption investigation was conducted for the samples, and the findings (shown in Fig. 2b) demonstrated the surface areas according to the BET (Brunauer-Emmett-Teller) method. The Fe_3O_4, Fe_3O_4@MON, Fe_3O_4@MON-Pd-1, and MON substances revealed surface areas of 60, 328, 227, and 945 m^2/g, respectively. This categorization falls under Type IV. These represent about 66% and 31% decrease in BET surface area of MON material after preparation of core-shell magnetic MON and immobilization of Pd NPs onto the MON's surface, respectively. The surface area decrease from 945 m^2/g to 328 m^2/g ascribed to covering the core Fe_3O_4 with the MON shell material, indicated that the entirety of the NPs were not covered by MON shell material. Exposed areas of bare Fe_3O_4 NPs contributed to lowering the resulting surface area of the sample (Fig. S7). However, the results of the second reduction approved the effective binding of Pd NPs to the outer materials.[176, 180, 182] Moreover, after studying the samples' pore sizes and the pore volumes before (Fe_3O_4@MON) and after palladium immobilization (Fe_3O_4@MON-Pd-1), characteristic trends were observed. Based on the pore size diagrams (Fig. S8), core-shell Fe_3O_4@MON and Fe_3O_4@MON-Pd-1 showed 2.30 and 2.15 nm pore sizes, and pore volumes decreased from 0.188 to 0.155 cm^3/g, respectively. These drops in the pore size and pore volume can be attributed to the insertion of some Pd NPs (smaller than 2.0 nm) into the cavities of the microporous organic networks.[183]

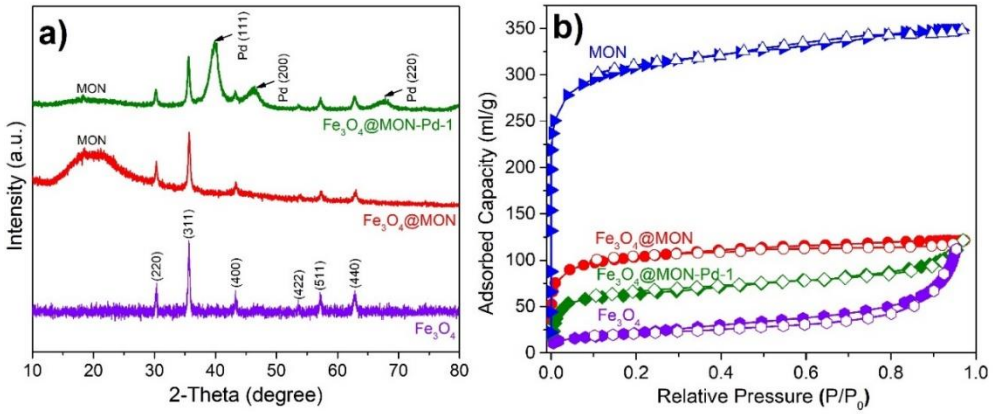

Fig. 2. a) XRD patterns of Fe_3O_4 MNP (violet pattern), Fe_3O_4@MON (red pattern) and catalyst-1 (green pattern). b) N_2 adsorption−desorption isotherms of Fe_3O_4 MNP (violet pattern), Fe_3O_4@MON (red pattern), catalyst-1 (green pattern) and MON material (blue pattern).

3.1.3. XPS Analysis

X-ray photoelectron spectroscopy (XPS) was used to investigate the elemental composition, bonding, and overall electronic structure of Fe_3O_4@MON and catalyst-1. As depicted in Fig. 3a, after the immobilization of Pd NPs on the Fe_3O_4@MON, in addition to carbon and nitrogen, some new peaks appeared and were assigned to the Pd NPs (purple spectrum). It is worth mention that XPS is only sensitive to a maximum depth of about 10 nm. This is simply an indication that the coating at the surface of the Fe_3O_4 cores is thicker than 10 nm and fully covers the cores, so we were not able to observe peaks related to Fe_3O_4 NPs. The high-resolution XPS curve of Pd 3p and Pd 3d showed the double peaks of Pd 3p with binding energies of 532.6 and 560.8 eV which could be attributed to the Cu(0) 3p3/2 and 3p1/2, respectively, and the double peaks of Pd 3d with binding energies of 335.8 and 340.9 eV were accredited to the Pd(0) 3d5/2 and 3d1/2, respectively, that confirmed the existence of metallic palladium and the absence of Pd oxide in the final catalyst (Fig. 3b and 3c).[184] Additionally, the N 1s high-resolution XPS spectrum demonstrated a separation into two distinct peaks, with values of 398.7 and 399.9 eV for Fe_3O_4@MON, and 399.0 and 400.3 eV for catalyst-1, respectively (Fig. 3d and 3e).[176, 185] The chemical shifts observed indicate that there is chelation occurring between the nitrogen present in the MON shell materials and the palladium NPs. This finding is consistent with the analysis performed using PiFM.

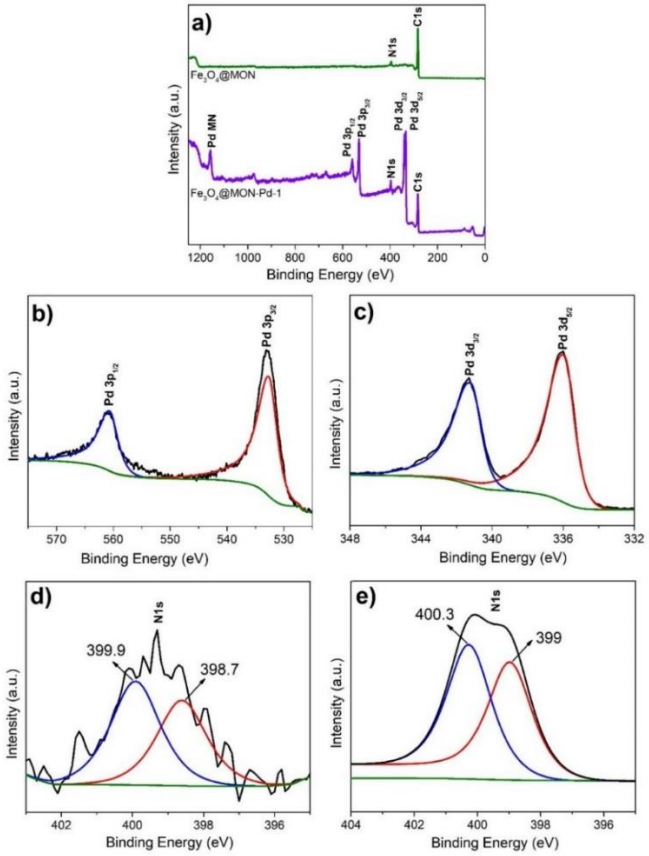

Fig. 3. Complete analysis of Fe_3O_4@MON and catalyst-1 through XPS survey (a), high-resolution XPS spectrum of Pd3p (b) and Pd3d (c) of catalyst-1-MC and high-resolution XPS spectrum of N1s of Fe_3O_4@MON (d) and N1s of catalyst-1-MC (e).

3.1.4. PiFM Analysis

The surface of Fe_3O_4@MON powder was investigated using PiFM analysis, which revealed the presence of spherical-shaped particles with diameters ranging from 300 to 500 nm (Fig. 4a). The spectroscopic signature of the MON material observed in the PiF-IR point spectrum replicated the findings from previous reports using FT-IR (Fig. 4b).[176] A strong and broad peak from ~1000 cm^{-1} to ~1150 cm^{-1} and a sharp peak at 1260 cm^{-1} was attributed to the aromatic rings and the aromatic amines, respectively. The peak observed at 1510 cm^{-1} on the spectrum can be attributed to the sharp and strong existence of C-N bonds. Additionally, a moderate peak identified around 1600 cm^{-1} on the spectrum was linked to the vibration modes of both aromatic compounds and compounds containing an NH_2 group.[186] Remarkably, alterations were observed in the PiF-IR spectrum once Pd NPs were affixed onto the MON shell material. Importantly, it was observed that the aromatic amine (1260 cm^{-1}) and the C-N functional groups (1510 cm^{-1}) exhibited a shift towards

bigger frequencies (1265 and 1518 cm^{-1}). This shift provided evidence supporting the successful interactions of Pd NPs with the aromatic amines.[187] Besides, a PiFM mapping technique was used to specifically identify C-N bonds within the same topography frame, as depicted in Figure 4c. The intensity of these bonds was consistently high across the entire image, indicating their ubiquitous presence. This observation supports the conclusion that the MON material effectively enveloped the MNPs' outer surface.

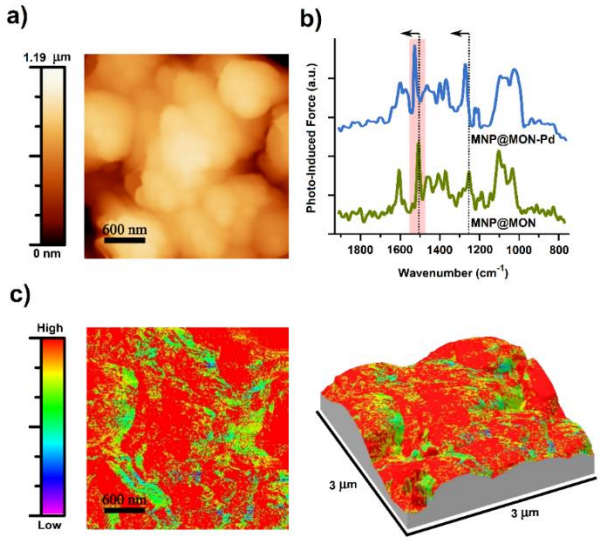

Fig. 4 AFM imaging of the Fe_3O_4@MON material as it was created (a). PiF-IR spectra of Fe_3O_4@MON and catalyst-1, showing shifts in the aromatic-NH_2 and C-N peaks indicated by dotted lines (b). The PiFM intensity color-map of the same topography frame focuses on the C-N bonds and is shown in plan view and in perspective view (c). The intensity of the signal corresponds to the detection of C-N bonds.

3.1.5. Magnetic analysis

In this research, the prepared catalyst has magnetic properties, and it can be separated from the reaction mixture easily using an external magnet. Thus, filtration, centrifugation and hard work up procedures are unnecessary. The magnetic properties of the catalyst has been studied with vibrating sample magnetometer (VSM) analysis (Fig. S9a) using magnetic hysteresis measurements. According to the outcomes, bare Fe_3O_4 has a bigger magnetic saturation value around 85 $emug^{-1}$, compared to Fe_3O_4@MON with core-shell structure (56 $emug^{-1}$) and catalyst-1 after Pd immobilization (41 $emug^{-1}$).[180] These curves were fully reversible, showing that the NPs display superparamagnetic properties. Also, the decrease from 85 to 41 $emug^{-1}$ had no effect on the ease in catalyst removal upon reaction completion. In 5 seconds placing the magnet on the wall of the reaction tube, the catalyst can be separated from the reaction mixture (Fig. S9b).

3.2. Catalytic Applications

3.2.1. Evaluation of Catalyst Activity

To evaluate the catalytic activity of the nanoheterogeneous magnetic Pd catalyst, the effects of the prepared catalysts were investigated for the Suzuki-Miyaura cross-coupling reaction. In this context, the reaction between iodobenzene (1.0 mmol) and phenylboronic acid (1.2 mmol) was chosen as the model reaction to prepare the biaryl compound of 3a. As a control experiment, the model reaction was performed without the catalyst and in the presence of only Fe_3O_4@MON. The Fe_3O_4@MON material was used as a catalyst to evaluate its behavior on the model reaction, maybe some $Pd(PPh_3)_2Cl_2$ remained in the material. However, for the preparation of 100 mg Fe_3O_4@MON, only the catalytic amount of 1.7 mg of $Pd(PPh_3)_2Cl_2$ was used and also after the preparation, the catalyst was washed with methanol, dichloromethane and water to remove palladium salt. The results showed that after 3 hours of running the reactions, no product was observed (Table 1, entry 1 and 2). These observations confirmed that there is no remaining palladium in the Fe_3O_4@MON material from $Pd(PPh_3)_2Cl_2$ and also Pd is necessary for the reaction. As a result, the catalysts that were created with varying amounts and sizes of palladium were employed to initiate the reaction process and determine the optimum conditions for a favorable outcome (Table 1, entries 3-6). Interestingly, we found that after just 30 minutes, the catalysts catalyze the reaction with high yields. Among catalyst-1 and catalyst-2; prepared with different reducing agents, catalyst-1 with smaller palladium size (1-5 nm) performed the model reaction with higher yield compared to catalyst-2 with bigger palladium size (5-15 nm) (Table 1, entries 4 and 6). These results are in agreement with a recently published paper.[188] Basically, the catalytic activity of the nanomaterial depends not only on the shape and size but also on the available surfaces and active sites. The larger surface area per unit mass of smaller Pd NPs can lead to higher performance in catalytic activity.[188-189] In contrast, among the catalysts utilizing varying levels of palladium concentrations (low, medium, and high), the catalyst containing medium amounts of Pd demonstrated superior outcomes when compared to the catalysts with low or high concentrations of palladium (Table 1, entries 3-5). In order to compare the results of the data (Table 1, entries 4 and 5), one-way analysis of variance test was used, and according to the results (Tables S1 and S2) a *p*-value of 0.0121 was obtained, and since this value is less than the 0.05 level, therefore, there is a significant difference between the results. Subsequently, the catalyst-1-MC was subjected to rigorous experimentation to determine its optimal quantity. To achieve this, smaller doses of catalyst-1-MC (0.1 and 0.05 mol%) were

employed in catalyzing the model reaction. It was observed that decreasing the catalyst amount resulted in a reduction of the reaction yield from 99% to 76% (Table 1, entries 7 and 8). Thus, 0.2 mol% of catalyst-1-MC was selected as an optimum amount to check other conditions (Table 1, entry 4).

Next, the best solvent, base and temperature were inquired (Table S3). On this basis, the model reaction was performed in the presence of catalyst-1-MC at different temperatures (Table S3, entries 1-3). Attractively, the catalyst was able to catalyze the synthesis of compound 3a at room temperature with excellent yield (Table S3, entry 1) and higher temperatures were not effective in improving the yield (Table S3, entries 2 and 3). Subsequently, the effects of none and different solvents were studied on the model reaction (Table S3, entries 4-13). The highest amount of compound 3a was obtained in EtOH and H_2O, both being polar and green solvents (Table S3, entries 9 and 10). When we mixed these solvents at a 1:1 ratio, 99% of product 3a was observed (Table S3, entry 13). We believed that adding EtOH to H_2O, completely dispersed the catalyst resulting in a reaction with higher yield. Optimization of the base was the last step. Accordingly, different bases including K_2CO_3, Cs_2CO_3, Na_2CO_3, NaOH, KOH and K_3PO_4 were used for the synthesis of 3a (Table S3, entries 14-18). Among various bases, K_2CO_3 showed better results (Table S3, entry 13). As a result, the best condition for the synthesis of 3a was the use of catalyst-1-MC (0.2 mol%), K_2CO_3, EtOH/H_2O and room temperature.

Table 1. Screening of the reaction condition for the Suzuki cross-coupling reaction (**3a**)[a]

Entry	Catalyst	Catalyst Amount (mol%)	Time (min)	Yield (%)[b]	TON/TOF (min^{-1})[c]
1	---	---	180	---	---
2	Fe_3O_4@MON	10 mg	180	---	---
3	Catalyst-1-LC[d]	0.3	30	85	283/9.44
4	Catalyst-1-MC[e]	0.2	30	99	495/16.5
5	Catalyst-1-HC[f]	0.2	30	94	470/15.6
6	Catalyst-2-MC	0.2	30	88	440/14.7
7	Catalyst-1-MC	0.1	60	87	870/14.5
8	Catalyst-1-MC	0.05	120	76	1520/12.6

[a] Reaction condition: iodobenzene (1.0 mmol), phenylboronic acid (1.2 mmol), K_2CO_3 (2.0 mmol), H_2O/EtOH (5.0 mL, 1:1) at 25 °C. [b] Isolated Yield. [c] Turn Over Number/Turn Over Frequency. [d] Low Pd concentration. [e] Medium Pd concentration. [f] High Pd concentration.

Considering the optimized reaction condition, the scope of the reaction was studied for the different aryl halides and phenylboronic acid in the presence of 0.2 mol% of catalyst-1-MC at room temperature (Table 2). As expected, iodine is a stronger leaving group compared to bromine and chlorine, thus, the Suzuki cross-coupling reactions with iodobenzene substituents showed higher product yields compared to bromobenzene and chlorobenzene substituents. In addition, the aryl halides with withdrawing functional groups like 3d had higher yields than aryl halides with donating functional groups such as 3g, 3h and 3l.

Table 2. Suzuki cross-coupling reactions catalyzed by catalyst-1-MC[a]

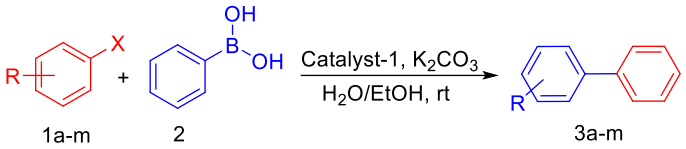

1a-m 2 3a-m

R	X	3	Time (min)	TON[b]	Yield (%)[c]
H	I	**3a**	30	495	99
H	Br	**3b**	45	475	95
H	Cl	**3c**	60	330	66
4-NO_2	I	**3d**	30	495	99
3-NO_2	I	**3e**	45	450	90
4-OH	I	**3f**	45	455	91
4-Ethyl	Br	**3g**	45	440	88
4-Me	Br	**3h**	45	455	91
3-Me	I	**3i**	45	475	95
2-Me	Br	**3j**	45	460	92
4-MeO	Cl	**3k**	0	240	48
4-MeO	Br	**3l**	0	445	89
2-MeO	Br	**3m**	0	465	93

[a] Reaction condition: aryl halides (1.0 mmol), phenylboronic acid (1.2 mmol), K_2CO_3 (2.0 mmol), catalyst-1-MC (0.2 mol%), H_2O/EtOH (5.0 mL, 1:1) at room temperature. [b] Isolated Yield. [c] Turn Over Number.

To further support the general applicability of the catalyst, the Sonogashira reaction (another type of cross-coupling reaction) was tested. The reaction between iodobenzene (1.0 mmol) and phenylacetylene (1.2 mmol) was chosen as a model reaction (Table S4). The catalysts' efficiency was reevaluated with different Pd sizes and concentrations (Table S4, entries 1-5). In parallel with the Suzuki reaction results, the highest amount of product 6a was obtained in the presence of

catalyst-1 with medium Pd concentration and small Pd sizes (less than 5 nm) (Table S4, entry 5). However, in comparison to the Suzuki reaction, the Sonogashira cross-coupling reaction demands higher temperatures (50 ^{o}C) and longer reaction time (60 min) to obtain the highest amount of product 6a (Table S5, entries 1-4). After monitoring the solvent effect (Table S5, entries 5-14), the best solvents were also found being the mixture of H_2O and EtOH, but in different ratio (Table S5, entry 14). Among different bases (Table S5, entries 15-19), sodium acetate was more effective to prepare the final Sonogashira product (Table S5, entry 14). Therefore, the optimized reaction condition was selected using sodium acetate and mixture of EtOH/H_2O at 50 ^{o}C for 1 h. Using these optimized reaction conditions, the scope of the reaction was investigated with different substituents of aryl halides (Table 3). Similar to the Suzuki cross coupling reaction results, the catalyst was able to synthesize all Sonogashira derivatives with good to excellent yields under the optimized reaction conditions (Table 3, entries 1-8).

Table 3. Sonogashira cross-coupling reactions catalyzed by catalyst-1-MC[a]

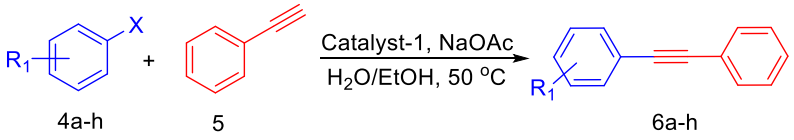

4a-h 5 6a-h

R_1	X	3	Time (min)	TON[b]	Yield (%)[c]
H	I	**6a**	60	485	97
H	Br	**6b**	60	460	92
4-NO_2	I	**6c**	60	480	96
4-Me	Br	**6d**	90	445	89
3-NO_2	I	**6e**	90	425	85
4-MeO	Br	**6f**	120	450	90
4-Ethyl	Br	**6g**	120	430	86
2-MeO	Br	**6h**	120	405	81

[a] Reaction condition: aryl halides (1.0 mmol), phenylacetylene (1.2 mmol), NaOAc (2.0 mmol), catalyst-1-MC (0.2 mol%), H_2O/EtOH (5.0 mL, 1:2) at 50 ^{o}C. [b] Isolated Yield. [c] Turn Over Number.

3.2.2. Reusability Test

This study focuses on the development of a diverse nano catalyst that possesses the capacity to be utilized repeatedly in numerous sequential reactions. Therefore, following the successful execution of the initial Suzuki model reaction, the magnet was positioned on the exterior surface of the

reaction vessel (as shown in Fig. S9b) to separate the catalyst from the mixture. Subsequently, the reaction mixture was easily poured out by decantation. Subsequently, the substance underwent a thorough cleansing process using water and ethanol (30 mL) thrice to eliminate any remaining initial substances. Following this, it was subjected to drought for the duration of 12 hours at a temperature of 80 ^{o}C in a vacuum oven. Subsequently, the catalyst was employed in a sequence of five model reactions in succession. As depicted in Fig. 5, the data indicates that the catalyst's effectiveness does not diminish significantly even after being utilized six times, resulting in a still favorable production yield (93%) during the sixth experiment. These observations confirmed that the Pd NPs have a strong connection on the surface of the catalyst and the latter can still catalyze the reaction after several cycles. However, we speculate that due to the mixing of the catalyst with organic precursors and then the agglomeration of NPs after each reaction caused intra-particle rearrangements resulting in some catalyst active surface blockages, leading to about 6 % decrease in catalyst activity after six times use.

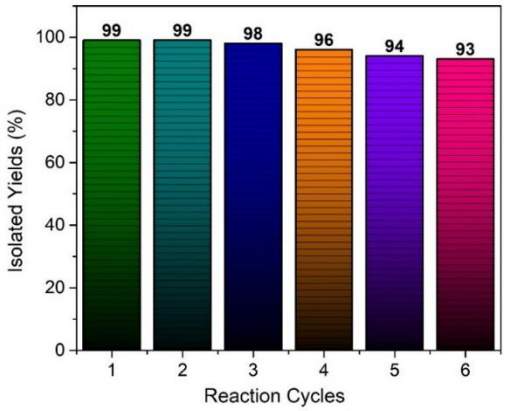

Fig. 5 The catalyst's reusability assessed for a model reaction.

3.2.3. Hot Filtration Test

Due to the dispersion of the catalyst in solution during the reaction, some Pd NPs may separate from the catalyst's surface. In order to assess this matter and ensure the consistent performance of Pd NPs, an experiment known as the hot filtration test was conducted to examine their catalytic stability and potential release. The model reaction was performed in the presence of 0.2 mol% of catalyst-1-MC, EtOH/H_2O as solvent and at room temperature. Following 15 minutes of initiating the reaction (resulting in a conversion of 50%), the experiment was halted, and the catalyst was

extracted from the reaction by putting an external magnet on the reaction vessel wall. Then, the reaction was resumed for another 15 minutes. We made the observation that the reaction cannot proceed without the catalyst, and it indicated that no leaching of Pd NPs occurred during the reaction. In addition, the reaction mixture was analyzed by ICP to detect possible leaching of Pd NPs, but no palladium element had been detected. These results are in agreement with the reusability tests and indicated the strong connection and immobilization of Pd NPs onto the MON shell materials.

3.2.4. Catalyst Stability Test

The prepared catalyst offers a major benefit through its distinctive properties as a heterogeneous and magnetic substance, facilitating easy removal from the reaction mixture and enabling its utilization in multiple subsequent reactions. As a result, once the reaction was finished, the catalyst was separated from the mixture using a magnet and purified by rinsing it three times with ethanol and water (30 mL each). Afterwards, it was dried in a vacuum oven at 80 ^{o}C for 12 hours. Then, it was characterized by HR-TEM, PXRD and ICP. As can be seen in Fig. 6a, the TEM image of reused catalyst-1-MC is alike to the fresh catalyst-1. Similarly, PXRD pattern of reused catalyst-1-MC was the same as that of the fresh one, and the palladium peaks at 2Θ = 40.5, 46.3 and 67.8 are present in PXRD pattern. ICP technique was the last analysis of the reused catalyst-1-MC to detect the Pd content. According to ICP analysis, the quantity of palladium in the reused catalyst (12.34 wt%) is almost identical to that found in the fresh catalyst. This finding provides evidence that palladium nanoparticles remain firmly attached to the MON materials' surface, and there is only a minimal variance of 0.2% between the fresh and reused catalysts.

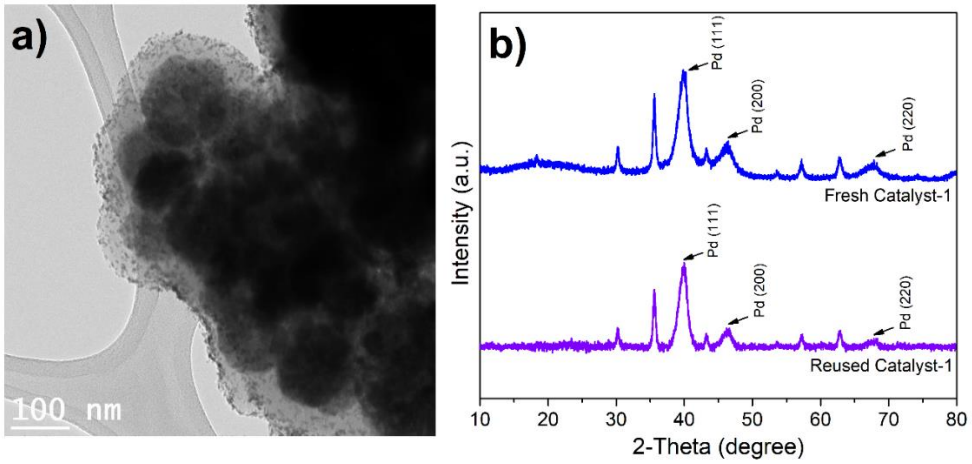

Fig. 6 HR-TEM image of reused catalyst-1-MC (a), PXRD patterns of fresh and reused catalyst (b).

3.2.5. Analyzing Catalyst Performance: A Comparative Study

In this section, we compared the obtained catalytic activities with some of the recently published papers based on Pd NPs immobilized on covalent organic frameworks (COFs) with similar structures to our designed catalyst (Table 4). It can be observed that the current catalyst is able to expedite the creation of biaryl **3a** within a very short timeframe of only 30 minutes. This remarkable speed in synthesis surpasses that of other catalysts, which typically require 60 to 300 minutes. Additionally, the output of the reaction using catalyst-1-MC demonstrates a greater yield in comparison to the majority of alternate catalysts (Table 4, entries 1-3 and 5-7). In addition, our catalyst can catalyze the synthesis 3a with only 0.2 mol% of catalyst, less than required in other reports (0.5 mol%). Also, we used the mixture of H_2O/EtOH as a green solvent in room temperature, ecologically and energetically better compared to DMF, THF, *p*-xylene and toluene (Table 4, entries 2-5). On the other hand, it is worth mentioning that our designed catalyst is not comparable with other catalysts with core-shell structures like Fe_3O_4@SiO_2-Pd(0) and all conditions including time of the reaction, temperature, solvent and even yield is improved (Table 4, entry 8 and 9).

Table 4. Comparison of catalyst-1-MC with other catalysts for the synthesis of biaryl **3a**

Entry	Catalyst (mol%)	Condition	Base	Temp. (°C)	Time (min)	Yield (%)[a]	Ref.
1	Pd@COF-NHC (0.5)	H_2O/EtOH	K_2CO_3	25	300	94	[190]
2	Pd/COF-LZU1 (0.5)	*p*-xylene	K_2CO_3	150	180	96	[191]
3	Pd-TAPB-BTCA (0.5)	THF	K_2CO_3	80	120	90	[192]
4	Pd@3D-COF (0.3)	DMF/H_2O	K_2CO_3	70	120	99	[178]
5	Pd/H_2P-Bp-COF (5.0)	toluene	K_2CO_3	110	90	98	[193]
6	Pd/Cy-pip (0.5)	H_2O/EtOH	K_2CO_3	110	60	88	[194]
7	Pd/COF-SMC_2 (0.5)	EtOH	Cs_2CO_3	80	60	96	[184c]
8	Fe_3O_4@SiO_2-Pd(0) (0.75)	IPA	K_2CO_3	80	360	98	[177]
9	Fe_3O_4@SiO_2-Pd(II) (0.5)	EtOH	K_2CO_3	80	180	98	[195]
10	**Catalyst-1-MC (0.2)**	**H_2O/EtOH**	**K_2CO_3**	**25**	**30**	**99**	**---**

[a] Isolated Yield

4. Conclusion

This study introduces a novel nano heterogeneous catalyst that involves the even attachment of Pd NPs onto the exterior of core-shell magnetic microporous materials. According to the XPS, TEM and PiFM analyses, the bigger Pd NPs (more than 2 nm) are on the surface of MON materials by chelation of the Pd NPs with the amine functional groups and the smaller ones (less than 2 nm) were inserted into the cavities of MON shell materials. The prepared nano magnetic catalysts were able to catalyze the Sonogashira and Suzuki cross-coupling reactions in mild conditions, green solvents with good to excellent yields. The outcomes exhibited that the catalyst with smaller Pd sizes and medium concentration has better performance to catalyze the C-C formation compared to catalyst with bigger Pd sizes and low and high Pd concentrations. Furthermore, the catalyst's magnetic characteristics and durability enable convenient extraction from the reaction mixture, permitting multiple reuses in subsequent reactions without significantly compromising the product's output.

Author Contributions

The manuscript was written through contributions of all authors. All authors have given approval to the final version of the manuscript.

Supporting Information

The Supporting Information is available free of charge athttps://pubs.acs.org.

Additional TEM, TEM mapping images, and EDX spectra of the prepared materials to confirm the size and morphology of the materials; pore size distributions of all samples; magnetization curves of the samples at room temperature; tables related to screen of the reaction conditions for the Suzuki and Sonogashira cross-coupling reactions.

Acknowledgments

This work was supported by Natural Science and Engineering Research Council of Canada (NSERC), the Canada Research Chairs program (CRC) and Canada Foundation for Innovation. We acknowledge all the characterization centers including NanoQAM, QCAM and LCM.

Funding Sources

This research was funded by NSERC, Canada Research Chair and CFI Canada.

4.3 Informations complémentaires

Les informations complémentaires relatives aux procédures expérimentales et aux caractérisations sont disponibles dans l'annexe C et sur le site web.
https://pubs.acs.org/doi/full/10.1021/acsanm.3c02990.

4.4 Contribution des auteurs pour cette étude

The first author of this article, who is also the author of this thesis, performed most of the synthesis and characterizations.
The second author, Hichem Gamraoui, assisted us in the synthesis of some starting materials and products.
The third author, Maziar Jafari, assisted us in PiFM analysis.
The fourth author, Zhiyuan Peng, assisted us in the interpretation of some analysis.
The fifth author, Professor Farid Moeinpour, assisted us in the interpretation of some analysis.
The corresponding author, Professor Mohamed Siaj, contributed to the manuscript and the submission process.

CHAPITRE 5
RÉSEAUX ORGANIQUES MICROPORUEUX MAGNÉTIQUES À COQUE DÉCORÉS PAR DES NANOPARTICULES DE CU POUR LA RÉACTION DE FIXATION DU CO2

5.1 Introduction

Dans la dernière section de ce projet, un réseau organique mésoporeux magnétique à coquille-core (MONs) a été préparé, et après l'immobilisation de nanoparticules de cuivre à sa surface et une caractérisation complète, il a été testé en tant que nanocatalyseur hétérogène pour la synthèse de différents carbonates via la réaction de fixation du CO_2.

5.2 Article publié pour cette étude

Core-shell magnetic microporous organic networks decorated by Cu nanoparticles for CO_2 fixation reaction, Microporous and Mesoporous Materials. 2023, 360, 112729.
https://www.sciencedirect.com/science/article/abs/pii/S1387181123003050.

Core-Shell Magnetic Microporous Organic Networks Decorated by Cu Nanoparticles for CO_2 Fixation Reaction

Amir Khojastehnezhad[a], Maryam Rajabzadeh[b], Maziar Jafari[a], Farid Moeinpour[c], Reza Khalifeh[b], Jacques Huot[d], Dongling Ma[e] and Mohamed Siaj[a*]

[a]Department of Chemistry, University of Quebec at Montreal, Montreal, QC H3C3P8, Canada

[b]Department of Chemistry, Shiraz University of Technology, Shiraz, 71555-313, Iran

[c]Department of Chemistry, Bandar Abbas Branch, Islamic Azad University, Bandar Abbas, Iran

[d]Institut de Recherche sur L'hydrogène, Université du Québec à Trois-Rivières, 3351 Boul. des Forges, Trois-Rivières, QC G9A 5H7, Canada

[e]Institut National de la Recherche Scientifique(INRS), Centre Énergie Materiaux et Télécommunications, 1650 Boul. Lionel-Boulet, Varennes, Québec J3X 1P7, Canada

Abstract

In this research, a core-shell magnetic (Fe_3O_4, MNP) microporous organic network (MON) was first prepared, then Cu nanoparticles (NPs) were uniformly immobilized on the surface of the MON shell material. According to XPS and XRD analyses, the copper NPs are composed of metallic and oxide (CuO/Cu_2O) components. TEM analysis showed that the size of the spherical $Cu/CuO/Cu_2O$ NPs immobilized on the MON surface is below 5 nm in diameter. XPS and photo PiFM analyses

confirmed Cu NPs' chelation by the amine groups on the surface of MON materials. MON-Cu/CuO/Cu_2O as a heterogeneous nanocatalyst was tested for the synthesis of different carbonates *via* the CO_2 fixation reaction. These compounds were successfully synthesized through the direct reaction between different epoxides and 0.5 MPa CO_2 with yields up to 95 %, in solvent-free conditions and with noticeable improvement in reaction times, reaching completion in as fast as 60 minutes.

Keywords: Microporous organic network; nanocatalyst; CO_2 fixation; CuO/Cu_2O; core-shell;

1. Introduction

Atmospheric CO_2 concentrations have significantly increased due to intensive fossil fuel combustion and caused serious global warming.[196] Although environmentally hazardous, CO_2 is an affordable, safe, and renewable resource for making valuable chemicals.[197] Gas phase CO_2 is thermodynamically stable and kinetically inert. It is, thus, less efficient as a potential starting reagent for chemical synthesis due to its inherent thermodynamic stability.[198] An astute strategy to overcome this limitation is to couple CO_2 with energetic reactants in the presence of a catalyst, which would decrease the kinetic barriers of the reaction.[199] Various high-energy chemicals, like CH_4,[200] H_2,[201] epoxides and more,[202]are used to catalyze the conversion of CO_2. Using epoxides as starting materials is particularly interesting to study the catalytic conversion of CO_2 into cyclic carbonates due to their high value-added and atom-efficient nature.[203] In addition to consuming the greenhouse gas by using them as a building block, cyclic carbonates promote environmental well-being by proposing green solvent alternatives to current commonly used solvents and substituting toxic reactants.[204] There are several ways to produce five-membered cyclic carbonates. Among these methods, the following can be mentioned: direct reaction of ethylene oxide groups with CO_2,[205] reaction of alkali metal carbonates with ethylene oxide,[206] oxidative carboxylation of alkenes,[207] and electrochemical CO_2 cycloaddition with epoxides.[208] A more common method involves reacting ethylene oxide with CO_2 at atmospheric and high pressures. This method can be applied easily and is highly effective for obtaining multifunctional cyclic carbonates from multifunctional epoxy resins.[206a] Since carbon dioxide is chemically inert, obtaining cyclic carbonates requires a catalytic system. Thus, a highly efficient and reusable catalyst is still needed to chemically stabilize carbon dioxide. Heterogeneous catalysts are attractive alternatives due to recovery, stability, reusability and compliance with green chemistry.[209] In this regard, a wide variety of heterogeneous catalysts have been reported,[210] including the use of

magnetic nanomaterials for fast separation and multiple recycling methods.[161, 211] Magnetic porous nanomaterials are widely used in many fields of catalysis and adsorption for their unique properties, including their stable porous structure, large surface area, and tunable pore sizes.[212] An emerging class of porous materials, microporous organic networks (MONs), are formed through the Sonogashira coupling of aromatic alkynes and halides.[166, 213] MONs as a novel class of microporous materials, have a large surface area, excellent solvent and thermal stability, tunable porosity, and a wide range of functions.[159] Palladium and copper were used as catalysts to construct MONs from alkyne-containing monomers and aryl halides. The three common methods to synthesize MONs are refluxed synthesis, Cu-free solvothermal synthesis, and stirring synthesis at room temperature.[213-214] Hence, in this study, the magnetic core-shell MON materials were first prepared, and then their surfaces were covered uniformly with Cu-based NPs (metallic Cu and copper oxides) to obtain a nanoheterogeneous magnetic copper catalyst (MNP@MON-Cu/CuO/Cu_2O) (Scheme 1). Thorough characterization of the MNP@MON-Cu/CuO/Cu_2O catalyst led to a new level of morphological observations and to understanding the reasons for efficient catalysis. TEM and EDX characterization showed a dense metal oxide core covered by a clear organic shell, in addition to revealing sub-5 nm Cu/CuO/Cu_2O speckles uniformly immobilized on the shell material, further supported by XRD analysis. The inclusion of Cu NPs was also observed by the decrease in porosity in a comparative BET experiment. XPS and PiFM brought insight into the chemical constitution of the catalyst and allowed assessing the effect of Cu NPs chelation spectroscopically. When the nanoheterogeneous materials were used to synthesize different carbonates via the CO_2 fixation reaction, the resulting MNP@MON-Cu/CuO/Cu_2O catalyst showed good to excellent results through a direct reaction between different epoxides and carbon dioxide gas, without the need to supplement with solvents and in notably fast reaction times.

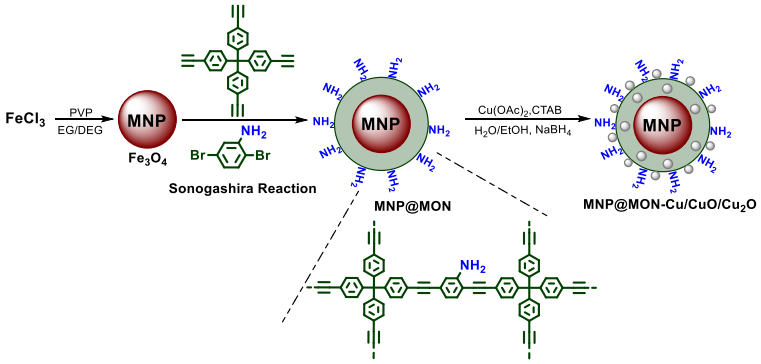

Scheme 1. Catalyst preparation (MNP@MON-Cu/CuO/Cu_2O).

2. Experimental Section

2.1. Materials

Chemicals were listed as follows: tetrakis(4-ethynylphenyl)methane ($C_{33}H_{20}$, 98% purity, TCI America), 2,5-dibromoaniline ($C_6H_5Br_2N$, 98% purity, Sigma-Aldrich), bis(triphenylphosphine)palladium(II) dichloride ($Pd(PPh_3)_2Cl_2$, 98% purity, Sigma-Aldrich), iron(III) chloride hexahydrate ($FeCl_3$ $6H_2O$, 98% purity, Sigma-Aldrich), hexadecyltrimethylammonium bromide ($CH_3(CH_2)_{15}N(Br)(CH_3)_3$, 98% purity, Sigma-Aldrich), copper(II) acetate ($Cu(CH_3COO)_2$, 98% purity, Sigma-Aldrich), sodium borohydride ($NaBH_4$, 98% purity, Sigma-Aldrich). All chemicals were used without any further purifications.

2.1.1. Material Characterization

The crystalline phases and structures of the as-obtained samples were measured via X-ray diffraction (XRD) with Cu Kα radiation (Bruker D8 advance, Billerica, MA, USA). X-ray photoelectron spectroscopy (XPS) for surface compositions and states was performed on an XPS PHI 5600-ci (Physical Electronics, Eden Prairie, MN, USA). A field-emission scanning electron microscope (FESEM, JSM7600F, JEOL, Akishima, Tokyo, Japan) was used to characterize the microstructures and morphologies of the as-obtained samples. Transmission electron microscopy (TEM) and high-resolution TEM (HRTEM) images were obtained on a JEOL JEM-2100F (JEOL) along with the energy-dispersive spectroscopy (STEM-EDX) (Oxford Instruments, Abingdon, Oxfordshire, UK). Further morphology and spectroscopy characterization was carried out by photo-induced force microscopy (PiFM) (VistaScope, MolecularVista.Inc, California, USA) by simultaneously measuring topography and assigning chemical identities to observed high-resolution features measuring less than the diffraction limit of light. The FT-IR analyses were performed with a Nicolet 6700 spectrometer with a smart iTR module from company Thermo Scientific**.** Thermogravimetric analysis (TGA Q500 from TA Instruments company), was carried out from room temperature to 800 ^oC at a heating rate of 10 ^oC min^{-1} and a N_2 flow rate of 20 mL min^{-1}. Besides, the BET measurements were utilized to find the surface area of the samples. The Nitrogen adsorption-desorption analyses were performed at 76.5 K with a TMAX-BSD-PM2 from TMAXCN company (China). Inductively coupled plasma optical emission spectrometry (ICP-OES) analysis was performed with Agilent machine (model 5100) using radial mode.

2.2. Methods

2.2.1. Synthesis of Core-Shell Magnetic MNP@MON

The Fe_3O_4 magnetic NPs were prepared according to literature.[95] Then, the synthesis of core-shell magnetic MON was performed according to the following method: the Fe_3O_4 NPs (100 mg) and toluene (7.5 mL) were mixed and sonicated for 15 min and afterwards, triethylamine (7.5 mL), CuI (0.50 mg, 2.6 μmol) and $Pd(PPh_3)_2Cl_2$ (1.7 mg, 2.4 μmol) were added to the mixture in a 100 mL three-necked flask. The mixture was mechanically stirred for 60 min (500 rpm) at 90 °C. Then, 2,5-dibromobenzenamine (30.1 mg, 0.12 mmol) and tetrakis(4-ethynylphenyl)methane (25.0 mg, 0.06 mmol) were added to the previous mixture under mechanical stirring. The stirring continued at the same temperature for an extra 5 h. After reaction completion the temperature was decreased to 25 ^oC, the core-shell magnetic MON were separated by an external magnet, washed three times with methanol, dichloromethane and water and dried in a vacuum oven at 100 ^oC for 24 h to obtain the final product.

2.2.2. Synthesis of Core-Shell Magnetic MNP@MON-Cu/CuO/Cu_2O

To synthesize Cu NPs (Cu/CuO/Cu_2O) immobilized on MNP@MON materials, 25 mg of MNP@MON materials were dispersed in a mixture of ethanol and water (10:10 mL) for 30 min in ultrasound. Then, a solution of copper acetate (12.5, 25 and 50 mg, low, medium and high Cu concentration), hexadecyltrimethyl ammonium bromide (5, 10 and 20 mg), sodium hydroxide (2.5, 5 and 10 mg) and water (2.5, 5 and 10 mL) was added under mechanical stirring at 60 ^oC. Afterwards, a solution of sodium borohydride (5, 10 and 20 mg) in water (5, 10 and 20 mL) was added dropwise (30 min) at 60 ^oC. Next, the mixture was transferred to a stainless-steel autoclave and heated in an oven for 12 h at 160 ^oC. Finally, it was cooled to room temperature, washed with water (three times) and dried at 80 ^oC for 24 h to obtain the final product (MNP@MON-Cu/CuO/Cu_2O).[215]

2.2.3. General Procedure for the Synthesis of Carbonate Derivatives

A high pressure stainless steel batch reactor was used and an epoxide (10 mL) was added to the reactor followed by the MNP@MON-Cu/CuO/Cu_2O (3 mg) and tetrabutyl ammonium bromide (5.0 mmol). The reactor was heated to 90 ^oC. The reaction was performed at the appropriate durations (Table 2) under 0.5 MPa CO_2. After, the stainless-steel reactor was cooled to room temperature and carbon dioxide gas was vented gradually. Finally, ethyl acetate was poured to the reaction mixture to dissolve the substances and the magnetic catalyst was separated from the

reaction mixture by an external magnet. To remove the co-catalyst, water was added to the remaining reaction mixture. Consequently, the organic layers were separated by a decanter funnel and dried with sodium sulfate. Column chromatography (ethyl acetate/hexane) was utilized to purify the final carbonate derivatives.

3. Results and Discussion

Nanoheterogeneous magnetic copper catalysts (MNP@MON-Cu/CuO/Cu_2O) have been designed according to the following synthetic steps. Firstly, the magnetic MON materials were prepared according to the literature,[176] then Cu NPs (metallic Cu and copper oxides (CuO/Cu_2O)) were immobilized on the surfaces of the MON materials by chelation of the Cu NPs with the amine functional groups (Scheme 1). After, the core/surface morphologies and chemical structure of the catalyst have been fully characterized by various techniques, including FT-IR, HR-TEM, TEM, SEM, EDX, ICP, TGA, XPS, BET, PiFM, and XRD.

3.1. Catalyst Characterization

3.1.1. TEM and SEM analyses

Electron microscopy was used to confirm the morphology and the size of the prepared nanomaterials. According to the TEM (Fig. 1a) and SEM (Fig. 1b) images, Fe_3O_4 MNPs are spherical. Fig. 1c (TEM) and Fig. 1d (SEM) show that the core-shell structures of MNPs after coating with MON materials are also spherical.[176] Fig. 1e, Fig. 1f and Fig. S1 confirm the uniform immobilization of Cu/CuO/Cu_2O spherical NPs (less than 5 nm in diameter) on the surface of MON shell materials. Based on XPS and PiFM analyses, Cu based NPs are linked to the MON's amine groups. Additionally, the TEM mapping image (Fig. 1g and S2) exhibits the elemental analysis of the prepared catalyst. Cu, in addition to Fe, O, C, and N confirms the successful immobilization of Cu NPs on the MON's surface. The EDX spectrum (Fig. S3) of the catalyst confirms the existence of C, Fe, O, N and Cu with wt% of 18.4, 54.9, 20.7, 1.1 and 4.9, respectively which agrees with the TEM mapping images and ICP observations. Inductive coupled plasma (ICP) has provided the exact amount of Cu in the sample. According to the ICP analysis, the amount of copper in the final catalyst (MNP@MON-Cu/CuO/Cu_2O) with different Cu concentrations (low, medium and high) is 3.38, 5.22 and 11.40 wt%, respectively. It is worth mentioning that the ICP analysis of the reused catalyst (after five times) with medium Cu concentration was approximately similar to the fresh catalyst (5.14 wt%), which confirms no leaching of Cu happening during the CO_2 fixation reaction.

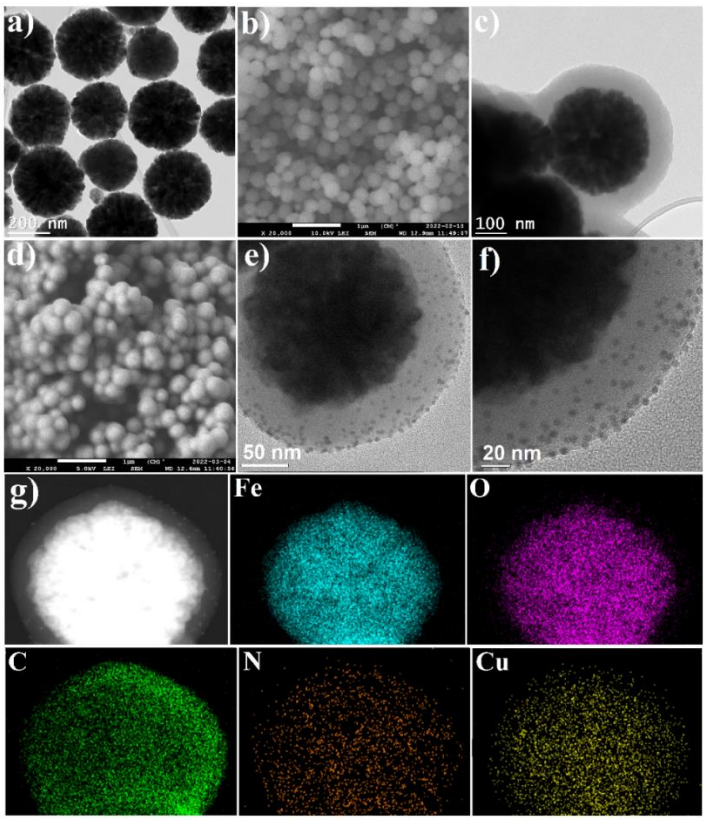

Fig. 1. TEM and SEM images of Fe_3O_4 MNP (**a** and **b**), MNP@MON (**c** and **d**), TEM image of MNP@MON-Cu/CuO/Cu_2O (**e** and **f**), and TEM mapping of MNP@MON-Cu/CuO/Cu_2O (**g**).

3.1.2. XRD analysis

Another technique to evaluate the crystal structure of the synthesized material is XRD analysis. As shown in Fig. 2, the XRD analysis has been performed for all prepared materials: Fe_3O_4 MNPs, MNP@MON and MNP@MON-Cu/CuO/Cu_2O NPs. XRD of iron oxide MNPs (Fig. 2, black pattern) exhibits six characteristic peaks at 2Θ = 30.09, 35.5, 43.0, 53.2, 57.2 and 62.11 corresponding to the (2 2 0), (3 1 1), (4 0 0), (4 2 2), (5 1 1) and (4 4 0) crystal planes of the cubic phase of Fe_3O_4 (JCPDS card No. 19–0629).[102] The XRD pattern of MNP@MON materials shows a relatively broad peak at around 15 to 25^o that is in agreement with the amorphous nature of MON materials (Fig. 2, red pattern).[180] In the XRD pattern of MNP@MON-Cu/CuO/Cu_2O (Fig. 2, blue pattern), there are new peaks assigned to Cu NPs (2Θ = 43.3 (1 1 1), 50.5 (2 0 0) and 74.8 (2 2 0), JCPDS file no. 04-0784),[216] CuO NPs (2Θ = 38.9 (0 0 2), 49.0 (2 0 2) and 53.6 (0 2 0), JCPDS file no. 48-1548) [217] and Cu_2O NPs (2Θ = 36.4 (1 1 1), 42.3 (2 0 0) and 61.3 (2 0 0), JCPDS file no. 05-0667).[218] Besides, the size of different copper NPs including CuO, Cu_2O and metallic Cu

were calculated by Scherrer equation from PXRD results and they were 4.56, 5.83 and 7.6 nm, respectively that are in agreement with TEM analysis. These peaks confirm the successful inclusion of metallic copper and copper oxides (CuO/Cu_2O) on the core-shell MON materials and this is in accordance with other analyses.

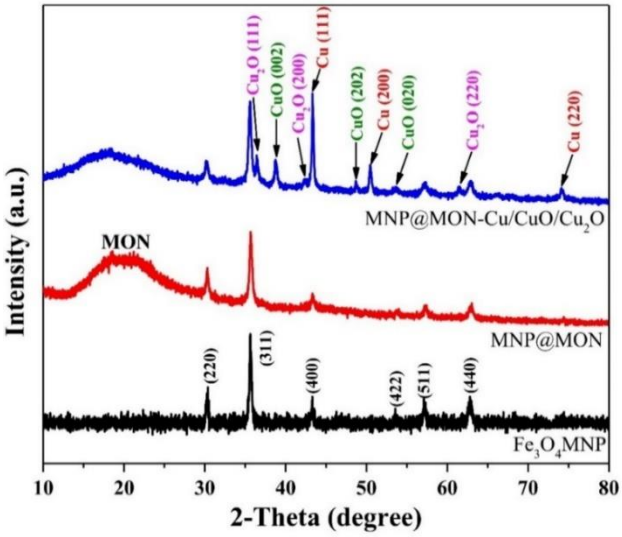

Fig. 2. XRD patterns of Fe_3O_4 MNP, MNP@MON and MNP@MON-Cu/CuO/Cu_2O.

3.1.3. TGA analysis

TGA analysis has been conducted to confirm the chemical and thermal stability of the materials. As depicted in Fig. S4 (black curve), Fe_3O_4 MNPs have a stable chemical structure and only 4% weight loss at around 600 ^oC attributed to the removal of hydroxyl functional groups on the MNPs. MON shell material in MNP@MON (Fig. S4, blue curve) showed thermal stability up to 400 ^oC with about 20% weight loss.[219] The final TGA curve (Fig. S4, red curve) related to MNP@MON-Cu/CuO/Cu_2O is similar to the previous one with about 2% more weight loss which could be assigned to the Cu NPs decorated onto the MON shell materials.

3.1.4. XPS analysis

To further elucidate the elemental composition, the density of the electronic states in the materials and the overall electronic structure and bonding, XPS analysis of MNP@MON and MNP@MON-Cu/CuO/Cu_2O are provided. As shown in Fig. 3a, after the immobilization of Cu NPs on the MNP@MON, new peaks that could be assigned to Cu/CuO/Cu_2O appeared (black spectrum). In the high-resolution XPS spectrum of Cu 2p, different oxidation states of Cu at around 930 to 965 eV were observed (metallic Cu, CuO and Cu_2O) that confirm the existence of Cu/CuO/Cu_2O in the

final catalyst (Fig. 3b).[220] In the case of CuO, the double peaks with binding energies of 934.9 and 955.2 eV were attributed to the Cu^{2+} 2p3/2 and Cu^{2+} 2p1/2, respectively, and showed the different chemical states of CuO NPs. On the other hand, there are two main peaks at 933.3 and 953.2 eV ascribed to the Cu^{+} 2p3/2 and Cu^{+} 2p1/2, respectively, which confirmed the successful formation of Cu_2O NPs. According to XPS analysis, Cu^{2+} 2p3/2 (CuO) has 2% atomic in addition to 0.7% and 0.6% for SU1 and SU2 shake up peaks (sum 3.3%) and Cu^{+} 2p3/2 (Cu_2O) has 6% atomic and only very small or no shake up peaks (sum 6%). Moreover, the high-resolution XPS spectrum of N 1s was divided to two peaks at 398.6 and 399.9 eV for MNP@MON and 399.0 and 400.2 eV for MNP@MON-Cu/CuO/Cu_2O, respectively (Fig. 3c and 3d).[176, 221] These chemical shifts demonstrated the chelation between nitrogen of MON materials and Cu NPs and they are in agreement with PiFM analyses.

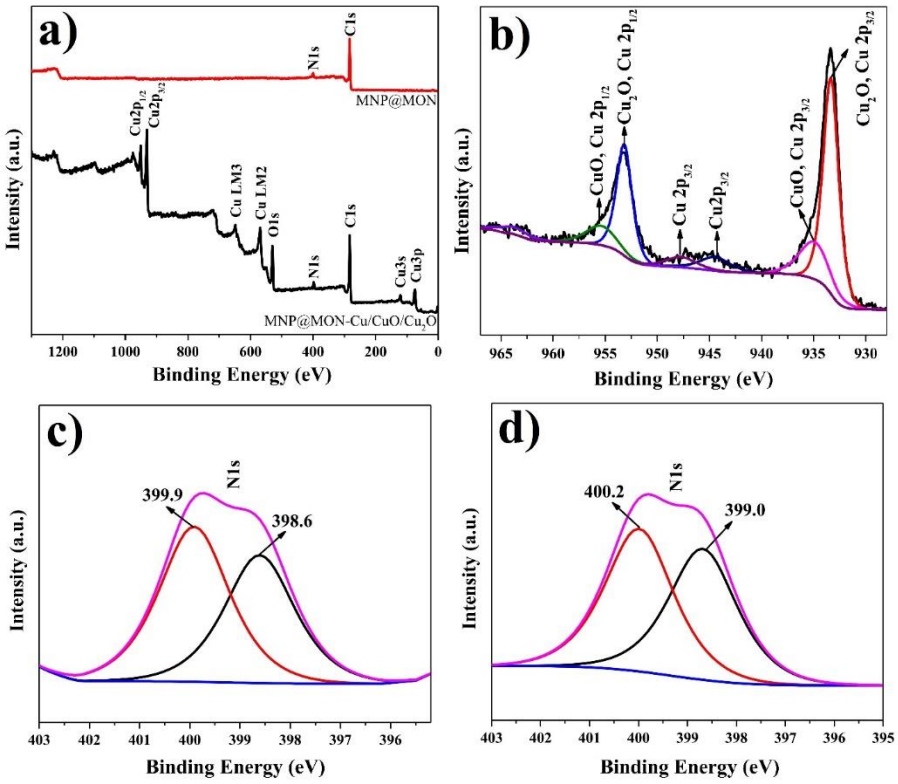

Fig. 3. Full survey XPS spectrum of MNP@MON and MNP@MON-Cu/CuO/Cu_2O (**a**), high-resolution XPS spectrum of Cu2p of MNP@MON-Cu/CuO/Cu_2O (**b**), N1s of MNP@MON (**c**) and N1s of MNP@MON-Cu/CuO/Cu_2O (**d**).

3.1.5. BET analysis

The N_2 adsorption−desorption of samples were investigated, and the results (Fig. 4 and Fig. S5) showed that the Brunauer−Emmett−Teller (BET) surface areas of MNP@MON and MNP@MON-Cu/CuO/Cu_2O were 328.40, and 240.88 m^2/g, respectively (Type IV). This represents about a 30% decrease in BET surface area confirmed by the successful chelation of Cu NPs on the shell materials.[180, 182] In addition, the pore volume and pore size of microporous nanomaterials were seen to decrease. Accordingly, the pore sizes of MNP@MON and MNP@MON-Cu/CuO/Cu_2O were 2.289 and 2.173 nm respectively and pore volumes were 0.1879 and 0.1309 cm^3/g.[176, 222] The pore volume exhibited about a 30% reduction, in agreement with the BET surface area, and these results showed that some smaller Cu NPs are probably inserted to the pores of the MON shell materials and it can led to the shifting the pore size distribution to lower diameters and maybe some minor changes in N_2-adsorption-desorption isotherms (Fig. S5).[180]

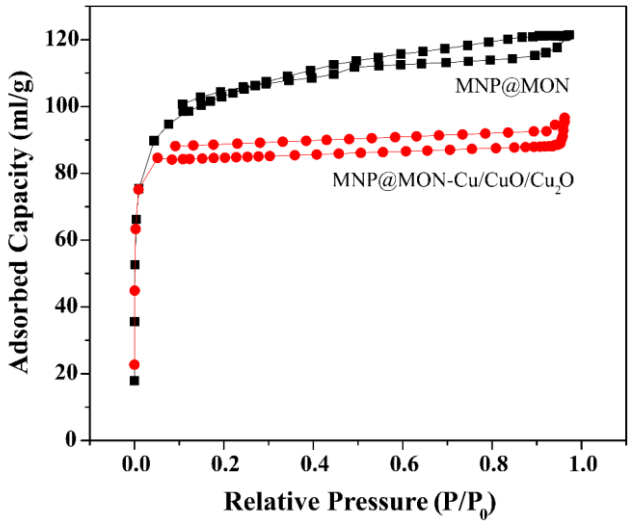

Fig. 4 N_2 adsorption−desorption isotherms of MNP@MON and MNP@MON-Cu/CuO/Cu_2O.

3.1.6. PiFM analysis

Topography images of the MNP@MON powder surface detected by PiFM showed spherical-like particles measuring about 300-500 nm in diameter. On each particle, a core component was slightly more elevated than a shell component. This feature contrasts between the metallic Fe_3O_4 core and the MON shell. The Fe_3O_4 core measured about 200 nm in diameter and the MON shell had a ~100 nm thickness (Fig. 5a). The PiF-IR point spectrum resulted in the same spectroscopic signature of

the MON material as previously reported by FTIR, (Fig. 5b).[176] From ~1000 cm^{-1} to ~1150 cm^{-1}, a strong and broad peak corresponded to the aromatic rings. The aromatic amines were observed as a sharp band at 1259 cm^{-1}. A noticeably sharp and intense peak found at 1511 cm^{-1} was ascribed to the C-N bonds. A medium intense peak appearing on the spectrum in the vicinity of 1600 cm^{-1} was assigned to both aromatic and aromatic-NH_2 vibration modes.[186] When copper-based NPs ($Cu/CuO/Cu_2O$) were immobilized on the surface of MON shell material, some changes occurred in the PiF-IR spectrum. Importantly, the aromatic-NH_2 (1259 cm^{-1}) and the C-N (1511 cm^{-1}) peaks experienced a shift towards higher frequencies (1264 and 1515 com^{-1}, blue shift), which confirmed the copper NPs chelation with amine functional groups.[187] Furthermore, PiFM mapping selective for C-N bonds was conducted on the same topography frame (Fig. 5c). The intensity was in the higher ranges throughout the entire image, signifying that C-N bonds were omnipresent. Accordingly, this justified the fact that the MON material was successfully coating the exterior of the MNPs.

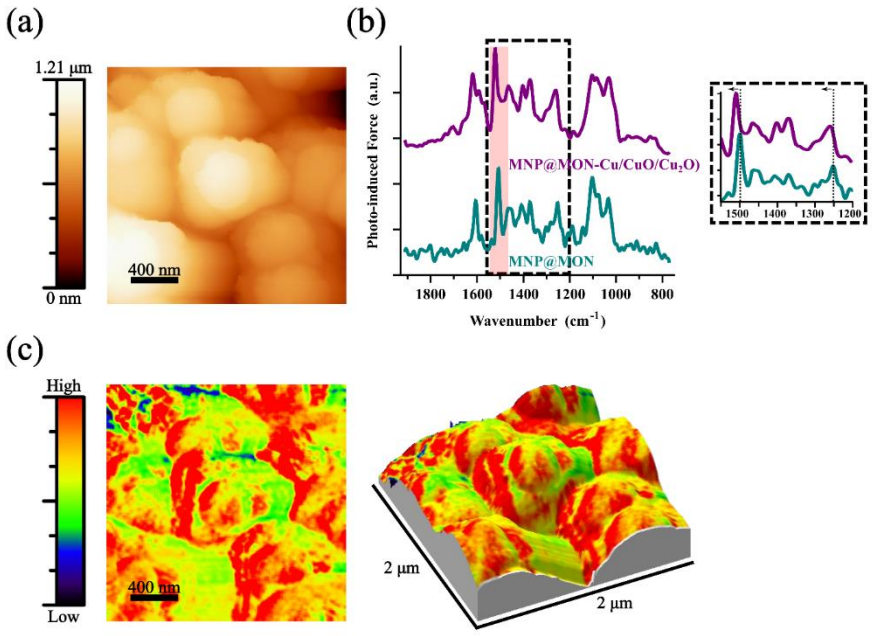

Fig. 5 AFM topography of the as-synthesized MNP@MON (**a**). PiF-IR spectra of MNP@MON and MNP@MON-Cu/CuO/Cu_2O (**b**). The dotted lines indicate the Aromatic-NH_2 and C-N peak shifts. The colored highlight represents the PiFM mapping frequency. Plan view and perspective views of the PiFM mapping selective for the C-N bonds on the same topography frame (**c**). The signal intensity is proportional to the C-N bond content.

3.2. Catalytic Applications

3.2.1. Reaction Condition Optimization

After characterization of the nanoheterogeneous magnetic copper catalyst, the effects of this prepared catalyst on the synthesis of cyclic carbonates have been investigated *via* the CO_2 fixation reaction. On this basis, the reaction between CO_2 and styrene oxide has been chosen as the model reaction. First, the model reaction was carried out in the absence of catalyst (MNP@MON-Cu/CuO/Cu_2O) and co-catalyst (tetra-butylammonium bromide), but no product was observed in this condition (Table 1, entry 1). Consequently, the prepared catalysts with different copper concentrations (low, medium and high) were utilized to catalyze and to find the most favorable reaction conditions (Table 1, entries 2-4). Interestingly, the catalysts with different Cu concentrations (without any co-catalyst) catalyze the reaction with high yields and the catalyst with medium Cu concentration had better results compared to the catalysts with low or high palladium concentrations (Table 1, entries 2-4). Thus, the catalyst with medium Cu concentration was selected as an optimal catalyst. After, in order to optimize the catalyst amount, lower and higher amounts of catalyst with medium Cu concentration was tested to catalyze the model reaction (table 1, entries 5 and 6). We realized that by decreasing the amount of catalyst, yield of the reaction reduced from 80% to 72% (Table 1, entry 5) and by increasing the amount of catalyst, the yield of the reaction did not show significant change (Table 1, entry 6). To improve the yield of the reaction, the next step was the use of a co-catalyst in the model reaction (entries 7-9). The results showed that by adding just 5.0 mol% of co-catalyst (tetra-butylammonium bromide), the yield of the reaction was increased to 92% (Table 1, entry 8). After finding the optimal combination of catalyst and co-catalyst, the effects of different CO_2 pressures (0.1, 0.3, 0.5, and 0.7 MPa) on the model reaction were studied (entries 10-12). The effective amount of the final product was obtained at 0.5 MPa of CO_2 (entry 8) and higher pressures did not have significant effect on the reaction (entry 10). The last step was temperature optimization (entries 13-16). The temperature was also important for running this reaction and the yield of the reaction at room temperature was low (entry 13), while increasing the temperature improved the yield and the highest amount of carbonate was obtained at 90 ^oC (entry 8).

Table 1. Screening of the reaction condition for the synthesis of 4-phenyl-1,3-dioxolan-2-one (**3a**)

Entry	Temperature (°C)	Catalyst (mg. mol%)	Co-Catalyst (mol%)[a]	P (MPa)	Time (min)	Yield (%)[b]	TON/TOF (min^{-1})[c]
1	90	---	---	0.8	120	---	---
2	90	3.0, 0.16[d]	---	0.5	60	49	306/5.1
3	90	3.0, 0.25[e]	---	0.5	60	80	320/5.3
4	90	3.0, 0.54[f]	---	0.5	60	81	150/2.5
5	90	1.0, 0.08	---	0.5	60	72	900/15
6	90	7.0, 0.58	---	0.5	60	82	141/2.4
7	90	3.0, 0.25	2.0	0.5	60	87	348/5.8
8	**90**	**3.0, 0.25**	**5.0**	**0.5**	**60**	**92**	368/6.1
9	90	3.0, 0.25	10	0.5	60	93	372/6.2
10	90	3.0, 0.25	5.0	0.7	60	94	376/6.3
11	90	3.0, 0.25	5.0	0.3	60	86	344/5.7
12	90	3.0, 0.25	5.0	0.1	60	75	300/5.0
13	25	3.0, 0.25	5.0	0.5	60	45	180/3.0
14	50	3.0, 0.25	5.0	0.5	60	62	248/4.1
15	70	3.0, 0.25	5.0	0.5	60	75	300/5.0
16	120	3.0, 0.25	5.0	0.5	60	90	360/6.0

[a] Tetra-butylammonium bromide, [b] Based on isolated yield, [c] Turn Over Number/Turn Over Frequency, [d] Low Cu concentration, [e] Medium Cu concentration, [f] High Cu concentration.

Considering the previous optimization reaction condition, the scope of the reaction has been examined for the different epoxides and in the presence of 0.5 MPa pressure of CO_2 and 3.0 mg of catalyst (Table 2). High yields of the reaction have been obtained for products 3a-i in just 60 min of reaction time, however for products 3j, 3k and 3l, the reaction was carried out during 2 to 3 hours while also returned high isolated yields. The different functional groups of these compounds, compared to products 3a to 3i, are responsible for differing optimal reaction times.

Table 2. Synthesis of cyclic carbonates in the presence of catalyst[a]

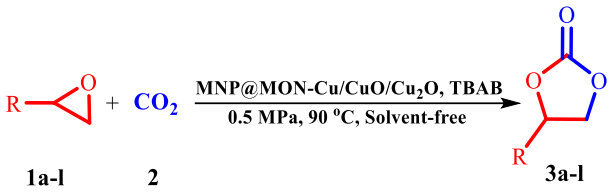

1a-l 2 3a-l

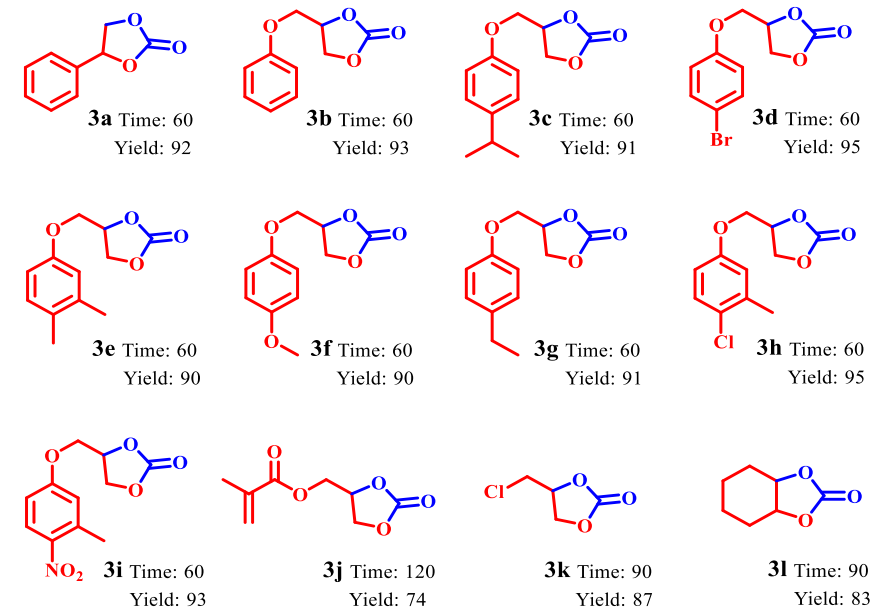

[a] Structures of some of the final products were charchetrized by ^{1}H-NMR and ^{13}C-NMR

3.2.2. Reusability Test, Kinetic Study and Hot Filtration Test

One of the advantages of this catalyst is its ability to be reused in multiple repeated reactions. Therefore, after completion of the first model reaction, the catalyst was separated from the reaction mixture and washed three times with ethyl acetate and acetone (30 mL), then dried in a vacuum oven for 12 h at 80 ^{o}C. It was then used for four repeated model reaction. According to Fig. 6a, there is no considerable decrease in catalytic efficiency after using the catalyst five times, and a high yield of the product was obtained (87%). This analysis showed that the catalyst structure is practically stable and it can still catalyze the reaction after several cycles. To evaluate the catalytic activity, stability and possible leaching of Cu NPs, the Kinetic study and hot filtration test were performed (Fig. 6b). Hence, to study the Kinetic of the CO_2 fixation reaction, the model reaction

has been carried out in the presence of 3.0 mg of MNP@MON-Cu/CuO/Cu_2O at 90 ^oC and 0.5 MPa of CO_2 pressure. As shown in Fig. 6b-1, the conversion of the styrene oxide to cyclic carbonate rapidly increased as a function of reaction time and about 70 % yield of the product was achieved after only 30 minutes. A slower reaction progression led to the maximum product yield achieved after an additional 30 minutes. This observation confirmed the high catalytic activity of Cu NPs immobilized on the magnetic MON. On the other hand, to investigate the hot filtration test, after 30 minutes of running the reaction (50% conversion), the reaction was stopped, the temperature of the reactor was brought to room temperature and carbon dioxide was gradually vented. Then, ethyl acetate was added to the reaction to dissolve all substances. The MNP@MON-Cu/CuO/Cu_2O NPs were removed by an external magnetic field and the residual solvent was removed by a rotavapor. Afterwards, the reaction was resumed for 30 minutes. It was found that without the catalyst, the reaction could not continue, and it revealed that no Cu NPs leaching had happened during the reaction (Fig. 6b-2). Moreover, the reaction mixture was analyzed by ICP to detect Cu, but no copper element had been detected, as expected from the hot filtration test.

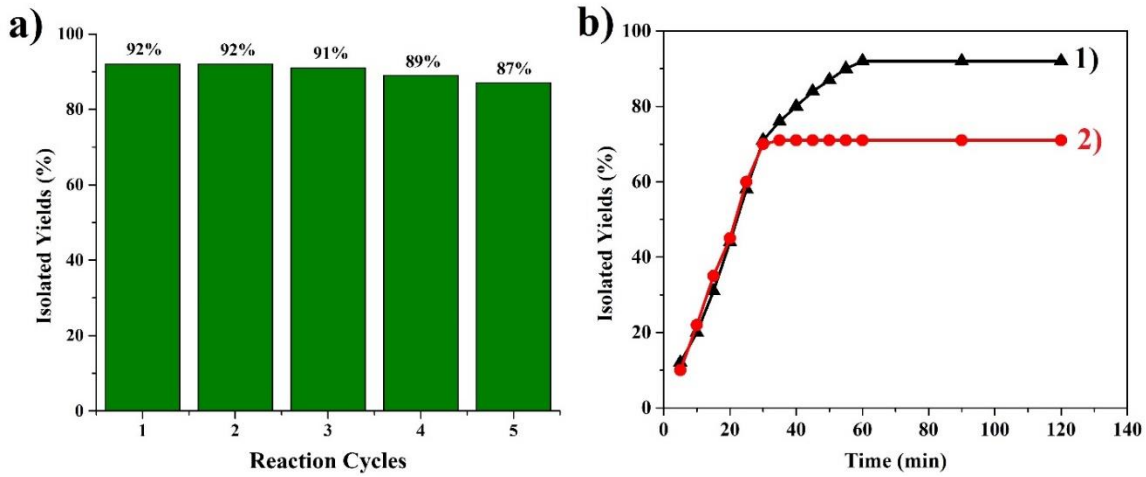

Fig. 6 Reusability test of the catalyst for the model reaction (**a**) and Kinetic diagram for CO_2 fixation reaction catalyzed by MNP@MON-Cu/CuO/Cu_2O NPs without (**b-1**) and with hot filtration test (**b-2**).

3.2.3. Catalyst Stability Test

Additionally, after running the reaction five times, the catalyst had been removed from the reaction mixture and was washed three times with ethyl acetate and acetone (30 mL) to remove any remaining materials. Then, it was placed in an ultrasound bath for 30 minutes, and afterwards, it was characterized with HR-TEM, XRD and FT-IR. As shown in Fig. 7a, the TEM image of reused

catalyst is identical to the fresh catalyst and Cu NPs are still uniformly immobilized on the surface of MON materials. Also, based on Fig. S6 and Fig. 7b related to FT-IR and XRD, respectively, the FT-IR spectrum and XRD pattern of reused catalyst are approximately same to the fresh ones, and all peaks correspond to Cu NPs are present in XRD pattern. The sizes of Cu NPs in the reused catalyst were calculated by Scherrer equation from PXRD results and they approximately were similar to the fresh catalyst to be 4.49, 5.88 and 7.9 nm, respectively. These findings confirm the strong connection between Cu NPs and amine groups on the surface of MON shell materials or the deeply inserted into the microporous MON materials pores, the Cu NPs strongly linked on the surface of MON materials and no leaching of Cu NPs after reusing the catalyst. So, there are no significant differences between the fresh and reused catalysts.

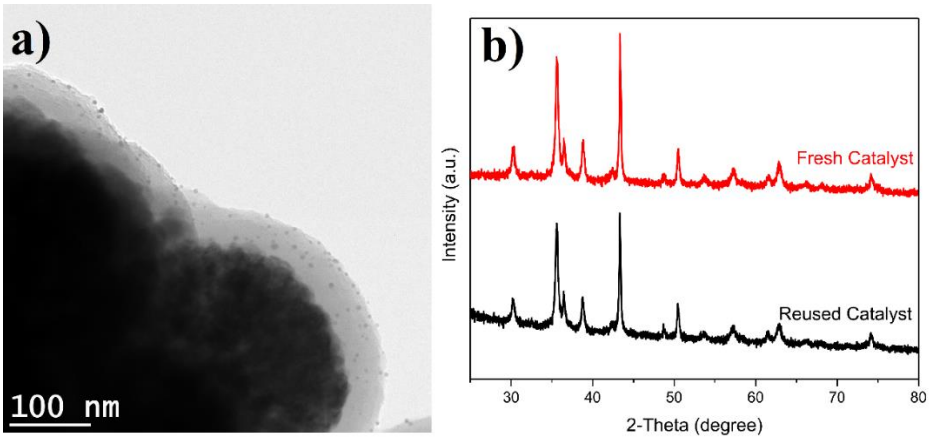

Fig. 7 HR-TEM image of reused MNP@MON-Cu/CuO/Cu_2O NPs after five reaction runs (**a**), XRD patterns of fresh and reused catalyst (**b**).

3.2.4. Proposed Mechanism

According to the results mentioned in Table 1 (entries 2–8), it is worth mentioning that the CO_2 fixation reaction can be carried out both in the absence and presence of the co-catalyst (TBAB). Thus, in accordance with previous studies,[102, 205b] two types of possible mechanisms illustrate the preparation of cyclic carbonates by MNP@MON-Cu/CuO/Cu_2O. In the first mechanism, the copper sites act as Lewis acid catalysts to activate the epoxide by coordinating oxygen.[223] Then, the bromine derived co-catalyst reacts with the activated epoxide and performs ring opening. The formed negatively charged oxygen makes a nucleophilic attack on carbon dioxide and produces the final carbonate derivatives (Scheme 2a). But in the second mechanism and in the absence of co-catalyst, partially negative oxygen of CO_2 can play the role of co-catalyst and attack to the

Cu(II)-coordinated epoxide,[205b] and generate the final carbonate derivatives (Scheme 2b). As depicted in in both mechanisms, Lewis acid capability of the Cu-catalyst has a significant effect in the progress of the cycling process.

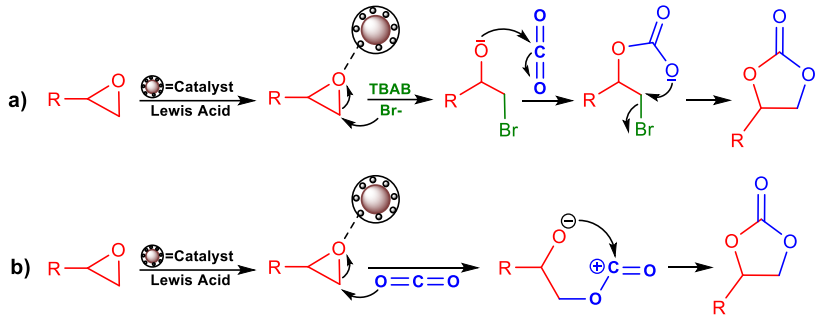

Scheme 2. Proposed mechanism for the synthesis of products in the presence and absence of co-catalyst.

3.2.5. Comparison of Catalyst's Activity

The research concluded with a comparison of the herein catalyst's activity with that of previously reported catalysts (Table 3). This table demonstrates that the present catalyst catalyzes the synthesis of carbonate 3a in only 60 minutes, much faster than other catalysts (3.0 to 48 h). Furthermore, as shown in this table, the yield of the reaction with MNP@MON-Cu/CuO/Cu_2O is higher compared to most other catalysts (entries 1-4 and 6).

Table 3. Comparison of MNP@MON-Cu/CuO/Cu_2O catalyst with other catalysts for the synthesis of styrene carbonate **3a**

Entry	Catalyst (mol%)	Condition	Co-Catalyst (mol%)	Temp. (°C)	Pressure (MPa)	Time (h)	Yield (%)	Ref.
1	Nb_2O_5	DMF	---	135	5	15	80	[224]
2	La-Zr Oxide	DMF	---	130	2.5	3	90	[225]
3	Zn-Mg-Al	TEA	---	140	2.5	3	89	[226]
4	$CuCo_2O_4$ (5.0)	---	TBAI[a] (8.0)	80	2	3	88	[227]
5	MOF (0.5)	---	TBAB (10)	60	0.1	8	99	[228]
6	COF (0.5)	---	TBAB (5.0)	40	0.1	48	88	[229]
7	$CuAl_2O_4$ (5.0)	---	TBAB (0.5)	85	0.3	10	98	[230]
8	**This study (0.25)**	---	**TBAB (5.0)**	**90**	**0.5**	**1**	**92**	---

[a] Tetra-butylammonium iodide

4. Conclusion

In this research, a new copper-based catalyst has been presented by the uniform immobilization of copper NPs including metallic Cu and copper oxides (CuO/Cu_2O) on the surface of core-shell magnetic microporous materials. Owing to the porosity of this material, some small sized Cu NPs were immobilized in the pores and some bigger sized Cu NPs were connected to the amine groups on the surface of MON materials by chelation interactions. This catalyst catalyzed the synthesis of carbonate substituents through the CO_2 fixation reaction in short reaction times and with good to excellent yields. In addition, due to the magnetic properties and stability of the catalyst, it can easily be separated from the reaction mixture and reused many times in the repeated reactions without any considerable decrease in product yield.

Author information

Corresponding Author

*(M. Siaj) E-mail: siaj.mohamed@uqam.ca; Tel: +1 514 987000 # 1921

Declaration of Competing Interest

There are no conflicts to declare.

Acknowledgments

This work was supported by Natural Science and Engineering Research Council of Canada (NSERC), the Canada Research Chairs program (CRC) and Canada Foundation for Innovation. We acknowledge all the characterization centers including NanoQAM, QCAM and LCM.

Funding Sources

This research was funded by NSERC, CRC and CFI Canada.

5.3 Informations complémentaires

Les informations complémentaires relatives aux procédures expérimentales et aux caractérisations sont disponibles dans l'annexe D et sur le site web.
https://www.sciencedirect.com/science/article/abs/pii/S1387181123003050.

5.4 Contribution des auteurs pour cette étude

Le premier auteur de cet article, qui est également l'auteur de cette thèse, a réalisé la plupart de la synthèse et des caractérisations.
La deuxième auteure, le Dr Maryam Rajabzadeh, et la cinquième auteure, le Dr Reza Khalifeh, nous ont aidés dans la synthèse du dérivé de carbonate et dans la réaction de fixation du CO_2.
Le troisième auteur, Maziar Jafari, nous a assistés dans l'analyse PiFM.
Le quatrième auteur, le Professeur Farid Moeinpour, le sixième auteur, le Professeur Jacques Huot, et le septième auteur, le Professeur Dongling Ma, nous ont assistés dans l'interprétation de certaines analyses.
L'auteur correspondant, le Professeur Mohamed Siaj, a contribué au manuscrit et au processus de soumission.

CONCLUSION

En conclusion, les efforts de recherche pluridisciplinaires décrits ci-dessus soulignent une démarche concertée pour relever les défis pressants dans les domaines des sciences environnementales et catalytiques. La première recherche vise à développer un innovant adsorbant magnétique COF fonctionnalisé avec de la thiosémicarbazide pour l'élimination ciblée du mercure. En utilisant une approche de PSM, l'étude améliore la polyvalence des COFs, contribuant à des solutions efficaces pour l'élimination des métaux lourds et renforçant la durabilité dans les processus de traitement de l'eau. La deuxième recherche ouvre la voie à une approche transformative de la synthèse des COFs en utilisant des HPAs Keggin en tant que catalyseurs. S'éloignant des conditions traditionnelles sévères, l'étude met l'accent sur les principes de la chimie verte, atteignant une production rapide, douce et évolutive de COFs 2D et 3D hautement cristallins et poreux. La synthèse de TAPA-TPT, un nouveau COF iminé 2D, démontre en outre les applications potentielles des COFs dans les supercondensateurs, alignées sur des pratiques durables. La troisième recherche se concentre sur le développement d'un nouveau catalyseur nanohétérogène pour la formation de liaisons C-C, ciblant spécifiquement la réaction de Suzuki. L'utilisation de matériaux MON cœur-écorce magnétiques, associés à des nanoparticules de Pd de taille contrôlée, met en évidence l'importance des catalyseurs hétérogènes recyclables et verts, conformément à une synthèse chimique durable et respectueuse de l'environnement. Enfin, la quatrième recherche s'efforce de concevoir et de synthétiser un nanocatalyseur hétérogène pour la fixation du CO_2, contribuant à la production de carbonates précieux. L'objectif principal est de fournir un catalyseur durable et efficace, abordant les préoccupations environnementales et respectant les principes de la chimie verte. Dans l'ensemble, ces recherches contribuent à l'avancement des connaissances, offrant des solutions potentielles à des défis environnementaux et catalytiques complexes tout en promouvant la durabilité et des pratiques respectueuses de l'environnement. À l'avenir, le domaine est prêt à progresser vers des méthodes de synthèse plus efficaces et respectueuses de l'environnement, avec un fort accent sur des matériaux évolutifs, polyvalents et recyclables pour diverses applications environnementales et énergétiques.

ANNEXE A
INFORMATIONS COMPLÉMENTAIRES

Post-Synthetic Modification of Core-Shell Magnetic Covalent Organic Frameworks for the Selective Removal of Mercury

Amir Khojastehnezhad[a], Farid Moeinpour[b], Maziar Jafari[a], Mohammad K. Shehab[c], Ahmad Samih ElDouhaibi[d], Hani M. El-Kaderi[c], and Mohamed Siaj[a*]

[a]*Department of Chemistry, University of Quebec at Montreal, Montreal, QC H3C3P8, Canada*

[b]*Department of Chemistry, Bandar Abbas Branch, Islamic Azad University, Bandar Abbas, Iran*

[c]*Department of Chemistry, Virginia Commonwealth University, Richmond, Virginia 23284, United States*

[d]*Department of Chemistry, Lebanese University, College of Science III, Campus Mont Miche, Lebanon*

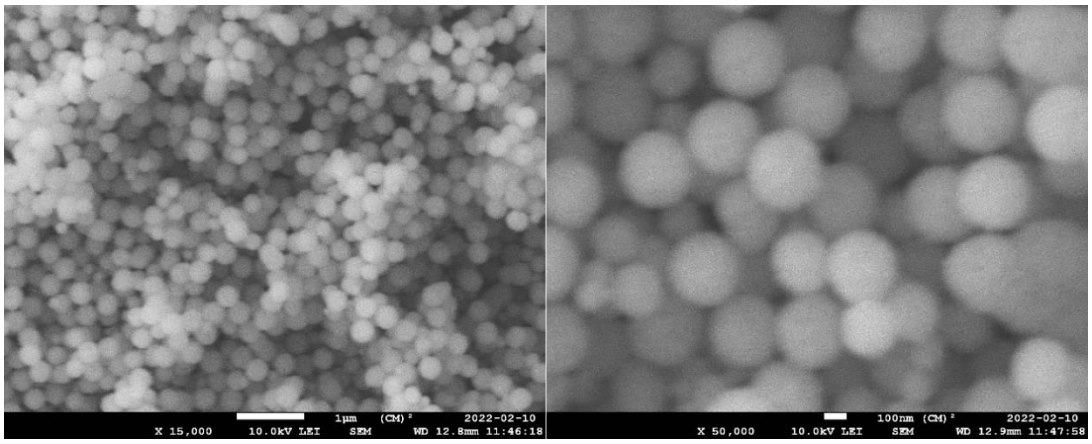

Figure S1. SEM image of Fe_3O_4 magnetic NPs.

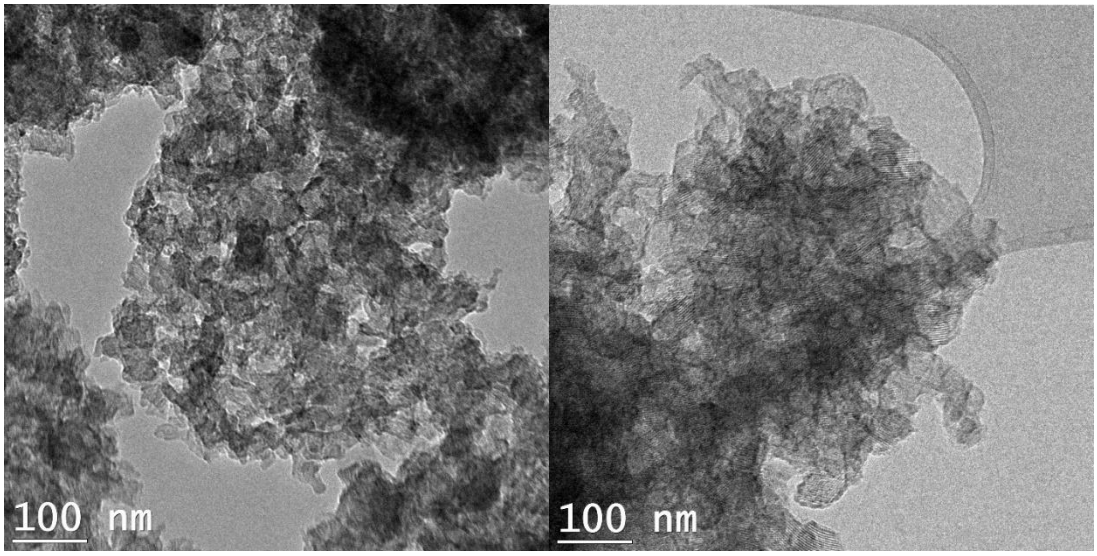

Figure S2. TEM images of COF.

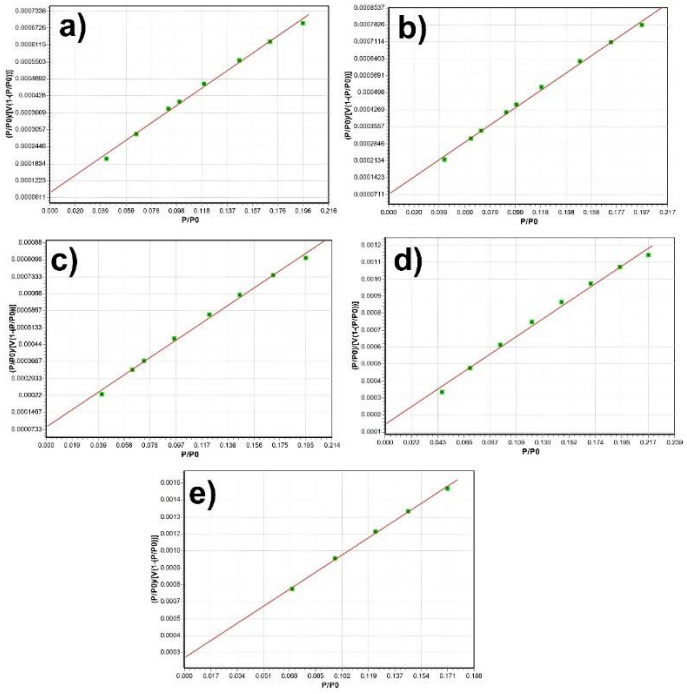

Figure S3. Specific BET surface area plots of COF (a), Fe_3O_4@COF (b), Fe_3O_4@RCOF (c), Fe_3O_4@RCOF-EBH (d) and Fe_3O_4@RCOF-EBH-TSC (e).

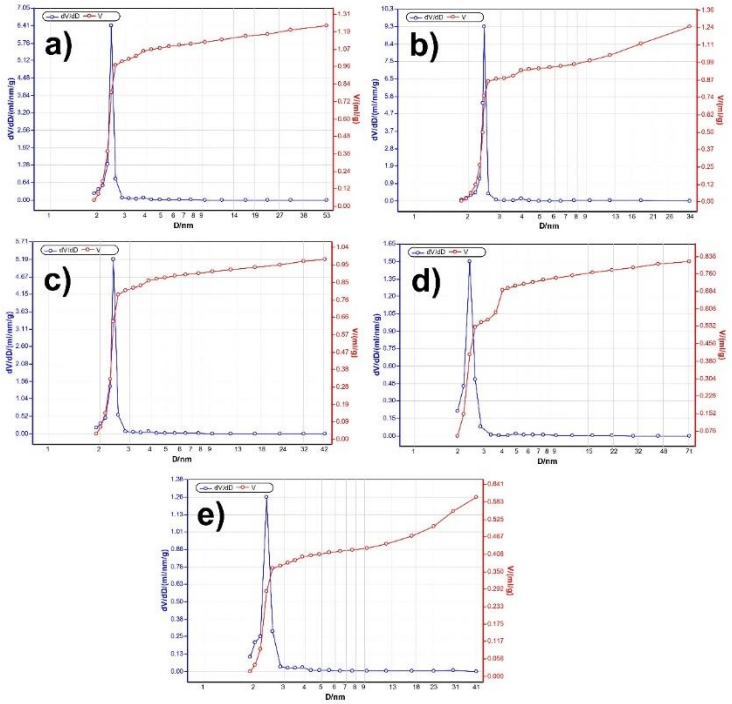

Figure S4. Pore size distribution plots of COF (a), Fe_3O_4@COF (b), Fe_3O_4@RCOF (c), Fe_3O_4@RCOF-EBH (d) and Fe_3O_4@RCOF-EBH-TSC (e).

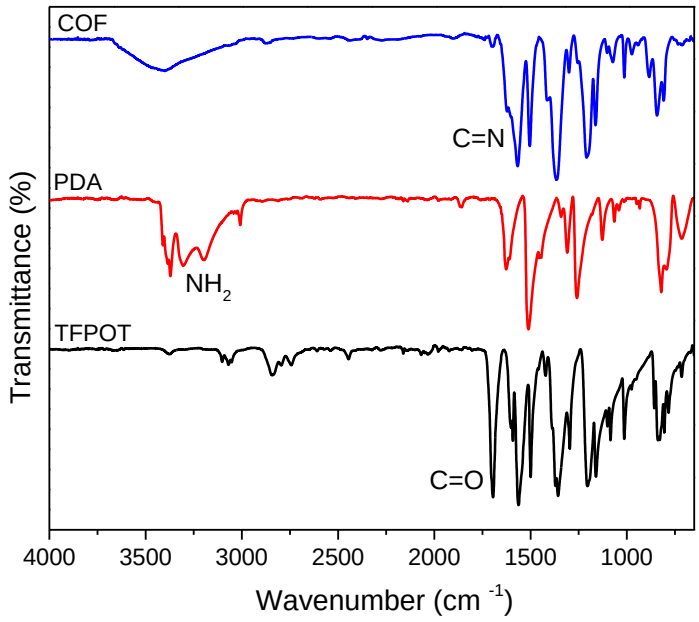

Figure S5. FT-IR spectrum of TFPOT (black spectrum), PDA (red spectrum) and COF (blue spectrum).

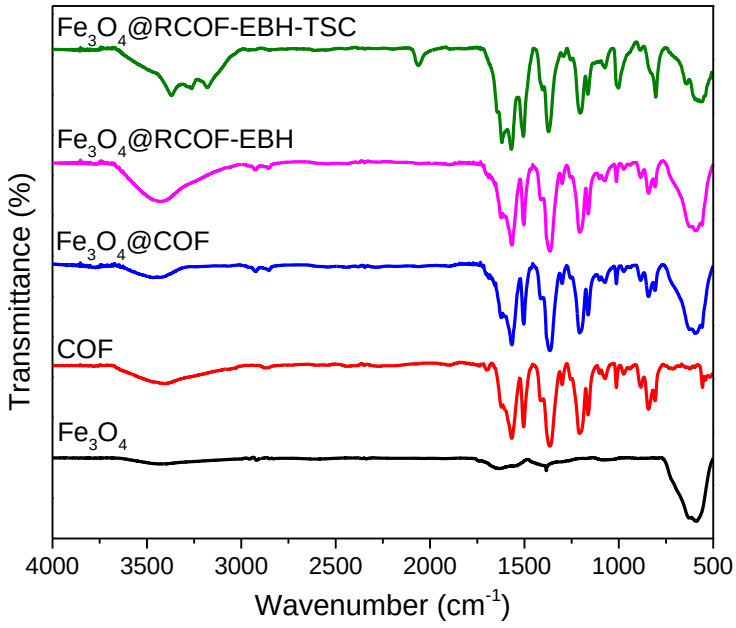

Figure S6. FT-IR spectrum of Fe_3O_4 (black spectrum), COF (red spectrum), Fe_3O_4@COF (blue spectrum), Fe_3O_4@RCOF-EBH (pink spectrum) and Fe_3O_4@RCOF-EBH-TSC (green spectrum).

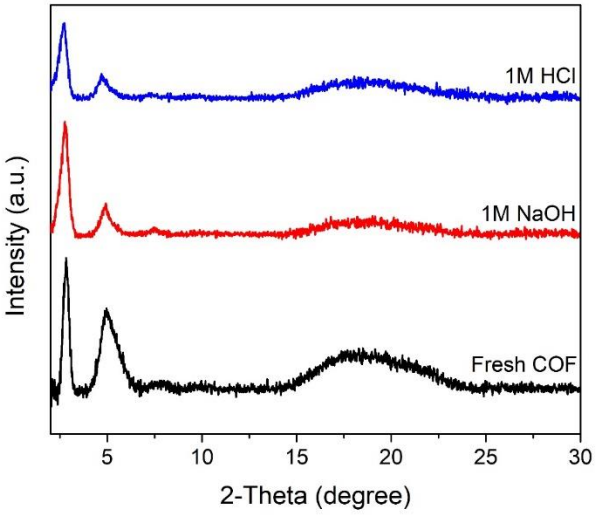

Figure S7. PXRD patterns of functionalized COF under different conditions at 25 ºC for 24 h.

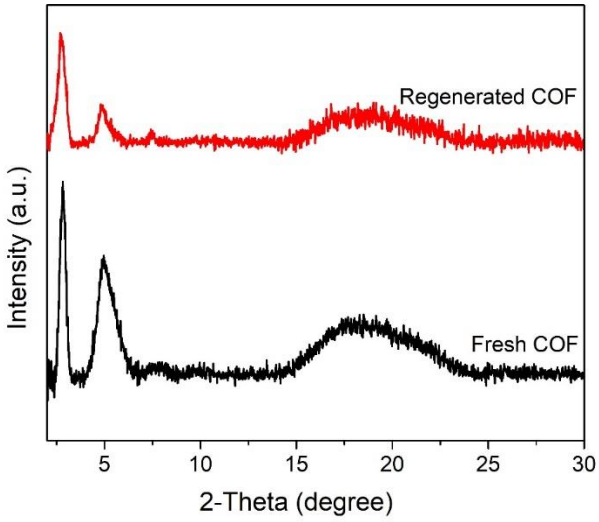

Figure S8. PXRD patterns of fresh (black PXRD pattern) and regenerated RCOF-EBH-TSC (red PXRD pattern).

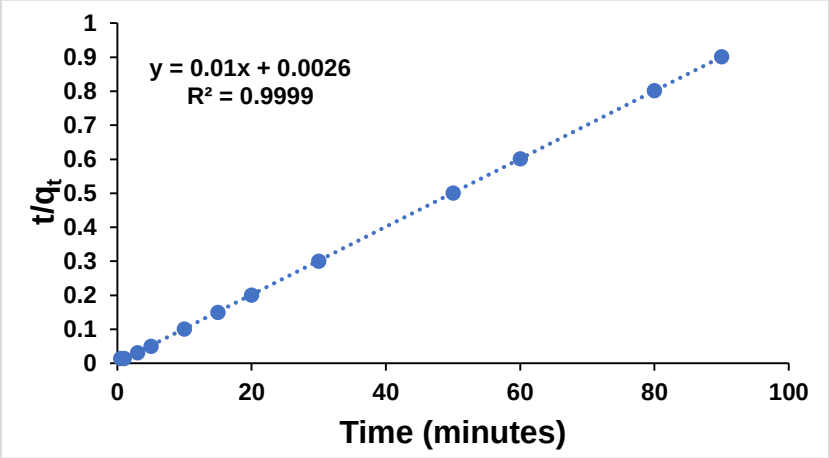

Figure S9. Linearized pseudo-second-order plot for Hg(II) adsorption on Fe_3O_4@RCOF-EBH-TSC.

Table S1. Kinetic model variables for Hg(II) adsorption on Fe_3O_4@RCOF-EBH-TSC.

Kinetic model	Parameters		
Pseudo-second order	$q_{e,cal}$ [a] (mg/g)	k_2	R^2
	100.00	0.038	0.999

[a] The experimental adsorption capacity at equilibrium (q_e) is equal to 99.30 mg/g.

Table S2. Langmuir and Freundlich isotherm factors for adsorption of Hg(II) on adsorbent.

	Langmuir				Freundlich		
T (K)	q_m (mg/g)	K_L (L/mg)	R_L [a] range	R^2	K_F [(mg/g)(L/mg)$^{1/n}$]	$1/n$	R^2
298	1400.852	0.394	0.337-0.012	0.961	356.533	0.333	0.931
308	1468.013	0.442	0.311-0.011	0.974	423.253	0.301	0.916
323	1530.165	0.770	0.206-0.006	0.989	536.043	0.270	0.931

[a] The range of initial concentrations of Hg(II) was 5-200 mg/L.

Table S3. K_d and $\propto_{t/c}$ of the multi-metals polluted water.

Metal ions	Ag^{+}	Fe^{3+}	Cd^{2+}	Pb^{2+}	Zn^{2+}	Mn^{2+}	Ni^{2+}	Hg^{2+}
K_d	2.15E+03	1.26E+03	9.53E+02	1.20E+03	7.07E+02	1.43E+03	7.76E+02	2.49E+06
$\propto_{t/c}$	8.64E-04	5.06E-04	3.83E-04	4.81E-04	2.84E-04	5.74E-04	3.12E-04	44.98

Table S4. Thermodynamic variables for the adsorption of Hg(II) on Fe_3O_4@RCOF-EBH-TSC.

T (K)	ΔG^{o} (kJ/mol)	ΔH^{o} (kJ/mol)	ΔS^{o} (kJ /mol K)
298	-13.440	30.651	0.147
308	-14.359		
323	-17.079		

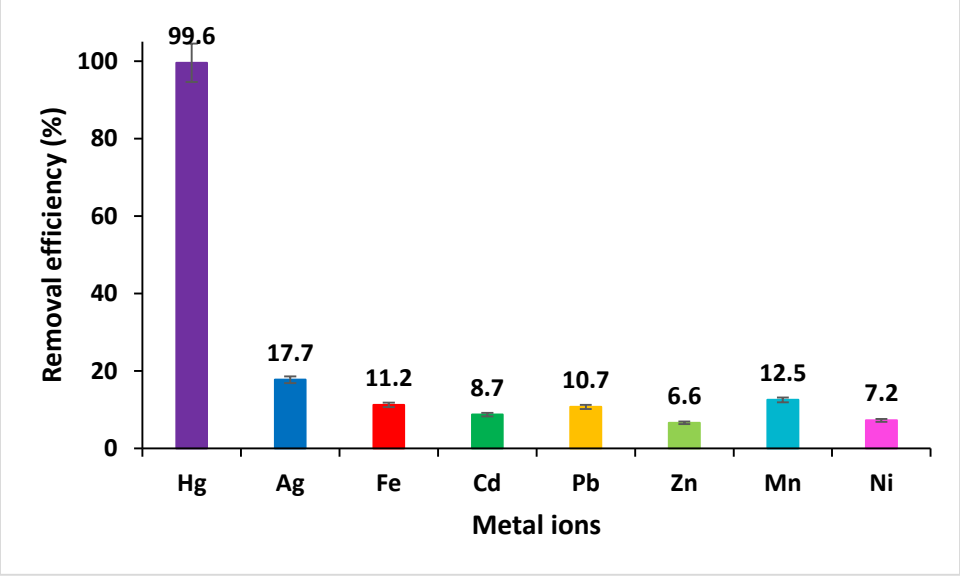

Figure S10. The removal efficiency of Fe_3O_4@RCOF-EBH-TSC for Hg(II) in presence of other competing metal ions at pH = 6 after 5 min.

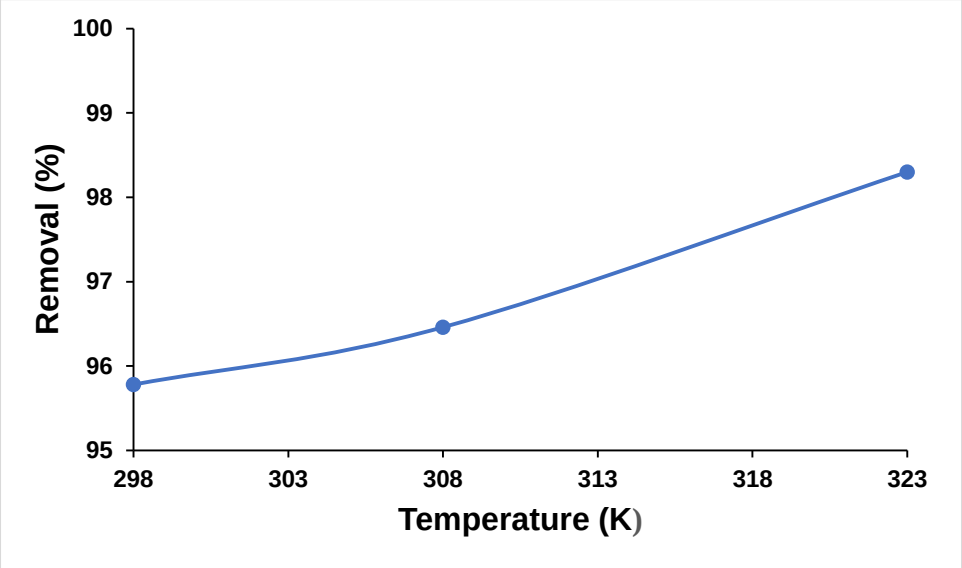

Figure S11. Temperature effect on Hg(II) removal by Fe_3O_4@RCOF-EBH-TSC.

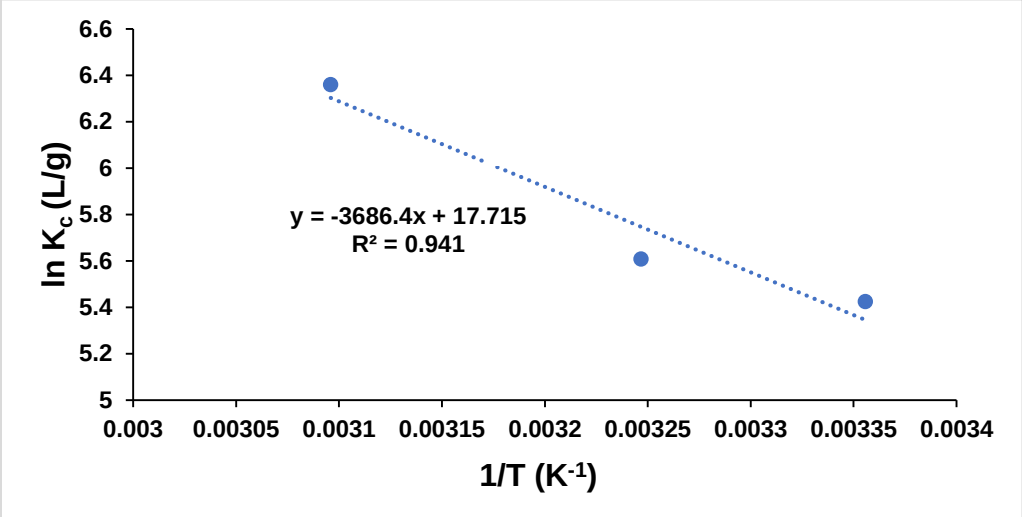

Figure S12. Plot of ln *K*c vs. 1/*T* for the Hg(II) adsorption on Fe_3O_4@RCOF-EBH-TSC.

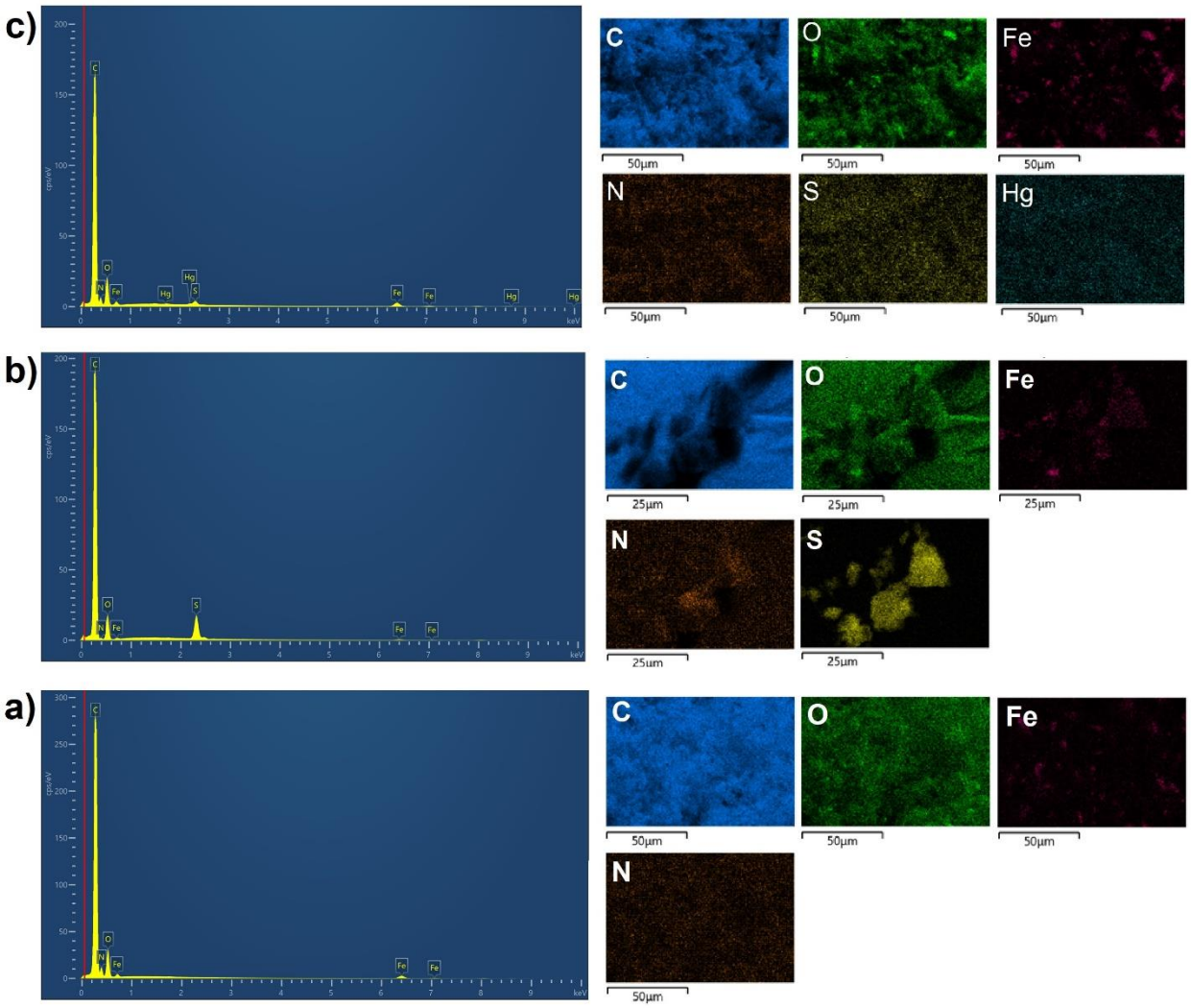

Figure S13. EDX and SEM mapping of Fe_3O_4@COF (**a**), Fe_3O_4@RCOF-EBH-TSC (**b**) and Fe_3O_4@RCOF-EBH-TSC after placing in Hg(II) solution (**c**).

ANNEXE B

INFORMATIONS COMPLÉMENTAIRES

Rapid, Mild and Catalytic Synthesis of 2D and 3D COFs with Promising Supercapacitor Applications

Amir Khojastehnezhad[a], Khaled Rhili[a], Mohammad Shehab[b], Hichem Gamraoui[a], Zhiyuan Peng[a], Ahmad Samih ElDouhaibi[c], Rachid Touzani[d], Belkheir Hammouti[e], Hani El-Kaderi[b], and Mohamed Siaj[a]
Email: siaj.mohamed@uqam.ca

[a]*Department of Chemistry, University of Quebec at Montreal, Montreal, QC H3C3P8, Canada*
[b]*Department of Chemistry, Virginia Commonwealth University, Richmond, Virginia 23284, United States*
[c]*Department of Chemistry, Lebanese University, College of Science III, Campus Mont Michel, Lebanon*
[d]*Laboratory of Applied and Environmental Chemistry, Mohammed first University, Oujda, Morocco*
[e]*Department of Chemistry, Euromed University of Fes, Fes Morocco*

Table of Contents **Page number**

Experimental Section

Materials

Acetone, *o*-dichlorobenzene (DCB), tetrahydrofuran (THF), *n*-butanol (n-BuOH), dioxane, mesitylene, acetone, ethanol (EtOH) and acetic acid (AcOH) were purchased from local chemical distributors. Chemicals were listed as follows: *p*-phenylenediamine ($C_6H_4(NH_2)_2$, 98% purity, Sigma-Aldrich), phosphotungstic acid ($H_3PW_{12}O_{40}$, 98% purity, Sigma-Aldrich), phosphomolybdic acid ($H_3PMo_{12}O_{40}$, 98% purity, Sigma-Aldrich), terephthalaldehyde ($C_6H_4(CHO)_2$, 99% purity, Sigma-Aldrich), hydrazine monohydrate ($NH_2NH_2{\cdot}H_2O$, 98% purity, Sigma-Aldrich), *p*-hydroxy benzaldehyde ($C_7O_2H_6$, 98% purity, Sigma-Aldrich), cyanuric chloride ($C_3Cl_3N_3$, 99% purity, Sigma-Aldrich), tetrakis(4-aminophenyl)methane ($C_{25}H_{24}N_4$, >90% purity, Sigma-Aldrich), and tris(4-aminophenyl)amine ($C_{18}H_{18}N_4$, 98%, TCI America). All chemicals were used without any further purifications.

Material Characterization

To characterize the morphologies and sizes of prepared samples, transmission electron microscopy (TEM), high-resolution TEM (HR-TEM) (Oxford Instruments, Abingdon, Oxfordshire, UK) were used. X-ray diffraction (XRD) with Cu Kα radiation (Bruker D8 advance, Billerica, MA, USA) was used to analyze the crystalline structures of the prepared samples. The FT-IR analyses were performed with a Nicolet 6700 spectrometer with a smart iTR module from company Thermo Scientific**.** Thermogravimetric analysis (TGA Q500 from TA Instruments company), was carried out from room temperature to 800 ^oC at a heating rate of 10 $^oC\ min^{-1}$ and a N_2 flow rate of 20 mL min^{-1}. Besides, the BET measurements were utilized to find the surface area of the samples. The Nitrogen adsorption-desorption analyses were performed at 76.5 K with a TMAX-BSD-PM2 from TMAXCN company (China). ^1H NMR and ^{13}C NMR spectra were recorded using dimethyl sulfoxide (DMSO)-d_6 as solvents at 300 and 150 MHz. Coupling constants (*J*) are expressed in hertz and chemical shifts are described in δ units and are expressed in ppm.

Methods

Synthesis of 2,4,6-tris-(4-formylphenoxy)-1,3,5-triazine (TPT)

The *p*-hydroxy benzaldehyde (14.64 mmol, 1800 mg) and NaOH (14.64 mmol, 585 mg) was dissolved in 100 mL round bottom flask and in the mixture of acetone:water (24:24 mL) and then, it was brought to 0 ^{o}C in the ice bath. Next, the cyanuric chloride (4.88 mmol, 900 mg) was dissolved in 24 mL of acetone and added to the previous solution droopingly (60 minutes). During the adding, the white solid was formed. The reaction was continued for 12 h at room temperature. After completion of the reaction, the white solid was filtered and washed with a lot of water. Finally, it was recrystallized with ethanol and after drying in the vacuum oven at 80 ^{o}C, the pure final product with 92 % of the yield was obtained (white solid, yield 88%, Scheme S1).

^{1}H NMR (300 MHz, $CDCl_3$): δ 10.1 (s, 3H), 7.95 (d, J = 8.6 Hz, 6H), 7.32 (d, J = 8.6 Hz, 6H). ^{13}C NMR (150 MHz, $CDCl_3$): δ 190.57, 173.25, 155.70, 134.50, 131.32, 122.21 (Fig. S1).

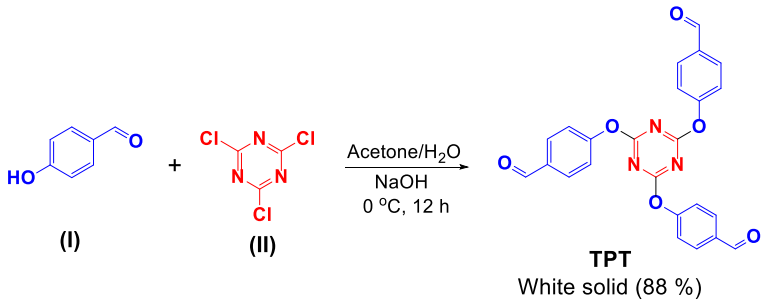

Scheme S1. Synthesis of TPT.

Catalytic synthesis of TPT-PDA COF

To a 15 mL high-pressure glass tube, the 2,4,6-tris(4-formylphenoxy)-1,3,5-triazine (TPT) (0.1 mmol, 44 mg), *p*-pheneylenediamine (PDA) (0.15 mmol, 16.25 mg), *n*-butanol (0.75 mL), and *o*-dichlorobenzene (1.0 mL) were added. The mixture was stirred vigorously for 10 minutes and sonicated for another 10 minutes to obtain a homogeneous solution. Then, the catalyst (1.0 mol %, 4 mg) was dissolved in *n*-butanol (0.25 mL) and added to the tube. Next, the mixture was capped and heated at different temperatures (25 to 120 ^{o}C) mentioned in results section without stirring for 2 h. The reaction mixture was cooled to room temperature then isolated by filtration. The resultant COF was washed extensively with anhydrous acetone and anhydrous THF. Afterwards, to remove the catalyst, it was washed again with ethanol in a Soxhlet extractor for 12 h and dried in a vacuum oven for 12 h at 80 °C to obtain the TPT-PDA COF (yellow solid, yield 92 %) (Scheme S2).

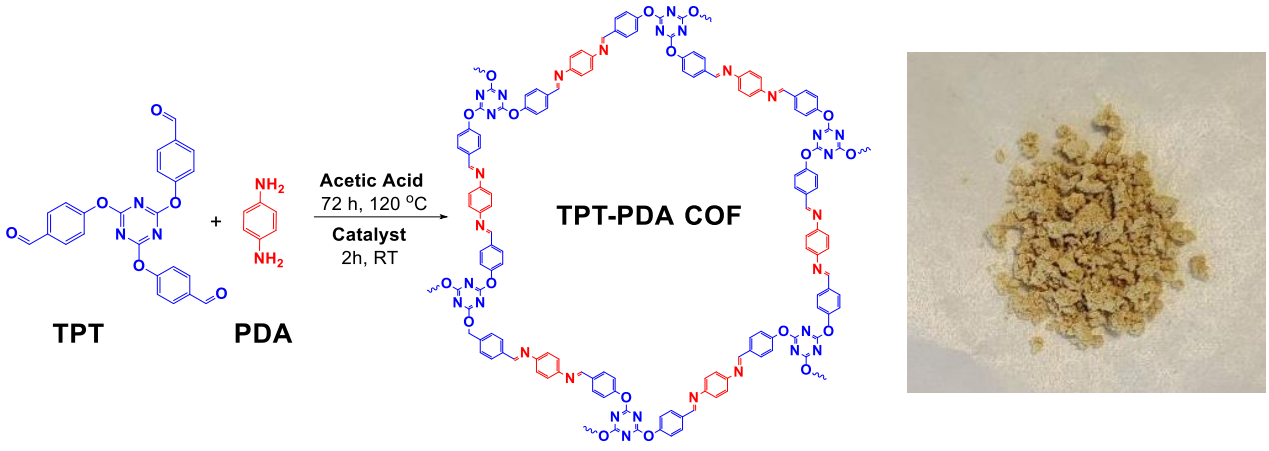

Scheme S2. Synthesis of TPT-PDA COF.

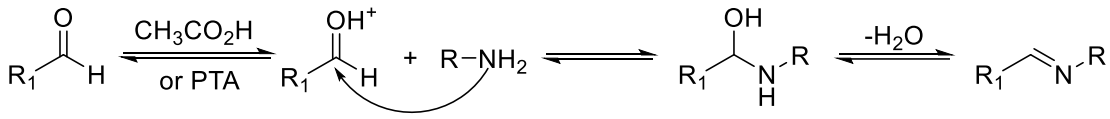

Scheme S3. Catalytic synthesis of imine-linked COFs via Schiff base polycondensation reaction.

Catalytic synthesis of TPT-HZ COF

To a 15 mL high-pressure glass tube, the 2,4,6-tris(4-formylphenoxy)-1,3,5-triazine (TPT) (0.1 mmol, 44 mg), hydrazine monohydrate (HZ) (0.15 mmol, 8.5 µL), mesitylene (1.0 mL), *o*-dichlorobenzene (0.5 mL) and ethanol (0.5 mL) were added. The mixture was stirred vigorously for 10 minutes and sonicated for another 10 minutes to obtain a homogeneous solution. Then, the catalyst (1.0 mol %, 4 mg) was dissolved in the ethanol (0.5 mL) and added to the tube. Next, the mixture was capped and continued the reaction at room temperature without stirring for 2 h. The reaction mixture was cooled to room temperature then isolated by filtration. The resultant COF was washed extensively with anhydrous acetone and anhydrous THF. Afterwards, to remove the catalyst, it was washed again with ethanol in a Soxhlet extractor for 12 h and dried in a vacuum oven for 12 h at 80 °C to obtain the TPT-HZ COF (pale-yellow solid, yield 90 %) (Scheme S4).

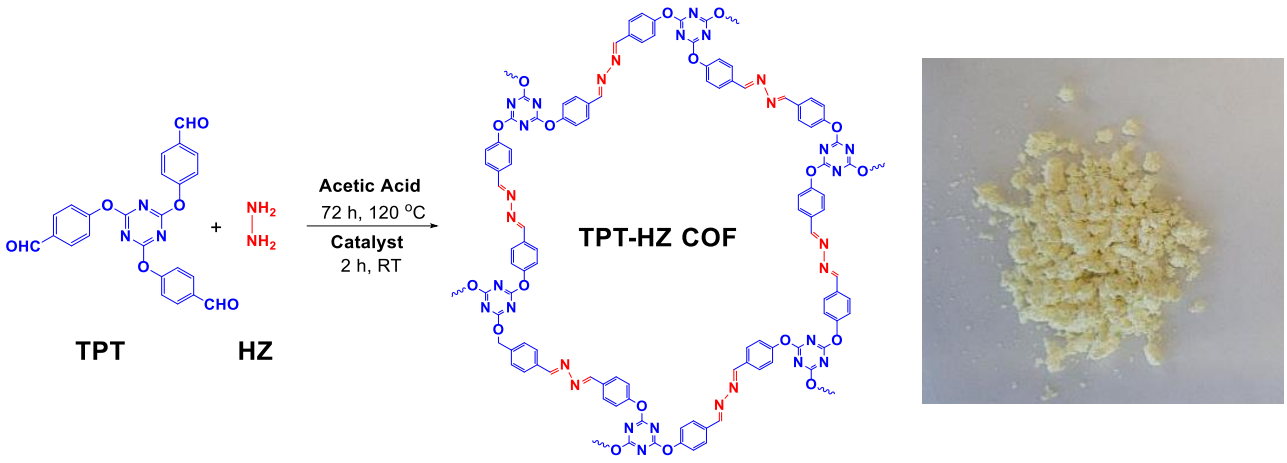

Scheme S4. Synthesis of TPT-HZ COF.

Catalytic synthesis of TAPA-TPA COF

To a 15 mL high-pressure glass tube, the tris(4-aminophenyl)amine (TAPA) (0.16 mmol, 46.5 mg), terephthaldehyde (TPA) (0.23 mmol, 30.8 mg), *n*-butanol (0.75 mL) and *o*-dichlorobenzene (1.0 mL) were added. The mixture was stirred vigorously for 10 minutes and sonicated for another 10 minutes to obtain a homogeneous solution. Then, the catalyst (1.0 mol %, 4mg) was dissolved in *n*-butanol (0.25 mL) and added to the tube. Next, the mixture was purged with N_2, capped, and heated at different temperatures (25 to 80 ^{o}C) mentioned in results section without stirring for 2 h. The reaction mixture was cooled to room temperature then isolated by filtration. The resultant COF was washed extensively with anhydrous acetone and anhydrous THF. Afterwards, to remove the catalyst, it was washed again with ethanol in a Soxhlet extractor for 12 h and dried in a vacuum oven for 12 h at 80 °C to obtain the TAPA-TPA COF (red solid, yield 86 %) (Scheme S5).

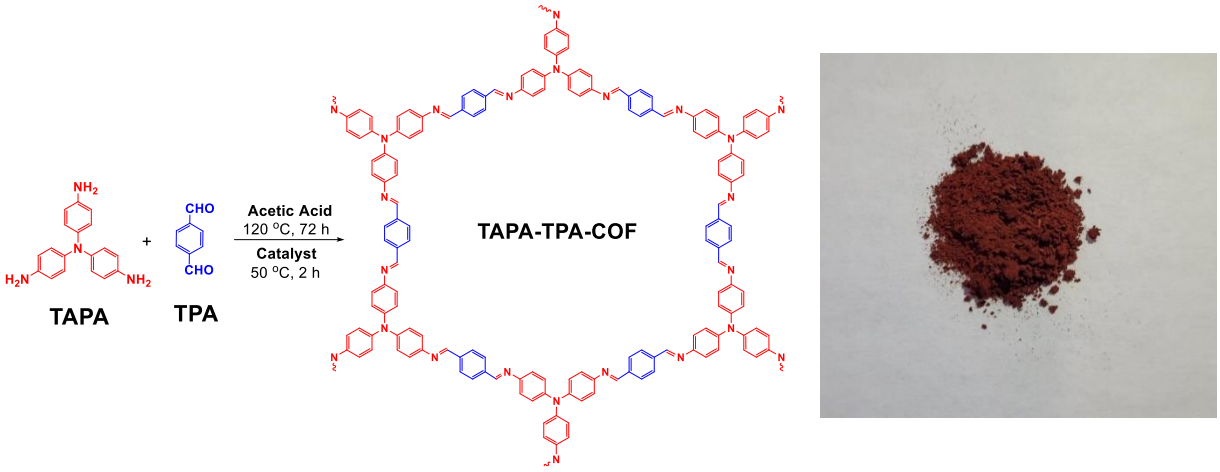

Scheme S5. Synthesis of TAPA-TPA COF.

Solvothermal synthesis of new TAPA-TPT COF

To a 15 mL high-pressure glass tube, the tris(4-aminophenyl)amine (TAPA) (0.22 mmol, 64 mg), 2,4,6-tris(4-formylphenoxy)-1,3,5-triazine (TPT) (0.15 mmol, 66 mg), *n*-butanol (3.0 mL) and *o*-dichlorobenzene (1.0 mL) were added. The mixture was stirred vigorously for 10 minutes and sonicated for another 10 minutes to obtain a homogeneous solution. Then, the acetic acid (0.2 mL, 6M) was added to the tube. Next, the mixture was purged with N_2, capped, and heated at 120 ^oC for 72 h. The reaction mixture was cooled to room temperature then isolated by filtration. The resultant COF was washed extensively with anhydrous acetone and anhydrous THF and dried in a vacuum oven for 12 h at 80 °C to obtain the TAPA-TPT COF (green solid, yield 85 %) (Scheme S6).

Catalytic synthesis of new TAPA-TPT COF

To a 15 mL high-pressure glass tube, the tris(4-aminophenyl)amine (TAPA) (0.22 mmol, 64 mg), 2,4,6-tris(4-formylphenoxy)-1,3,5-triazine (TPT) (0.15 mmol, 66 mg), *n*-butanol (2.5 mL) and *o*-dichlorobenzene (1.0 mL) were added. The mixture was stirred vigorously for 10 minutes and sonicated for another 10 minutes to obtain a homogeneous solution. Then, the catalyst (1.0 mol %, 6 mg) was dissolved in *n*-butanol (0.5 mL) and added to the tube. Next, the mixture was purged with N_2, capped, and heated at different temperatures (25 to 80 ^oC) mentioned in results section without stirring for 2 h. The reaction mixture was cooled to room temperature then isolated by filtration. The resultant COF was washed extensively with anhydrous acetone and anhydrous THF. Afterwards, to remove the catalyst, it was washed again with ethanol in a Soxhlet extractor for 12 h and dried in a vacuum oven for 12 h at 80 °C to obtain the TAPA-TPT COF (green solid, yield 86%) (Scheme S6).

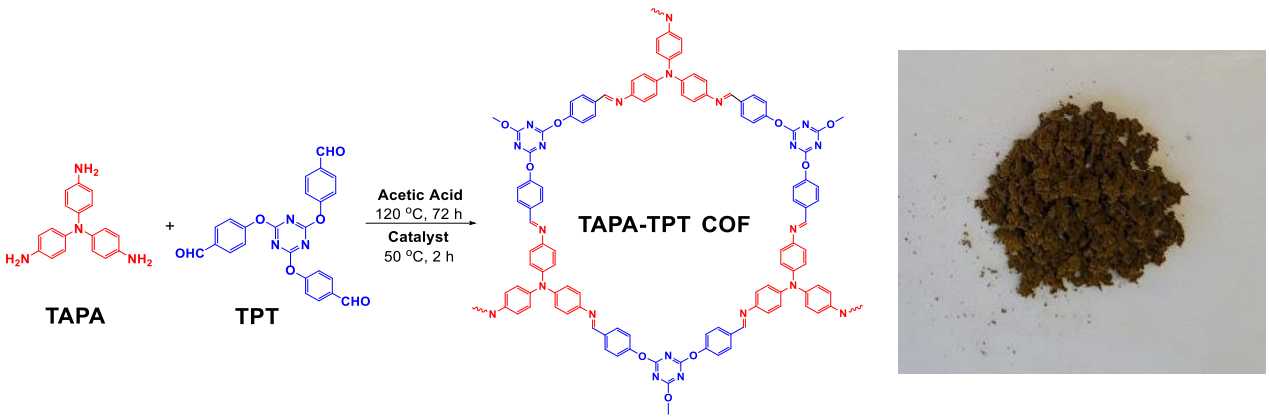

Scheme S6. Synthesis of new TAPA-TPT COF.

Catalytic synthesis of 3D COF-300

To a 15 mL high-pressure glass tube, the tetrakis(4-aminophenyl)methane (TAM) (0.1 mmol, 40 mg), terephthaldehyde (TPA) (0.18 mmol, 24 mg) and dioxane (1.5 mL) were added. The mixture was stirred vigorously for 10 minutes and sonicated for another 10 minutes to obtain a homogeneous solution. Then, the catalyst (1.0 mol %, 3 mg) was dissolved in H_2O (0.5 mL) and added to the tube. Next, the mixture was purged with N_2, capped, and heated at different temperatures (25 to 80 °C) mentioned in results section without stirring for 2 to 6 h. The reaction mixture was cooled to room temperature then isolated by filtration. The resultant COF was washed extensively with anhydrous THF. Afterwards, to remove the catalyst, it was washed again with ethanol in a Soxhlet extractor for 12 h and dried in a vacuum oven for 12 h at 80 °C to obtain the COF-300 (yellow solid, yield 70 %) (Scheme S7).

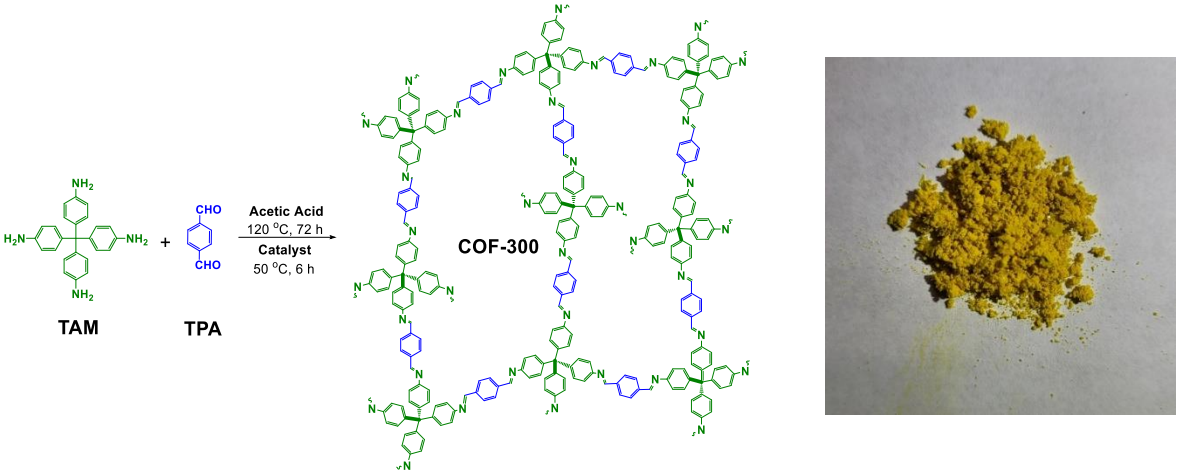

Scheme S7. Synthesis of COF-300.

Carbonization

The as-synthesized materials TAPA-TPT COF was carbonized under argon atmosphere at 800 ^{o}C for 2 h with a heating rate of 5 ^{o}C/min and then cooled to room temperature.

Electrochemical Tests

The electrochemical performance of the synthesized material was evaluated through cyclic voltammetry (CV), galvanostatic charge/discharge (GCD) in a typical three-electrode cell with 1 M H_2SO_4 aqueous solution as the electrolyte. The working electrode was prepared by mixing the as prepared materials with 10 µL of Nafion™ solution (5 wt%) and1 mL water-ethanol solution with a volume ratio of 4:1, and the mix was then sonicated for 30 minutes. 18µL of the resulting ink was drop-casted onto glassy carbon electrode (GC, A = 0.1256 cm^2) and dried in air at room temperature. An Ag/AgCl electrode and a platinum wire were employed as reference electrode and counter electrode, respectively. The primary testing being performed was CV at different scan rates ranging from 5 to 100 mV s^{-1} with the voltage ranging from 0 V to 0.8 V. GCD curves were obtained at current density ranging from 0.5 to 20 A g^{-1}.

The specific capacitance C (F g^{-1}) was determined from GCD curves according to the following equation:

$$C = \frac{I * \Delta t}{m * \Delta V} \qquad (1)$$

where 'I' is the charge-discharge current (A); $\triangle t$ is the discharge time (s); $\triangle V$ is the potential window(V); and m is the active material loading in the working electrode (g).

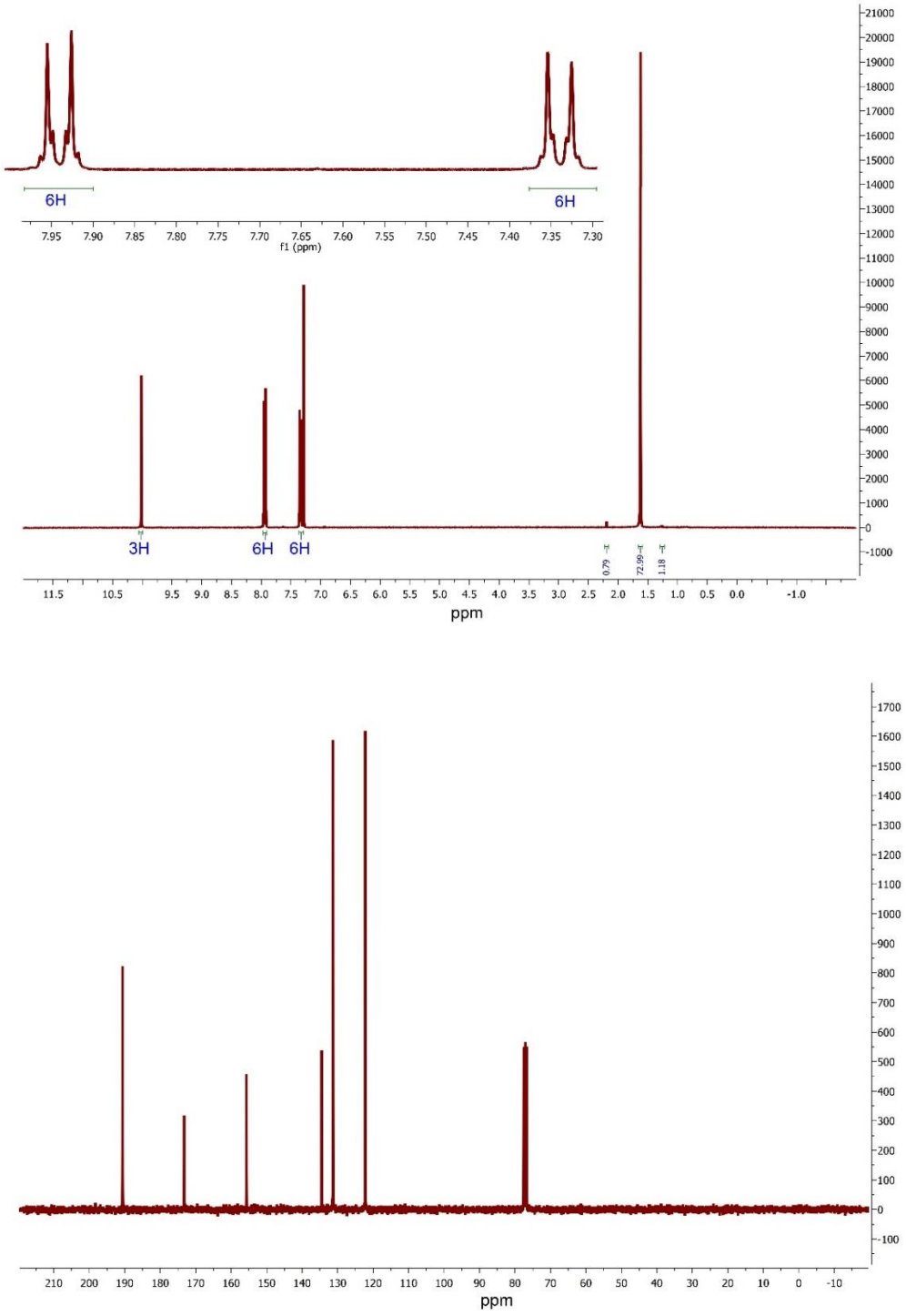

Figure S1. ^{1}H NMR and ^{13}C-NMR spectra of TPT.

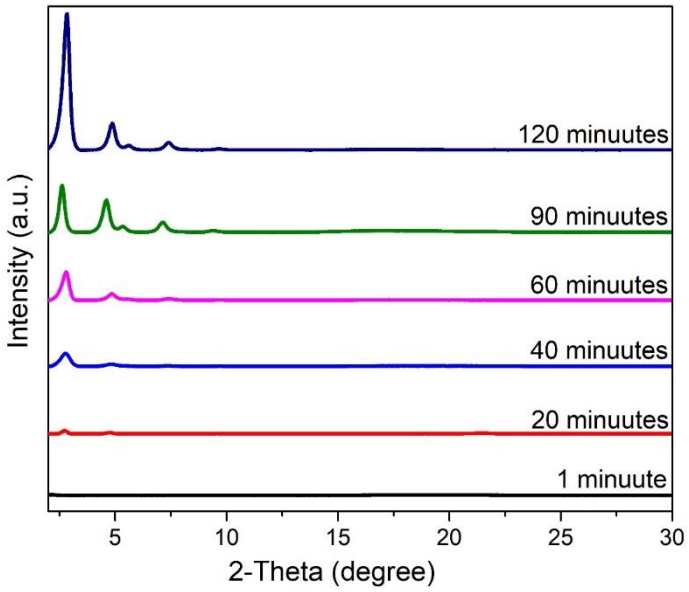

Figure S2. PXRD patterns of prepared TPT-PDA COF in different times.

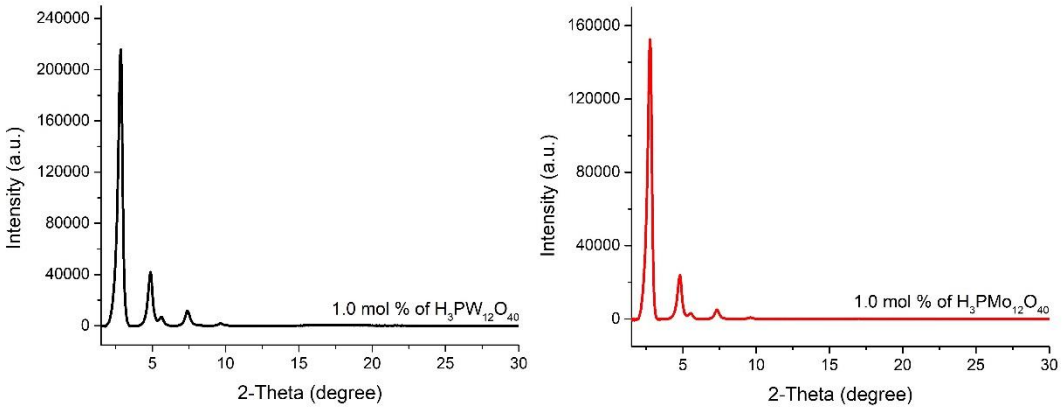

Figure S3. PXRD patterns of prepared TPT-PDA COF in the presence of different catalysts, PTA ($H_3PW_{12}O_{40}$) and PMA ($H_3PMo_{12}O_{40}$).

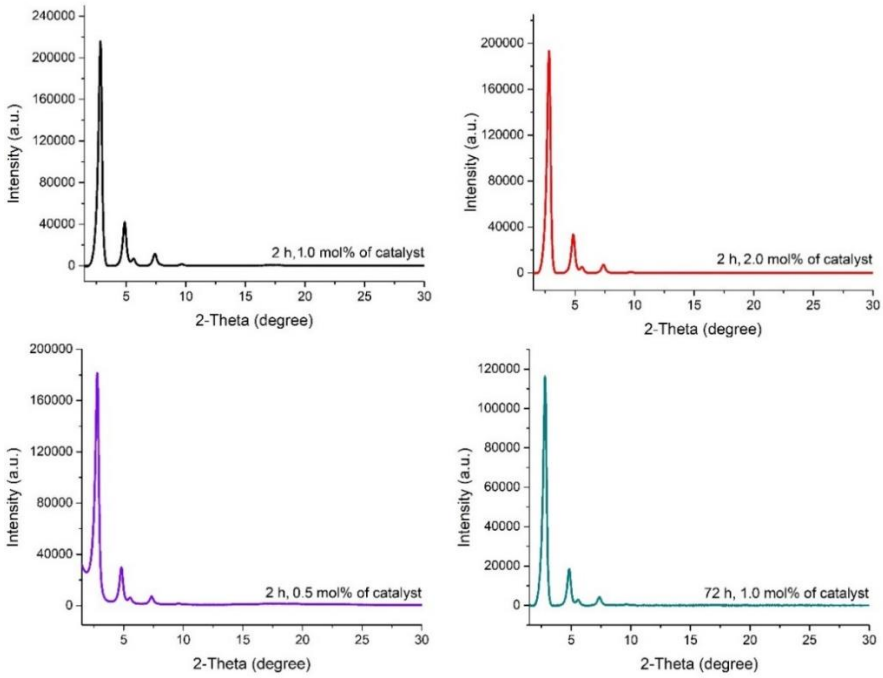

Figure S4. PXRD patterns of prepared TPT-PDA COF in different amounts of PTA.

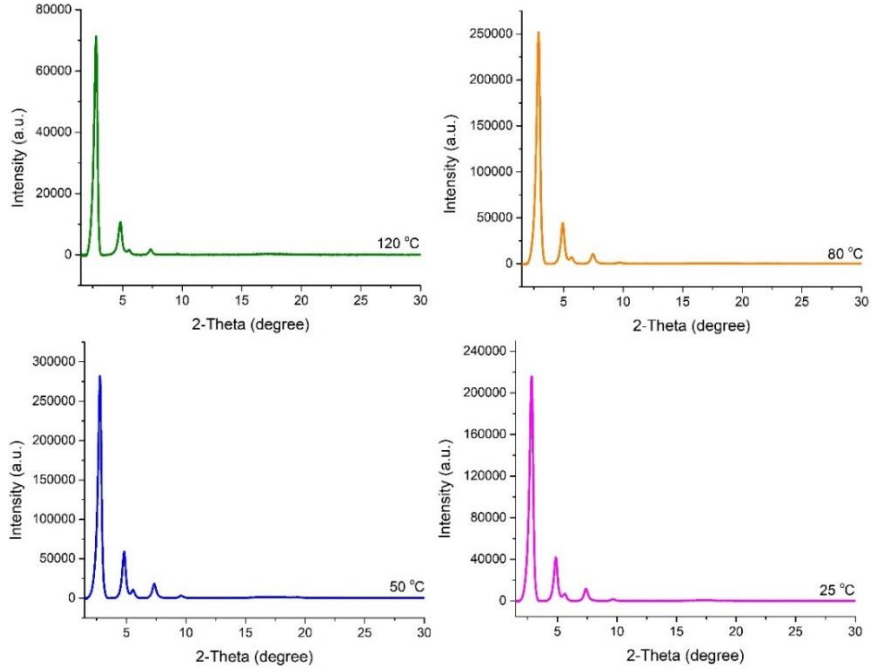

Figure S5. PXRD patterns of prepared TPT-PDA COF in different temperatures (120, 80, 50 and 25 °C).

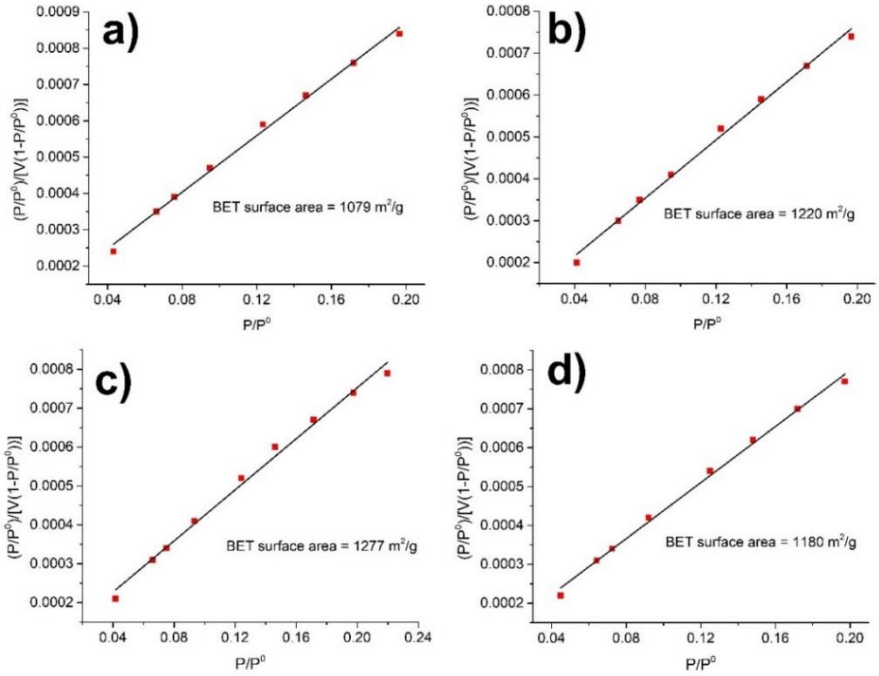

Figure S6. Specific BET surface area plots of TPT-PDA COF in different temperatures (a) 120 ºC, (b) 80 ºC, (c) 50 ºC and (d) 25 ºC.

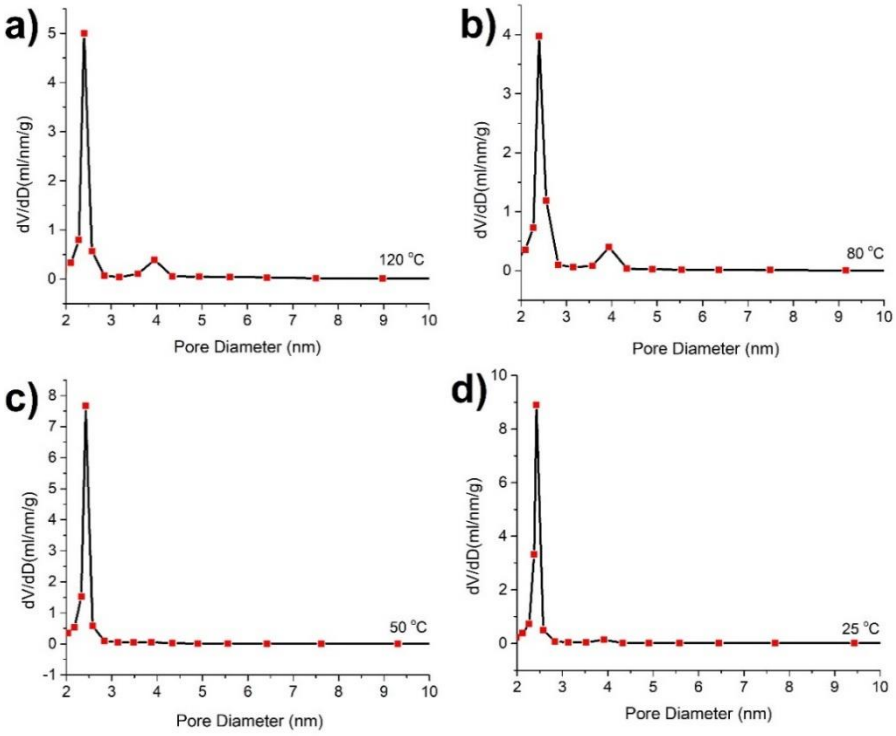

Figure S7. Pore size distribution plots of TPT-PDA COF in different temperatures (a) 120 ºC, (b) 80 ºC, (c) 50 ºC and (d) 25 ºC.

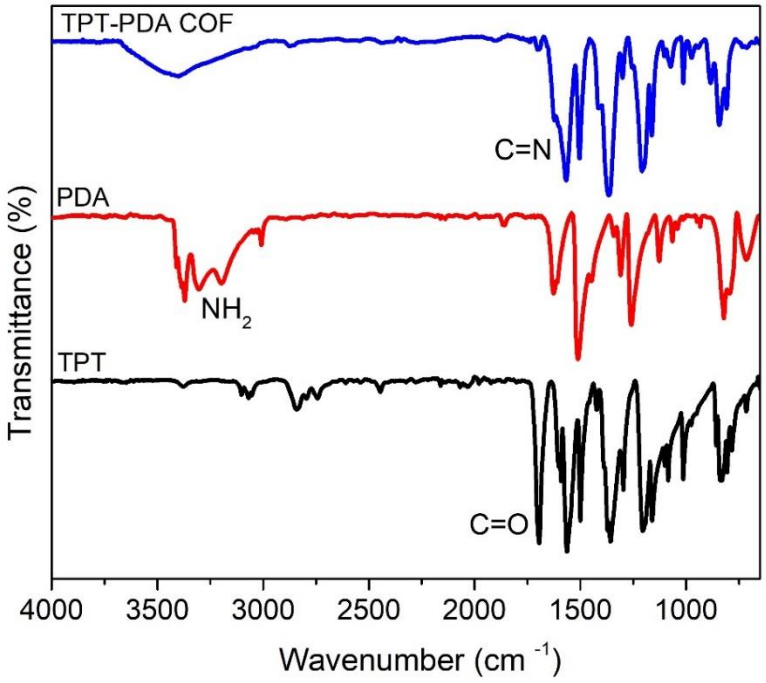

Figure S8. FT-IR spectra of TPT (black spectrum), PDA (red spectrum) and TPT-PDA COF (blue spectrum).

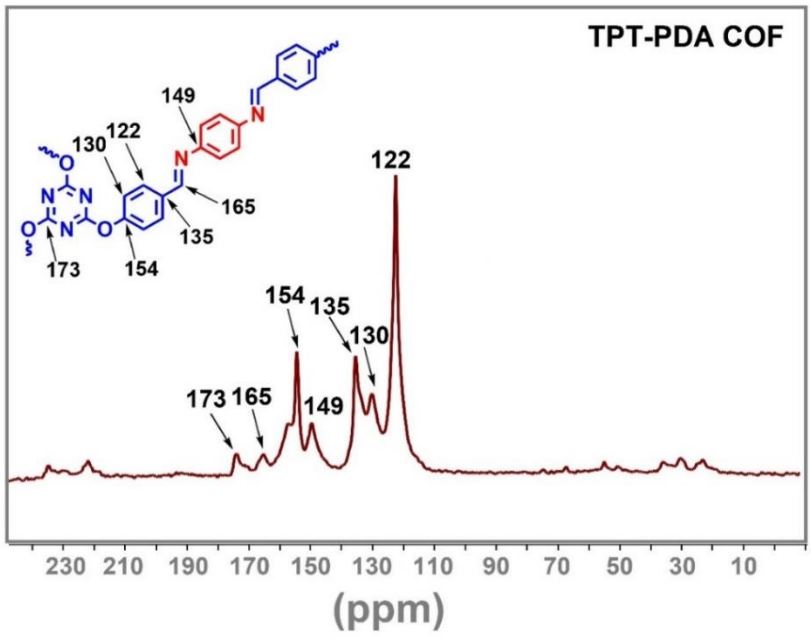

Figure S9. ^{13}C CP/MAS NMR spectra of TPT-PDA COF.

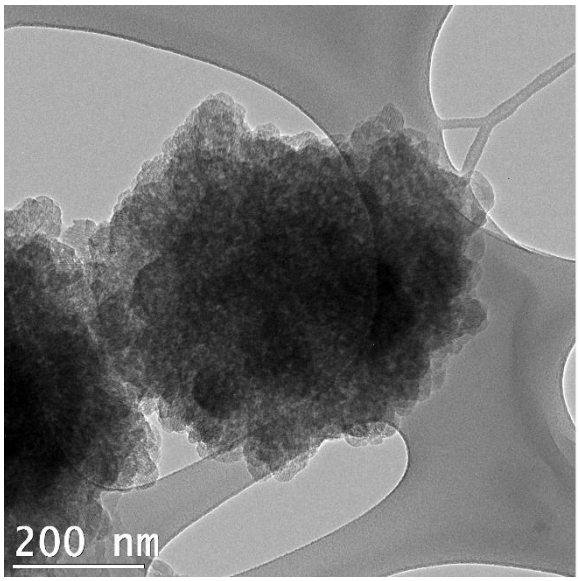

Figure S10. TEM image of TPT-PDA COF prepared in the presence of PTA at room temperature.

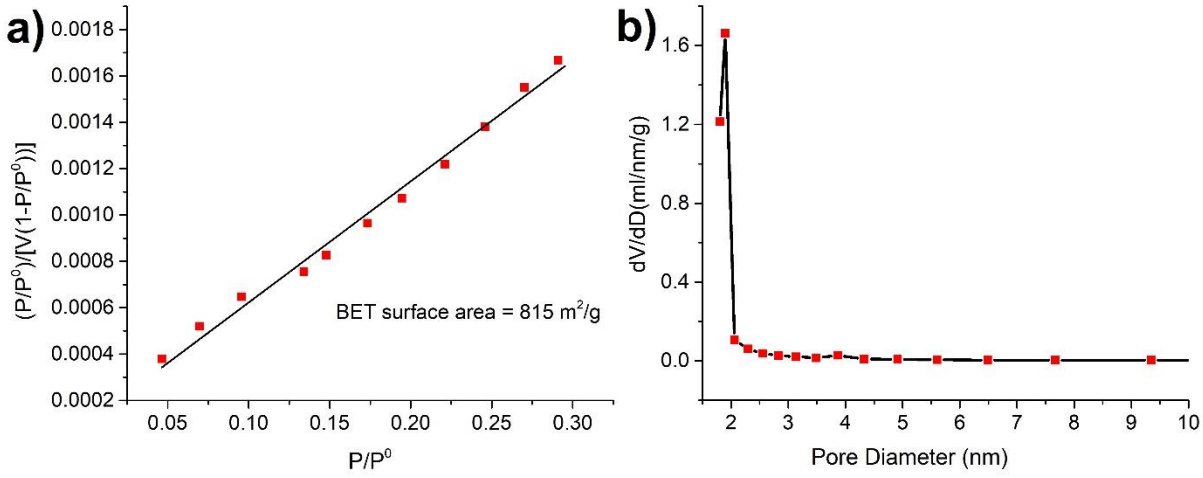

Figure S11. Specific BET surface area (**a**) and pore size distribution plots of TPT-HZ COF (**b**).

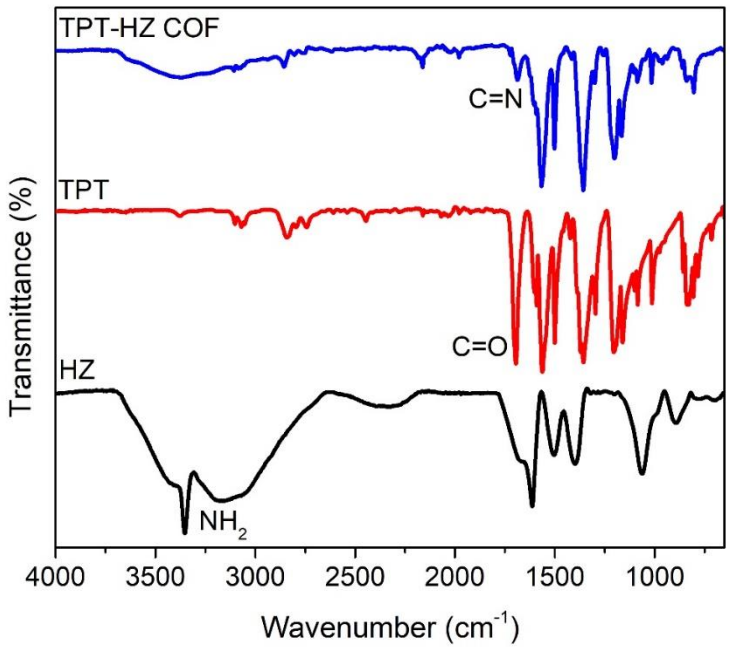

Figure S12. FT-IR spectra of HZ (black spectrum), TPT (red spectrum) and TPT-HZ COF (blue spectrum).

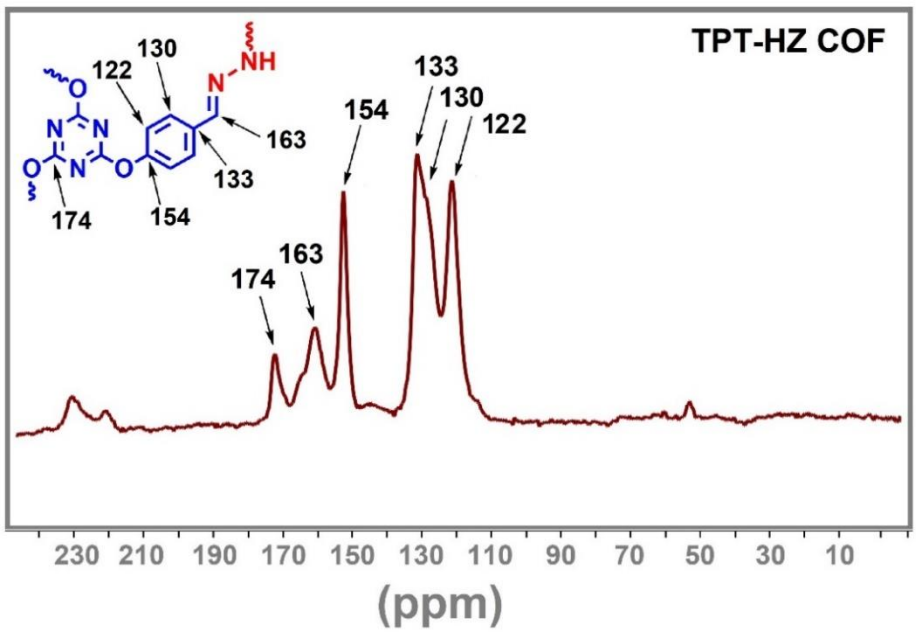

Figure S13. ^{13}C CP/MAS NMR spectra of TPT-HZ COF.

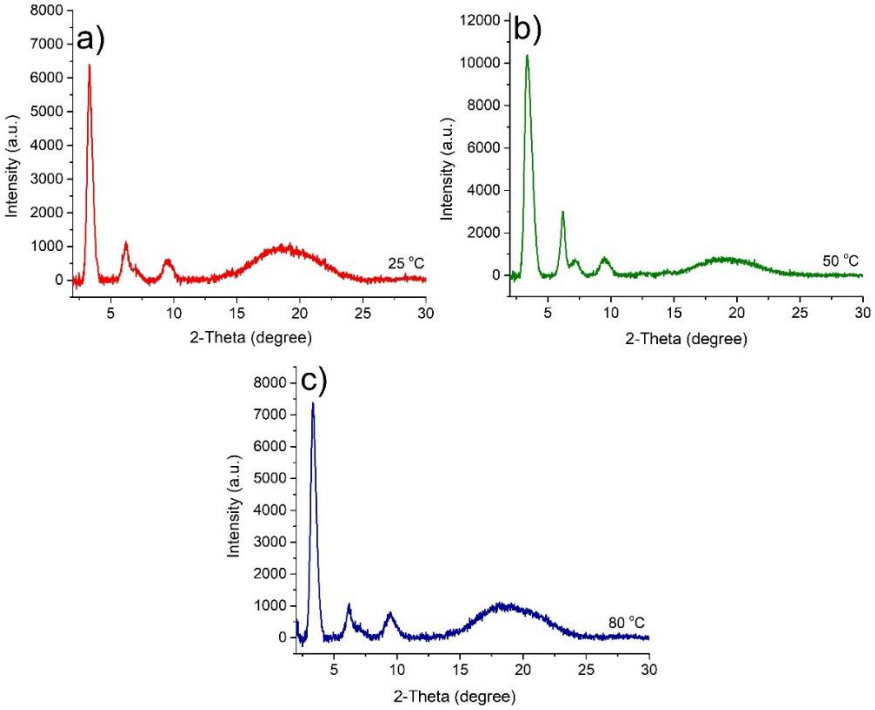

Figure S14. PXRD patterns of prepared TAPA-TPA COF in different temperatures (a) 25 °C, (b) 50 °C and (c) 80 °C.

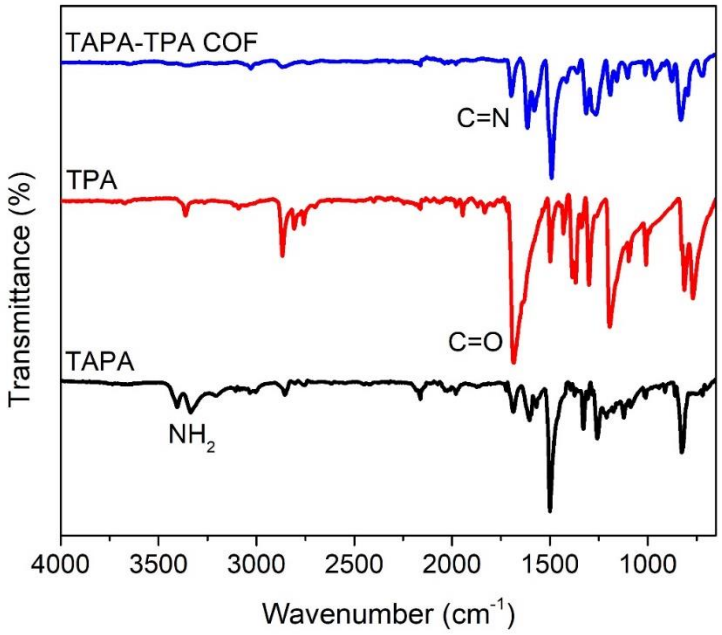

Figure S15. FT-IR spectra of TAPA (black spectrum), TPA (red spectrum) and TAPA-TPA COF (blue spectrum).

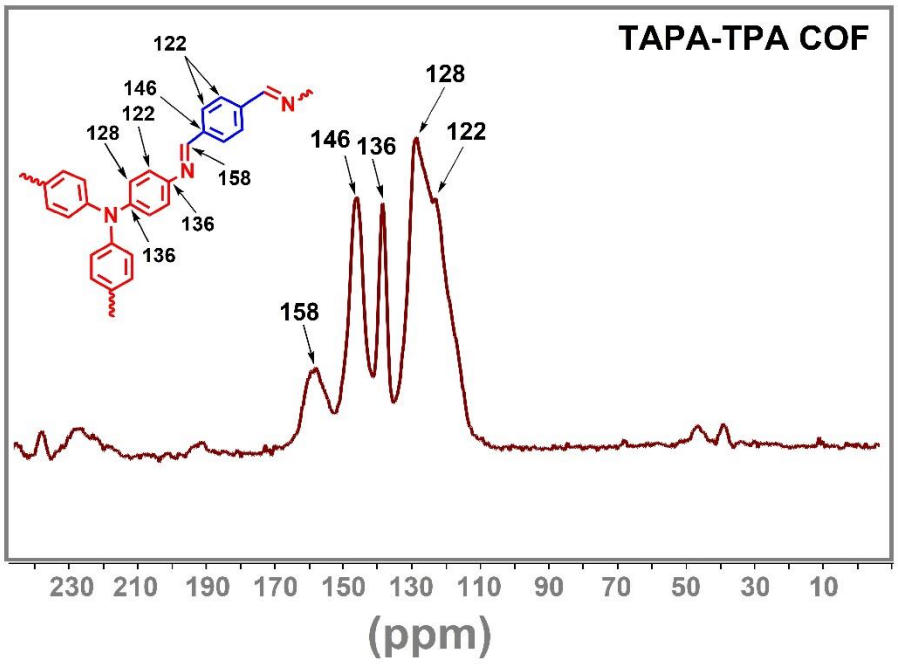

Figure S16. ^{13}C CP/MAS NMR spectra of TAPA-TPA COF.

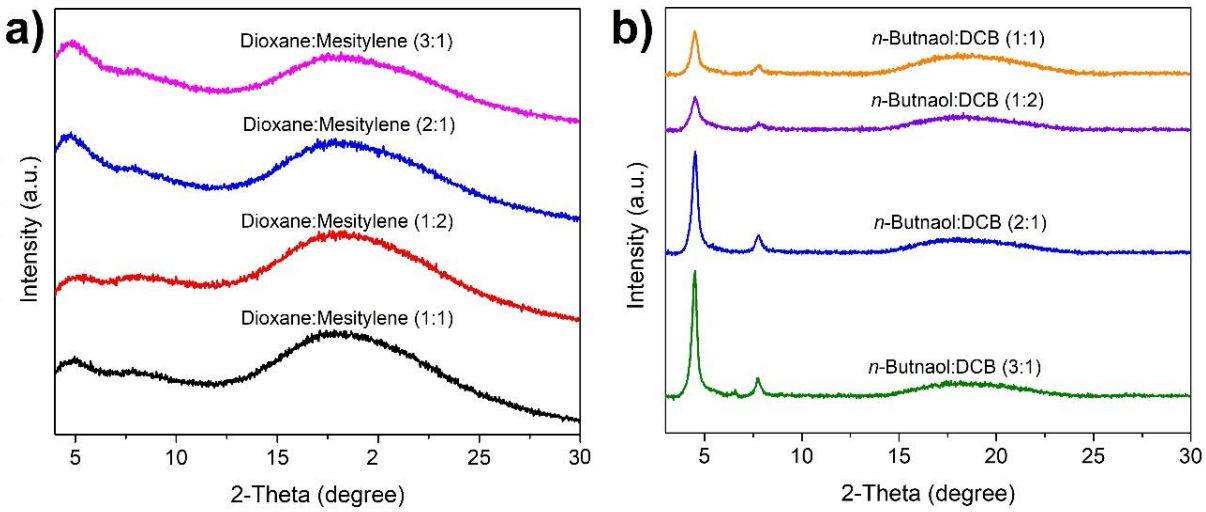

Figure S17. PXRD patterns of solvothermal synthesis of TAPA-TPT COF in different solvents, dioxane/mesitylene (**a**), and *n*-butanol/DCB (**b**).

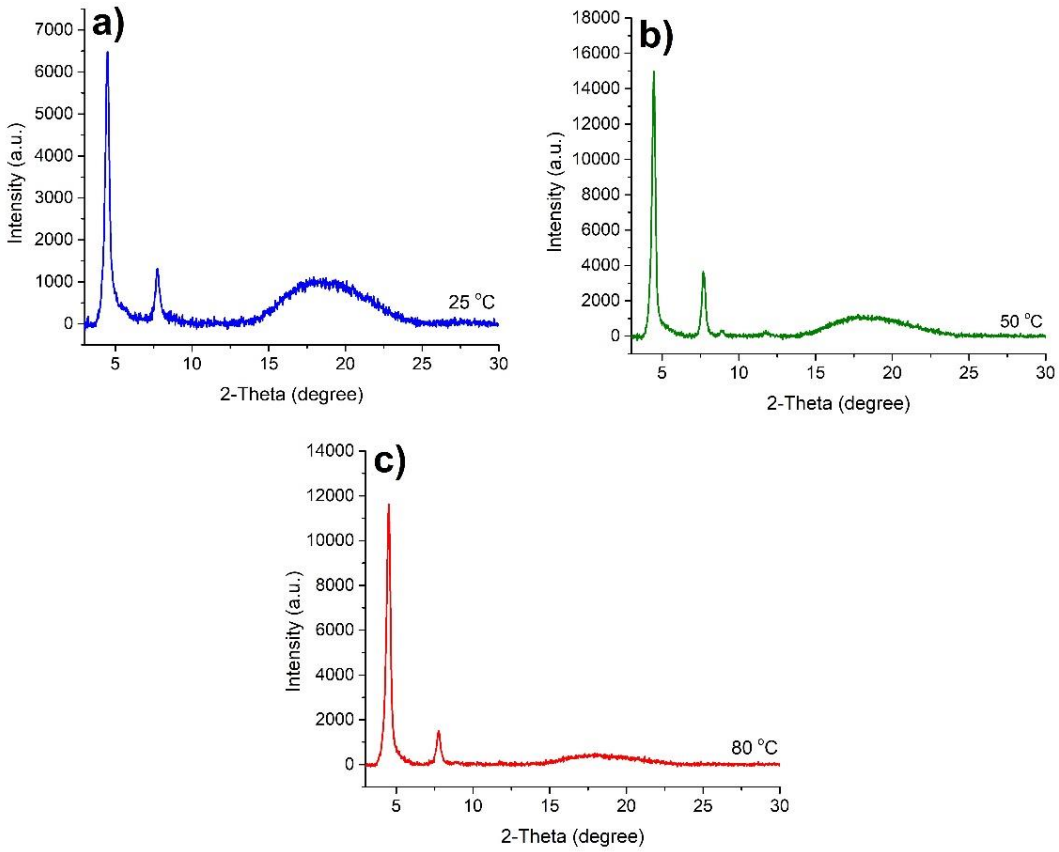

Figure S18. PXRD patterns of catalytic synthesis of TAPA-TPT COF in different temperatures (**a**) 25 ºC, (**b**) 50 ºC, and (**c**) 80 ºC.

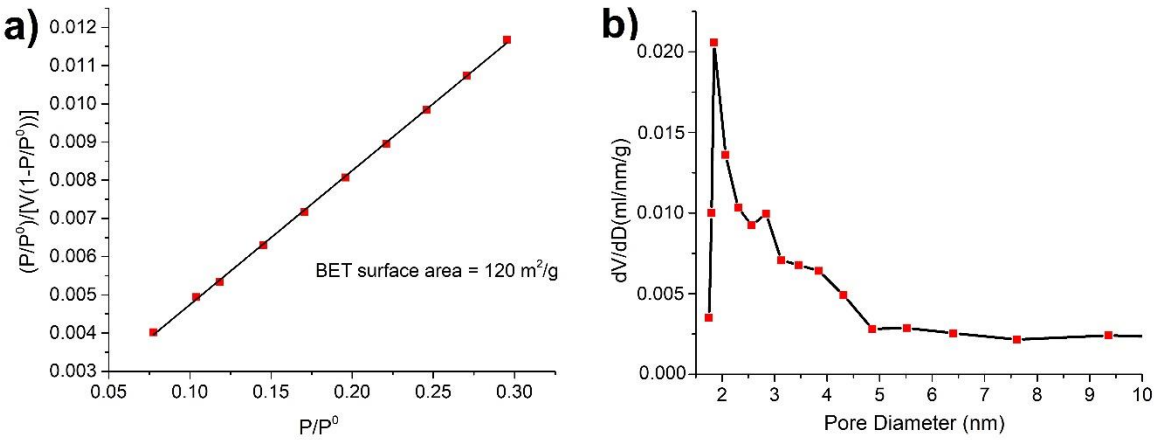

Figure S19. Specific BET surface area (a) and ore size distribution plots of TAPA-TPT COF (b).

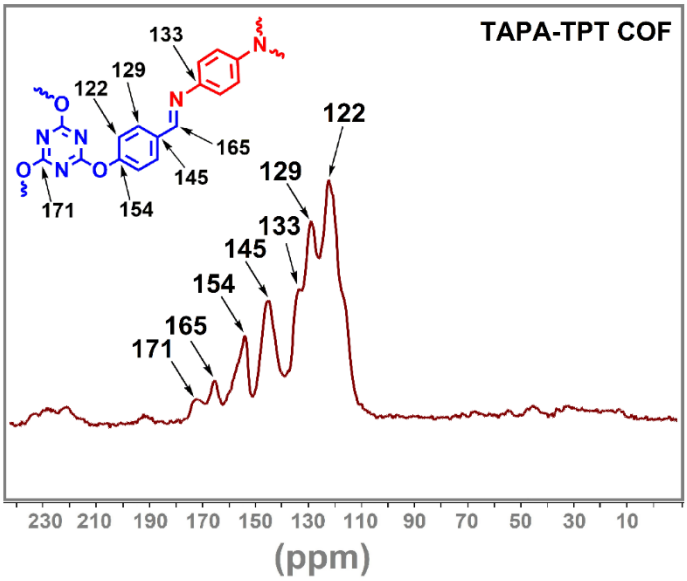

Figure S20. ^{13}C CP/MAS NMR spectra of TAPA-TPT COF.

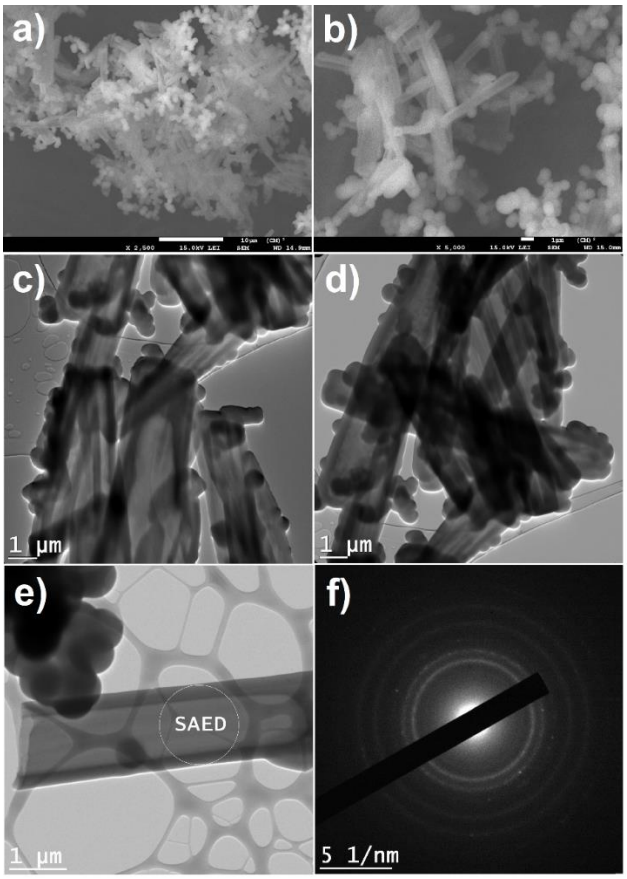

Figure S21. SEM (a-c), TEM images (d-h) and corresponding SAED pattern of the TAPA-TPT COF (i).

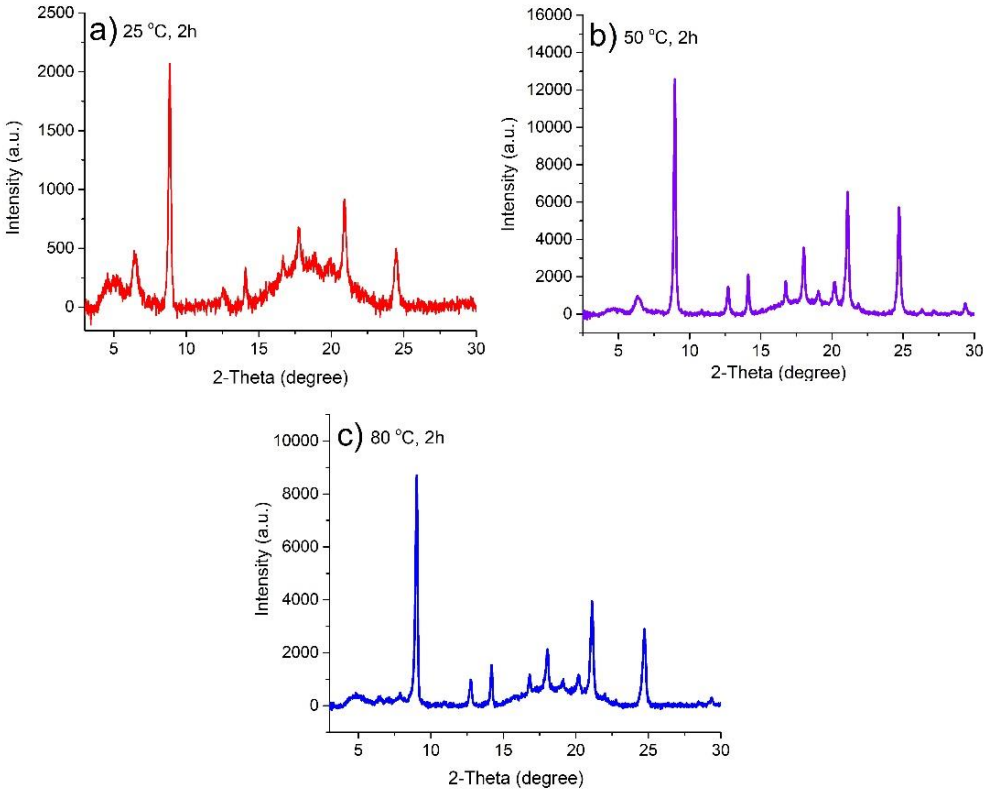

Figure S22. PXRD patterns of catalytic synthesis of COF-300 in different temperatures (a) 25 °C, (b) 50 °C, and (c) 80 °C.

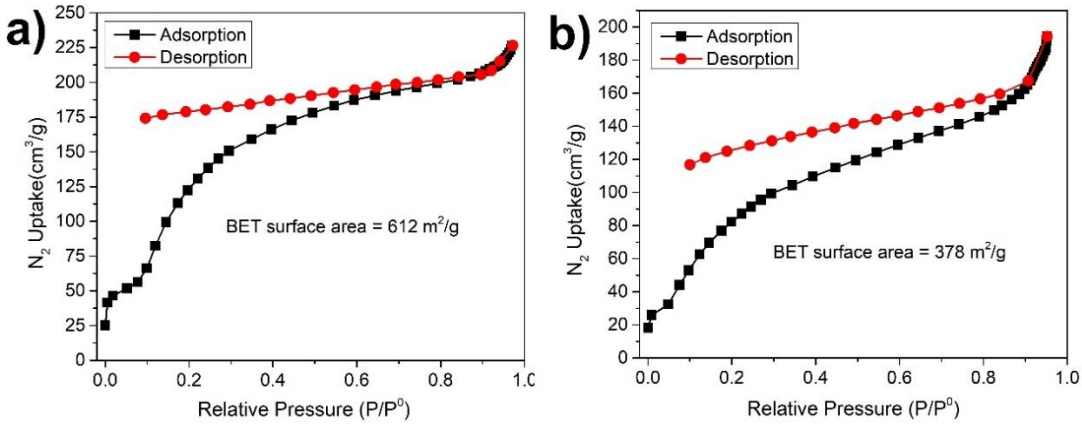

Figure S23. N_2 adsorption-desorption isotherms of prepared COF-300 at 50 °C (a) and 80 °C (b).

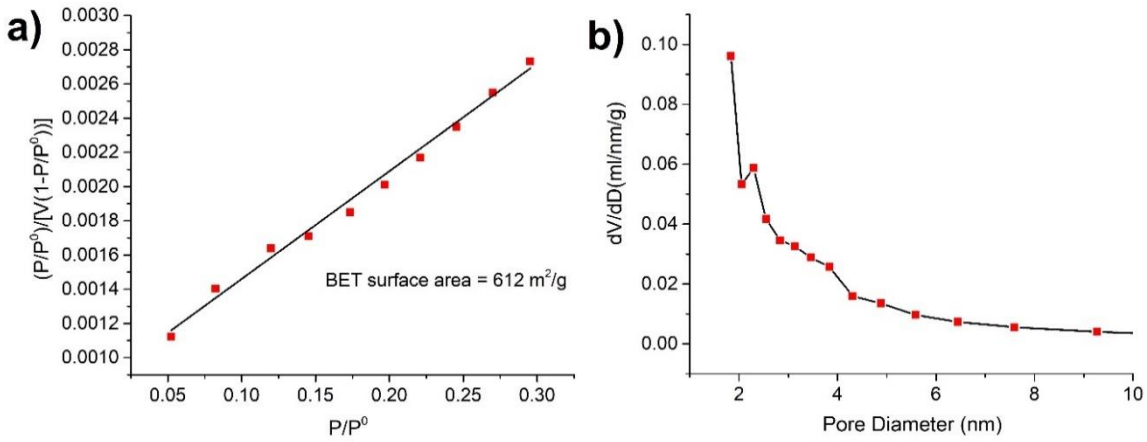

Figure S24. Specific BET surface area (a) and ore size distribution plots of COF-300 (b).

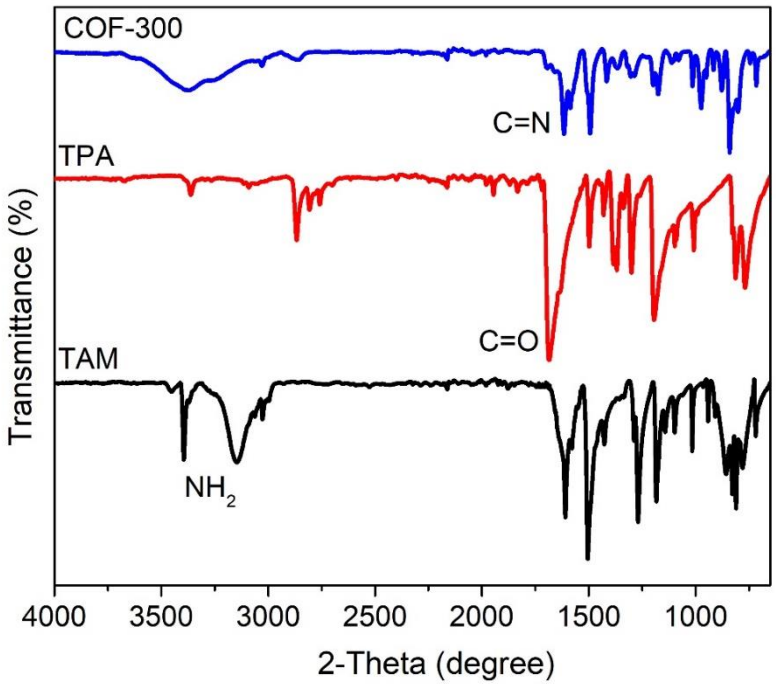

Figure S25. FT-IR spectra of TAM (black spectrum), TPA (red spectrum) and COF-300 (blue spectrum).

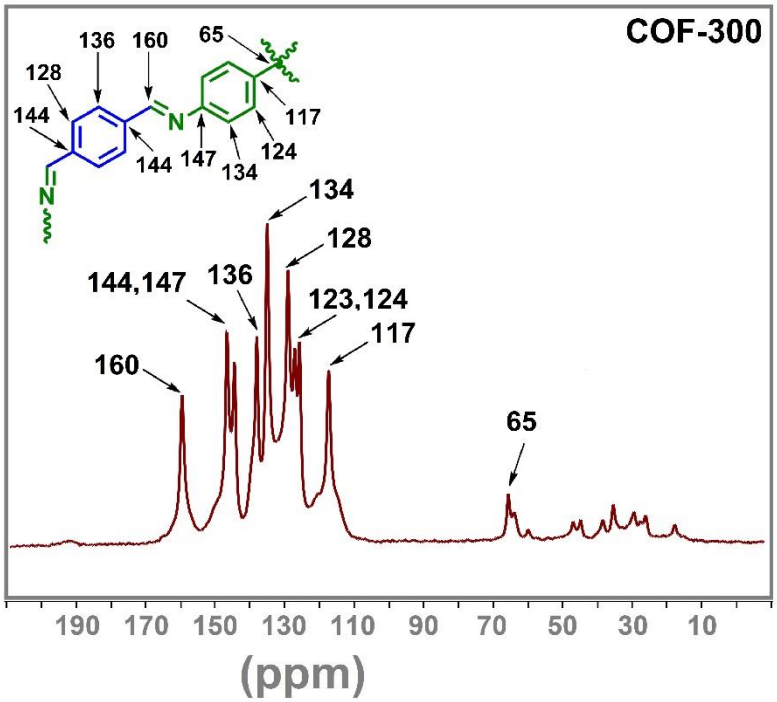

Figure S26. ^{13}C CP/MAS NMR spectra of COF-300.

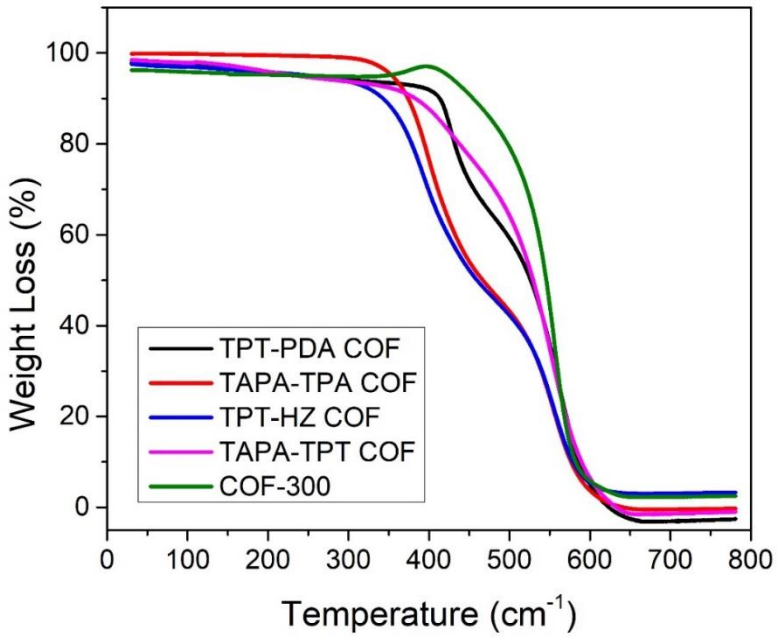

Figure 27. TGA plots of TPT-PDA COF (black curve), TPT-HZ COF (blue curve), TAPA-TPA COF (red curve), COF-300 (green curve), and TAPA-TPT COF (pink curve).

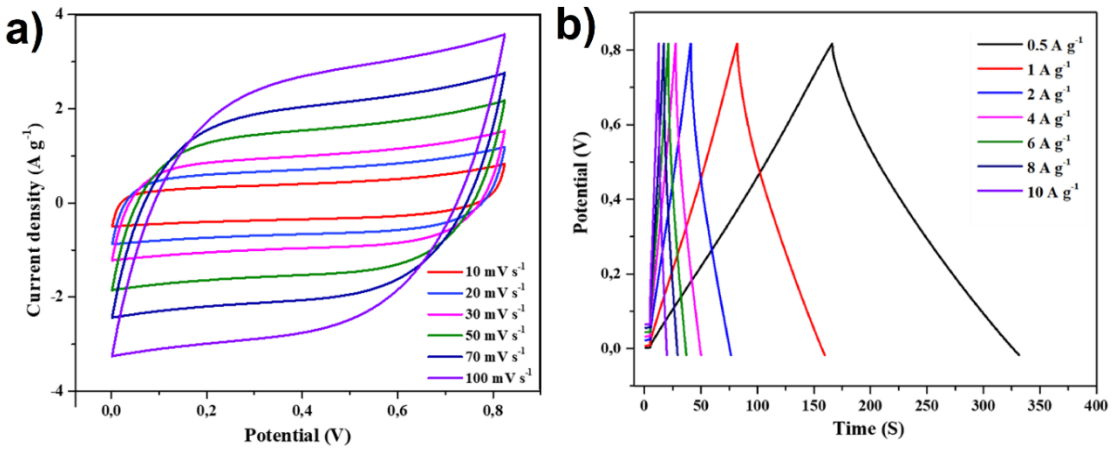

Figure S28. Electrochemical performance of the TAPA-TPT COF (prepared with traditional method) electrode in 1M H_2SO_4, measured using a three-electrode system: (**a**) CV curves recorded at various scan rates, (**b**) galvanostatic charge-discharge curves recorded at various current density.

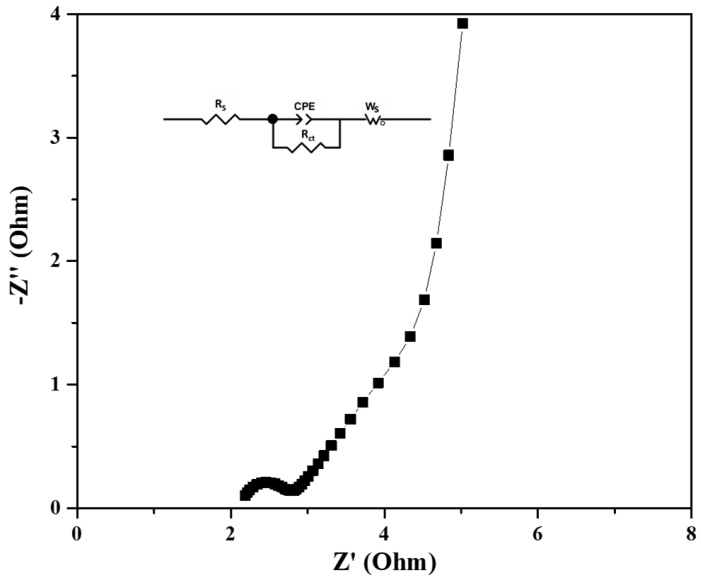

Figure 29. Nyquist plots of TAPA-TPT COF electrode over the frequency range from 0.01 Hz to 100 kHz.

ANNEXE C

INFORMATIONS COMPLÉMENTAIRES

Size-Dependent Catalytic Activity of Palladium Nanoparticles Decorated on Core-Shell Magnetic Microporous Organic Networks

Amir Khojastehnezhad[a], Hichem Gamraoui[a], Maziar Jafari[a], Zhiyuan Peng[a], Farid Moeinpour[b], and Mohamed Siaj[a*]

Email: siaj.mohamed@uqam.ca

[a]*Department of Chemistry, University of Quebec at Montreal, Montreal, QC H3C3P8, Canada*
[b]*Department of Chemistry, Bandar Abbas Branch, Islamic Azad University, Bandar Abbas, Iran*

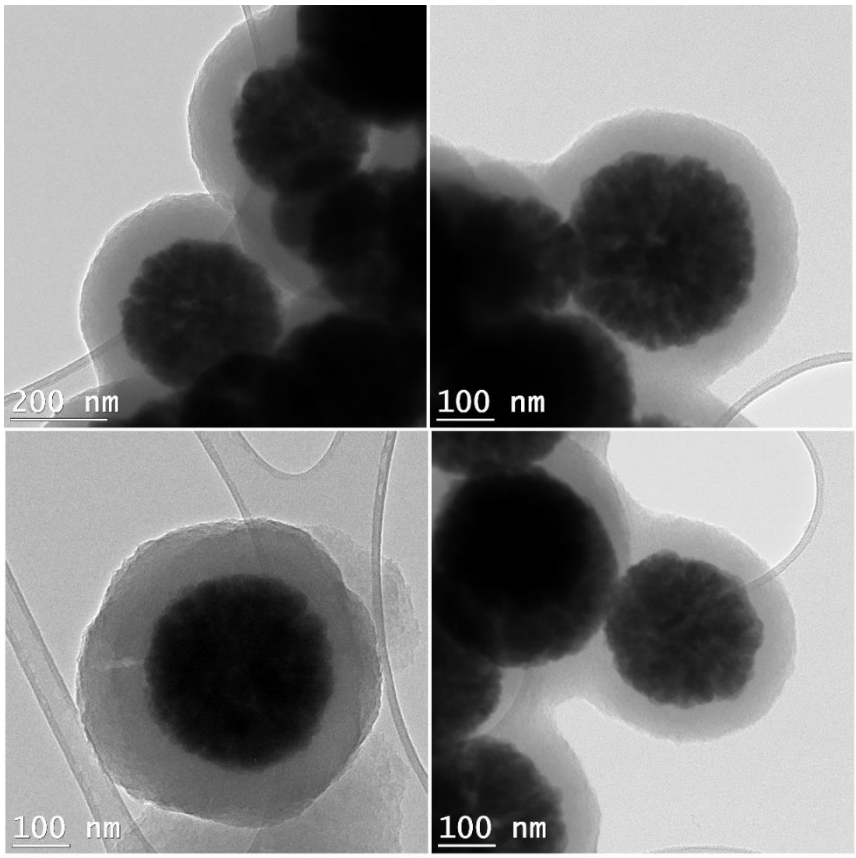

Fig. S1. TEM images of core-shell Fe_3O_4@MON.

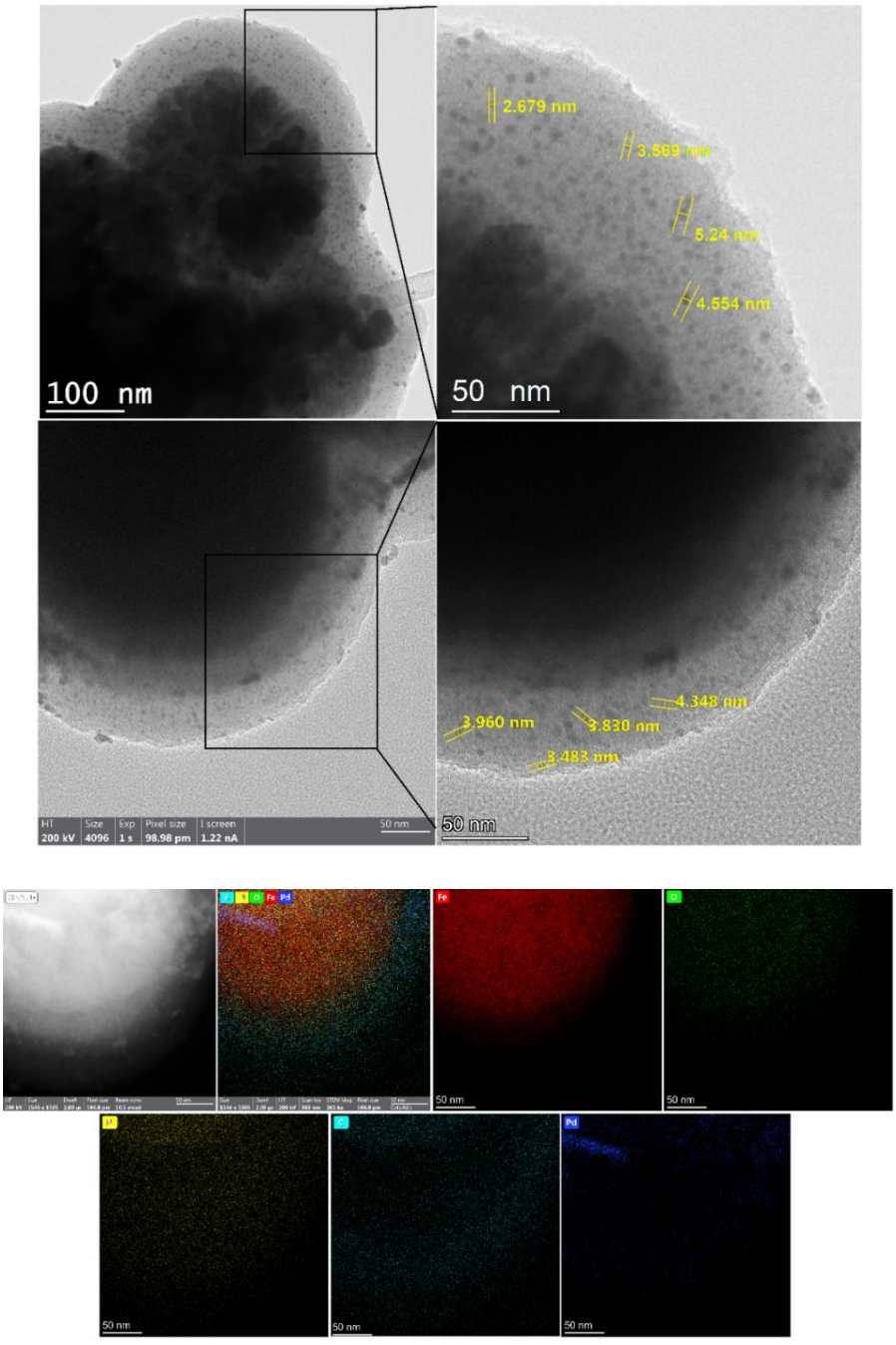

Fig. S2. HR-TEM and TEM mapping images of catalyst-1 (Pd sizes between 1 to 5 nm).

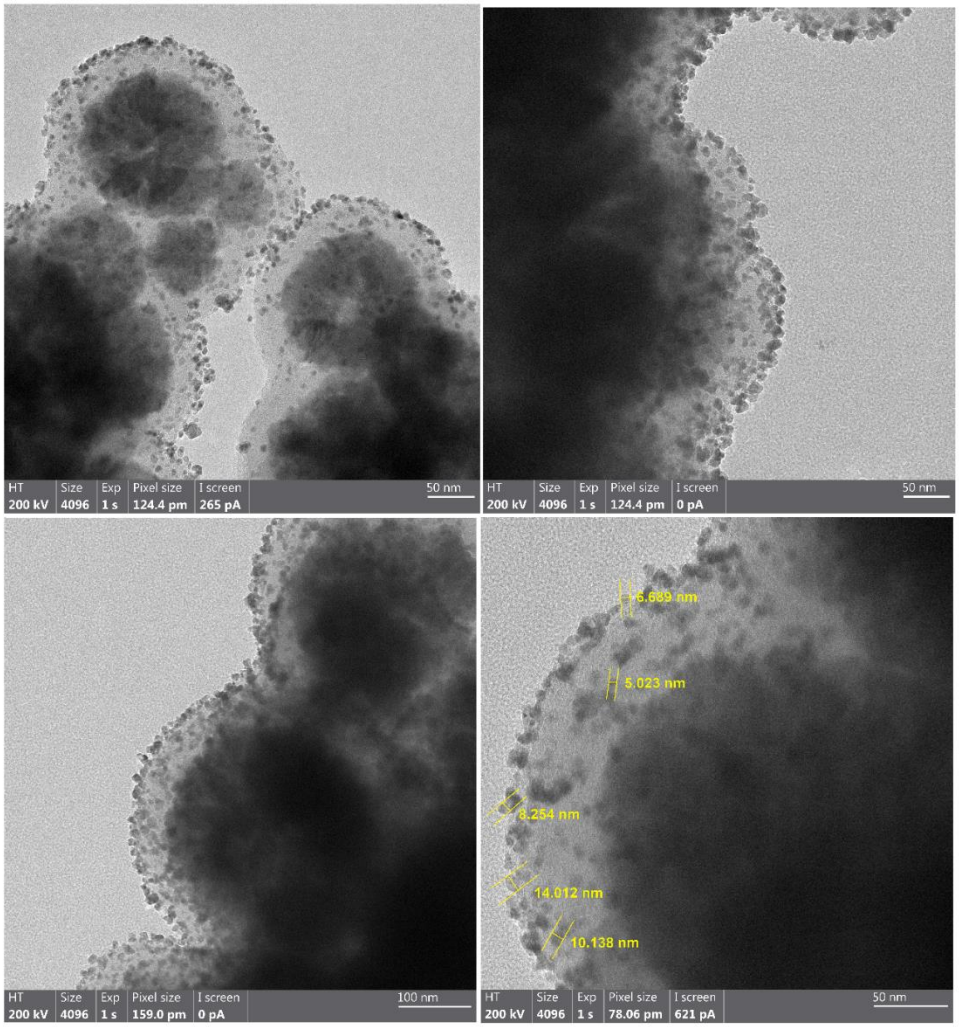

Fig. S3. TEM and HR-TEM images of catalyst-2 (Pd sizes between 5 to 15 nm).

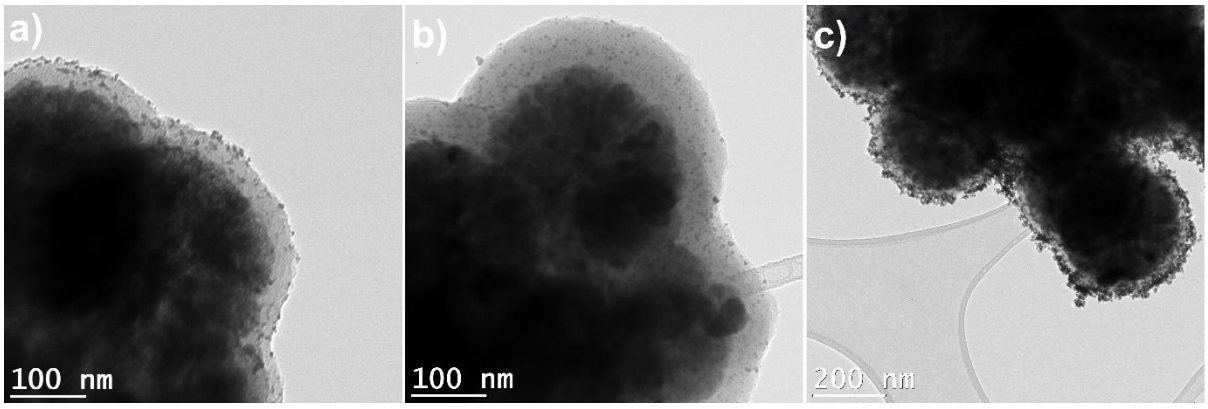

Fig. S4. TEM images of Fe_3O_4@MON-Pd-1 with different Pd concentrations; low (**a**), medium (**b**) and high (**c**) concentrations.

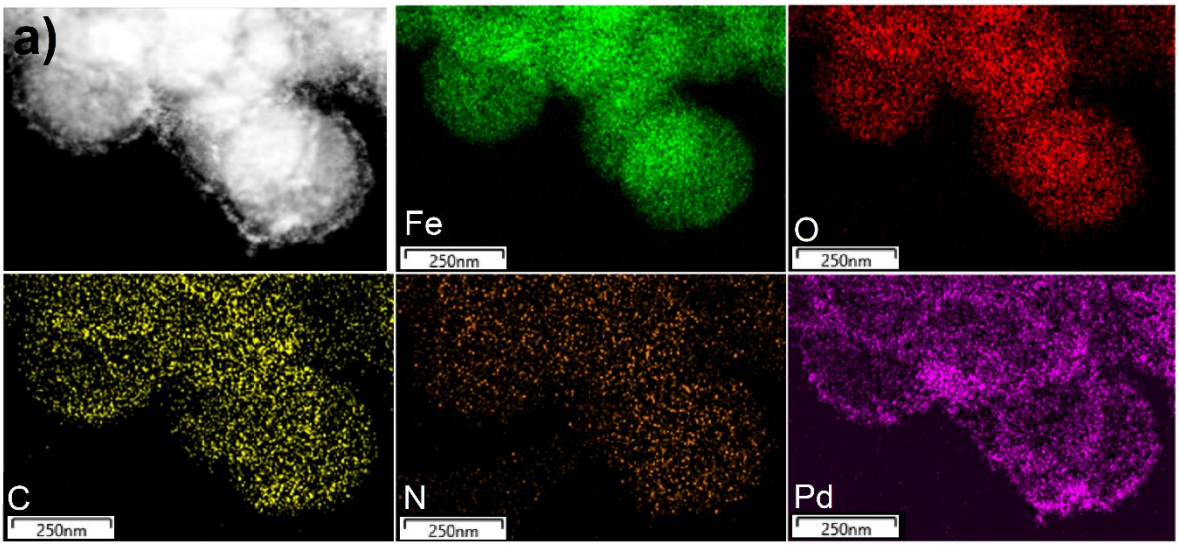

Fig. S5. TEM mapping images of Fe_3O_4@MON-Pd-1 (high Pd concentration).

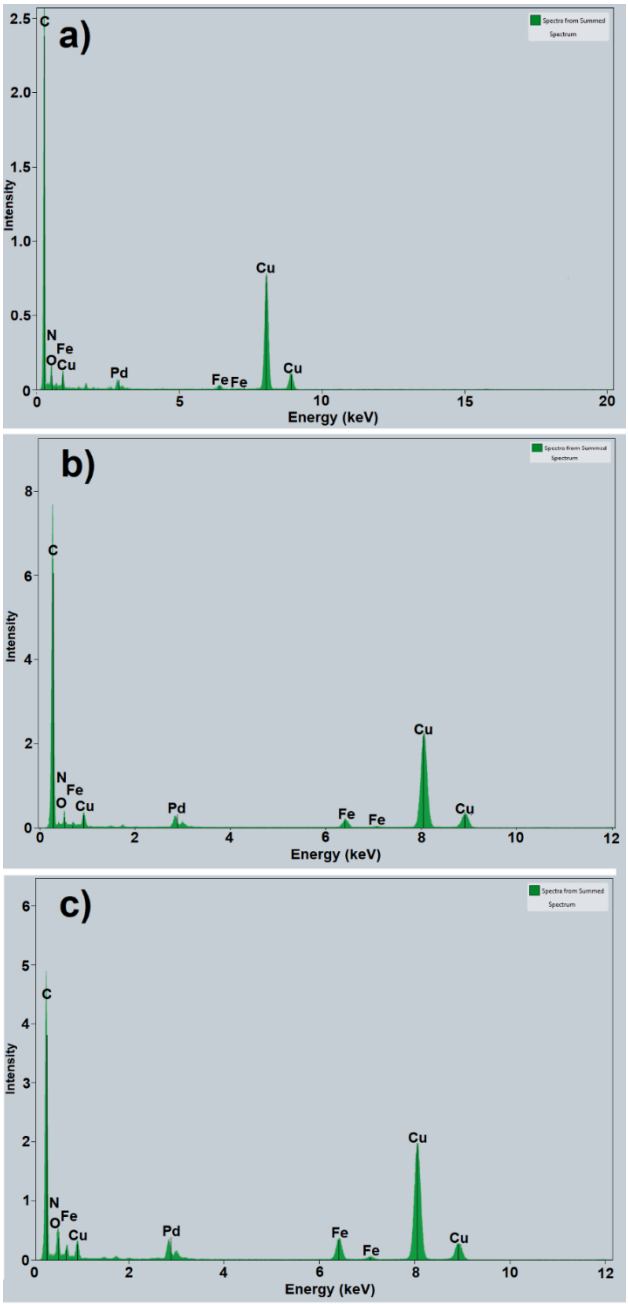

Fig. S6. EDX spectrum of Fe_3O_4@MON-Pd-1 with different Pd concentrations; low (**a**), medium (**b**) and high (**c**) concentrations.

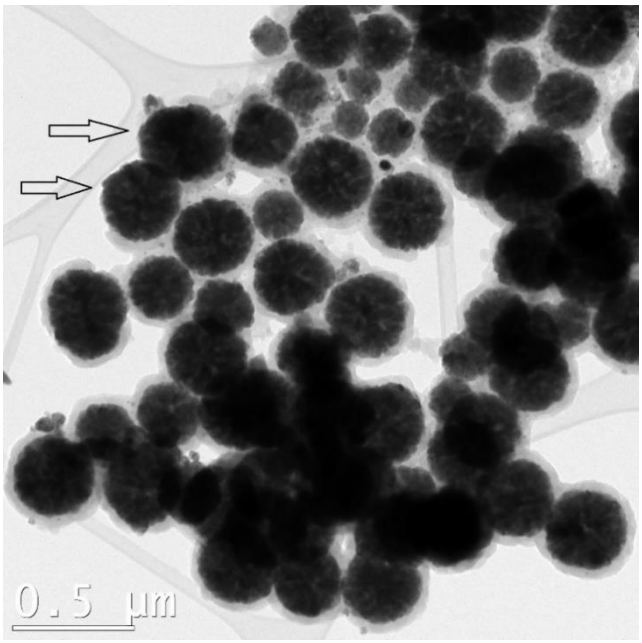

Fig. S7. TEM image of core-shell Fe_3O_4@MON NPs (some Fe_3O_4 NPs are not covered by MON shell material).

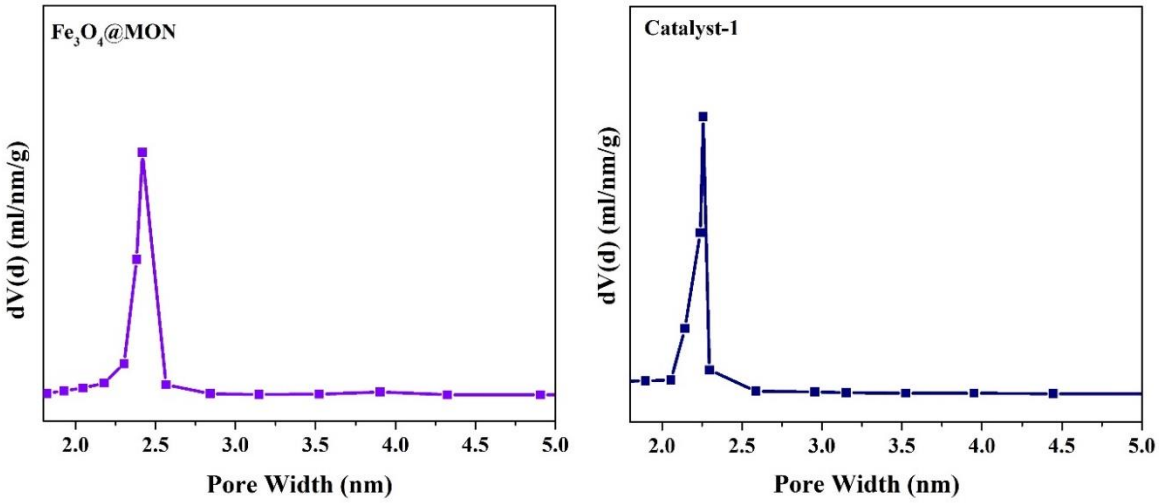

Fig. S8. Pore size distributions of Fe_3O_4@MON (purple curve) and catalyst-1 (blue curve).

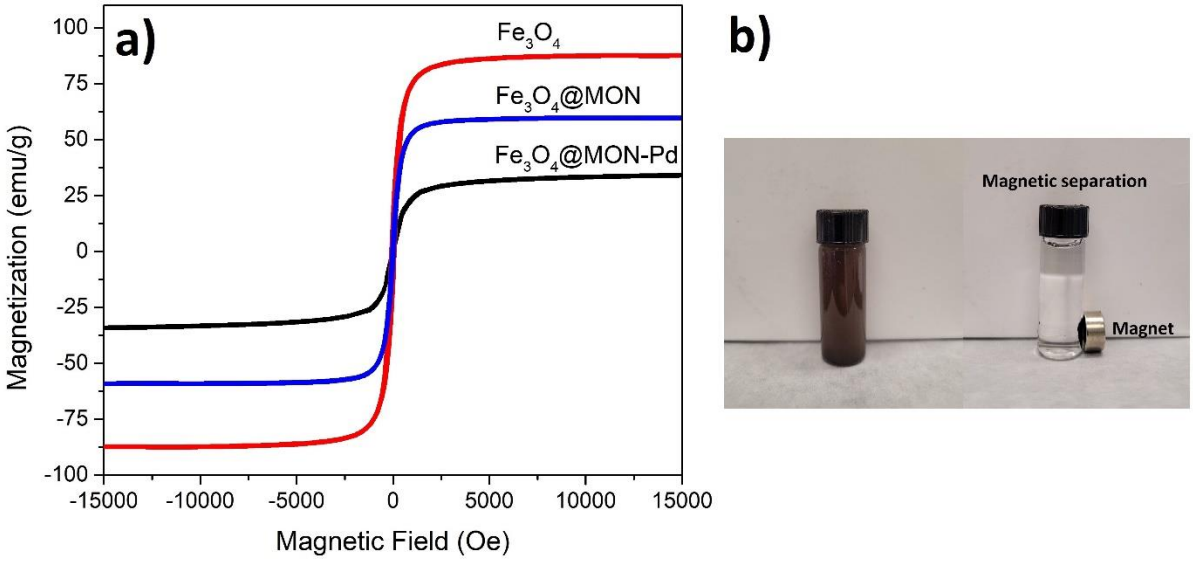

Fig. S9. Magnetization curves of Fe_3O_4, Fe_3O_4@MON and Fe_3O_4@MON-Pd-1 at room temperature.

ANOVA Summary

Source	Degrees of Freedom DF	Sum of Squares SS	Mean Square MS	F-Stat	P-Value
Between Groups	1	38.0012	38.0012	18.9848	0.0121
Within Groups	4	8.0067	2.0017		
Total:	5	46.0078			

Table S1

Group 1 (% yields in case of Catalyst-1-MC): 99, 99.1, 99
Group 2 (% yields in case of Catalyst-1-HC): 94, 92, 96

Table S2

Data summary

Groups	N	Mean	Std. Dev.	Std. Error
Group 1	3	99.0333	0.0577	0.0333
Group 2	3	94	2	1.1547

Table S3. Screening of the reaction condition for the Suzuki cross-coupling reaction (**3a**)[a]

Entry	Solvent	Base	Temp. (°C)	Time (min)	Yield (%)[b]
1	H_2O/EtOH (1:1)	K_2CO_3	25	30	99
2	H_2O/EtOH (1:1)	K_2CO_3	50	20	88
3	H_2O/EtOH (1:1)	K_2CO_3	100	20	91
4	----	K_2CO_3	25	30	84
5	THF	K_2CO_3	25	30	71
6	DMF	K_2CO_3	25	30	58
7	Dioxane	K_2CO_3	25	30	69
8	MeOH	K_2CO_3	25	30	84
9	EtOH	K_2CO_3	25	30	92
10	H_2O	K_2CO_3	25	30	90
11	H_2O/EtOH (1:2)	K_2CO_3	25	30	96
12	H_2O/EtOH (2:1)	K_2CO_3	25	30	95
13	H_2O/EtOH (1:1)	K_2CO_3	25	30	99
14	H_2O/EtOH (1:1)	Cs_2CO_3	25	30	89
15	H_2O/EtOH (1:1)	Na_2CO_3	25	30	74
16	H_2O/EtOH (1:1)	NaOH	25	30	66
17	H_2O/EtOH (1:1)	KOH	25	30	75
18	H_2O/EtOH (1:1)	K_3PO_4	25	30	79

[a] Reaction condition: iodobenzene (1.0 mmol), phenylboronic acid (1.2 mmol), base (2.0 mmol), catalyst-1-MC (0.2 mol%) and solvent (5.0 mL). [b] Isolated Yield.

Table S4. Screening of the reaction condition for the Sonogashira cross-coupling reaction (**6a**)[a]

Entry	Catalyst	Catalyst Amount (mol%)	Time (min)	Yield (%)[b]	TON/TOF (min^{-1})[c]
1	Catalyst-1-LC[d]	0.3	60	83	276/4.60
2	Catalyst-1-MC[e]	0.2	60	97	485/8.08
3	Catalyst-1-HC[f]	0.2	60	91	460/7.66
4	Catalyst-2-MC	0.2	60	84	420/7.00
5	Catalyst-2-MC	0.3	60	90	300/5.00

[a] Reaction condition: iodobenzene (1.0 mmol), phenylacetylene (1.2 mmol), base (2.0 mmol), and solvent (5.0 mL) at 50 °C. [b] Isolated Yield. [c] Turn Over Number/Turn Over Frequency. [d] Low Pd concentration. [e] Medium Pd concentration. [f] High Pd concentration.

Table S5. Screening of the reaction condition for the Sonogashira cross-coupling reaction (**6a**)[a]

Entry	Solvent	Base	Temp. (°C)	Time (min)	Yield (%)[b]
1	H_2O/EtOH (1:2)	NaOAc	50	30	79
2	H_2O/EtOH (1:2)	NaOAc	25	60	88
3	H_2O/EtOH (1:2)	NaOAc	50	60	97
4	H_2O/EtOH (1:2)	NaOAc	100	60	96
5	----	NaOAc	50	180	58
6	THF	NaOAc	50	60	51
7	DMF	NaOAc	50	60	78
8	Dioxane	NaOAc	50	60	59
9	MeOH	NaOAc	50	60	76
10	EtOH	NaOAc	50	60	84
11	H_2O	NaOAc	50	60	85
12	H_2O/EtOH (1:1)	NaOAc	50	60	87
13	H_2O/EtOH (2:1)	NaOAc	50	60	90
14	H_2O/EtOH (1:2)	NaOAc	50	60	97
15	H_2O/EtOH (1:2)	Cs_2CO_3	50	60	79
16	H_2O/EtOH (1:2)	Na_2CO_3	50	60	81
17	H_2O/EtOH (1:2)	NaOH	50	60	55
18	H_2O/EtOH (1:2)	KOH	50	60	62
19	H_2O/EtOH (1:2)	K_3PO_4	50	60	75

[a] Reaction condition: iodobenzene (1.0 mmol), phenylacetylene (1.2 mmol), base (2.0 mmol), catalyst-1-MC (0.2 mol%) and solvent (5.0 mL). [b] Isolated Yield.

ANNEXE D

INFORMATIONS COMPLÉMENTAIRES

Core-Shell Magnetic Microporous Organic Networks Decorated by Cu Nanoparticles for CO_2 Fixation Reaction

Amir Khojastehnezhad[a], Maryam Rajabzadeh[b], Maziar Jafari[a], Farid Moeinpour[c], Reza Khalifeh[b], Jacques Huot[d], Dongling Ma[e] and Mohamed Siaj[a*]

[a]*Department of Chemistry, University of Quebec at Montreal, Montreal, QC H3C3P8, Canada*

[b]*Department of Chemistry, Shiraz University of Technology, Shiraz, 71555-313, Iran*

[c]*Department of Chemistry, Bandar Abbas Branch, Islamic Azad University, Bandar Abbas, Iran*

[d]*Institut de Recherche sur L'hydrogène, Université du Québec à Trois-Rivières, 3351 Boul. des Forges, Trois-Rivières, QC G9A 5H7, Canada*

[e]*Institut National de la Recherche Scientifique(INRS), Centre Énergie Materiaux et Télécommunications, 1650 Boul. Lionel-Boulet, Varennes, Québec J3X 1P7, Canada*

Spectra Data

4-phenyl-1,3-dioxolan-2-one (Table 2, 3a)

^{1}H NMR ($CDCl_3$, 300 MHz): δ (ppm): 4.33 (t, 1H, *J*= 9Hz), 4.80 (t, 1H, *J*= 9 Hz), 5.68 (t, 1H, *J*= 9Hz), 7.34-7.45 (m, 5H). ^{13}C NMR (75 MHz, $CDCl_3$), δ (ppm): 71.2, 78.0, 125.9, 129.2, 129.7, 135.8, 154.9.

4-(phenoxymethyl)-1,3-dioxolan-2-one (Table 2, 3b)

^{1}H NMR ($CDCl_3$, 300 MHz): δ (ppm): 4.05-4.20 (m, 2H), 4.45-4.58 (m, 2H), 4.93-4.99 (m, 1H), 6.84 (d, 2H, *J*= 9 Hz), 6.95 (t, 1H, *J*= 9 Hz), 7.24 (t, 2H, *J*= 9 Hz). ^{13}C NMR (75 MHz, $CDCl_3$), δ (ppm): 66.2, 66.8, 74.1, 114.6, 122.0, 129.7, 154.6, 157.7.

4-((4-methoxyphenoxy)methyl)-1,3-dioxolan-2-one (Table 2, 3f)

^{1}H NMR ($CDCl_3$, 300 MHz): δ (ppm): 3.78 (s, 3H), 4.14 (d, 2H, *J*= 24Hz), 4.56 (d, 2H, *J*= 21Hz), 5.01 (s, 1H), 6.85 (s, 4H). ^{13}C NMR ($CDCl_3$, 100 MHz): δ (ppm): 55.71, 66.22, 67.82, 74.40, 76.81, 77.44, 114.76, 115.79.

4-((4-isopropylphenoxy) methyl)-1,3-dioxolan-2-one (Table 2, 3g)

^{1}H NMR ($CDCl_3$, 100 MHz): δ (ppm): 1.22 (d, 6H, *J*=6Hz), 2.82-2.93 (m, 1H), 4.12-4.24 (m, 2H), 4.51-4.60 (m, 2H), 4.98-5.05 (m, 1H), 6.84 (d, 2H, *J*= 6), 7.15 (d, 1H, *J*= 9). ^{13}C NMR ($CDCl_3$, 75 MHz): δ (ppm): 24.2, 33.3, 66.3, 67.0, 74.4, 114.5, 127.5, 142.4, 154.9, 155.9.

4-((3-chloro-3-methylphenoxy) methyl)-1,3-dioxolan-2-one (Table 2, 3h)

^{1}H NMR ($CDCl_3$, 300 MHz): δ (ppm): 2.33 (s, 3H), 4.07-4.22 (m, 2H), 3.86-3.89 (m, 1H), 4.49-4.63 (m, 2H), 5.01-5.05 (m, 1H), 6.66-6.69 (m, 1H), 6.79 (s, 1H), 7.23 (s, 1H). ^{13}C NMR ($CDCl_3$, 100 MHz): δ (ppm): 20.27, 55.13, 57.25, 74.24, 113.13, 117.30, 129.76, 137.40, 156.32.

4-((3-methyl-4-nitrophenoxy)methyl)-1,3-dioxolan-2-one (Table 2, 3i)

^{1}H NMR ($CDCl_3$, 300 MHz): δ (ppm): 2.64 (s, 3H), 3.77 (dd, 1H, J_1= 6 Hz, J_2= 6 Hz), 3.86- 3.89 (m, 1H), 4.12-4.15 (m, 3H), 6.84 (d, 2H, *J*= 6Hz), 8.09 (d, 1H, *J*= 6Hz). ^{13}C NMR ($CDCl_3$, 100 MHz): δ (ppm): 21.66, 63.38, 69.49, 70.15, 77.047, 77.35, 112.35, 117.94, 127.57, 137.14, 161.89.

(2-oxo-1,3-dioxolan-4-yl)methyl methacrylate (Table 2, 3j)

^{1}H NMR ($CDCl_3$, 300 MHz): δ (ppm): 1.88 (s, 3H), 4.23-4.40 (m, 3H), 4.53 (t, 1H, *J*= 9 Hz), 4.90-4.97 (m, 1H), 5.60 (s, 1H), 6.08 (s, 1H). ^{13}C NMR (75 MHz, $CDCl_3$), δ (ppm): 18.1, 63.4, 66.1, 73.8, 127.3, 135.1, 154.5, 166.7.

hexahydrobenzo[d][1,3]dioxol-2-one (Table 2, 3l)

^{1}H NMR ($CDCl_3$, 300 MHz): δ (ppm): 1.28-1.34 (m, 2H), 1.42-1.46 (m, 2H), 1.71-1.77 (m, 4H), 4.59 (s, 2H). ^{13}C NMR (75 MHz, $CDCl_3$), δ (ppm): 18.9, 26.2, 74.7, 155.2.

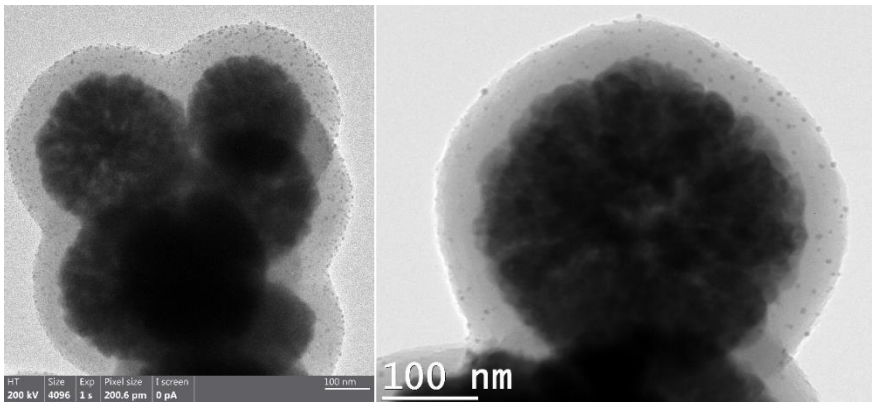

Fig. S1. HR-TEM images of MNP@MON-Cu/CuO/Cu_2O.

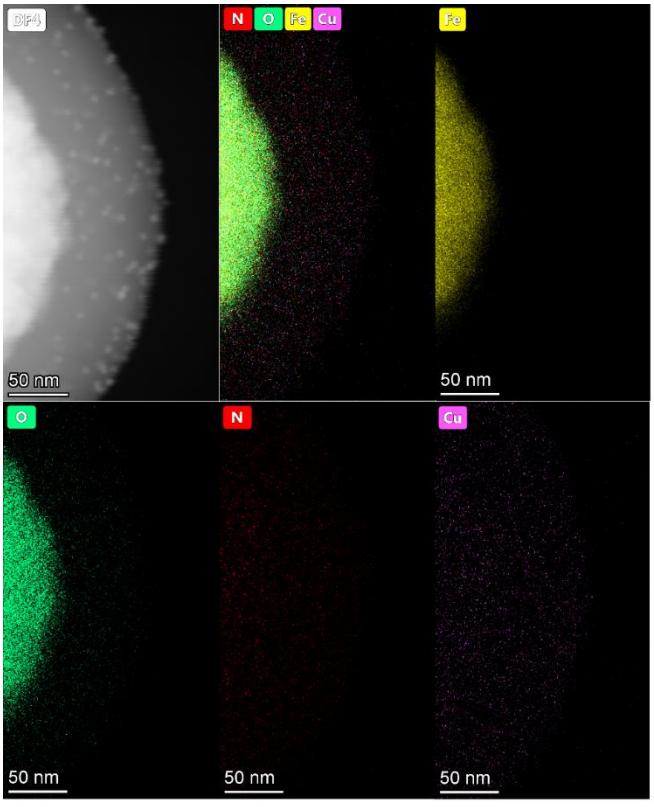

Fig. S2. HR-TEM mapping of MNP@MON-Cu/CuO/Cu_2O.

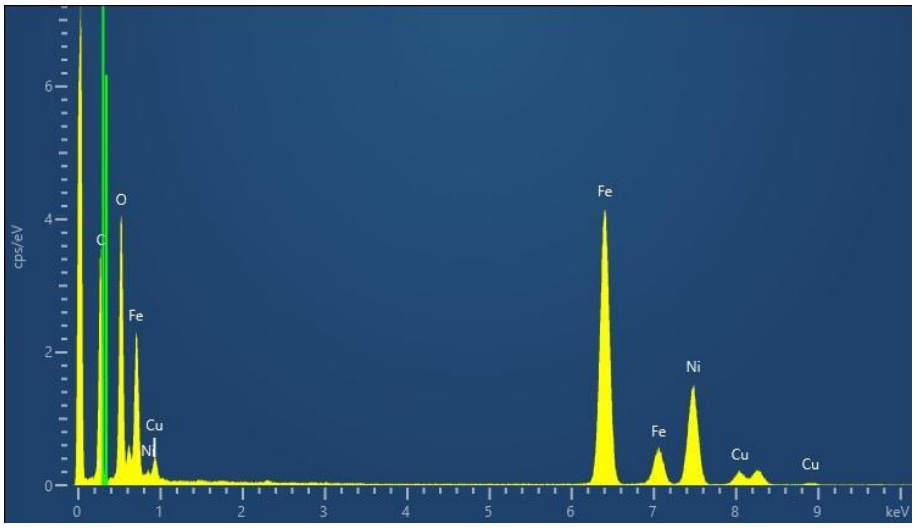

Fig. S3. EDX spectrum of MNP@MON-Cu/CuO/Cu_2O.

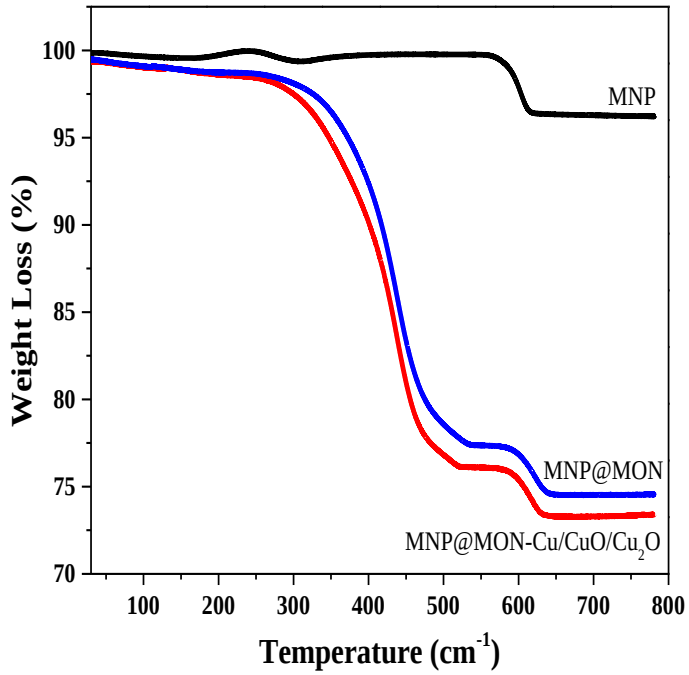

Fig. S4. TGA plot of (a) Fe_3O_4 MNP, (b) MNP@MON and (c) MNP@MON-Cu/CuO/Cu_2O.

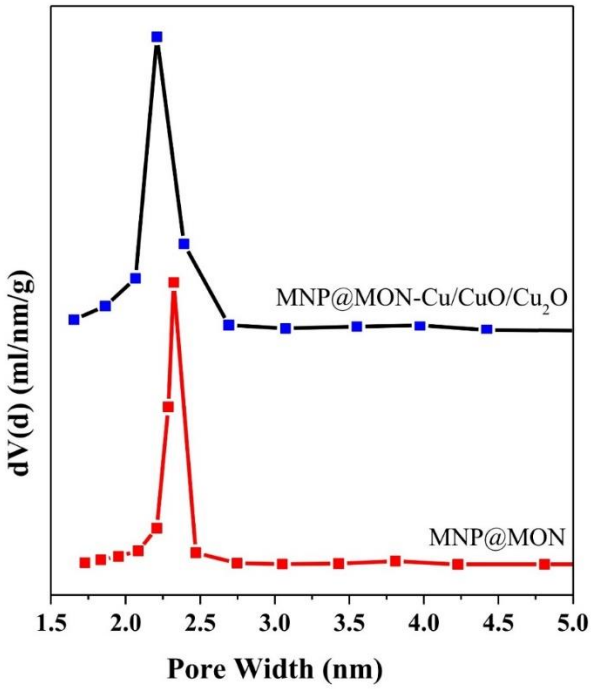

Fig. S5. Pore size distribution of MNP@MON and MNP@MON-Cu/CuO/Cu_2O.

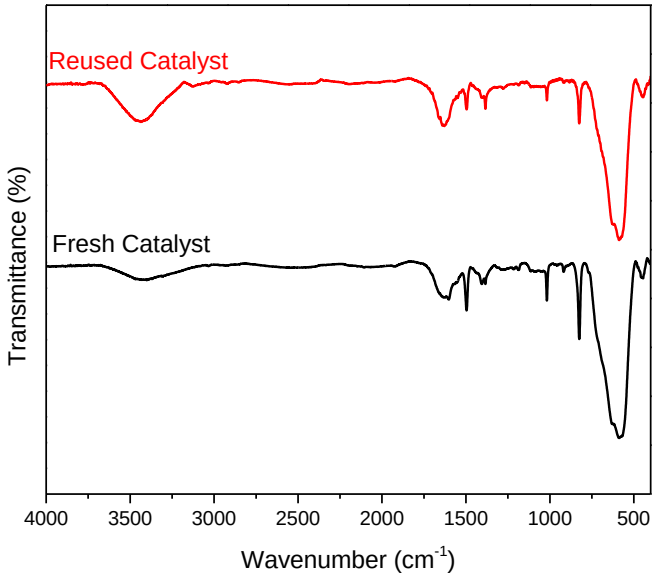

Fig. S6. FT-IR spectrum of fresh and reused MNP@MON-Cu/CuO/Cu_2O.

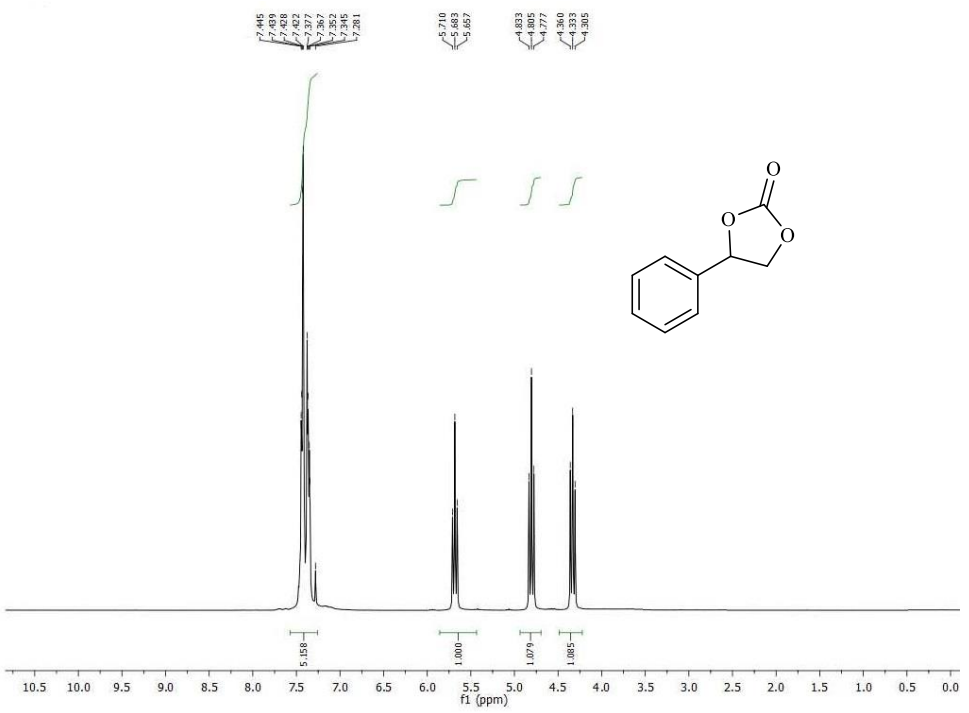

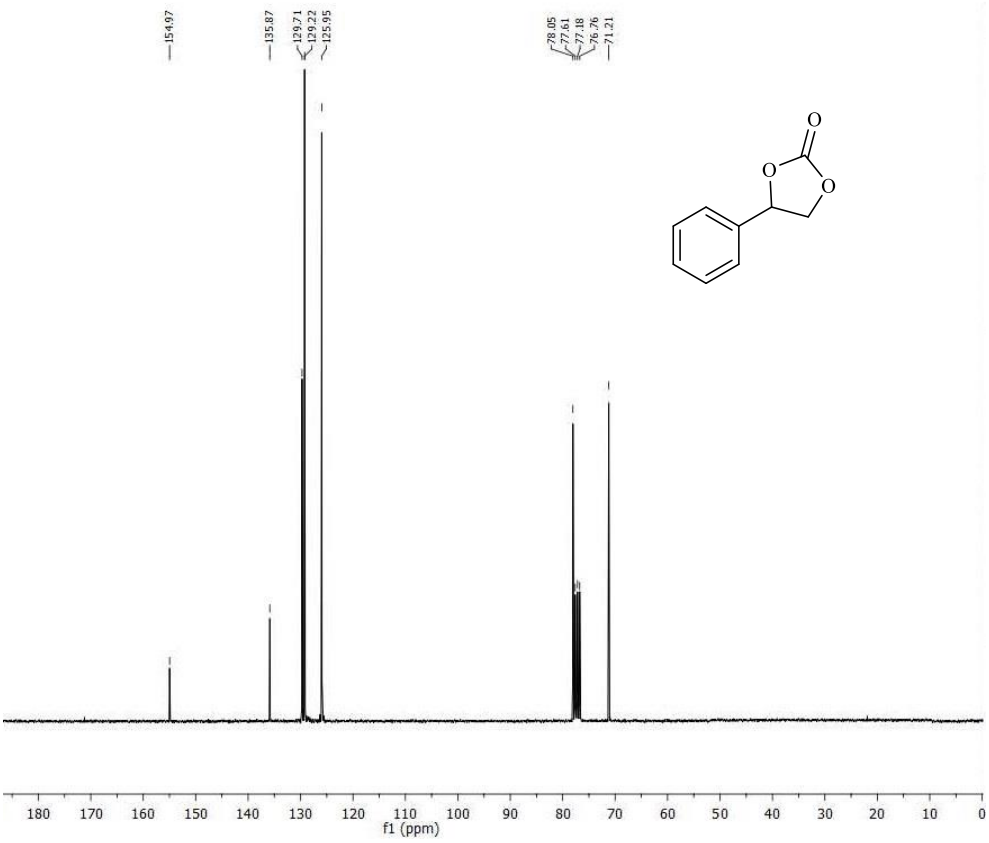

^{1}H and ^{13}C NMR spectrum of (Table 2, **3a**).

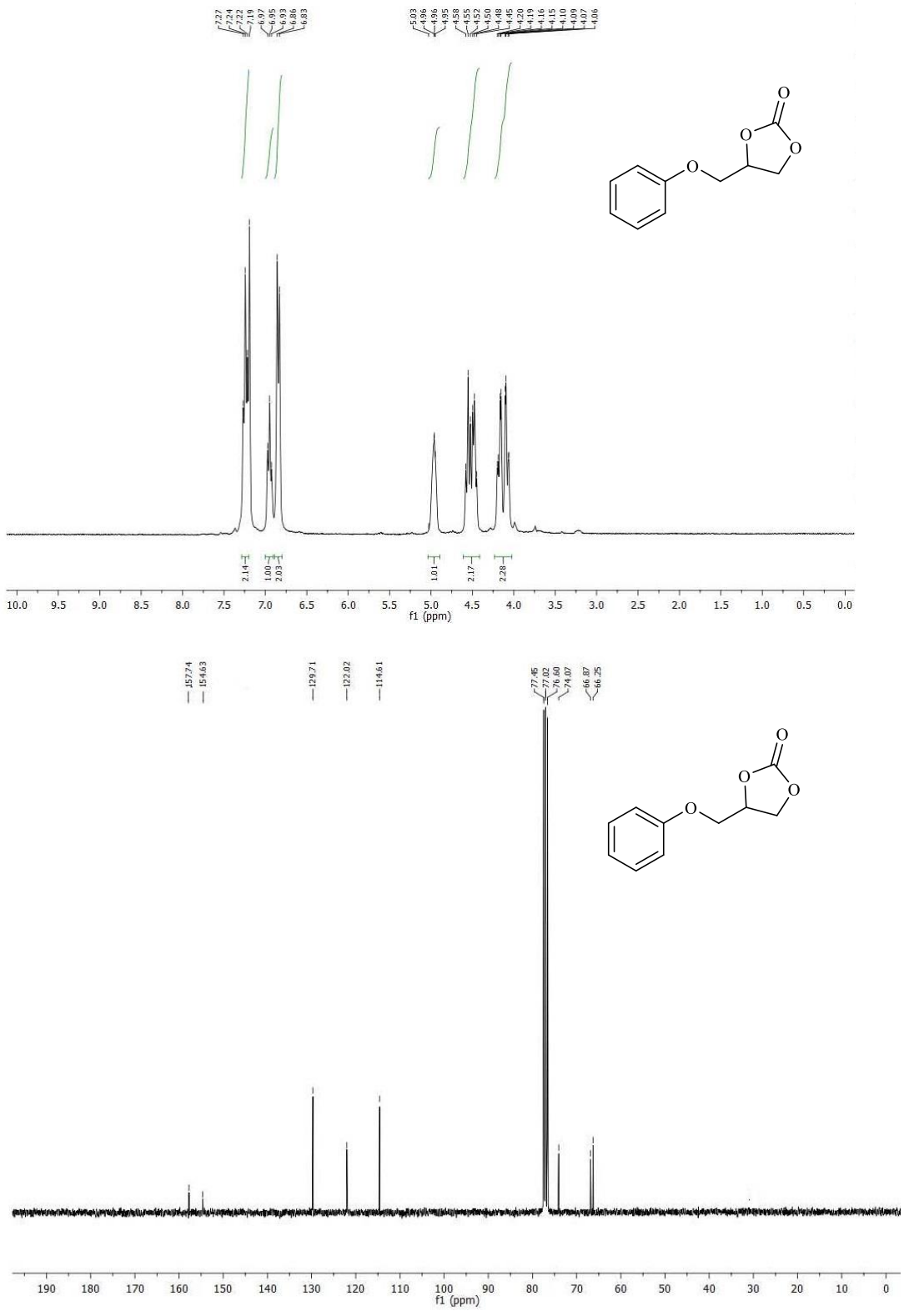

^{1}H and ^{13}C NMR spectrum of (Table 2, **3b**).

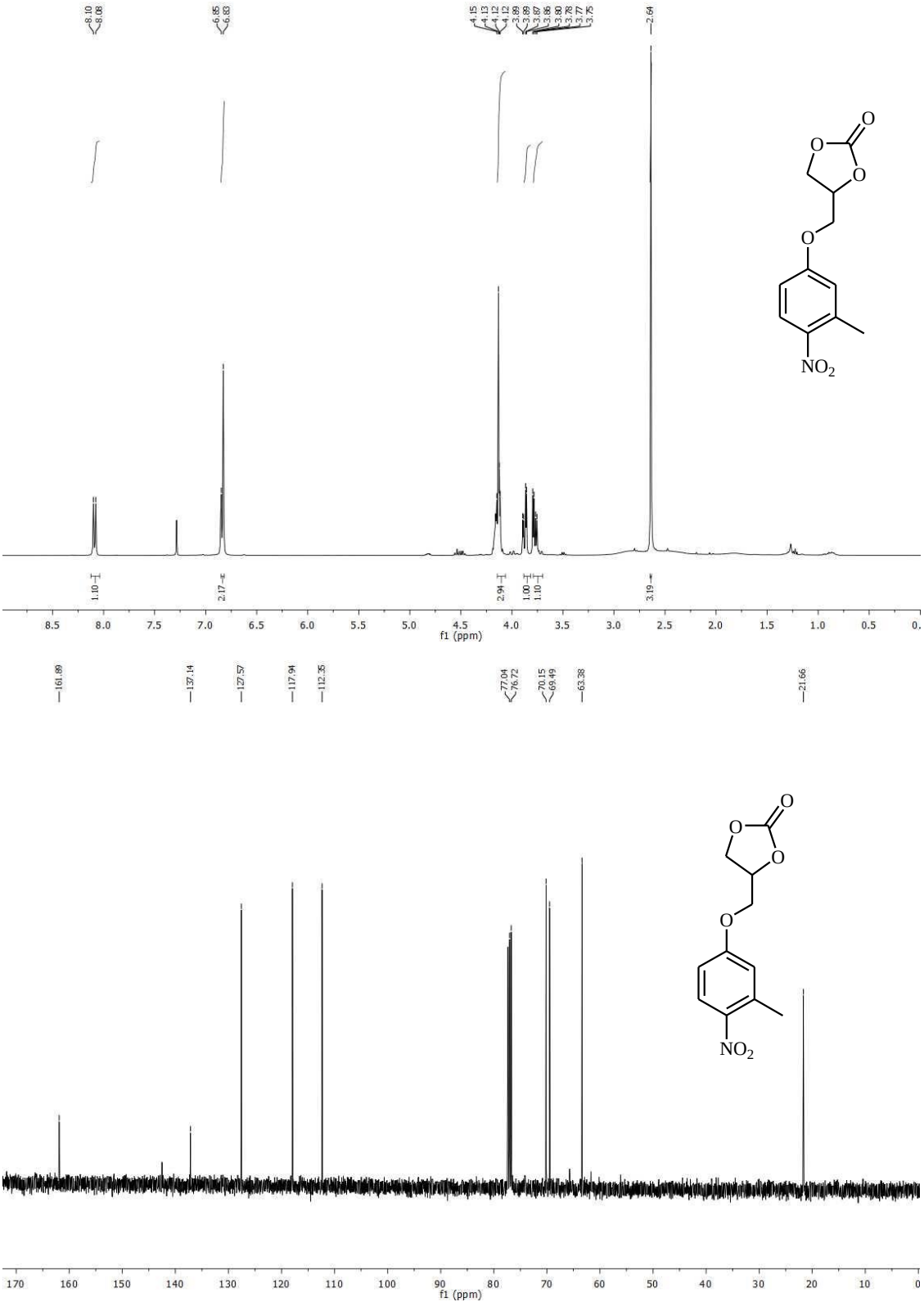

^{1}H and ^{13}C NMR spectrum of (Table 2, **3i**).

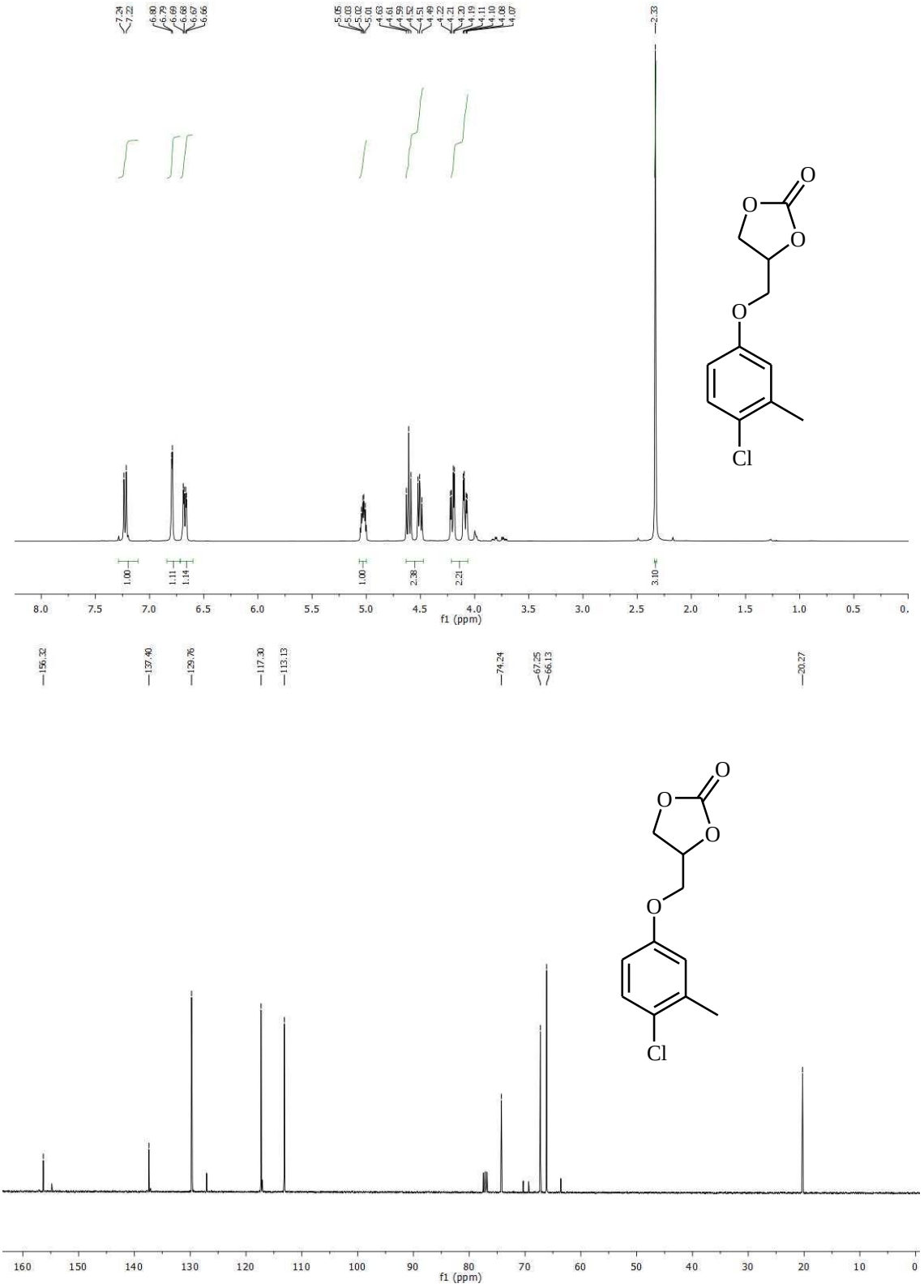

^{1}H and ^{13}C NMR spectrum of (Table 2, **3h**).

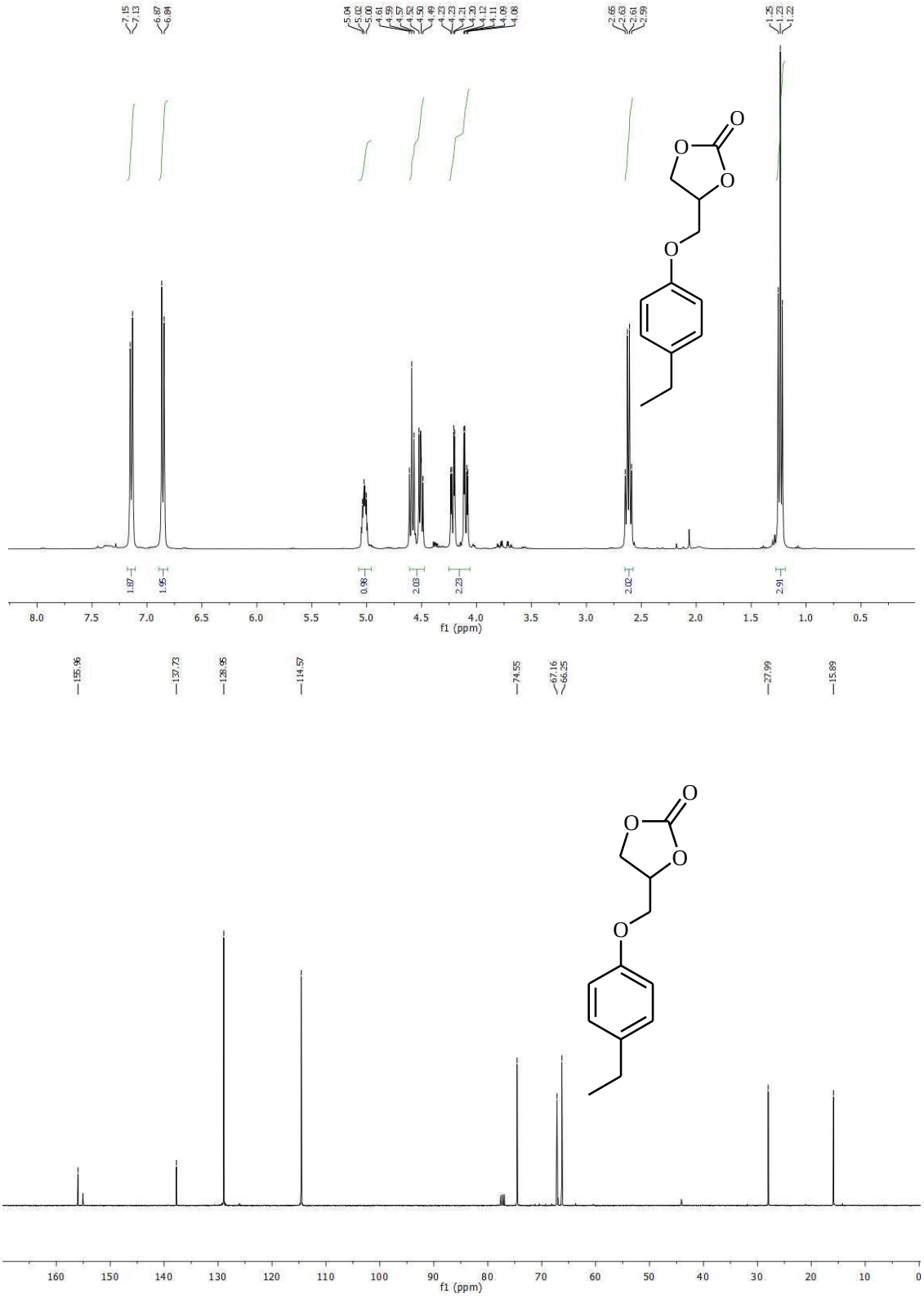

^{1}H and ^{13}C NMR spectrum of (Table 2, **3g**).

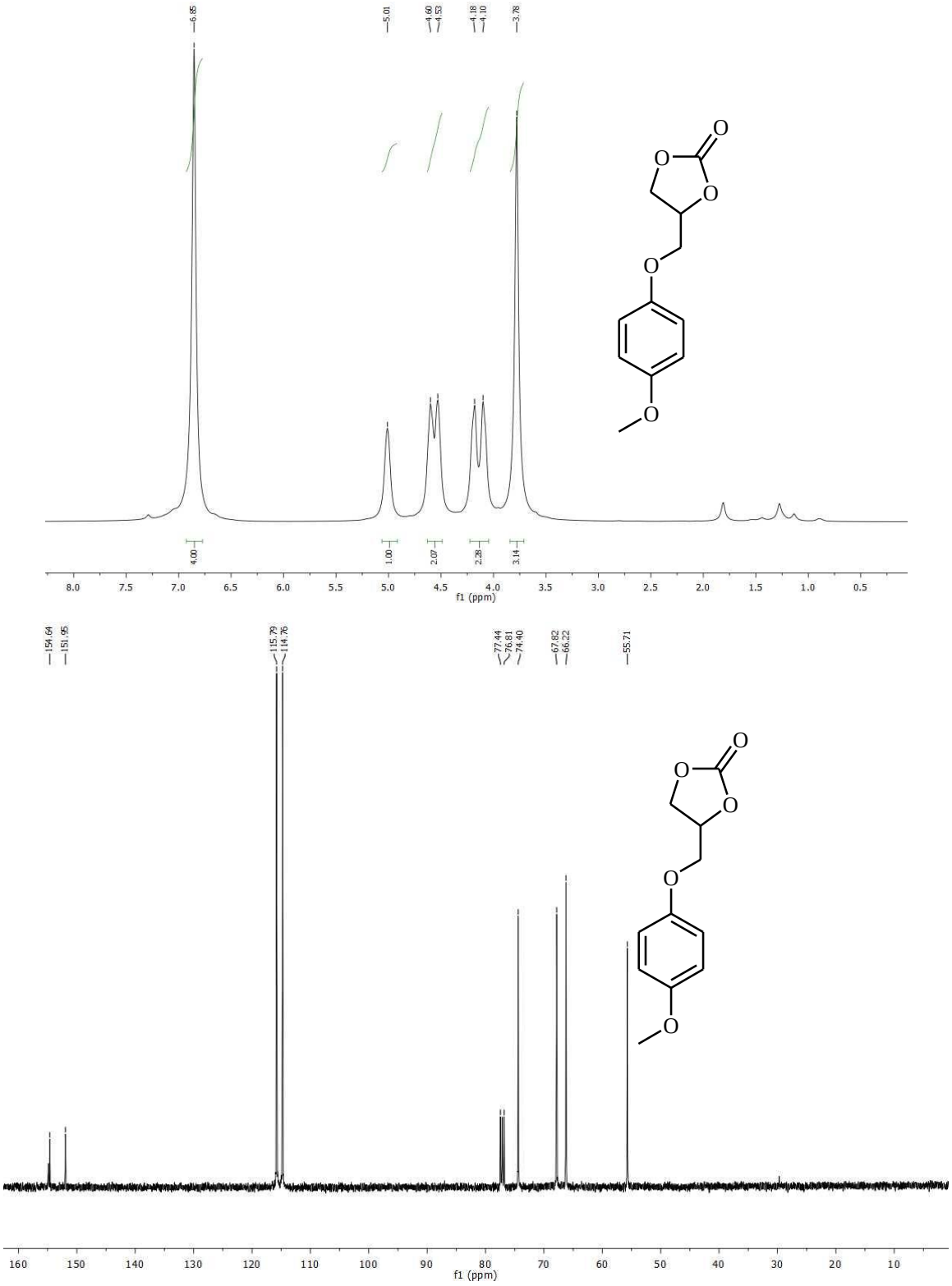

^{1}H and ^{13}C NMR spectrum of (Table 2, **3f**).

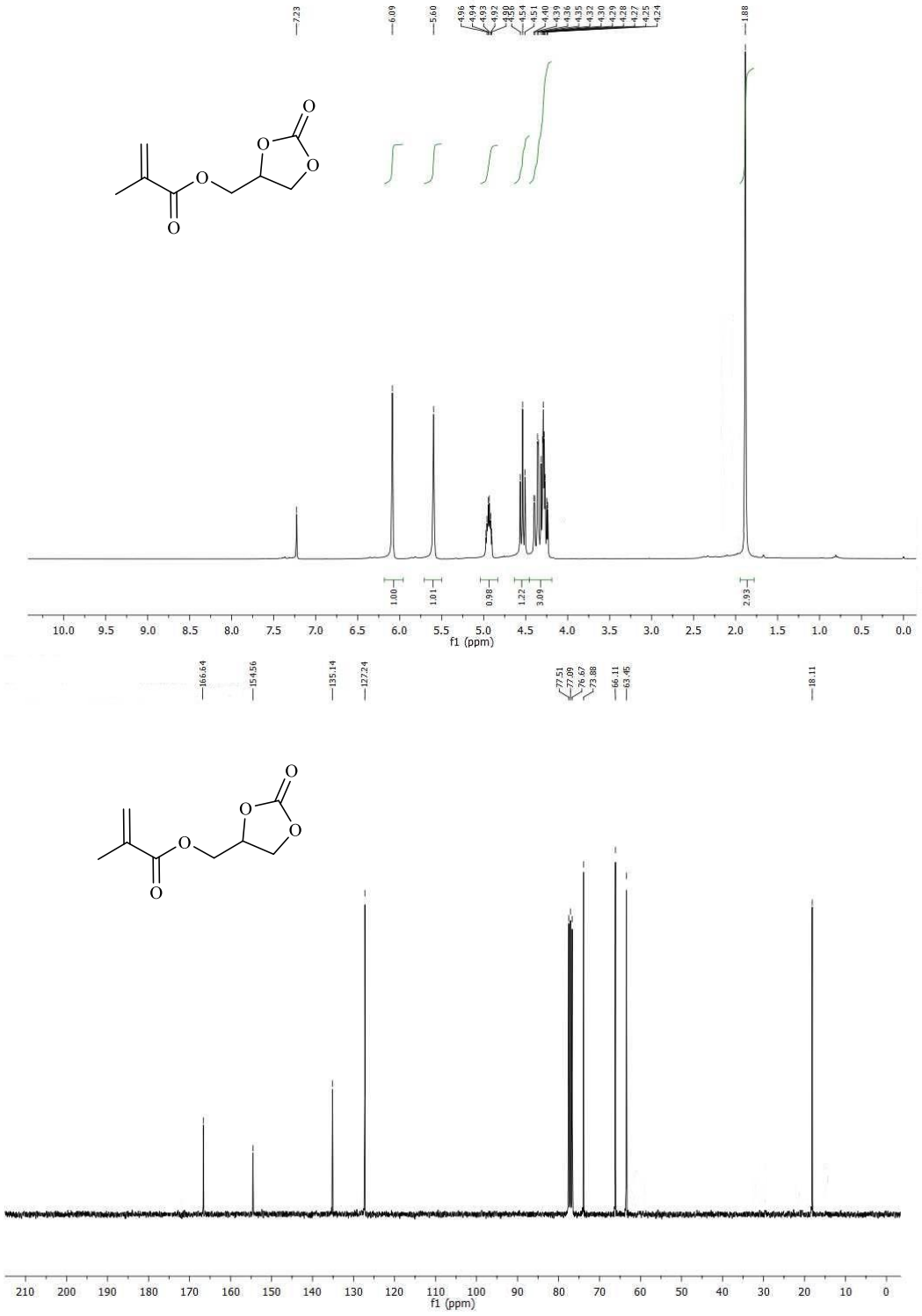

^{1}H and ^{13}C NMR spectrum of (Table 2, **3j**).

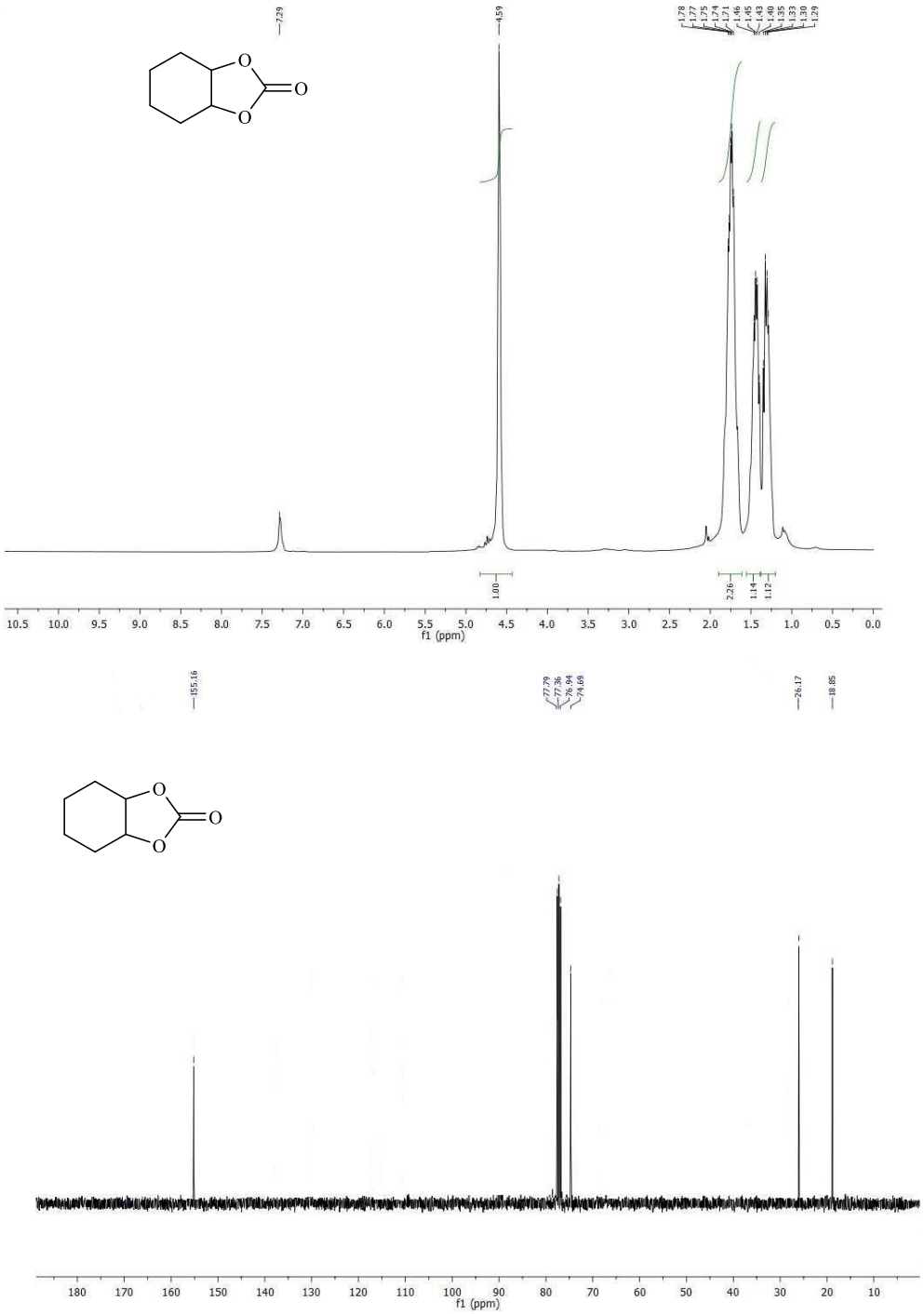

^{1}H and ^{13}C NMR spectrum of (Table 2, **3l**).

BIBLIOGRAPHIE

[1] a) S.-Y. Ding, W. J. C. S. R. Wang, *Chem. Soc. Rev.* **2013**, *42*, 548-568; b) M. S. Lohse, T. J. A. F. M. Bein, *Adv. Funct. Mater.* **2018**, *28*, 1705553; c) J. Wang, S. J. C. C. R. Zhuang, *Coord. Chem. Rev.* **2019**, *400*, 213046.

[2] a) S. Lu, Y. Hu, S. Wan, R. McCaffrey, Y. Jin, H. Gu, W. J. J. o. t. A. C. S. Zhang, *J. Am. Chem. Soc.* **2017**, *139*, 17082-17088; b) Z. Kang, Y. Peng, Y. Qian, D. Yuan, M. A. Addicoat, T. Heine, Z. Hu, L. Tee, Z. Guo, D. J. C. o. M. Zhao, *Chem. Mater.* **2016**, *28*, 1277-1285; c) S. Wang, Q. Wang, P. Shao, Y. Han, X. Gao, L. Ma, S. Yuan, X. Ma, J. Zhou, X. J. J. o. t. A. C. S. Feng, *J. Am. Chem. Soc.* **2017**, *139*, 4258-4261; d) D. M. Maklavany, Z. Rouzitalab, M. Bazmi, M. Askarieh, A. J. A. S. C. Nabavi-Pelesaraei, Engineering, *ACS Sustain. Chem. Eng.* **2023**.

[3] a) P. J. Waller, F. Gándara, O. M. Yaghi, *Acc. Chem. Res.* **2015**, *48*, 3053-3063; b) P. J. Waller, F. Gándara, O. M. J. A. o. c. r. Yaghi, *Acc. Chem. Res.* **2015**, *48*, 3053-3063.

[4] a) Z. Li, X. Feng, Y. Zou, Y. Zhang, H. Xia, X. Liu, Y. J. C. C. Mu, *Chem. Commun.* **2014**, *50*, 13825-13828; b) Z. Wang, S. Zhang, Y. Chen, Z. Zhang, S. J. C. S. R. Ma, *Chem. Soc. Rev.* **2020**, *49*, 708-735; c) V. Hasija, S. Patial, P. Raizada, A. A. P. Khan, A. M. Asiri, Q. Van Le, V.-H. Nguyen, P. J. C. C. R. Singh, *Coord. Chem. Rev.* **2022**, *452*, 214298.

[5] A. P. Cote, A. I. Benin, N. W. Ockwig, M. O'Keeffe, A. J. Matzger, O. M. J. s. Yaghi, *Science* **2005**, *310*, 1166-1170.

[6] Q. Guan, G.-B. Wang, L.-L. Zhou, W.-Y. Li, Y.-B. J. N. A. Dong, *Nanoscale Adv.* **2020**, *2*, 3656-3733.

[7] R. Freund, O. Zaremba, G. Arnauts, R. Ameloot, G. Skorupskii, M. Dincă, A. Bavykina, J. Gascon, A. Ejsmont, J. J. A. C. I. E. Goscianska, *Angew. Chem. Int.* **2021**, *60*, 23975-24001.

[8] a) R. Liu, K. T. Tan, Y. Gong, Y. Chen, Z. Li, S. Xie, T. He, Z. Lu, H. Yang, D. J. C. S. R. Jiang, *Chem. Soc. Rev.* **2021**, *50*, 120-242; bN. Huang, P. Wang, D. J. N. R. M. Jiang, *Nat. Rev. Mater.* **2016**, *1*, 1-19.

[9] a) X. Chen, K. Geng, R. Liu, K. T. Tan, Y. Gong, Z. Li, S. Tao, Q. Jiang, D. J. A. C. I. E. Jiang, *Angew. Chem. Int.* **2020**, *59*, 5050-5091; b) Q. Yang, M. Luo, K. Liu, H. Cao, H. J. A. C. B. E. Yan, *Appl. Catal. B* **2020**, *276*, 119174.

[10] J. L. Sheng, H. Dong, X. B. Meng, H. L. Tang, Y. H. Yao, D. Q. Liu, L. L. Bai, F. M. Zhang, J. Z. Wei, X. J. J. C. Sun, *ChemCatChem* **2019**, *11*, 2313-2319.

[11] a) X. Liu, D. Huang, C. Lai, G. Zeng, L. Qin, H. Wang, H. Yi, B. Li, S. Liu, M. J. C. S. R. Zhang, *Chem. Soc. Rev.* **2019**, *48*, 5266-5302; b) J. Liu, N. Wang, L. J. C. A. A. J. Ma, *Chem. Asain J.* **2020**, *15*, 338-351; cP. Ghosh, P. J. C. C. Banerjee, *Chem. Commun.* **2023**.

[12] Y. Li, W. Chen, G. Xing, D. Jiang, L. J. C. S. R. Chen, *Chem. Soc. Rev.* **2020**, *49*, 2852-2868.

[13] W. Huang, Y. Jiang, X. Li, X. Li, J. Wang, Q. Wu, X. J. A. A. M. Liu, Interfaces, *ACS Appl. Mater. Interfaces* **2013**, *5*, 8845-8849.

[14] a) F. Wiesbrock, R. Hoogenboom, U. S. J. M. R. C. Schubert, *Macromol. Rapid Commun.* **2004**, *25*, 1739-1764; b) R. Hoogenboom, U. S. J. M. R. C. Schubert, *Macromol. Rapid Commun.* **2007**, *28*, 368-386; c) N. A. Khan, S. H. J. C. C. R. Jhung, *Coord. Chem. Rev.* **2015**, *285*, 11-23.

[15] N. L. Campbell, R. Clowes, L. K. Ritchie, A. I. J. C. o. M. Cooper, *Chem. Mater.* **2009**, *21*, 204-206.

[16] a) S. T. Emmerling, L. S. Germann, P. A. Julien, I. Moudrakovski, M. Etter, T. Friščić, R. E. Dinnebier, B. V. J. C. Lotsch, *Chem* **2021**, *7*, 1639-1652; b) A. Krusenbaum, S. Grätz, G. T. Tigineh, L. Borchardt, J. G. J. C. S. R. Kim, *Chem. Soc. Rev.* **2022**, *51*, 2873-2905.
[17] Y. Yang, W. Zhao, H. Niu, Y. J. A. A. M. Cai, Interfaces, *ACS Appl. Mater. Interfaces* **2021**, *13*, 42035-42043.
[18] B. P. Biswal, S. Chandra, S. Kandambeth, B. Lukose, T. Heine, R. J. J. o. t. A. C. S. Banerjee, *J. Am. Chem. Soc.* **2013**, *135*, 5328-5331.
[19] J. Maschita, T. Banerjee, G. Savasci, F. Haase, C. Ochsenfeld, B. V. J. A. C. I. E. Lotsch, *Angew. Chem. Int.* **2020**, *59*, 15750-15758.
[20] Y.-L. Wang, B. Li, S. Sarman, F. Mocci, Z.-Y. Lu, J. Yuan, A. Laaksonen, M. D. J. C. r. Fayer, *Chem. Rev.* **2020**, *120*, 5798-5877.
[21] a) A. J. Greer, J. Jacquemin, C. J. M. Hardacre, *Molecules* **2020**, *25*, 5207; b) B. Weyershausen, K. J. G. C. Lehmann, *Green Chem.* **2005**, *7*, 15-19.
[22] X. Guan, Y. Ma, H. Li, Y. Yusran, M. Xue, Q. Fang, Y. Yan, V. Valtchev, S. J. J. o. t. A. C. S. Qiu, *J. Am. Chem. Soc.* **2018**, *140*, 4494-4498.
[23] A. de la Peña Ruigómez, D. Rodríguez-San-Miguel, K. C. Stylianou, M. Cavallini, D. Gentili, F. Liscio, S. Milita, O. M. Roscioni, M. L. Ruiz-González, C. J. C. A. E. J. Carbonell, *Chem. Eur. J.* **2015**, *21*, 10666-10670.
[24] Y. Peng, W. K. Wong, Z. Hu, Y. Cheng, D. Yuan, S. A. Khan, D. J. C. o. M. Zhao, *Chem. Mater.* **2016**, *28*, 5095-5101.
[25] a) W. Ma, G. Li, C. Zhong, Y. Yang, Q. Sun, D. Ouyang, W. Tong, W. Tian, L. Zhang, Z. J. C. C. Lin, *Chem. Commun.* **2021**, *57*, 7362-7365; b) G. Lin, C. Gao, Q. Zheng, Z. Lei, H. Geng, Z. Lin, H. Yang, Z. J. C. C. Cai, *Chem. Commun.* **2017**, *53*, 3649-3652.
[26] a) E. L. Spitler, M. R. Giovino, S. L. White, W. R. J. C. S. Dichtel, *Chem. Sci.* **2011**, *2*, 1588-1593; b) A. Acharjya, P. Pachfule, J. Roeser, F. J. Schmitt, A. J. A. C. I. E. Thomas, *Angew. Chem. Int.* **2019**, *58*, 14865-14870; c) J.-C. Wang, X. Kan, J.-Y. Shang, H. Qiao, Y.-B. J. J. o. t. A. C. S. Dong, *J. Am. Chem. Soc.* **2020**, *142*, 16915-16920.
[27] a) B. Zhang, H. Mao, R. Matheu, J. A. Reimer, S. A. Alshmimri, S. Alshihri, O. M. J. J. o. t. A. C. S. Yaghi, *J. Am. Chem. Soc.* **2019**, *141*, 11420-11424; b) Y. Li, Q. Wu, X. Guo, M. Zhang, B. Chen, G. Wei, X. Li, X. Li, S. Li, L. J. N. c. Ma, *Nat. Commun.* **2020**, *11*, 1-9; c) J. Á. Martín-Illán, D. Rodríguez-San-Miguel, C. Franco, I. Imaz, D. Maspoch, J. Puigmartí-Luis, F. J. C. C. Zamora, *Chem. Commun.* **2020**, *56*, 6704-6707.
[28] B. J. Smith, A. C. Overholts, N. Hwang, W. R. J. C. C. Dichtel, *Chem. Commun.* **2016**, *52*, 3690-3693.
[29] S. Kim, H. C. J. C. C. Choi, *Commun. Chem.* **2019**, *2*, 1-8.
[30] S.-T. Yang, J. Kim, H.-Y. Cho, S. Kim, W.-S. J. R. a. Ahn, *RSC Adv.* **2012**, *2*, 10179-10181.
[31] H. Wei, S. Chai, N. Hu, Z. Yang, L. Wei, L. J. C. C. Wang, *Chem. Commun.* **2015**, *51*, 12178-12181.
[32] M. Zhang, J. Chen, S. Zhang, X. Zhou, L. He, M. V. Sheridan, M. Yuan, M. Zhang, L. Chen, X. J. J. o. t. A. C. S. Dai, *J. Am. Chem. Soc.* **2020**, *142*, 9169-9174.
[33] D. Zhu, Z. Zhang, L. B. Alemany, Y. Li, N. Nnorom, M. Barnes, S. Khalil, M. M. Rahman, P. M. Ajayan, R. J. C. o. M. Verduzco, *Chem. Mater.* **2021**, *33*, 3394-3400.
[34] Y. Liu, Y. Zhu, S. B. Alahakoon, E. J. A. M. L. Egap, *ACS Mater. Lett.* **2020**, *2*, 1561-1566.
[35] M. Matsumoto, R. R. Dasari, W. Ji, C. H. Feriante, T. C. Parker, S. R. Marder, W. R. J. J. o. t. A. C. S. Dichtel, *J. Am. Chem. Soc.* **2017**, *139*, 4999-5002.

[36] S. Karak, S. Kandambeth, B. P. Biswal, H. S. Sasmal, S. Kumar, P. Pachfule, R. J. J. o. t. A. C. S. Banerjee, *J. Am. Chem. Soc.* **2017**, *139*, 1856-1862.
[37] X. Li, C. Yang, B. Sun, S. Cai, Z. Chen, Y. Lv, J. Zhang, Y. J. J. o. M. C. A. Liu, *Chem. Mater.* **2020**, *8*, 16045-16060.
[38] L. Cusin, H. Peng, A. Ciesielski, P. J. A. C. Samorì, *Angew. Chem. Int.* **2021**, *133*, 14356-14370.
[39] H. Liu, J. Chu, Z. Yin, X. Cai, L. Zhuang, H. J. C. Deng, *Chem* **2018**, *4*, 1696-1709.
[40] P. J. Waller, S. J. Lyle, T. M. Osborn Popp, C. S. Diercks, J. A. Reimer, O. M. J. J. o. t. A. C. S. Yaghi, *J. Am. Chem. Soc.* **2016**, *138*, 15519-15522.
[41] X. Han, J. Huang, C. Yuan, Y. Liu, Y. J. J. o. t. A. C. S. Cui, *J. Am. Chem. Soc.* **2018**, *140*, 892-895.
[42] F. Haase, E. Troschke, G. Savasci, T. Banerjee, V. Duppel, S. Dörfler, M. M. Grundei, A. M. Burow, C. Ochsenfeld, S. J. N. c. Kaskel, *Nat. Commun.* **2018**, *9*, 2600.
[43] X.-T. Li, J. Zou, T.-H. Wang, H.-C. Ma, G.-J. Chen, Y.-B. J. J. o. t. A. C. S. Dong, *J. Am. Chem. Soc.* **2020**, *142*, 6521-6526.
[44] J. L. Segura, S. Royuela, M. M. J. C. S. R. Ramos, *Chem. Soc. Rev.* **2019**, *48*, 3903-3945.
[45] aN. A. Rejali, M. Dinari, Y. J. C. C. Wang, *Chem. Commun.* **2023**; bJ. H. Kim, D. W. Kang, H. Yun, M. Kang, N. Singh, J. S. Kim, C. S. J. C. S. R. Hong, *Chem. Soc. Rev.* **2022**, *51*, 43-56; cH. Ding, A. Mal, C. J. M. C. F. Wang, *Mater. Chem. Front.* **2020**, *4*, 113-127.
[46] S. J. Lyle, T. M. Osborn Popp, P. J. Waller, X. Pei, J. A. Reimer, O. M. J. J. o. t. A. C. S. Yaghi, *J. Am. Chem. Soc.* **2019**, *141*, 11253-11258.
[47] H. Lyu, H. Li, N. Hanikel, K. Wang, O. M. J. J. o. t. A. C. S. Yaghi, *J. Am. Chem. Soc.* **2022**, *144*, 12989-12995.
[48] aH. Wei, S. Chai, N. Hu, Z. Yang, L. Wei, L. J. C. C. Wang, *Chem. Commun.* **2015**, *51*, 12178-12181; bZ. Yang, D. J. T. J. o. P. C. C. Cao, *J. Phys. Chem. C* **2012**, *116*, 12591-12598; cJ.-H. Guo, H. Zhang, Z.-P. Liu, X.-L. J. T. J. o. P. C. C. Cheng, *J. Phys. Chem. C* **2012**, *116*, 15908-15917.
[49] H. Furukawa, O. M. J. J. o. t. A. C. S. Yaghi, *J. Am. Chem. Soc.* **2009**, *131*, 8875-8883.
[50] Q. Gao, X. Li, G.-H. Ning, H.-S. Xu, C. Liu, B. Tian, W. Tang, K. P. J. C. o. M. Loh, *Chem. Mater.* **2018**, *30*, 1762-1768.
[51] aJ. Li, X. Jing, Q. Li, S. Li, X. Gao, X. Feng, B. J. C. S. R. Wang, *Chem. Soc. Rev.* **2020**, *49*, 3565-3604; bY. He, N. An, C. Meng, K. Xie, X. Wang, X. Dong, D. Sun, Y. Yang, Z. J. J. o. M. C. A. Hu, *J. Mater. Chem. A* **2022**, *10*, 11030-11038; cA. Khayum M, V. Vijayakumar, S. Karak, S. Kandambeth, M. Bhadra, K. Suresh, N. Acharambath, S. Kurungot, R. J. A. a. m. Banerjee, interfaces, *ACS Appl. Mater. Int.* **2018**, *10*, 28139-28146.
[52] J. Lv, Y. X. Tan, J. Xie, R. Yang, M. Yu, S. Sun, M. D. Li, D. Yuan, Y. J. A. C. Wang, *Angew. Chem. Int.* **2018**, *130*, 12898-12902.
[53] M. Chafiq, A. Chaouiki, Y. G. J. E. S. M. Ko, *Energy Storage Mater.* **2023**, 103014.
[54] T. K. Dutta, A. J. C. A. A. J. Patra, *Chem. Asain J.* **2021**, *16*, 158-164.
[55] aY. Zhi, Z. Wang, H. L. Zhang, Q. J. S. Zhang, *Small* **2020**, *16*, 2001070; bZ. Liang, R. Shen, Y. H. Ng, Y. Fu, T. Ma, P. Zhang, Y. Li, X. J. C. C. Li, *Chem Catal.* **2022**, *2*, 2157-2228.
[56] H. Wang, H. Wang, Z. Wang, L. Tang, G. Zeng, P. Xu, M. Chen, T. Xiong, C. Zhou, X. J. C. S. R. Li, *Chem. Soc. Rev.* **2020**, *49*, 4135-4165.
[57] Y. Xu, X. Shi, R. Hua, R. Zhang, Y. Yao, B. Zhao, T. Liu, J. Zheng, G. J. A. C. B. E. Lu, *Appl. Catal. B* **2020**, *260*, 118142.

[58] X. Wang, L. Chen, S. Y. Chong, M. A. Little, Y. Wu, W.-H. Zhu, R. Clowes, Y. Yan, M. A. Zwijnenburg, R. S. J. N. C. Sprick, *Nat. Chem.* **2018**, *10*, 1180-1189.

[59] aX. Zhang, G. Li, D. Wu, B. Zhang, N. Hu, H. Wang, J. Liu, Y. J. B. Wu, Bioelectronics, *Biosens. Bioelectron.* **2019**, *145*, 111699; bH. Singh, V. K. Tomer, N. Jena, I. Bala, N. Sharma, D. Nepak, A. De Sarkar, K. Kailasam, S. K. J. J. o. M. C. A. Pal, *J. Mater. Chem. A* **2017**, *5*, 21820-21827; cH. Zuo, Y. Li, Y. J. A. a. m. Liao, interfaces, *ACS Appl. Mater. Interfaces* **2019**, *11*, 39201-39208.

[60] aY. Peng, Y. Huang, Y. Zhu, B. Chen, L. Wang, Z. Lai, Z. Zhang, M. Zhao, C. Tan, N. J. J. o. t. A. C. S. Yang, *J. Am. Chem. Soc.* **2017**, *139*, 8698-8704; bC.-Y. Zheng, H.-L. Qian, C. Yang, X.-Q. Ran, X.-P. J. A. s. Yan, *ACS Sensors* **2023**.

[61] G. Chen, H.-H. Lan, S.-L. Cai, B. Sun, X.-L. Li, Z.-H. He, S.-R. Zheng, J. Fan, Y. Liu, W.-G. J. A. a. m. Zhang, interfaces, *ACS Appl. Mater. Interfaces* **2019**, *11*, 12830-12837.

[62] M. C. Scicluna, L. J. A. A. N. M. Vella-Zarb, *ACS Appl. Nano Mater.* **2020**, *3*, 3097-3115.

[63] G. Zhang, X. Li, Q. Liao, Y. Liu, K. Xi, W. Huang, X. J. N. C. Jia, *Nat. Commun.* **2018**, *9*, 2785.

[64] X. Shi, Y. Yao, Y. Xu, K. Liu, G. Zhu, L. Chi, G. J. A. A. M. Lu, Interfaces, *ACS Appl. Mater. Int.* **2017**, *9*, 7481-7488.

[65] S. Liu, C. Hu, Y. Liu, X. Zhao, M. Pang, J. J. C. A. E. J. Lin, *Chem. Eur. J.* **2019**, *25*, 4315-4319.

[66] Y. Yu, C.-K. Chen, W.-C. Law, H. Sun, P. N. Prasad, C. J. P. C. Cheng, *Polymer Chem.* **2015**, *6*, 953-961.

[67] F. Ahmadijokani, A. Ghaffarkhah, H. Molavi, S. Dutta, Y. Lu, S. Wuttke, M. Kamkar, O. J. Rojas, M. J. A. F. M. Arjmand, *Adv. Funct. Mater.* **2023**, 2305527.

[68] E. A. Gendy, J. Ifthikar, J. Ali, D. T. Oyekunle, Z. Elkhlifia, I. I. Shahib, A. I. Khodair, Z. J. J. o. E. C. E. Chen, *J. Environ. Chem. Eng.* **2021**, *9*, 105687.

[69] S. Samajdar, S. K. Lakhera, S. J. C. Ghosh, *Chemosphere* **2023**, 141028.

[70] A. Manna, A. K. Maharana, G. Rambabu, S. Nayak, S. Basu, S. J. A. A. P. M. Das, *ACS Appl. Polym. Mater.* **2021**, *3*, 5527-5535.

[71] aS.-Y. Ding, M. Dong, Y.-W. Wang, Y.-T. Chen, H.-Z. Wang, C.-Y. Su, W. J. J. o. t. A. C. S. Wang, *J. Am. Chem. Soc.* **2016**, *138*, 3031-3037; bQ. Sun, B. Aguila, J. Perman, L. D. Earl, C. W. Abney, Y. Cheng, H. Wei, N. Nguyen, L. Wojtas, S. J. J. o. t. A. C. S. Ma, *J. Am. Chem. Soc.* **2017**, *139*, 2786-2793.

[72] Z. Rahman, V. P. J. E. m. Singh, assessment, *Environ. Monit. Assess.* **2019**, *191*, 1-21.

[73] aW. F. Fitzgerald, D. R. Engstrom, C. R. Hammerschmidt, C. H. Lamborg, P. H. Balcom, A. L. Lima-Braun, M. H. Bothner, C. M. J. E. s. Reddy, technology, *Environ. Sci. Technol.* **2018**, *52*, 7614-7620; bY. Zhang, H. Li, J. Chang, X. Guan, L. Tang, Q. Fang, V. Valtchev, Y. Yan, S. J. S. Qiu, *Small* **2021**, *17*, 2006112.

[74] aY. Li, T. Hu, R. Chen, R. Xiang, Q. Wang, Y. Zeng, C. J. C. E. J. He, *Chem. Eng. J.* **2020**, *398*, 125566; bB. Manna, C. R. J. A. S. C. Raj, Engineering, *ACS Sustain. Chem. Eng.* **2018**, *6*, 6175-6182; cN. Yousef, R. Farouq, R. J. D. Hazzaa, W. Treatment, *Desalin. Water Treat.*

2016, *57*, 21925-21938; dZ. Huang, M. Zhao, C. Wang, S. Wang, L. Dai, L. J. A. A. M. Zhang, Interfaces, *ACS Appl. Mater. Int.* **2020**, *12*, 41294-41302.

[75] aC. Ji, J. Zhang, R. Jia, W. Zhang, L. Lv, B. J. C. E. J. Pan, *Chem. Eng. J.* **2021**, *414*, 128812; bC. Ji, D. Wu, J. Lu, C. Shan, Y. Ren, T. Li, L. Lv, B. Pan, W. J. W. R. Zhang, *Water Res.* **2021**, *189*, 116599; cM. Ikram, F. Hu, G. Peng, M. Basharat, N. Jabeen, K. Pan, Y. J. A. A. M. Gao, Interfaces, *ACS Appl. Mater. Int.* **2021**, *13*, 51799-51806.

[76] aF. Lu, D. J. C. C. R. Astruc, *Coord. Chem. Rev.* **2018**, *356*, 147-164; bZ. Tauanov, J. Lee, V. J. J. o. M. L. Inglezakis, *J. Mol. Liq.* **2020**, *305*, 112825; cK. Wang, L. Yang, H. Li, F. J. A. a. m. Zhang, interfaces, *ACS Appl. Mater. Int.* **2019**, *11*, 21815-21821.
[77] aB. Li, Y. Zhang, D. Ma, Z. Shi, S. J. N. c. Ma, *Nat. Commun.* **2014**, *5*, 1-7; bS. Zhang, Y. Zhang, J. Liu, Q. Xu, H. Xiao, X. Wang, H. Xu, J. J. C. E. J. Zhou, *Chem. Eng. J.* **2013**, *226*, 30-38; cC. Ji, Y. Ren, H. Yu, M. Hua, L. Lv, W. J. C. E. J. Zhang, *Chem. Eng. J.* **2022**, *430*, 132960.
[78] M. Zhao, Z. Huang, S. Wang, L. Zhang, Y. J. A. a. m. Zhou, interfaces, *ACS Appl. Mater. Int.* **2019**, *11*, 46973-46983.
[79] S. Bao, Y. Wang, Z. Wei, W. Yang, Y. Yu, Y. J. J. o. H. M. Sun, *J. Hazard. Mater.* **2021**, *416*, 125825.
[80] G.-P. Li, K. Zhang, P.-F. Zhang, W.-N. Liu, W.-Q. Tong, L. Hou, Y.-Y. J. I. C. Wang, *Inorg. Chem.* **2019**, *58*, 3409-3415.
[81] L. Huang, Q. J. A. S. C. Shuai, Engineering, *ACS Sustain. Chem. Eng.* **2019**, *7*, 9957-9965.
[82] D. Zhang, L. Wang, H. Zeng, B. Rhimi, C. J. E. S. N. Wang, *Environ. Sci. Technol.* **2020**, *7*, 793-802.
[83] M. K. Shehab, K. S. Weeraratne, T. Huang, K. U. Lao, H. M. J. A. A. M. El-Kaderi, Interfaces, *ACS Appl. Mater. Int.* **2021**, *13*, 15083-15091.
[84] Y. Liu, Y. Ma, Y. Zhao, X. Sun, F. Gándara, H. Furukawa, Z. Liu, H. Zhu, C. Zhu, K. J. S. Suenaga, *Science* **2016**, *351*, 365-369.
[85] Q. Fang, J. Wang, S. Gu, R. B. Kaspar, Z. Zhuang, J. Zheng, H. Guo, S. Qiu, Y. J. J. o. t. A. c. s. Yan, *J. Am. Chem. Soc.* **2015**, *137*, 8352-8355.
[86] P. J. Waller, F. Gándara, O. M. J. A. o. c. r. Yaghi, *Acc. Chem. Res.* **2015**, *48*, 3053-3063.
[87] N. Li, J. Du, D. Wu, J. Liu, N. Li, Z. Sun, G. Li, Y. J. T. T. i. A. C. Wu, *Trends Anal. Chem.* **2018**, *108*, 154-166.
[88] S. Li, Y. Yang, H. Shan, J. Zhao, Z. Wang, D. Cai, P. Qin, J. Baeyens, T. J. S. Tan, P. Technology, *Sep. Purif. Technol.* **2019**, *220*, 283-292.
[89] H.-J. Da, C.-X. Yang, H.-L. Qian, X.-P. J. J. o. M. C. A. Yan, *J. Mater. Chem.* **2020**, *8*, 12657-12664.
[90] aR.-H. Xu, W.-R. Cui, C.-R. Zhang, X.-R. Chen, W. Jiang, R.-P. Liang, J.-D. J. C. E. J. Qiu, *Chem. Eng. J.* **2021**, *419*, 129550; bH.-L. Qian, M.-S. Zhu, M.-L. Du, X.-Q. Ran, X.-P. J. J. o. H. M. Yan, *J. Hazard. Mater.* **2022**, *427*, 128156.
[91] aY. Jiang, C. Liu, A. J. A. a. m. Huang, interfaces, *ACS Appl. Mater. Int.* **2019**, *11*, 32186-32191; bY. Li, C. Wang, S. Ma, H. Zhang, J. Ou, Y. Wei, M. J. A. a. m. Ye, interfaces, *ACS Appl. Mater. Int.* **2019**, *11*, 11706-11714; cL. Huang, R. Shen, R. Liu, Q. J. J. o. h. m. Shuai, *J. Hazard. Mater.* **2020**, *392*, 122320.
[92] aW.-R. Cui, W. Jiang, C.-R. Zhang, R.-P. Liang, J. Liu, J.-D. J. A. S. C. Qiu, Engineering, *ACS Sustain. Chem. Eng.* **2019**, *8*, 445-451; bJ. L. Segura, M. J. Mancheño, F. J. C. S. R. Zamora, *Chem. Soc. Rev.* **2016**, *45*, 5635-5671.
[93] A. Manna, A. K. Maharana, G. Rambabu, S. Nayak, S. Basu, S. J. A. A. P. M. Das, *ACS Appl. Mater. Int.* **2021**, *3*, 5527-5535.
[94] L. Guo, S. Jia, C. S. Diercks, X. Yang, S. A. Alshmimri, O. M. J. A. C. Yaghi, *Angew. Chem. Int.* **2020**, *132*, 2039-2043.
[95] S. Xuan, F. Wang, Y.-X. J. Wang, C. Y. Jimmy, K. C.-F. J. J. o. M. C. Leung, *J. Mater. Chem.* **2010**, *20*, 5086-5094.

[96] aM. W. Hussain, A. Giri, A. J. S. E. Patra, Fuels, *Sustain. Energy Fuels* **2019**, *3*, 2567-2571; bP. Jin, X. Niu, F. Zhang, K. Dong, H. Dai, H. Zhang, W. Wang, H. Chen, X. J. A. a. m. Chen, interfaces, *ACS Appl. Mater. Int.* **2020**, *12*, 20414-20422.
[97] X. Hou, H. Zhang, B.-C. Chen, Z. Guo, A. Singh, A. Goswami, J. L. Gilmore, J. E. Sheppeck, A. J. Dyckman, P. H. J. O. P. R. Carter, Development, *Org. Process Res. Dev.* **2017**, *21*, 200-207.
[98] aS. Mitra, H. S. Sasmal, T. Kundu, S. Kandambeth, K. Illath, D. Diaz Diaz, R. J. J. o. t. A. C. S. Banerjee, *J. Am. Chem. Soc.* **2017**, *139*, 4513-4520; bP. Wang, F. Zhou, C. Zhang, S.-Y. Yin, L. Teng, L. Chen, X.-X. Hu, H.-W. Liu, X. Yin, X.-B. J. C. s. Zhang, *Chem. Sci.* **2018**, *9*, 8402-8408.
[99] Y. Zhi, Z. Li, X. Feng, H. Xia, Y. Zhang, Z. Shi, Y. Mu, X. J. J. o. M. C. A. Liu, *J. Mater. Chem. A* **2017**, *5*, 22933-22938.
[100] aC. Gao, G. Lin, Z. Lei, Q. Zheng, J. Lin, Z. J. J. o. M. C. B. Lin, *J. Mater. Chem. B* **2017**, *5*, 7496-7503; bY. Wu, N. Sun, C. J. A. a. m. Deng, interfaces, *ACS Appl. Mater. Int.* **2020**, *12*, 9814-9823.
[101] D.-G. Wang, N. Li, Y. Hu, S. Wan, M. Song, G. Yu, Y. Jin, W. Wei, K. Han, G.-C. J. A. a. m. Kuang, interfaces, *ACS Appl. Mater. Int.* **2018**, *10*, 42233-42240.
[102] F. Taghavi, A. Khojastehnezhad, R. Khalifeh, M. Rajabzadeh, F. Rezaei, K. Abnous, S. M. J. N. J. o. C. Taghdisi, *New J. Chem.* **2021**, *45*, 15405-15414.
[103] L. Grunenberg, G. k. Savasci, M. W. Terban, V. Duppel, I. Moudrakovski, M. Etter, R. E. Dinnebier, C. Ochsenfeld, B. V. J. J. o. t. A. C. S. Lotsch, *J. Am. Chem. Soc.* **2021**, *143*, 3430-3438.
[104] M. Thommes, K. Kaneko, A. V. Neimark, J. P. Olivier, F. Rodriguez-Reinoso, J. Rouquerol, K. S. J. P. Sing, a. chemistry, *Pure Appl. Chem.* **2015**, *87*, 1051-1069.
[105] S.-L. Ji, H.-L. Qian, C.-X. Yang, X. Zhao, X.-P. J. A. a. m. Yan, interfaces, *ACS Appl. Mater. Int.* **2019**, *11*, 46219-46225.
[106] P. Das, G. Chakraborty, S. K. J. A. a. m. Mandal, interfaces, *ACS Appl. Mater. Int.* **2020**, *12*, 10224-10232.
[107] M. Zhang, R. Zheng, Y. Ma, R. Chen, X. Sun, X. J. M. Sun, M. Materials, *Microporous Mesoporous Mater.* **2019**, *285*, 70-79.
[108] F.-F. Li, W.-R. Cui, W. Jiang, C.-R. Zhang, R.-P. Liang, J.-D. J. J. o. h. m. Qiu, *J. Hazard. Mater.* **2020**, *392*, 122333.
[109] Q. Yan, H. Xu, X. Jing, H. Hu, S. Wang, C. Zeng, Y. J. R. a. Gao, *RSC Adv.* **2020**, *10*, 17396-17403.
[110] A. Shahravan, T. Desai, T. J. A. P. L. Matsoukas, *Appl. Phys. Lett.* **2012**, *101*, 251603.
[111] A. B. Albadarin, J. Mo, Y. Glocheux, S. Allen, G. Walker, C. J. C. e. j. Mangwandi, *Chem. Eng. J.* **2014**, *255*, 525-534.
[112] G. Lin, S. Wang, L. Zhang, T. Hu, J. Peng, S. Cheng, L. J. J. o. C. P. Fu, *J. Clean. Prod.* **2018**, *192*, 639-646.
[113] aG. Xu, L. Wang, Y. Xie, M. Tao, W. J. J. o. h. m. Zhang, *J. Hazard. Mater.* **2018**, *344*, 679-688; bP. L. Yap, S. Kabiri, D. N. Tran, D. J. A. a. m. Losic, interfaces, *ACS Appl. Mater. Int.* **2018**, *11*, 6350-6362; cB. Ram, G. S. J. C. E. J. Chauhan, *Chem. Eng. J.* **2018**, *331*, 587-596.
[114] I. J. J. o. t. A. C. s. Langmuir, *J. Am. Chem. Soc.* **1918**, *40*, 1361-1403.
[115] E. Zandi-Mehri, L. Taghavi, F. Moeinpour, I. Khosravi, S. J. J. o. M. L. Ghasemi, *J. Mol. Liq.* **2022**, 119407.
[116] H. J. J. P. c. Freundlich, *J. Phys. Chem.* **1906**, *57*, 1100-1107.

[117] N. Huang, L. Zhai, H. Xu, D. J. J. o. t. A. C. S. Jiang, *J. Am. Chem. Soc.* **2017**, *139*, 2428-2434.
[118] J. S. Yamani, A. W. Lounsbury, J. B. J. W. r. Zimmerman, *Water Res.* **2016**, *88*, 889-896.
[119] L. N. Pincus, H. E. Rudel, P. V. Petrović, S. Gupta, P. Westerhoff, C. L. Muhich, J. B. J. E. S. Zimmerman, Technology, *J. Environ. Sci. Technol.* **2020**, *54*, 9769-9790.
[120] K. Leus, J. P. H. Perez, K. Folens, M. Meledina, G. Van Tendeloo, G. Du Laing, P. J. F. D. Van Der Voort, *Faraday Discuss.* **2017**, *201*, 145-161.
[121] W. Ruan, H. Liu, Y. Qi, M. Zhou, H. Wu, H. J. F. Yang, *Fuel* **2022**, *319*, 123816.
[122] G. Lin, B. Zeng, X. Liu, J. Li, B. Zhang, L. J. J. o. C. P. Zhang, *J. Clean. Prod.* **2022**, *381*, 134766.
[123] F. Pan, C. Tong, Z. Wang, F. Xu, X. Wang, B. Weng, D. Pan, R. J. J. o. M. S. Zhu, Technology, *J. Mater. Sci. Technol.* **2021**, *93*, 89-95.
[124] A. Chakraborty, S. Sarkar, R. Kyarikwal, P. Nag, S. R. Vennapusa, S. J. A. A. P. M. Mukhopadhyay, *ACS Appl. Polym. Mater.* **2022**, *4*, 8118-8126.
[125] C. D. Wagner, *Handbook of x-ray photoelectron spectroscopy: a reference book of standard data for use in x-ray photoelectron spectroscopy*, Perkin-Elmer, **1979**.
[126] H. Yamamoto, K. Ishihara, *Acid Catalysis in Modern Organic Synthesis, Vol. 1*, Wiley-VCH Weinheim, **2008**.
[127] A. Kokel, C. Schäfer, B. J. C. O. S. Török, *Curr. Org. Chem.* **2019**, *16*, 615-649.
[128] P. Anastas, N. J. C. S. R. Eghbali, *Chem. Soc. Rev.* **2010**, *39*, 301-312.
[129] M. J. A. C. A. G. Timofeeva, *Appl. Catal. A: Gen.* **2003**, *256*, 19-35.
[130] G. Lin, H. Ding, D. Yuan, B. Wang, C. J. J. o. t. A. C. S. Wang, *J. Am. Chem. Soc.* **2016**, *138*, 3302-3305.
[131] J. R. Miller, P. J. s. Simon, *Science* **2008**, *321*, 651-652.
[132] T. Liu, F. Zhang, Y. Song, Y. J. J. o. M. C. A. Li, *J. Mater. Chem. A* **2017**, *5*, 17705-17733.
[133] A. Halder, M. Ghosh, A. Khayum M, S. Bera, M. Addicoat, H. S. Sasmal, S. Karak, S. Kurungot, R. J. J. o. t. A. C. S. Banerjee, *J. Am. Chem. Soc.* **2018**, *140*, 10941-10945.
[134] M. A. Hanif, S. Nisar, U. J. C. R. Rashid, *Catal. Rev.* **2017**, *59*, 165-188.
[135] Y. Wu, X. Ye, X. Yang, X. Wang, W. Chu, Y. J. I. Hu, e. c. research, *Ind. Eng. Chem. Res.* **1996**, *35*, 2546-2560.
[136] aS. Ishikawa, N. Noda, M. Wada, S. Tsurumi, W. J. A. C. Ueda, *ACS Catal.* **2020**, *10*, 10535-10545; bL. Chen, J.-T. Ren, Z.-Y. J. A. C. B. E. Yuan, *Appl. Catal. B* **2022**, *305*, 121044; cC. J. Ribeiro, M. M. Pereira, E. F. Kozhevnikova, I. V. Kozhevnikov, E. V. Gusevskaya, K. A. J. C. T. da Silva Rocha, *Catal. Today* **2020**, *344*, 166-170; dH. Eshghi, A. Khojastehnezhad, F. Moeinpour, S. Rezaeian, M. Bakavoli, M. Teymouri, A. Rostami, K. J. T. Haghbeen, *Tetrahedron* **2015**, *71*, 436-444.
[137] aM. J. da Silva, D. M. Chaves, R. C. da Silva, J. B. Gabriel Filho, C. G. O. Bruziquesi, A. A. J. C. E. S. Al-Rabiah, *Chem. Eng. J.* **2022**, *247*, 116913; bN. V. Gromov, T. B. Medvedeva, I. A. Lukoyanov, V. N. Panchenko, M. N. Timofeeva, O. P. Taran, V. N. J. C. Parmon, *Catalysts* **2022**, *12*, 1252; cH. Eshghi, A. Khojastehnezhad, F. Moeinpour, M. Bakavoli, S. M. Seyedi, M. J. R. a. Abbasi, *RSC Adv.* **2014**, *4*, 39782-39789.
[138] aE. Hamzehpoor, C. Ruchlin, Y. Tao, C.-H. Liu, H. M. Titi, D. F. J. N. C. Perepichka, *Nat. Chem.* **2023**, *15*, 83-90; bA. M. Evans, I. Castano, A. Brumberg, L. R. Parent, A. R. Corcos, R. L. Li, N. C. Flanders, D. J. Gosztola, N. C. Gianneschi, R. D. J. J. o. t. A. C. S. Schaller, *J. Am. Chem. Soc.* **2019**, *141*, 19728-19735.
[139] aD. L. Pastoetter, S. Xu, M. Borrelli, M. Addicoat, B. P. Biswal, S. Paasch, A. Dianat, H. Thomas, R. Berger, S. J. A. C. I. E. Reineke, *Angew. Chem. Int.* **2020**, *59*, 23620-23625;

bC.-P. Niu, C.-R. Zhang, X. Liu, R.-P. Liang, J.-D. J. N. C. Qiu, *Nat. Commun.* **2023**, *14*, 4420.
[140] A. Khojastehnezhad, F. Moeinpour, M. Jafari, M. K. Shehab, A. Samih ElDouhaibi, H. M. El-Kaderi, M. J. A. A. M. Siaj, Interfaces, *ACS Appl. Mater. Int.* **2023**.
[141] Y. Li, W. Chen, W. Hao, Y. Li, L. J. A. A. N. M. Chen, *ACS Appl. Nano Mater.* **2018**, *1*, 4756-4761.
[142] aR. Luo, R. Liu, Y. Li, Y. Li, C. J. C. He, *Cellulose* **2022**, *29*, 2553-2563; bL. Lan, F. Liu, Y. Dan, L. J. N. J. o. C. Jiang, *New J. Chem.* **2020**, *44*, 2986-2995.
[143] D. Sun, Y. Ke, T. M. Mattox, B. A. Ooro, H.-C. J. C. c. Zhou, *Chem. Commun.* **2005**, 5447-5449.
[144] R. Chen, T. Hu, W. Zhang, C. He, Y. J. M. Li, M. Materials, *Microporous Mesoporous Mater.* **2021**, *312*, 110739.
[145] aG. Das, D. B. Shinde, S. Kandambeth, B. P. Biswal, R. J. C. C. Banerjee, *Chem. Commun.* **2014**, *50*, 12615-12618; bS. Kandambeth, A. Mallick, B. Lukose, M. V. Mane, T. Heine, R. J. J. o. t. A. C. S. Banerjee, *J. Am. Chem. Soc.* **2012**, *134*, 19524-19527.
[146] X. Feng, X. Ding, D. J. C. S. R. Jiang, *Chem. Soc. Rev.* **2012**, *41*, 6010-6022.
[147] aT. Ma, L. Wei, L. Liang, S. Yin, L. Xu, J. Niu, H. Xue, X. Wang, J. Sun, Y.-B. J. N. C. Zhang, *Nat. Commun.* **2020**, *11*, 6128; bF. J. Uribe-Romo, J. R. Hunt, H. Furukawa, C. Klock, M. O'Keeffe, O. M. J. J. o. t. A. C. S. Yaghi, *J. Am. Chem. Soc.* **2009**, *131*, 4570-4571; cT. Ma, E. A. Kapustin, S. X. Yin, L. Liang, Z. Zhou, J. Niu, L.-H. Li, Y. Wang, J. Su, J. J. S. Li, *Science* **2018**, *361*, 48-52.
[148] Y. Chen, Z.-L. Shi, L. Wei, B. Zhou, J. Tan, H.-L. Zhou, Y.-B. J. J. o. t. A. C. S. Zhang, *J. Am. Chem. Soc.* **2019**, *141*, 3298-3303.
[149] F. J. Uribe-Romo, J. R. Hunt, H. Furukawa, C. Klöck, M. O'Keeffe, O. M. J. J. o. t. A. C. S. Yaghi, *J. Am. Chem. Soc.* **2009**, *131*, 4570-4571.
[150] aH. Cheng, F. Yi, A. Gao, H. Liang, D. Shu, X. Zhou, C. He, Z. J. A. A. E. M. Zhu, *ACS Appl. Energy Mater.* **2019**, *2*, 4084-4091; bL. Wan, R. Xiao, J. Liu, Y. Zhang, J. Chen, C. Du, M. J. A. S. S. Xie, *Appl. Surf. Sci.* **2020**, *518*, 146265.
[151] A. Khayum M, V. Vijayakumar, S. Karak, S. Kandambeth, M. Bhadra, K. Suresh, N. Acharambath, S. Kurungot, R. Banerjee, *ACS applied materials & interfaces* **2018**, *10*, 28139-28146.
[152] S. Umezawa, T. Douura, K. Yoshikawa, Y. Takashima, M. Yoneda, K. Gotoh, V. Stolojan, S. R. P. Silva, Y. Hayashi, D. Tanaka, *Carbon* **2021**, *184*, 418-425.
[153] T. K. Dutta, A. Patra, *Chemistry–An Asian Journal* **2021**, *16*, 158-164.
[154] aZ. Chen, S. Zhao, Y. Zhou, C. Yu, W. Zhong, W. J. N. Yang, *Nanoscale* **2018**, *10*, 15229-15237; bM. Zhou, F. Pu, Z. Wang, S. J. C. Guan, *Carbon* **2014**, *68*, 185-194.
[155] aD. Antiohos, K. Pingmuang, M. S. Romano, S. Beirne, T. Romeo, P. Aitchison, A. Minett, G. Wallace, S. Phanichphant, J. J. E. A. Chen, *Electrochim. Acta* **2013**, *101*, 99-108; bL. Li, F. Lu, R. Xue, B. Ma, Q. Li, N. Wu, H. Liu, W. Yao, H. Guo, W. J. A. a. m. Yang, interfaces, *ACS Appl. Mater. Int.* **2019**, *11*, 26355-26363.
[156] F. Xu, R. Cai, Q. Zeng, C. Zou, D. Wu, F. Li, X. Lu, Y. Liang, R. J. J. o. M. C. Fu, *J. Mater. Chem.* **2011**, *21*, 1970-1976.
[157] L. Miao, D. Zhu, M. Liu, H. Duan, Z. Wang, Y. Lv, W. Xiong, Q. Zhu, L. Li, X. J. C. E. J. Chai, *Chem. Eng. J.* **2018**, *347*, 233-242.
[158] X.-Q. He, Y.-Y. Cui, C.-X. J. A. A. M. Yang, Interfaces, *ACS Appl. Mater. Int.* **2021**, *13*, 39905-39914.

[159] aR. Dawson, D. J. Adams, A. I. J. C. S. Cooper, *Chem. Sci.* **2011**, *2*, 1173-1177; bM. H. Kim, J. Choi, K. C. Ko, K. Cho, J. H. Park, S. M. Lee, H. J. Kim, Y.-J. Ko, J. Y. Lee, S. U. J. C. C. Son, *Chem. Commun.* **2018**, *54*, 5134-5137; cX. Zhuang, F. Zhang, D. Wu, N. Forler, H. Liang, M. Wagner, D. Gehrig, M. R. Hansen, F. Laquai, X. J. A. C. I. E. Feng, *Angew. Chem. Int.* **2013**, *52*, 9668-9672.

[160] L. Stadler, M. Homafar, A. Hartl, S. Najafishirtari, M. Colombo, R. Zboril, P. Martin, M. B. Gawande, J. Zhi, O. J. A. S. C. Reiser, Engineering, *ACS Sustain. Chem. Eng.* **2018**, *7*, 2388-2399.

[161] S. Shylesh, V. Schuenemann, W. R. J. A. C. I. E. Thiel, *Angew. Chem. Int.* **2010**, *49*, 3428-3459.

[162] R. A. J. G. C. Sheldon, *Green Chem.* **2017**, *19*, 18-43.

[163] A. K. Sharma, P. Mehara, P. J. A. C. Das, *ACS Catal.* **2022**, *12*, 6672-6701.

[164] Z. Khorsandi, A. R. Hajipour, M. R. Sarfjoo, R. S. J. G. C. Varma, *Green Chem.* **2021**, *23*, 5222-5229.

[165] aS. Luo, Z. Zeng, G. Zeng, Z. Liu, R. Xiao, M. Chen, L. Tang, W. Tang, C. Lai, M. J. A. a. m. Cheng, interfaces, *ACS Appl. Nano Mater.* **2019**, *11*, 32579-32598; bS. Bera, F. Banerjee, S. K. J. A. A. N. M. Samanta, *ACS Appl. Nano Mater.* **2023**.

[166] aH. S. Lee, J. Choi, J. Jin, J. Chun, S. M. Lee, H. J. Kim, S. U. J. C. C. Son, *Chem. Commun.* **2012**, *48*, 94-96; bJ. Chun, J. H. Park, J. Kim, S. M. Lee, H. J. Kim, S. U. J. C. o. M. Son, *Chem. Mater.* **2012**, *24*, 3458-3463; cJ. Chun, S. Kang, N. Park, E. J. Park, X. Jin, K.-D. Kim, H. O. Seo, S. M. Lee, H. J. Kim, W. H. J. J. o. t. A. C. S. Kwon, *J. Am. Chem. Soc.* **2014**, *136*, 6786-6789.

[167] aN. Miyaura, T. Yanagi, A. J. S. C. Suzuki, *Synth. Commun.* **1981**, *11*, 513-519; bD. Shen, Y. Xu, S.-L. J. J. o. t. A. C. S. Shi, *J. Am. Chem. Soc.* **2019**, *141*, 14938-14945; cP. Ruiz-Castillo, S. L. J. C. r. Buchwald, *Chem. Rev.* **2016**, *116*, 12564-12649.

[168] J. P. Wolfe, R. A. Singer, B. H. Yang, S. L. J. J. o. t. A. C. S. Buchwald, *J. Am. Chem. Soc.* **1999**, *121*, 9550-9561.

[169] aJ. K. J. A. C. I. E. i. E. Stille, *Angew. Chem. Int.* **1986**, *25*, 508-524; bÁ. J. C. r. Molnár, *Chem. Rev.* **2011**, *111*, 2251-2320; cA. M. Dreis, C. J. J. J. o. t. A. C. S. Douglas, *J. Am. Chem. Soc.* **2009**, *131*, 412-413; dM. Bahadori, S. Tangestaninejad, M. Moghadam, V. Mirkhani, A. Mechler, I. Mohammadpoor-Baltork, F. J. M. Zadehahmadi, M. Materials, *Micropor. Mesopor. Mat.* **2017**, *253*, 102-111; eL. Zhang, H. Yu, S. Gao, H. Wang, Z. He, K. J. C. E. J. Huang, *Chem. Eng. J.* **2021**, *423*, 130237; fK. Hong, M. Sajjadi, J. M. Suh, K. Zhang, M. Nasrollahzadeh, H. W. Jang, R. S. Varma, M. J. A. A. N. M. Shokouhimehr, *ACS Appl. Nano Mater.* **2020**, *3*, 2070-2103.

[170] N. Miyaura, K. Yamada, A. J. T. L. Suzuki, *Tetrahedron Lett.* **1979**, *20*, 3437-3440.

[171] T. Vlaar, E. Ruijter, R. V. J. A. S. Orru, Catalysis, *Adv. Synth. Catal.* **2011**, *353*, 809-841.

[172] A. O. King, N. Okukado, E.-i. J. J. o. t. C. S. Negishi, *Chem. Commun.* **1977**, 683-684.

[173] K. J. J. o. o. c. Sonogashira, *J. Organomet. Chem.* **2002**, *653*, 46-49.

[174] K. Tamao, K. Sumitani, M. J. J. o. t. A. C. S. Kumada, *J. Am. Chem. Soc.* **1972**, *94*, 4374-4376.

[175] aR. Martin, S. L. J. A. o. c. r. Buchwald, *Acc. Chem. Res.* **2008**, *41*, 1461-1473; bK. Surana, B. Chaudhary, M. Diwaker, S. J. M. Sharma, *MedChemComm* **2018**, *9*, 1803-1817; cJ.-C. Wang, C.-X. Liu, X. Kan, X.-W. Wu, J.-L. Kan, Y.-B. J. G. C. Dong, *Green Chem.* **2020**, *22*, 1150-1155; dM. Bazmi, S. Askari, E. Ghasemy, A. Rashidi, E. J. J. o. T. A. Ettefaghi, Calorimetry, *J. Therm. Anal. Calorim.* **2019**, *138*, 69-79.

[176] Z.-D. Du, Y.-Y. Cui, C.-X. Yang, X.-P. J. A. A. N. M. Yan, *ACS Appl. Nano Mater.* **2019**, *2*, 1232-1241.
[177] W. Li, B. Zhang, X. Li, H. Zhang, Q. J. A. C. A. G. Zhang, *Appl. Catal. A* **2013**, *459*, 65-72.
[178] Q. Sun, C. Wu, Q. Pan, B. Zhang, Y. Liu, X. Lu, J. Sun, L. Sun, Y. J. C. Zhao, *ChemNanoMat* **2021**, *7*, 95-99.
[179] P. S. Roy, J. Bagchi, S. K. J. C. Bhattacharya, S. A. Physicochemical, E. Aspects, *Colloids Surf. A: Physicochem. Eng.* **2010**, *359*, 45-52.
[180] X.-Q. He, Y.-Y. Cui, X.-H. Lin, C.-X. J. T. Yang, *Talanta* **2021**, *233*, 122471.
[181] G. K. Reddy, C. Ling, T. C. Peck, H. J. R. a. Jia, *RSC Adv.* **2017**, *7*, 19645-19655.
[182] H. Zhang, Q. Hu, J. Liu, P. Zhang, S. Fu, S. J. A. A. N. M. Wu, *ACS Appl. Nano Mater.* **2022**.
[183] aN. Nouruzi, M. Dinari, B. Gholipour, M. Afshari, S. J. A. A. N. M. Rostamnia, *ACS Appl. Nano Mater.* **2022**, *5*, 6241-6248; bG. Kumar, R. S. Pillai, H. K. Noor-ul, S. J. A. C. B. E. Neogi, *Appl. Catal. B* **2021**, *292*, 120149.
[184] aD. Mandal, K. J. Kim, J. S. J. L. Lee, *Langmuir* **2012**, *28*, 10310-10317; bC.-H. Liao, J.-Y. Chen, G.-Y. Liu, Z.-R. Xu, S. Lee, C.-K. Chiang, Y.-T. J. A. o. Hsieh, *ACS Omega* **2022**, *7*, 19930-19938; cJ. Liu, H. Zhan, N. Wang, Y. Song, C. Wang, X. Wang, L. Ma, L. J. A. A. N. M. Chen, *ACS Appl. Nano Mater.* **2021**, *4*, 6239-6249.
[185] L. Zhong, J. Zhang, Q. Zhang, M. Chen, Z. J. R. a. Huang, *RSC Adv.* **2017**, *7*, 39244-39257.
[186] D. J. Kiemle, R. M. Silverstein, F. X. Webster, *Identification spectrométrique de composés organiques-3ème édition*, De Boeck Superieur, **2016**.
[187] aC. Ling, F.-Q. Liu, C. Xu, T.-P. Chen, A.-M. J. A. a. m. Li, interfaces, *ACS Appl. Mater. Int.* **2013**, *5*, 11808-11817; bM. J. Laudenslager, J. D. Schiffman, C. L. J. B. Schauer, *Biomacromolecules* **2008**, *9*, 2682-2685.
[188] S. Chatterjee, S. K. J. A. o. Bhattacharya, *ACS Omega* **2018**, *3*, 12905-12913.
[189] aA. Roucoux, J. Schulz, H. J. C. r. Patin, *Chem. Rev.* **2002**, *102*, 3757-3778; bJ. R. Heath, C. M. Knobler, D. V. J. T. J. o. P. C. B. Leff, *J. Phys. Chem. B* **1997**, *101*, 189-197.
[190] J. Yang, Y. Wu, X. Wu, W. Liu, Y. Wang, J. J. G. C. Wang, *Green Chem.* **2019**, *21*, 5267-5273.
[191] S.-Y. Ding, J. Gao, Q. Wang, Y. Zhang, W.-G. Song, C.-Y. Su, W. J. J. o. t. A. C. S. Wang, *J. Am. Chem. Soc.* **2011**, *133*, 19816-19822.
[192] I. Romero-Muñiz, A. Mavrandonakis, P. Albacete, A. Vega, V. Briois, F. Zamora, A. E. J. A. C. I. E. Platero-Prats, *Angew. Chem. Int.* **2020**, *59*, 13013-13020.
[193] Y. Hou, X. Zhang, J. Sun, S. Lin, D. Qi, R. Hong, D. Li, X. Xiao, J. J. M. Jiang, M. Materials, *Microporous Mesoporous Mater.* **2015**, *214*, 108-114.
[194] Z.-L. Du, Q.-Q. Dang, X.-M. J. I. Zhang, E. C. Research, *Ind. Eng. Chem. Res.* **2017**, *56*, 4275-4280.
[195] X. Le, Z. Dong, Z. Jin, Q. Wang, J. J. C. C. Ma, *Catal. Commun.* **2014**, *53*, 47-52.
[196] aL. Guo, K. J. Lamb, M. J. G. C. North, *Green Chem.* **2021**, *23*, 77-118; bJ. Zhang, C. D. Sewell, H. Huang, Z. J. A. E. M. Lin, *Adv. Energy Mater.* **2021**, *11*, 2170186; cY. Ma, X. Yi, S. Wang, T. Li, B. Tan, C. Chen, T. Majima, E. R. Waclawik, H. Zhu, J. J. N. c. Wang, *Nat. Commun.* **2022**, *13*, 1-10; dS. Wang, M. Xu, T. Peng, C. Zhang, T. Li, I. Hussain, J. Wang, B. J. N. c. Tan, *Nat. Commun.* **2019**, *10*, 1-10.
[197] aJ. Artz, T. E. Müller, K. Thenert, J. Kleinekorte, R. Meys, A. Sternberg, A. Bardow, W. J. C. r. Leitner, *Chem. Rev.* **2018**, *118*, 434-504; bW. K. Fan, M. J. C. E. J. Tahir, *Chem. Eng. J.* **2022**, *427*, 131617.

[198] aZ. Zhan, H. Wang, Q. Huang, S. Li, X. Yi, Q. Tang, J. Wang, B. J. S. Tan, *Small* **2022**, *18*, 2105083; bC. Liu, L. Yang, J. Zhang, J. J. I. C. F. Sun, *Inorg. Chem. Front.* **2020**, *7*, 1140-1147.
[199] aR. Yan, K. Chen, Z. Li, Y. Qu, L. Gao, H. Tong, Y. Li, J. Li, Y. Hu, K. J. C. Guo, *ChemSusChem* **2021**, *14*, 738-744; bT. Sakakura, J.-C. Choi, H. J. C. r. Yasuda, *Chem. Rev.* **2007**, *107*, 2365-2387.
[200] M. Li, Z. Sun, Y. H. J. J. o. M. C. A. Hu, *J. Mater. Chem.* **2021**, *9*, 12495-12520.
[201] Y. Ni, Z. Chen, Y. Fu, Y. Liu, W. Zhu, Z. J. N. c. Liu, *Nat. Commun.* **2018**, *9*, 1-7.
[202] K. Cai, P. Liu, P. Chen, C. Yang, F. Liu, T. Xie, T. J. J. o. C. U. Zhao, *J. CO2 Util.* **2021**, *51*, 101658.
[203] aC. Liu, L. Shi, J. Zhang, J. J. C. E. J. Sun, *Chem. Eng. J.* **2022**, *427*, 131633; bX. Zhang, J. Wang, Y. Bian, H. Lv, B. Qiu, Y. Zhang, R. Qin, D. Zhu, S. Zhang, D. J. J. o. C. U. Li, *J. CO2 Util.* **2022**, *58*, 101924; cN. Haque, S. Biswas, S. Ghosh, A. H. Chowdhury, A. Khan, S. M. J. A. A. N. M. Islam, *ACS Appl. Nano Mater.* **2021**, *4*, 7663-7674.
[204] P. P. J. C. O. i. G. Pescarmona, S. Chemistry, *Curr. Opin. Green Sustain. Chem.* **2021**, *29*, 100457.
[205] aM. Cokoja, C. Bruckmeier, B. Rieger, W. A. Herrmann, F. E. J. A. C. I. E. Kühn, *Angew. Chem. Int.* **2011**, *50*, 8510-8537; bF. Moeinpour, R. Khalifeh, M. Rajabzadeh, F. Rezaei, S. J. C. L. Javdan, *Catal. Lett.* **2022**, 1-12; cE. Liu, J. Zhu, W. Yang, F. Liu, C. Huang, S. J. A. A. N. M. Yin, *ACS Appl. Nano Mater.* **2020**, *3*, 3578-3584.
[206] aD. C. J. P. i. O. C. Webster, *Prog. Org. Coat.* **2003**, *47*, 77-86; bF. Tabarkhoon, H. Abolghasemi, A. Rashidi, M. Bazmi, M. S. Alivand, F. Tabarkhoon, M. V. Farahani, M. D. J. C. E. J. Esrafili, *Chem. Eng. J.* **2023**, *456*, 140973.
[207] D. Bai, H. J. G. C. Jing, *Green Chem.* **2010**, *12*, 39-41.
[208] aA. B. Paninho, A. N. Mustapa, K. T. Mahmudov, A. J. Pombeiro, M. F. C. Guedes da Silva, M. D. Bermejo, Á. Martín, M. J. Cocero, A. V. J. C. Nunes, *Catalysts* **2021**, *11*, 872; bP. H. Boushehri, A. Hafizi, M. Rahimpour, R. J. T. i. C. Khalifeh, *Top. Catal.* **2021**, 1-12.
[209] aJ.-R. Li, C. Chen, X.-B. Liu, Y.-L. J. E. S. Hu, P. Research, *Environ. Sci. Pollut. Res.* **2022**, *29*, 83247-83261; bX. B. Liu, Q. Rong, J. Tan, C. Chen, Y. L. J. F. i. C. Hu, *Front. Chem.* **2022**, *9*, 1220; cY. L. Hu, J. R. Li, C. Chen, X. B. Liu, Q. J. S. C. Rong, Pharmacy, *Sustain. Chem. Pharm.* **2022**, *29*, 100779.
[210] aO. Sodpiban, C. Phungpanya, S. Del Gobbo, S. Arayachukiat, T. Piromchart, V. J. C. E. J. D'Elia, *Chem. Eng. J.* **2021**, *422*, 129930; bZ. Wang, Y. Wang, Q. Xie, Z. Fan, Y. J. N. J. o. C. Shen, *New J. Chem.* **2021**, *45*, 9403-9408; cO. Sodpiban, S. Del Gobbo, S. Barman, V. Aomchad, P. Kidkhunthod, S. Ould-Chikh, A. Poater, V. D'Elia, J.-M. J. C. S. Basset, Technology, *Catal. Sci. Technol.* **2019**, *9*, 6152-6165; dV. Aomchad, S. Del Gobbo, P. Yingcharoen, A. Poater, V. J. C. T. D'Elia, *Catal. Today* **2021**, *375*, 324-334; eS. Arayachukiat, C. Kongtes, A. Barthel, S. V. Vummaleti, A. Poater, S. Wannakao, L. Cavallo, V. J. A. S. C. D'Elia, Engineering, *ACS Sustain. Chem. Eng.* **2017**, *5*, 6392-6397.
[211] aV. Polshettiwar, R. Luque, A. Fihri, H. Zhu, M. Bouhrara, J.-M. J. C. r. Basset, *Chem. Rev.* **2011**, *111*, 3036-3075; bD. Wang, D. J. C. R. Astruc, *Chem. Rev.* **2014**, *114*, 6949-6985.
[212] Q. Zhang, X. Yang, J. J. A. A. N. M. Guan, *ACS Appl. Nano Mater.* **2019**, *2*, 4681-4697.
[213] J. X. Jiang, F. Su, A. Trewin, C. D. Wood, N. L. Campbell, H. Niu, C. Dickinson, A. Y. Ganin, M. J. Rosseinsky, Y. Z. J. A. C. Khimyak, *Angew. Chem. Int.* **2007**, *119*, 8728-8732.

[214] aM. Trunk, A. Herrmann, H. Bildirir, A. Yassin, J. Schmidt, A. J. C. A. E. J. Thomas, *Chem. Eur. J.* **2016**, *22*, 7179-7183; bY.-Y. Cui, H.-B. Ren, C.-X. Yang, X.-P. J. C. E. J. Yan, *Chem. Eng. J.* **2019**, *368*, 589-597.
[215] Z. Zhang, L. Sun, Z. Wu, Y. Liu, S. J. N. J. o. C. Li, *New J. Chem.* **2020**, *44*, 6420-6427.
[216] M. S. Usman, N. A. Ibrahim, K. Shameli, N. Zainuddin, W. M. Z. W. J. M. Yunus, *Molecules* **2012**, *17*, 14928-14936.
[217] D. Zhu, L. Wang, W. Yu, H. J. s. r. Xie, *Sci. Rep.* **2018**, *8*, 1-12.
[218] K. Wang, X. Dong, C. Zhao, X. Qian, Y. J. E. A. Xu, *Electrochim. Acta* **2015**, *152*, 433-442.
[219] Z.-D. Du, Y.-Y. Cui, C.-X. Yang, X.-P. J. T. Yan, *Talanta* **2020**, *206*, 120179.
[220] aX. Li, W. Kong, X. Qin, F. Qu, L. J. M. A. Lu, *Microchim. Acta* **2020**, *187*, 1-9; bP. Wang, Y. H. Ng, R. J. N. Amal, *Nanoscale* **2013**, *5*, 2952-2958; cG. Panzeri, M. Cristina, M. Jagadeesh, G. Bussetti, L. J. S. r. Magagnin, *Sci. Rep.* **2020**, *10*, 1-10.
[221] aS. Liu, Q. Zou, Y. Ma, W. Sun, Y. Li, J. Zhang, C. Zhang, L. He, Y. Sun, Q. J. J. o. M. S. Chen, *J. Mater. Sci.* **2020**, *55*, 16171-16183; bZ. Zhou, P. Zhao, C. Wang, P. Yang, Y. Xie, J. J. M. A. Fei, *Microchim. Acta* **2020**, *187*, 1-9.
[222] B. Lim, J. Jin, J. Yoo, S. Y. Han, K. Kim, S. Kang, N. Park, S. M. Lee, H. J. Kim, S. U. J. C. C. Son, *Chem. Commun.* **2014**, *50*, 7723-7726.
[223] aY. Pu, Y. Luo, X. Wei, J. Sun, L. Li, W. Zou, L. J. A. C. B. E. Dong, *Appl. Catal. B* **2019**, *254*, 580-586; bM. A. Nasseri, S. A. Alavi, M. Kazemnejadi, A. J. R. a. Allahresani, *RSC Adv.* **2019**; cB. Wang, G. Yang, Q. Yang, B. Li, D. Wang, Y. Peng, J. Li, C. Lu, J. J. A. A. M. Crittenden, Interfaces, *ACS Appl. Mater. Int.* **2021**, *13*, 27106-27118.
[224] M. Aresta, A. Dibenedetto, L. Gianfrate, C. Pastore, *J. Mol. Catal.* **2003**, *204*, 245-252.
[225] P. R. Tambe, G. D. Yadav, *Clean Technol. Environ. Policy* **2018**, *20*, 345-356.
[226] W.-L. Dai, S.-F. Yin, R. Guo, S.-L. Luo, X. Du, C.-T. Au, *Catal. Lett.* **2010**, *136*, 35-44.
[227] D. Prasad, K. N. Patil, J. T. Bhanushali, B. M. Nagaraja, A. H. Jadhav, *Catal. Sci. Technol.* **2019**, *9*, 4393-4412.
[228] Y.-L. Wu, G.-P. Yang, S. Cheng, J. Qian, D. Fan, Y.-Y. Wang, *ACS Appl. Mater. Int.* **2019**, *11*, 47437-47445.
[229] Y. Zhi, P. Shao, X. Feng, H. Xia, Y. Zhang, Z. Shi, Y. Mu, X. Liu, *J. Mater. Chem.* **2018**, *6*, 374-382.
[230] R. Khalifeh, M. Karimi, M. Rajabzadeh, A. Hafizi, F. S. Nogorani, *J. CO2 Util.* **2020**, *41*, 101233.